Elucidating the mechanism of AP axis alignment in the *C. elegans* embryo

DISSERTATION

zur Erlangung des akademischen Grades

Doctor rerum naturalium
(Dr. rer. nat.)

vorgelegt

dem Bereich Mathematik und Naturwissenschaften
der Technischen Universität Dresden

von

B.Tech. Archit Bhatnagar

eingereicht am 28.03.2023

Die Dissertation wurde in der Zeit von September 2018 bis März 2023
Max-Planck-Institut für molekulare Zellbiologie und Genetik angefertigt.

To my parents and sister...

Abbreviations

AP Anteroposterior

ATP Adenosine Tri-Phosphate

MTOC Microtubule-organizing center

NMY-2 Non-Muscle myosin II

RNA Ribonucleic acid

RNAi RNA mediated interference

GFP Green Fluorescent Protein

PAR Partitioning defective

aPARs Anterior PAR proteins

pPARs Posterior PAR proteins

NGM Nematode Growth Medium

BF BrightField

dsRNA Double-stranded RNA

FIJI Fiji Is Just ImageJ

PIV Particle Image Velocimetry

MATLAB MATrix LABoratory

TUB Tubulin

Abstract

Development of a single-cell embryo into an adult multi-cellular organism features the establishment of upto three anatomical body axes - anteroposterior, dorsoventral and left-right. It has been observed in many organisms that these body axes can consistently orient relative with respect to the geometric features of the embryo in many organisms. One such example is observed in the model organism *Caenorhabditis elegans* (*C. elegans*), where the Anteroposterior (AP) axis coincides with the geometric long axis of the ellipsoidal embryo – the shape being imposed by the surrounding eggshell. In *C. elegans*, the AP axis is established at the one-cell stage via its polarization by PAR polarity proteins. This cell polarization proceeds via a self-organized mechanochemical feedback between the PAR proteins and mechanical flows in the actomyosin cortex, resulting in the formation of two mutually exclusive domains of Anterior PAR proteins and Posterior PAR proteins proteins on the cortex denoting the future anterior and posterior end of the embryo – and thus establishing the AP axis. The initial orientation of the AP axis is determined by the site of sperm entry at fertilization. However, the nascent AP axis that forms after fertilization is observed to actively re-orient – indicated by the movement of the PAR domains and concurrent migration (here termed posteriorisation) of the sperm-donated male pronucleus – such that it aligns with the long axis of the ellipsoidal embryo, if it is not already aligned. In effect, the site of sperm entry only determines which half of the embryo becomes the posterior half of the embryo. This phenomenon of active re-orientation of the AP axis, that ensures that the AP axis aligns with the long axis of the embryo, is termed AP axis alignment. The work described in this thesis investigates the mechanism of this AP axis alignment in the *C. elegans* embryo.

Anterior-directed flows in the actomyosin cortex observed during AP axis establishment have also been found to be essential for AP axis alignment. In this thesis, two possible mechanisms of AP axis alignment are considered, both of which are consequences of these cortical flows. Cortical flows at the embryo surface can drive flows in the bulk cytoplasm in the embryo, generating cytoplasmic flows which point towards the sperm-donated male pronucleus as it posteriorises. Previous studies have proposed that these cytoplasmic flows could push onto the male pronucleus, and due to the ellipsoidal geometry of the embryo, drive it towards the closest tip of the embryo. This proposed mechanism is referred to as the cytoplasmic flow-dependent mechanism in this thesis. Another mechanism proposed in this thesis postulates that the reorientation of the AP axis occurs via the repositioning of the pseudocleavage furrow. The pseudocleavage furrow is a contractile ring-like structure that forms at the boundary of the two PAR domains during AP axis establishment. The pseudocleavage furrow forms as a result of compressive alignment of actin filaments in the actomyosin cortex due to cortical flows. In cases where the AP axis is not aligned with the long axis of the embryo, the pseudocleavage furrow is not perpendicular to the long axis of the embryo. In such cases, active anisotropic stresses generated in the actomyosin cortex could force the rotation of the pseudocleavage furrow akin to an elastic rubber-band on an ellipsoid, and cause the AP axis to re-orient towards the long axis of the embryo. This proposed mechanism is referred to as the pseudocleavage furrow-dependent mechanism in this thesis.

This thesis investigates the role played by the two mechanisms in AP axis alignment. This is accomplished in the following way: a theoretical model of the AP axis alignment is introduced, consisting of a description of the actomyosin cortex as an active nematic fluid present on the 2D surface of a fixed ellipsoid representing the embryo. This description of the cortex incorporates both the cytoplasmic flow-dependent mechanism and the pseudocleavage furrow-dependent mechanism. RNAi experiments in the *C. elegans* embryo that remove the pseudocleavage furrow, in conjuction with numerical simulations using the theoretical model, show that the pseudocleavage furrow-dependent mechanism is the predominant mechanism that drives AP axis alignment, while cytoplasmic flow-dependent mechanism plays only a minor role. RNAi experiments that modify the geometry of the *C. elegans* embryo – specifically, generate rounder embyros – show that embryo geometry can influence the rate of re-orientation of the AP axis during AP axis alignment – with slower AP axis alignment in rounder embryos. Such an relation between embryo geometry and AP axis alignment is found to be consistent with pseudocleavage furrow-dependent mechanism, both via predictions made using the theoretical model and using a simplified effective model of a contractile ring (or elastic rubber-band) on a fixed ellipsoid.

Altogether, the work presented in this thesis shows AP axis alignment observed in the *C. elegans* embryo is driven primarily by the anisotropic stresses in the actomyosin cortex that generate the pseudocleavage furrow. The work here also shows that the AP axis alignment process is sensitive to the geometry of the embryo. In effect, active mechanical flows in the actomyosin cortex translate the ellipsoidal geometry of the embryo into a robust orientation of the AP axis of the *C. elegans* embryo. Mechanical flows such as these are not exclusive to *C. elegans*, nor are specific orientations of the body axes with respect to the embryo geometry. The results in this thesis thus point towards a possibly general role of the interactions between mechanical flows and embryo geometry to properly orient the body axes of the developing embryos of many multi-cellular organisms.

Contents

List of Figures

Chapter 1

Introduction

Development of a multi-cellular organism typically starts with a one-cell embryo. This one cell, generated as a result of fertilization (i.e. fusing of the male and female gametes), divides to give rise to the multiple cells and cell types that would eventually form the adult organism. A key question is how the correct arrangement of cells achieved. During development, upto three body axes: anterior-posterior (head-tail), dorsal-ventral (back-front) and left-right, are established. By patterning along these established body axes, proper arrangement of cells can be ensured during development [2].

Thus, the body axes serve as the system of spatial axes that allow the embryo to specify position of cells. How are then these body axes established? For many organisms, the embryos start out with few initial asymmetries. Instead, external cues – such as site of sperm (i.e. male gamete) entry, unequal cell division patterns, and gravity – are utilized to break the symmetry in the embryo and initiate the establishment of body axes [2]. Mechanical forces coupled together with chemical patterns translate these external cues into an internal asymmetry of the embryo, by reorganizing certain determinants in the embryo [2, 3]. As the embryo grows, this unequal distribution of determinants spans across the embryo, thus establishing a body axis [4, 5].

It has been observed that the orientation of body axes is relatively fixed with respect to the geometric features of the embryo in many organisms (Figure 1.1). For example, in many nematodes (roundworms; see Figure 1.1a for an example in *C. elegans*) the Anteroposterior axis is established at the one-cell stage, and forms along the long axis of the ellipsoidal embryo [2, 6]. In insect embryos such as fruit flies (see Figure 1.1b for an example in *Drosophila*), the AP axis forms along the long axis of oocyte [2, 7–10]. In chick embryos, Von Baer's rule indicates that the AP axis typically forms perpendicular to the long axis of the egg [2, 11], but this can be entrained by gravity [12]. In mouse embryos (see Figure 1.1c), the AP axis initially forms along the axis of the cylindrically-shaped implanted embryo, but then is re-aligned to be along its short axis and transverse to its initial location [13–16].

How does this orientation with respect to geometry achieved? Given that mechanical forces are involved in the establishment of body axes, could it be possible that the mechanical forces involved in body axes establishment play a role in achieving this relative orientation? Studies in the mouse embryo seem to suggest so [14–16], but how do mechanical forces enforce this relative orientation is not understood. In this thesis, this problem is studied in the the context of AP axis establishment in the *C. elegans* embryo - a nematode. The aim of this thesis is to understand the mechanism(s) that ensure the alignment of the AP axis of the *C. elegans* embryo along the long axis of the ellipsoidal embryo.

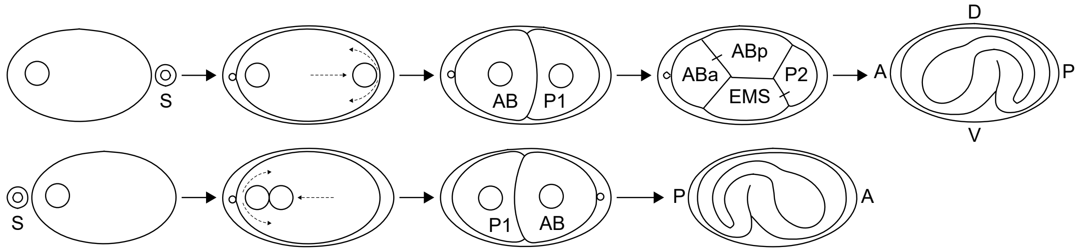

(a) AP axis in *C. elegans* establishes along the long axis of the ellipsoidal embryo, with posterior half determined by site of sperm entry [6]. S denotes the sperm at fertilization; AB, P1, ABa, ABp, P2, EMS are names of subsequent blastomeres in embryogenesis (see subsection 1.3.1 and [17]). Top: Sperm enters on the right, away from the female pronucleus – leading to an embryo with anterior on the left and posterior on the right. Bottom: Sperm enters on the left – leading to an embryo with anterior on the right and posterior on the left. DV indicates dorso-ventral axis. Adapted from [2]

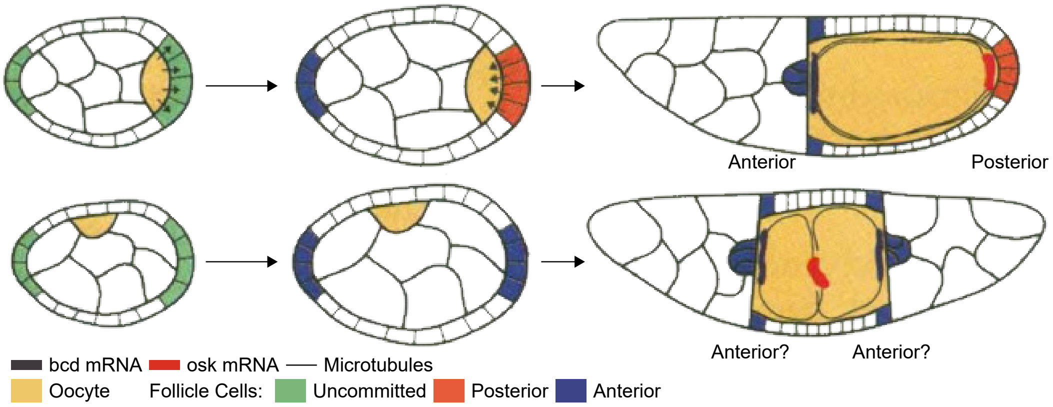

(b) AP axis in *Drosophila* is established along the long axis during oogenesis, with posterior half determined by location of oocyte within the germline cyst [10]. Top: in the usual case, the oocyte migrates towards the posterior of the cyst, specifying the posterior follicle cells that help determine the posterior end. Bottom: if this migration does not occur, no AP axis is established. Adapted from [10]

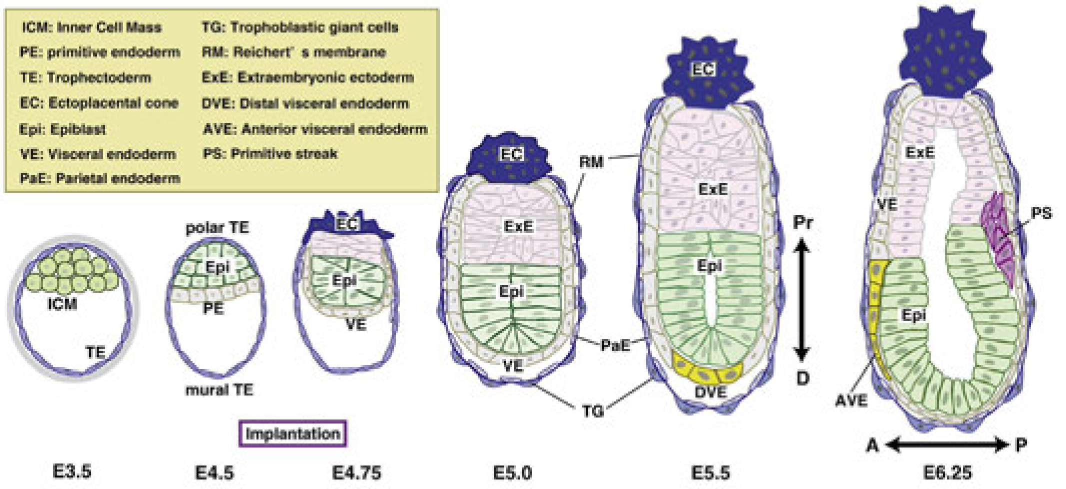

(c) AP axis in mouse is established during uterine implantation. Initial AP axis forms along the long axis (Proximal-Distal) of the cylindrical embryo, indicated by the emergence of distal visceral endoderm (DVE) cells at E5.5. AP axis reorients to the short axis as the DVE cells migrate to the lateral side, forming anterior visceral endoderm (AVE). Adapted from [16]

Figure 1.1: Comparing orientation of AP axes with embryo geometry in different model organisms: *C. elegans*, *Drosophila*, and mouse

In this chapter, the general features of the cytoskeleton in eukaryotic cells are first introduced. The actomyosin cortex, an important higher-order structure of cytoskeletonal elements present in almost all eukaryotic cells, is also described. Next, hydrodynamic theory of active matter is introduced – the theoretical framework which will be used to model the actomyosin cortex in chapter 2. Next, the model organism used in this thesis is introduced: *Caenorhabditis elegans*. The early development of *C. elegans* embryo is described, with focus on the establishment of AP axis in the one-cell stage of the *C. elegans* embryo. Next, the phenomenon of AP axis alignment – the active reorientation of the AP axis such that it aligns with the geometric long axis of the ellipsoidal embryo – is described. Possible mechanisms of AP axis alignment which have been suggested in previous studies, and explored in this thesis, are described. Finally, an overview of the thesis is provided – encapsulating the work done in this thesis on elucidating the mechanism of AP axis alignment in *C. elegans* embryo.

1.1 Cytoskeleton

As noted above, mechanics plays an important role in the establishment of body axes. Cells thus need to react to the mechanics of their surrounding, and modify their own mechanical properties in response to different stimuli. The structure that allows cells to actively modify their mechanical properties, and perform mechanical tasks, is the cytoskeleton [18–20]. It is essential in many cellular processes: maintaining cell shape [18, 21, 22], driving locomotion [20], and cell division [18, 23]. Its role is to provide the cell with a dynamic mechanical scaffolding, allowing the cell to act as a highly adaptive mechanical entity to achieve different tasks [18–20].

The cytoskeleton is commonly defined as a network of protein filaments that extend throughout the cytoplasm of eukaryotic cells, although analogous filaments have also been identified in prokaryotes [24]. This meshwork of filaments is complemented by motor proteins that exert force betwen the filaments, crosslinking proteins that tie these filaments in the meshwork and various associated proteins that modify and remodel the meshwork [18–20]. In this section, the elements that make up the cytoskeleton in the eukaryotic cells are introducted. Also introduced is the actomyosin cortex, a thin layer of cytoskeletonal elements present just below the cell membrane [18, 25], and the primary force-generating mechanical structure that this thesis focuses on.

1.1.1 Main constituents of the cytoskeleton

Protein Filaments

Protein filaments provide the backbone of the cytoskeleton. In eukaryotic cells, the cytoskeleton is composed of three principal types of protein filaments: actin filaments, intermediate filaments and microtubules. Monomeric protein subunits build each of these filaments. In contrast to usual polymers, these filaments are held together by non-covalent bonds, allowing fast assembly and disassembly [18].

Actin filaments

Actin filaments (or F-actin) are right-handed double helix composed of two protofilaments, each being a chain of actin monomers (or G-actin) [26, 27] (see Figure 1.2a). Actin filaments are thin, with a typical diameter of around 7 nm [28], and flexible, with a typical persistence length of 17 µm [29, 30]. The pitch of the helix formed by the protofilaments is typically around 37 nm. Polymerisation of actin filaments is fueled by hydrolysis of Adenosine Tri-Phosphate (ATP) at the binding site on the monomers as they bind to the filament [31]. Actin filaments are structurally polar, with a defined (+) or barbed end where new monomers preferentially bind, and a (-) or pointed end where monomers preferentially unbind [26, 27, 32]. Thus, actin filaments can undergo tread-milling, regulated by ATP [33].

Actin filaments often gets organized into higher-order structure, such as the actomyosin cortex (described below), to perform various functions such as migration [34], cell division [35] and control of cell shape [36].

Microtubules

Microtubules are rigid hollow rod-like polymers, formed by the polymerization of a dimer of two globular proteins, α-tubulin and β-tubulin [18, 37] (see Figure 1.2b). These dimers polymerize to form linear protofilaments that associate laterally to form the microtubule [18]. Slight offset between protofilaments generates a pseudo-helical structure [38]. The typical “13-3” arrangement, composed of 13 protofilaments with 3 dimer offset between neighbouring pairs, has a diameter of approximately 25 nm, and a persistence length of approx 5 mm [18, 30, 39, 40] – practically rigid in most cells, given their typical sizes. Similar to actin filaments, microtubules are also polar, with a fast growing (+) end and a slow growing (-) end [41]. Microtubules serve various functions such as providing mechanical support, facilitating cell migration and locomotion [42], acting as pathways for intracellular transport [18], and centering of the mitotic spindle [43–45].

Centrosome: Microtubules usually are nucleated at, and extend outwards from, a Microtubule-organizing center (MTOC), to which the (-) ends are attached. In animal cells, the major MTOC is the centrosome, typically present near the nucleus when the cell is not dividing. At mitosis (i.e. when the cell is dividing), the centrosome duplicates [18]. In most animal cells, a centrosome consists of a pair of cylinders (centrioles) surrounded by a meshwork of pericentriolar material [46]. Complexes of γ-tubulin in the centrosome serve as the nucleation sites for microtubule assembly [47]. In many animals, centrosomes play an important role in the formation of the mitotic spindle, an array of microtubules and associated proteins responsible for proper segregation of genetic material in the daughter cells after division [18, 48].

Intermediate filaments

Different cell types also produce other filaments, with a typical diameter of 10 nm. They typically play a structural role and provide mechanical support – see [18, 22] for a more detailed review.

Motor proteins

Motor proteins convert the chemical energy released in ATP hydrolysis into mechanical work [18, 19, 49, 50]. Motor proteins are categorized into three super-families, distinguished by the type of filaments they bind to. *Myosins* are motors associated with actin filaments, while *kinesins* and *dyenins* bind to microtubules instead [18]. Molecular motors perform various functions [18], such as cargo transport [51] and serving as force generators for contraction of large-scale structures [50, 52].

Generally, motor proteins share a common set of “mechanical parts”: a track on which the motor walks (typically the protein filaments), some fuel (typically ATP), a transducer and force generator that converts the chemical energy of the fuel into a “power stroke” to generate mechanical force and a lever that transmits that force to the track [53]. This is illustrated using the example of a particular myosin - NMY-2, which is a major component of the actomyosin cortex.

Non-Muscle myosin II

Non-Muscle myosin II (NMY-2) is a member of the myosin super-family of motor proteins, and therefore a molecular motor that acts on actin filaments (see Figure 1.2c). It is a major contractile protein of non-muscle eukaryotic cells [18, 54]. NMY-2 forms a hexamer consisting of three pairs of polypeptides: two heavy chains, two regulatory light chains involved in regulation of NMY-2 activity and two essential light chains which stabilize the heavy chain conformation [54, 55]. Each heavy chain has a motor domain on one end (N-terminus) that binds to actin filament and ATP, followed by a neck domain to which the regulatory light chains bind, and a coiled-coil domain on the other end (C-terminus) that facilitates dimerization of the heavy chain [54–56]. NMY-2 usually organizes into myosin minifilaments, consists of around 28 NMY-2 units [54, 55].

How does the NMY-2 motor generate force? As depicted in Figure 1.2d, when not bound to ATP myosin has a strong affinity to actin filament. ATP binding leads to dissociation of the motor domain from the actin filaments, and ATP hydrolysis ensues. During this step, the neck domain bends, allowing the motor domain to sample sites on the actin filaments. As myosin binds again to the filament, the products of ATP hydrolysis are released, resulting in the force generating step (that is, the power stroke) that displaces the motor along the filament with 5 nm displacement, and returns it back to the initial state [56–59]. Thus, the motor domains act as the transducer and force generators, the neck domain as the lever, the actin filament as the track and ATP as fuel for the NMY-2 motor [53, 56]. NMY-2 is a non-processive motor (it only makes one step before it detaches from the track [50, 53]) with a low duty cycle (fraction of time spent bound to actin filament [50, 53]) [60, 61]. Minifilaments of NMY-2 can slide actin filaments past each other, by creating force dipoles [55, 62, 63]. NMY-2 also serves as an actin crosslinker [64–66].

Associated proteins

Most of the known cytoskeletal proteins are neither filamentenous nor motors. Instead, they modify and interact with the existing protein filaments and motors, to dynamically alter the mechanical properties of the cytoskeleton. A comprehensive overview of the these proteins and their functions is presented in [18, 26]; here only a brief review of some of the important functions these proteins fulfill is presented.

Nucleators help initiate the formation of protein filaments, by providing a nucleation point. *Capping proteins* bind to the ends of filaments, blocking polymerisation at the end where they bind. These proteins thus can either stabilise or de-stabilise a protein filament, depending on where they bind. *Severing proteins* cut filaments. *Crosslinkers* and *bundling proteins* organize protein filaments into structured networks, and modify them. *Sequestering proteins* help with recycling unbound monomers, while *Sidebinding proteins* act as molecular rulers. *Linkers* link

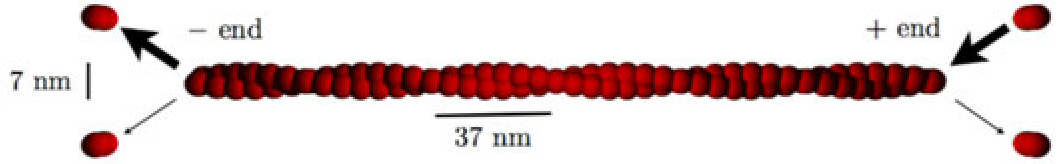

(a) Sketch of an actin filament, red circles denote monomeric G-actin. Arrows indicate rate of chemical reaction at each end. Adapted from [67]

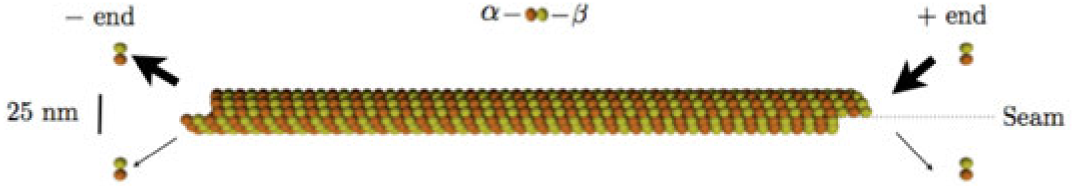

(b) Sketch of a “13-3” microtubule, composed of α and β tubules. Arrows indicate rate of chemical reaction at each end. Adapted from [67]

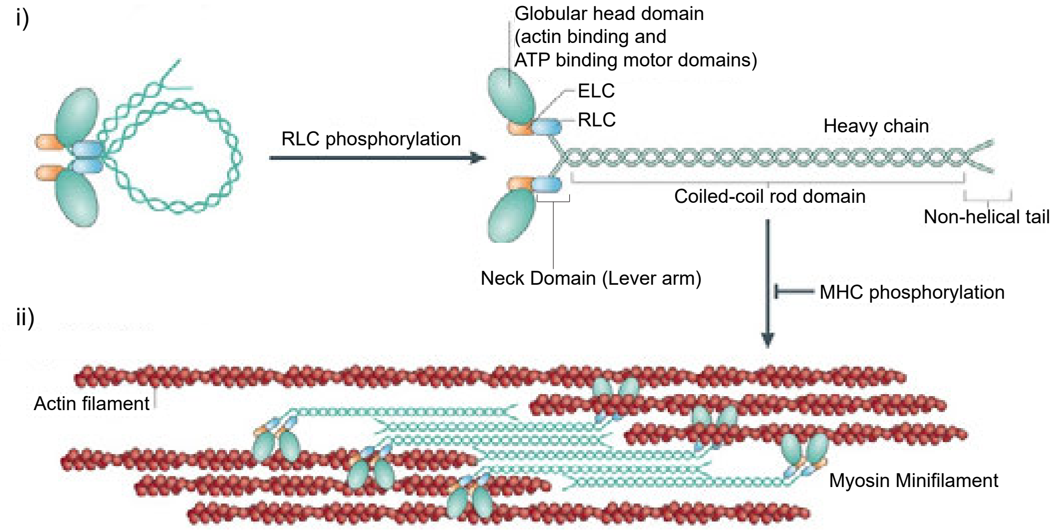

(c) Schematic of the forms of NMY-2 motor protein. i) NMY-2 converts from inactive state (left) to active state (right) via phosphorylation. Active state has three domains: the globular head containing the motor and actin binding domains, the neck domain or lever arm, and a long coiled-coil domain of heavy chains. ii) NMY-2 can assemble into bipolar filaments – myosin minifilaments – and can slide antiparallel actin filaments past each other. Adapted from [55]

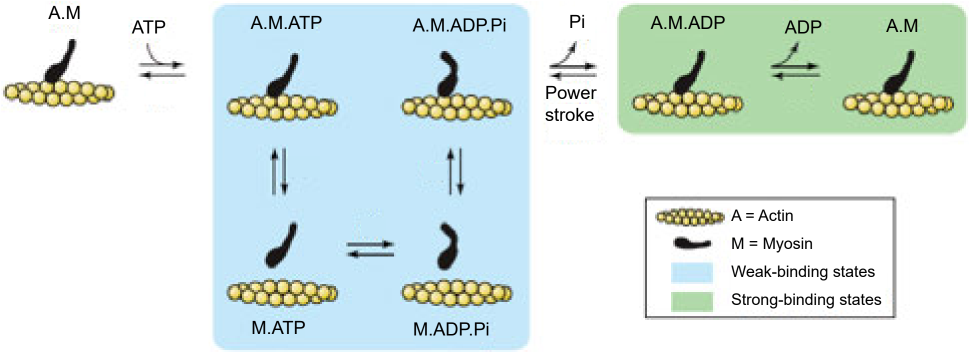

(d) Schematic of the power stroke of NMY-2. Refer to text for details on power stroke. Adapted from [57]

Figure 1.2: Main constituents of the cytoskeleton in eukaryotic cells

filaments of different kinds, allowing different filaments (such as the microtubules and actin filaments) to influence each other. *Regulators* regulate the action of other proteins. Note that individual proteins can have multiple functions, and thus belong to multiple categories.

1.1.2 Actomyosin cortex

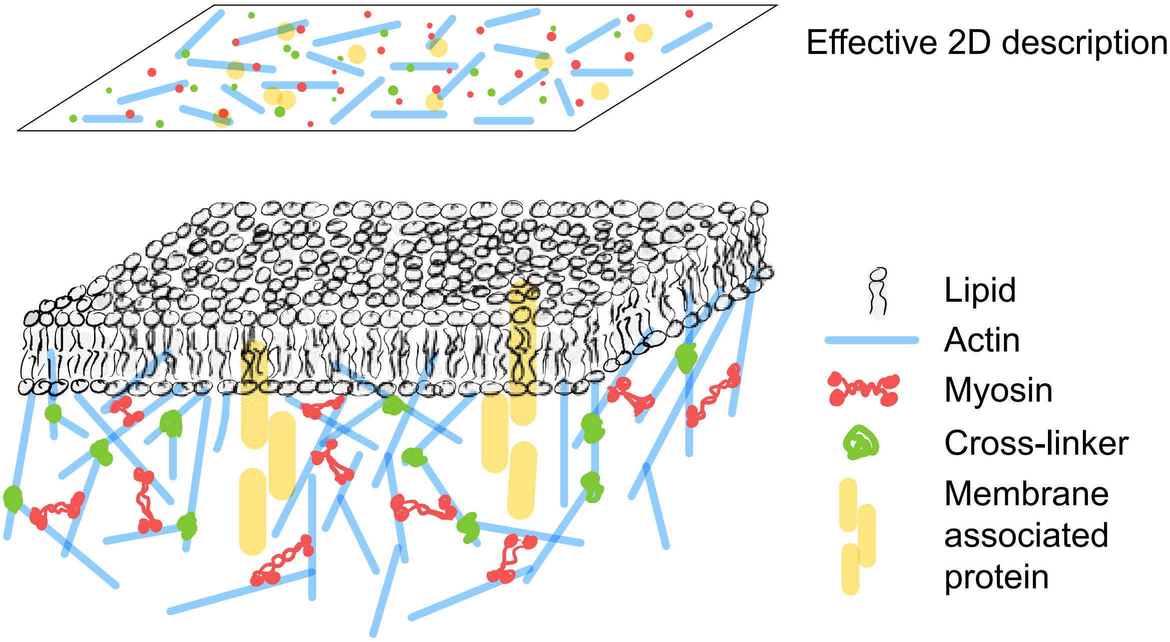

Figure 1.3: Sketch of the actomyosin cortex as a quasi-2D polymeric meshwork of actin filaments below the cell membrane (composed of lipids) and interspersed with myosin motors and other proteins. Top represents an effective 2D representation of the actomyosin cortex that could be obtained by averaging over the thickness of the cortex. Adapted from [68]

The actomyosin cortex, also called the cell cortex, is a thin (around few hundred nanometers [69]) polymeric meshwork of cross-linked actin filaments, interspersed with myosin motors and associated proteins, that lies just below the cell membrane of most eukaryotic cells [18, 70] (see Figure 1.3). Analysis using cryo-electron tomography and atomic force microscopy revealed that actin filaments organize in both isotropic meshworks and actin bundles [71–75].

The cortex is not, however, a static structure – ATP hydrolysis fuels the polymerization and de-polymerization of actin filaments, activity of the associated proteins, and force generation by myosin motors. This external energy input and resultant active remodeling of the cortex drives it far from equilibrium, and makes it a very dynamic structure. This highly cross-linked and dynamic nature of the cortex makes it behave like a viscoelastic material [25, 68], as confirmed by laser ablation experiments [76, 77]. In live cells, the active remodeling in the cortex occurs on timescales of around 30 s [78], and elastic stresses relax on comparable timescales [76]. As a consequence, the cortex can effectively be considered as a viscous fluid on longer timescales. Force generation by myosin motors confer the cortex with a tendency to actively contract [52] – the actomyosin cortex can thus be considered as active viscous fluid.

Actomyosin cortex helps the cell to adapt to changing environmental conditions by controlling cell mechanics. The cortex determines the stiffness of the cell surface, and opposes osmotic pressure [79]. Global increase in contractility of the cortex facilitates the rounding of the cell before its division [80]. Local changes in cortex contractility can create gradients of cortical tension. Such changes can aid in cell migration, via retraction of the rear of the cell from the substrate [55]. Developmental processes at the tissue scale can also be directed by the cortex of the constituent cells [81] – such as dorsal closure in *Drosophila* [82] and convergence extension in *Xenopus* [83]. section 1.4 discusses how local changes in contractility in the one-cell stage *C. elegans* embryo drive flows in the actomyosin cortex of the *C. elegans* embryo, and what role these cortical flows play in the AP axis establishment of *C. elegans* [77].

1.2 Hydrodynamic theory of active fluids

As discussed in the previous section, the actomyosin cortex can and has been modelled as an active viscous fluid in many previous studies [25, 68, 76–78, 84, 85]. General physical principles that govern the behaviour of active biological materials such as the actomyosin cortex can be identified using a hydrodynamic approach [3, 25, 84–91]. By its generic nature, such an approach is not unique to the actomyosin cortex, and has been used to describe other active materials such as bird flocks [92–94], swarms of hydrodynamically interacting swimmers [95, 96], active polar gels [85, 87, 89–91, 97], active nematic fluids [85, 90, 98–100] and active solids [85, 101–103]. While the microscopic mechanisms at play in these different active materials can differ considerably, in the hydrodynamic limit – that is, on large length and long time-scales compared to the microscopic mechanisms of the active material at hand – general properties of active materials are described by a general hydrodynamic theory corresponding to conservation laws and broken continuous symmetries in the material [85–87, 90, 91]. In such a theory, a small set of phenomenological coefficients capture the details of the microscopic mechanisms at play in the particular active material under consideration.

This section reviews the general hydrodynamic theory of active fluids based on irreversible thermodynamics. This hydrodynamic theory is a generalization of the hydrodynamics and statistical mechanics of liquid crystals [104] to systems maintained away from thermodynamic equilibrium by chemical processes driven by fuel(s) provided in external reservoir(s). In the context of the actomyosin cortex, ATP may serve the role of such a chemical fuel – utilized by myosin motors to generate mechanical forces in the cortex. Hydrodynamic equations that govern the properties of active fluids can be obtained systematically, by first identifying the conjugate pairs of thermodynamic fluxes and forces. Constitutive material relations can then be expressed via a linear coupling between the thermodynamic fluxes and forces, respecting the Onsager reciprocity relation [105–108] and Curie symmetry principle [109] Phenomenological constants that capture various microscopic processes appear in these constitutive relations. This section closely follows the description presented in [67, 85, 86].

At a microscopic level, any active fluid is made up of a large number N of discrete molecules, each with individual mass, position and velocity. A description of the fluid in microscopic details requires that all of the $6N$ degrees of freedoms be tracked, which is infeasible for any active fluid given the large number of molecules involved. Instead, a coarse-grained description of the active fluid is utilized – in which the fluid is divided into a large number of small volume elements, each of volume V. Using this description, densities of molecular components, momentum and energy can be defined for each volume element. To obtain a continuous description of these densities, the continuum limit is considered. Under this limit, the volume $V \to 0$, with the understanding that the volume still remains large compared to the molecular length scales of the fluid at hand. It is assumed that this continuum limit can always be considered. Altogether, this allows the properties of the active fluid to be described by continuous functions: such as mass density $\rho = \rho(\vec{r})$, flow velocity $\vec{v} = \vec{v}(\vec{r})$ etc. (where $\vec{r}$ is the position vector). The aim of the general hydrodynamic theory reviewed here is to derive dynamic equations for these continuous functions representing the local properties of the active fluid.

Note that Einstein summation is used throughout this section – summation over repeated indices is implied. Greek alphabet indices assume values x, y, z – corresponding to the three spatial axes.

1.2.1 Conservation Laws

Mass, momentum, angular momentum and energy are conserved quantities, at all scales – microscopic or macroscopic. This also remains valid in active fluids. Thus, local conservation laws, expressed in terms of the coarsed-grained properties of the active fluid, can be written.

Mass conservation

Consider a fixed volume V within the fluid, with boundary Ω, with mass density (mass per unit volume) ρ and flow velocity $\vec{v}$ at any given position $\vec{r}$. Then, the flux of mass flowing out of this fluid is given by:

$$\text{Mass flux outwards} = \int_\Omega \rho\vec{v} \cdot \mathrm{d}\vec{\Omega}$$

However, since mass is conserved within this volume, this flux must match the change in total mass of the volume of fluid. Thus,

$$\int_\Omega \rho\vec{v} \cdot \mathrm{d}\vec{\Omega} = -\frac{\mathrm{d}}{\mathrm{d}t}\int_V \rho \,\mathrm{d}V = -\int_V \frac{\partial \rho}{\partial t}\,\mathrm{d}V$$

where t is time. The exchange of derivative and integral is allowed since V is fixed. Note that this is true for any arbitrary volume V – however small or big. Thus, using Gauss' theorem, the following continuity equation can be written:

$$\partial_t \rho + \partial_\alpha (\rho v_\alpha) = 0 \tag{1.1}$$

The mass flux – that is, momentum density – is thus given by $g_\alpha = \rho v_\alpha$

Energy conservation

Similar to mass density, an energy density e can be defined for the active fluid. Energy conservation implies that e obeys the following continuity equation:

$$\partial_t e + \partial_\alpha J^{(e)}_\alpha = 0 \tag{1.2}$$

where $\vec{J}^{(e)}$ is the energy flux. This flux term can be split into two parts: a convective flux $e\vec{v}$ and a relative flux $\vec{j}^{(e)}$:

$$J^{(e)}_\alpha = e v_\alpha + j^{(e)}_\alpha \tag{1.3}$$

This relative flux $\vec{j}^{(e)}$ describes the flux of energy in a co-moving reference frame with respect to the volume element at the given position in the fluid. Thus, this relative flux denotes the intrinsic changes in energy density at a given position in the fluid, separate from the changes in energy density caused due to exchange with surrounding volume elements.

Momentum and Angular Momentum conservation

As noted earlier, the momentum density is given by $g_\alpha = \rho v_\alpha$. Momemtum conservation then requires that the following continuity equation is obeyed:

$$\partial_t g_\alpha + \partial_\beta \left(g_\alpha v_\beta \right) = \partial_\beta \sigma_{\alpha\beta} \tag{1.4}$$

Here, the momentum flux due to convection is $g_\alpha v_\beta$. The total change in momentum of any volume element must match the forces applied onto it on its surface – which is given by the stress $\sigma_{\alpha\beta}$. Using Gauss' theorem leads to Equation 1.4.

Similar continuity equations for angular momentum can also be considered – as presented in [67, 85]. However, note that for a non-trivial continuity equation for angular momentum, there must be intrinsic (or spin) angular momentum in the active fluid under consideration. For simplicity, it is assumed that the active fluid under consideration does not have any such intrinsic angular momentum – both in this section and in chapter 2. Thus, angular momentum is conserved, and consequently stress $\sigma_{\alpha\beta}$ is symmetric.

Also, using Equation 1.1 and Equation 1.4 along with $g_\alpha = \rho v_\alpha$ yields:

$$\rho \left(\partial_t v_\alpha + v_\beta \partial_\beta v_\alpha \right) = \partial_\beta \sigma_{\alpha\beta} \tag{1.5}$$

Particle number conservation

The general case of a multi-species active fluid consisting of $N+1$ different species of particles is first considered. In this fluid, the particle number density (number of particles per unit volume) for species i is denoted as $n^{(i)}$, with $i = 0, \ldots, N$. Using the same method as above, the continuity equation for $n^{(i)}$ can be written as:

$$\partial_t n^{(i)} + \partial_\alpha J_\alpha^{(i)} = r^{(i)} \tag{1.6}$$

where $\vec{J}^{(i)}$ is the flux of particles of species i, and $r^{(i)}$ the reaction rate accounting for all the chemical reactions in which species i participates. Note that the number of particles of species i is not conserved in the presence of chemical reactions (that is, a non-zero $r^{(i)}$).

The flux term $\vec{J}_\alpha^{(i)}$ can be split into a convective flux $n^{(i)} v_\alpha$ and a relative flux $\vec{j}^{(i)}$:

$$J_\alpha^{(i)} = n^{(i)} v_\alpha + j_\alpha^{(i)} \tag{1.7}$$

This relative flux $\vec{j}^{(i)}$ describes the movements of species i relative to the volume element at the given position in the fluid – and thus relative to the local flow of the fluid. Since the mass density can expressed in terms of $n^{(i)}$ as $\rho = \sum_{i=0}^{N} m^{(i)} n^{(i)}$ (where $m^{(i)}$ is the mass of

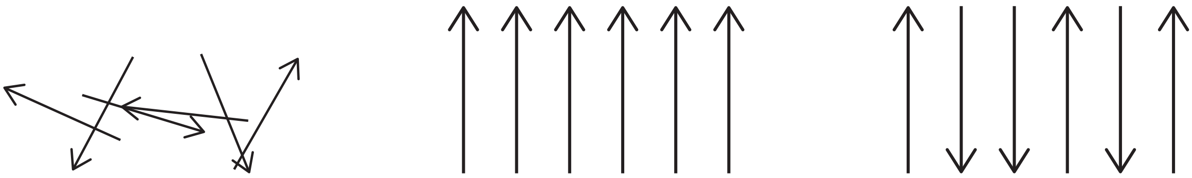

(a) Isotropic ordering. $\|\vec{p}\| = 0; \quad \|\vec{n}\| = 0$

(b) Polar ordering. $\|\vec{p}\| = 1; \quad \|\vec{n}\| = 1$

(c) Nematic ordering. $\|\vec{p}\| = 0; \quad \|\vec{n}\| = 1$

Figure 1.4: Continuous broken symmetries in complex fluids. The arrows represent the microscopic orientation $\vec{a}$ of the particles that constitute the fluid. The system is in isotropic state in Figure 1.4a due to the random orientation of $\vec{a}$, in a polar state in Figure 1.4b due to the orientation vectors $\vec{a}$ being aligned and parallel and in a nematic state in Figure 1.4c due to the orientation vectors $\vec{a}$ being aligned but anti-parallel.

each particle of species i), mass conservation Equation 1.1 and particle number conservation Equation 1.6 dictate that:

$$\sum_{i=0}^{N} m^{(i)} j_\alpha^{(i)} = 0, \quad \text{and} \quad \sum_{i=0}^{N} m^{(i)} r^{(i)} = 0$$

with the latter of the two corresponding to the Laviosier's principle of mass conservation in chemical reactions. Using these, the relative flux and reactive rate for one species can be expressed in terms of those for other species. Choosing $i = 0$ yields $j_\alpha^{(0)} = -\frac{1}{m^{(0)}} \sum_{i=1}^{N} m^{(i)} j_\alpha^{(i)}$ and $r^{(0)} = -\frac{1}{m^{(0)}} \sum_{i=1}^{N} m^{(i)} r^{(i)}$. Thus, $\vec{j}^{(0)}$ and $r^{(0)}$ can be eliminated. For M linearly independent chemical reactions, additional M relations between the species – based on the chemical reactions under considerations – can also be derived. Thus, for an active fluid with $N + 1$ species involved in M reactions, $N - M$ independent conservation laws can be obtained for the species number densities $n^{(i)}$. Note that none of the species $i = 0, \ldots, N$ are part of fuel(s) in the external reservoir. For any such fuel species, the above considerations may not apply due to the reservoir.

For the rest of this discussion, a simpler version of active fluids is assumed – a three component fluid with the fluid particles, fuel molecules and their reaction products. Furthermore, it is assumed that the concentrations of the fuel and reaction products in the fluid are kept constant via contact with the external reservoir, thus implying $\vec{j}^{(i)} = 0$. The fluid is then kept out of equilibrium by consumption of the chemical fuel at a fixed reaction rate r. In the context of the actomyosin cortex, this scenario represents the simplest description of consumption of ATP (as fuel) by myosin motors – with the local reaction rate r of ATP hydrolysis proportional to the local myosin concentration.

1.2.2 Continuously broken symmetries

In complex active fluids, the constituent molecules can be anisotropic. Many active fluids in biological systems are complex fluids – such as the actomyosin cortex, in which the actin filaments are structurally polar (see subsection 1.1.1). Arrangement or bundling of these actin filaments can further break local symmetry – creating polar or nematic order throughout the fluid.

In the context of the hydrodynamic theory discussed here, this effect can be captured by endowing each of the constituent particles of the active fluid with an orientation unit vector $\vec{a}$. Note that these orientation vector are a property of each particle – and is thus not a coarse-grained variable that can be directly used in the hydrodynamic theory. Instead, coarse-grained variables can be derived by inspecting the local distribution of these orientation vectors in a volume element at the position of interest. If all the moments of the local distribution of $\vec{a}$ (that is, within the volume element) vanish, the fluid is isotropic – and thus does not possess any local order. This is the case for all simple fluid, and with many active fluids. Consequently, locally ordered fluids have non-vanishing moments.

If the first moment of the local distribution of $\vec{a}$ is non-zero, the fluid has a polar order. For each volume element, a polarity vector $\vec{p}$ can be then defined as the first moment:

$$\vec{p}(\vec{r}) = \langle \vec{a} \rangle_{\text{Volume element at } \vec{r}} \tag{1.8}$$

where the average is taken in the volume element at the position $\vec{r}$. Under the continuum limit, the polarity vector is a continuous vector function defined at each position and is the coarse-grained order parameter that characterises the local polar order in the active fluid. At any given position, the polarity vector has magnitude of 1 if the underlying orientation vectors in the volume element are perfectly aligned and parallel. The polarity vector is $\vec{0}$ for an isotropic fluid, or if the orientation vectors are aligned but anti-parallel.

If the second moment of the local distribution of $\vec{a}$ is non-zero, the fluid has a nematic order. For each volume element, a nematic tensor $Q_{\alpha\beta}$ can be then defined as the second moment:

$$Q_{\alpha\beta}(\vec{r}) = \left\langle a_\alpha a_\beta - \frac{1}{3}\delta_{\alpha\beta} \right\rangle_{\text{Volume element at } \vec{r}} \tag{1.9}$$

where the average is taken in the volume element at the position $\vec{r}$, and the nematic tensor is written for a fluid in 3-dimensions. Under the continuum limit, the nematic tensor $Q_{\alpha\beta}$ is a continuous function defined at each position and is the coarse-grained order parameter that characterises local nematic order in the active fluid. Note that in Equation 1.9, $\vec{a} \to -\vec{a}$ does not change the nematic tensor $Q_{\alpha\beta}$ – indicating that the nematic tensor $Q_{\alpha\beta}$ is a measure of the alignment of orientation vectors, but not if those vectors are parallel. Specifically, this implies that the case of orientation vectors being aligned but anti-parallel has a nematic order, but not a polar order. As before, the nematic tensor is zero for an isotropic fluid.

From the definition in Equation 1.9, one may note that $Q_{\alpha\beta}$ is symmetric ($Q_{\alpha\beta} = Q_{\beta\alpha}$) and traceless ($Q_{\gamma\gamma} = \left\langle a_\gamma a_\gamma - \frac{1}{3}\delta_{\gamma\gamma} \right\rangle = \left\langle 1 - \frac{3}{3} \right\rangle = 0$). In the case of uniaxial nematic ordering where $Q_{\alpha\beta}$ has two equal eigenvalues, $Q_{\alpha\beta}$ may instead be written as:

$$Q_{\alpha\beta} = S\left(n_\alpha n_\beta - \frac{1}{3}\delta_{\alpha\beta}\right) \tag{1.10}$$

where the unit vector $\vec{n}$ is the nematic director and scalar $S \in [-\,1/2\,,1]$ corresponds to the degree of alignment of the orientation vectors along the nematic director $\vec{n}$. The nematic director is an eigenvector of the third non-equal eigenvalue of $Q_{\alpha\beta}$. The nematic order of the active fluid may equivalently be represented using the nematic director field. For the isotropic case, $S = 0$; while for the fully aligned case, $S = 1$.

Higher order moments of the local distribution of $\vec{a}$ are usually ignored. In the discussion that follows and in chapter 2, the focus is on the nematic tensor $Q_{\alpha\beta}$ and therefore active nematic fluids. Note that as the actomyosin cortex may be considered as an active nematic 2-dimensional fluid on the cell membrane [68, 90] (see chapter 2). In 2-dimension, only a uniaxial nematic ordering is possible – as $Q_{\alpha\beta}$ cannot have more than 1 independent eigenvalue.

1.2.3 Irreversible thermodynamics of active fluids

Entropy production

To be able to apply thermodynamic principles to derive the hydrodynamic theory for active fluids, a key assumption of local equilibrium is made. Specifically, it is assumed that each of the volume elements that comprise the active fluid are individually in thermodynamic equilibrium, but out of equilibrium with their neighbours. In this case, the active fluid is locally at equilibrium, but is globally maintained away from equilibrium. Such a local equilibrium can be considered if the small volume elements equilibriate at short times compared to the slow hydrodynamics time scales at large scales.

Consider now only a single volume element (with volume V) at a position $\vec{r}$. Its "macroscopic" state – as the volume element is still large enough to contain a large number of constituent particles of the fluid – is then defined by the various coarse-grained variables defined before, such as: mass density ρ, internal energy e and nematic tensor $Q_{\alpha\beta}$ for the active nematic fluid. Under the local equilibrium, one may then define the free energy $F = fV$ and entropy $S = sV$ of this volume element as a function of these coarse-grained variables. Equivalently, for the active fluid, free energy density (free energy per unit volume) f and entropy density (entropy per unit volume) s can be defined. Due to local equilibrium at each volume element, both $s = -\frac{\partial f}{\partial T}$ and $f = e - Ts$ are valid – where T is the temperature of the local volume element. Here, only the isothermal case is considered: thus T is the temperature of the whole fluid. Note that the whole fluid is not at equilibrium, in contrast to the locally equilibriated volume elements. However, the fluid's free energy and entropy are well-defined as a sum of local contributions of the locally equilibriated volume elements, and can be expressed in terms of free energy density f and entropy density s as:

$$F = \int f \, \mathrm{d}V \, ; \quad S = \int s \, \mathrm{d}V \tag{1.11}$$

where the integration is performed over the whole fluid.

Consider now the change in the total entropy of the fluid. The change in entropy may be written as a sum of two terms:

$$\mathrm{d}S = \mathrm{d_e}S + \mathrm{d_i}S \tag{1.12}$$

where $\mathrm{d_e}S$ is the entropy supplied to the fluid by its surroundings (and thus extrinsic to the fluid), and $\mathrm{d_i}S$ is the entropy produced inside the fluid (and thus intrinsic to the fluid).

The second law of thermodynamics states that the irreversible processes in a non-equilibrium system, such as the active fluid, lead to intrinsic production of entropy, implying:

$$\mathrm{d_i}S \geq 0$$

with equality only for an equilibrium system. The entropy supplied however can be positive, negative or zero – depending on the interaction of the fluid with its surroundings. Defining the flux of entropy as $\vec{J}^{(S)}$, and the entropy production rate per unit volume as θ, Equation 1.12 can be transformed into a continuity equation for the local entropy density s:

$$\partial_t s + \partial_\alpha J_\alpha^{(S)} = \theta \tag{1.13}$$

where $\theta > 0$ to satisfy the second law of thermodynamics. Note that $\mathrm{d}_e S = -\partial_\alpha J_\alpha^{(S)}$ – the entropy supplied to the local volume element is related to the entropy flux entering the local volume element. Such a transformation is only possible because of assumption of local equilibrium – without this assumption, a local entropy density s and entropy production per unit volume θ do not make sense.

Using Equation 1.2 and Equation 1.13, along with $f = e - Ts$, one may then write a continuity equation for the free energy density f:

$$\partial_t f = \partial_t e - T\partial_t s = -\partial_\alpha J_\alpha^{(e)} - T J_\alpha^{(s)} - T\theta \implies \partial_t f + \partial_\alpha J_\alpha^{(f)} = -T\theta \tag{1.14}$$

where $\vec{J}^{(f)} = \vec{J}^{(e)} - T\vec{J}^{(s)}$ is identified as the flux of free energy. Thus, the rate of change of the free energy of the fluid $F = \int f \,\mathrm{d}V$ for a fixed volume $\mathcal{V}$ of fluid is given by:

$$\frac{\mathrm{d}F}{\mathrm{d}t} = \int_{\mathcal{V}} (-T\theta)\,\mathrm{d}V + \int_{\partial\mathcal{V}} \vec{J}^{(f)} \cdot \mathrm{d}\vec{\Omega} \tag{1.15}$$

The surface integral term can be interpreted as the work done on the fluid at its surface.

Another way to obtain the rate of change of the free energy of the fluid would be to specify the free energy density f. Given the assumption of local equilibrium for each volume element, the free energy per unit volume of the volume element in a co-moving frame can be written. Let this relative free energy density be denoted as $f_0 = f_0(Q_{\alpha\beta}, \partial_\gamma Q_{\alpha\beta})$, which depends on the local nematic tensor and its gradients for the active nematic fluid. Then,

$$f = \frac{g_\alpha g_\alpha}{2\rho} + f_0(Q_{\alpha\beta}, \partial_\gamma Q_{\alpha\beta}); \quad F = \int_{\mathcal{V}} \mathrm{d}V \left(\frac{g_\alpha g_\alpha}{2\rho} + f_0(Q_{\alpha\beta}, \partial_\gamma Q_{\alpha\beta}) \right) \tag{1.16}$$

The rate of change of the free energy can then be obtained directly from Equation 1.16. Comparing the bulk term of the time derivative of free energy thus obtained to Equation 1.15 then yields the entropy production rate per unit volume θ.

Linear Response theory

In general, the rate of entropy production can be expressed as a sum of products of generalized thermodynamics forces F_n and their conjugate thermodynamic fluxes J_n:

$$T\theta = \sum_n J_n F_n \tag{1.17}$$

where index n specifies a thermodynamic variable or a tensor/vector component of a given variable. Summation over such an index are explicitly noted here (and thus do not follow the Einstein convention). Equivalently, J_n and F_n can be identified from the expression of rate of entropy production derived previously, using Equation 1.17. Note that at equilibrium, all J_n and F_n vanish – leading to $\theta = 0$, as expected for a system at equilibrium.

Close to equilibrium, the thermodynamic fluxes J_n can be expressed as linear functions of the thermodynamic forces F_n:

$$J_n = \sum_m L_{nm} F_m \tag{1.18}$$

and thus,

$$T\theta = \sum_m L_{nm} F_n F_m \tag{1.19}$$

where L_{nm} are Onsager coefficients that capture the active fluid's material properties. Note that L_{nm} themselves can be scalars, vectors or tensors, as is the case with J_n and F_n. Equation 1.18 gives the constitutive equations of the material. The second law of thermodynamics requires that $\theta > 0$ for systems not in equilibrium, for all values of the thermodynamic forces F_n. Thus, the matrix L_{nm} must be positive definite for the active fluid. This leads to:

$$L_{nn} > 0; \quad L_{nn} L_{mm} \geq \frac{1}{4}(L_{nm} + L_{mn})^2 \tag{1.20}$$

for the diagonal elements L_{nn} and off-diagonal elements L_{nm}, L_{mn}.

Curie symmetry principle

In principle, Equation 1.18 allows for any thermodynamic flux J_n to be expressed as a linear function of all thermodynamic forces F_n. However, all the fluxes J_n and F_n do not possess the same tensorial character, not do they possess the same symmetry properties. The expansion of a thermodynamic flux J_n into thermodynamic forces F_n must respect the symmetry properties and tensorial character of the flux J_n – this is the Curie symmetry principle. This principle restricts the choices of L_{nm}. For example, in isotropic systems, the Curie principle can be used to show that fluxes and forces of different tensorial ranks do not couple [86].

Onsager reciprocity relations

Another restriction on L_{nm} arises from the Onsager reciprocity relations. These relations arise as a result of invariance under time reversal of microscopic mechanisms. For these relations, the signature ϵ of the thermodynamic fluxes J_n and forces F_n under time reversal must first be specified. Note that since entropy production θ has the signature $\epsilon(\theta) = -1$, the signatures of force F_n is opposite to that of its conjugate flux J_n: $\epsilon(F_n) = -\epsilon(J_n)$, as a consequence of Equation 1.17. From Equation 1.18, a coefficient L_{nm} couples a flux J_n to a force F_m. Thus, the coefficients L_{nm} can be classified based on the signature of the corresponding thermodynamic fluxes and forces they couple: L_{nm} is a reactive coupling if $\epsilon J_n = \epsilon(F_m)$, and dissipative if $\epsilon J_n = -\epsilon(F_m)$. Reactive coupling are denoted as L^r_{nm}, dissipative coupling as L^d_{nm}. Then, Onsager reciprocity relations state that:

$$L^r_{nm} = -L^r_{mn} \tag{1.21a}$$

$$L^d_{nm} = L^d_{mn} \tag{1.21b}$$

Note that, by the definition of reactive and dissipative coupling, coupling between a force and its conjugate flux is always dissipative: $L_{nn} = L^d_{nn}$. Essentially, the Onsager relations allow decomposition of the Onsager coefficient matrix L_{nm} into a symmetric dissipative part L^d_{nm} and an antisymmetric reactive part L^r_{nm}.

Hydrodynamics of an active isotropic fluid

The above concepts may be illustrated with an example of an active isotropic fluid. The free energy density of such a fluid is given by $f = \frac{g_\alpha g_\alpha}{2\rho} + f_0$, where f_0 is dependent on the fuel that drives this fluid out of equilibrium. Here, the fluid is considered to be under pressure p. Then, Equation 1.16 can be written as:

$$F = \int \mathrm{d}V \left[\frac{g_\alpha g_\alpha}{2\rho} + f_0\right] - (\text{Work done by pressure}) \tag{1.22}$$

Note that f_0 is a volume term, since the fuel reaction happens in all volume elements.

As an example, let the activity in this fluid be driven by hydrolysis of ATP into ADP and $\mathrm{P_i}$:

$$\mathrm{ATP} \rightarrow \mathrm{ADP} + \mathrm{P_i}$$

Note that this reaction happens at all locations in the fluid. Let μ_{ATP}, μ_{ADP}, μ_{P} be the chemical potentials for ATP, ADP and $\mathrm{P_i}$ respectively. The change in free energy density in the co-moving frame f_0 then can be written as:

$$\delta f_0 = \mu_{\mathrm{ATP}}\delta c_{\mathrm{ATP}} + \mu_{\mathrm{ADP}}\delta c_{\mathrm{ADP}} + \mu_{\mathrm{P}}\delta c_{\mathrm{P}} \tag{1.23}$$

where c_{ATP}, c_{ADP}, c_{P} are the concentrations of ATP, ADP and $\mathrm{P_i}$ respectively. Matter conservation for the chemical reaction above requires that:

$$\delta c_{\mathrm{ATP}} + \delta c_{\mathrm{ADP}} = 0; \quad \delta c_{\mathrm{ATP}} + \delta c_{\mathrm{P}} = 0 \tag{1.24}$$

Thus, the rate of change in f_0 may be written as:

$$\delta f_0 = (\mu_{\mathrm{ATP}} - \mu_{\mathrm{ADP}} - \mu_{\mathrm{P}})\delta c_{\mathrm{ATP}} = \Delta\mu\delta c_{\mathrm{ATP}} \implies \frac{\mathrm{d}f_0}{\mathrm{d}t} = \Delta\mu\frac{\mathrm{d}c_{\mathrm{ATP}}}{\mathrm{d}t} = -r\Delta\mu \tag{1.25}$$

where $\Delta\mu$ is the difference in chemical potential for the ATP hydrolysis reaction, and $r = -\frac{\mathrm{d}c_{\mathrm{ATP}}}{\mathrm{d}t}$ is the rate of consumption of ATP and thus the reaction rate of ATP hydrolysis.

Returning to Equation 1.22, the rate of work done by pressure (opposing change in volume of each volume element) is given by $p\partial_\alpha v_\alpha \,\mathrm{d}V$. From this and Equation 1.25, the rate of change of free energy of the fluid can be derived:

$$\begin{aligned}\frac{\mathrm{d}F}{\mathrm{d}t} &= \int \mathrm{d}V \left[\frac{\partial}{\partial t}\left(\frac{g_\alpha g_\alpha}{2\rho}\right) - r\Delta\mu - p\partial_\alpha v_\alpha\right] = \int \mathrm{d}V \left[\frac{g_\alpha}{\rho}\partial_t g_\alpha - \frac{g_\alpha g_\alpha}{2\rho^2}\partial_t\rho - r\Delta\mu - p\partial_\alpha v_\alpha\right] \\ &= \int \mathrm{d}V \left[v_\alpha\left(\partial_\beta\sigma_{\alpha\beta} - \partial_\beta(g_\alpha v_\beta)\right) + \frac{v_\alpha v_\alpha}{2}\partial_\beta g_\beta - p\partial_\alpha v_\alpha - r\Delta\mu\right] \\ &= \int \mathrm{d}V \left[v_\alpha\partial_\beta\sigma_{\alpha\beta} - \left(v_\alpha\partial_\beta(g_\alpha v_\beta) - \frac{v_\alpha v_\alpha}{2}\partial_\beta g_\beta\right) - p\partial_\alpha v_\alpha - r\Delta\mu\right]\end{aligned}$$

where Equation 1.1 and Equation 1.4 have been used, and $g_\alpha = \rho v_\alpha$. Now,

$$\begin{aligned}
&\frac{v_\alpha v_\alpha}{2}\partial_\beta g_\beta = \frac{1}{2}\partial_\beta(\rho v_\alpha v_\alpha v_\beta) - \rho v_\beta v_\alpha \partial_\beta v_\alpha \\
&v_\alpha \partial_\beta (g_\alpha v_\beta) = \partial_\beta(\rho v_\alpha v_\alpha v_\beta) - \rho v_\alpha v_\beta \partial_\beta v_\alpha \\
&\implies v_\alpha \partial_\beta (g_\alpha v_\beta) - \frac{v_\alpha v_\alpha}{2}\partial_\beta g_\beta = \frac{1}{2}\partial_\beta(\rho v_\alpha v_\alpha v_\beta) \\
&v_\alpha \partial_\beta \sigma_{\alpha\beta} = \partial_\beta v_\alpha \sigma_{\alpha\beta} - \sigma_{\alpha\beta}\partial_\beta v_\alpha
\end{aligned}$$

Using these, the rate of change of free energy is given by:

$$\frac{\mathrm{d}F}{\mathrm{d}t} = \int -\left[\sigma_{\alpha\beta}\partial_\beta v_\alpha + p\partial_\alpha v_\alpha - r\Delta\mu\right]\mathrm{d}V + \int \mathrm{d}V\,\partial_\beta\left[\frac{\rho v_\alpha v_\alpha v_\beta}{2} + v_\alpha \sigma_{\alpha\beta}\right] \tag{1.26}$$

Comparing to Equation 1.15, the entropy production rate can be written as:

$$T\theta = \sigma_{\alpha\beta}\partial_\beta v_\alpha + p\partial_\alpha v_\alpha + r\Delta\mu \tag{1.27}$$

Note that the entropy production is not in the form required by Equation 1.17 (since at equilibrium neither $\sigma_{\alpha\beta}$ nor p vanish). To do so, the stress tensor $\sigma_{\alpha\beta}$ and velocity gradient $\partial_\beta v_\alpha$ are decomposed. For $\sigma_{\alpha\beta}$:

$$\sigma_{\alpha\beta} = \left[\sigma_{\alpha\beta} - \frac{1}{d}\sigma_{\gamma\gamma}\delta_{\alpha\beta}\right] + \left[\frac{1}{d}\sigma_{\gamma\gamma} + p\right]\delta_{\alpha\beta} - p\delta_{\alpha\beta} = \tilde{\sigma}^{d,s}_{\alpha\beta} + \sigma^d\delta_{\alpha\beta} - p\delta_{\alpha\beta}$$

where $\tilde{\sigma}^{d,s}_{\alpha\beta} = \sigma_{\alpha\beta} - \frac{1}{d}\sigma_{\gamma\gamma}\delta_{\alpha\beta}$ is the symmetric traceless part of $\sigma_{\alpha\beta}$, $\sigma^d = \frac{1}{d}\sigma_{\gamma\gamma} + p$ is isotropic part of the stress $\sigma_{\alpha\beta}$ and d is the number of space dimensions. Note that the notation followed here is borrowed from [85]. The superscript d refers to the deviatoric part of the stress – that is, the stress tensor excess from the equilibrium stress. Since for the isotropic fluid, the equilibrium stress tensor is just $-p\delta_{\alpha\beta}$, the above definitions are obtained. For $\partial_\beta v_\alpha$:

$$\partial_\beta v_\alpha = \left[\frac{\partial_\beta v_\alpha + \partial_\alpha v_\beta}{2} - \frac{1}{d}\partial_\gamma v_\gamma \delta_{\alpha\beta}\right] + \frac{\partial_\beta v_\alpha - \partial_\alpha v_\beta}{2} + \frac{1}{d}\partial_\gamma v_\gamma \delta_{\alpha\beta} = \tilde{v}_{\alpha\beta} + \omega_{\alpha\beta} + \frac{1}{d}\partial_\gamma v_\gamma \delta_{\alpha\beta}$$

where $\tilde{v}_{\alpha\beta} = \frac{\partial_\beta v_\alpha + \partial_\alpha v_\beta}{2} - \frac{1}{d}\partial_\gamma v_\gamma \delta_{\alpha\beta}$ is the symmetric traceless part of $\partial_\beta v_\alpha$, $\omega_{\alpha\beta} = \frac{\partial_\beta v_\alpha - \partial_\alpha v_\beta}{2}$ is the antisymmetric part of $\partial_\beta v_\alpha$ and $\frac{1}{d}\partial_\gamma v_\gamma$ is the local expansion rate of the fluid. Rewriting Equation 1.27:

$$T\theta = \tilde{\sigma}^{d,s}_{\alpha\beta}\tilde{v}_{\alpha\beta} + \sigma^d \partial_\gamma v_\gamma + r\Delta\mu \tag{1.28}$$

Note that each of $\tilde{\sigma}^{d,s}$, σ^d and $\Delta\mu$ go to zero at equilibrium – first two because the stress at equilibrium is just $-p\delta_{\alpha\beta}$ and $\Delta\mu$ since at equilibrium the chemical potential difference would be zero (indicating that the hydrolysis reaction does not have preferred direction). Thus, Equation 1.28 is in the form of Equation 1.17.

Using Equation 1.28, the thermodynamic fluxes and forces can be identified. In here, the choice of forces and fluxes is made are shown in Table 1.1. Note that the choice of fluxes and forces is arbitrary – a force may be treated as a flux and vice versa. Only the pairs themselves are determined by Equation 1.28.

Flux J_n	Force F_n	Time reversal signature $\epsilon(J_n), \epsilon(F_n)$	Rotation symmetry
$\tilde{\sigma}^{d,s}_{\alpha\beta}$	$\tilde{v}_{\alpha\beta}$	1,-1	Traceless symmetric tensor
σ^d	$\partial_\gamma v_\gamma$	1,-1	Scalar
r	$\Delta\mu$	-1,1	Scalar

Table 1.1: Conjugate thermodynamic fluxes and forces for a simple isotropic fluid

Using Equation 1.18 and Equation 1.21, the following can be written:

$$\tilde{\sigma}^{d,s}_{\alpha\beta} = (L_{11})\tilde{v}_{\alpha\beta} + (L_{12})\partial_\gamma v_\gamma + (L_{13})\Delta\mu \tag{1.29a}$$

$$\sigma^d = (L_{12})\tilde{v}_{\alpha\beta} + (L_{22})\partial_\gamma v_\gamma + (L_{23})\Delta\mu \tag{1.29b}$$

$$r = (-L_{13})\tilde{v}_{\alpha\beta} + (-L_{23})\partial_\gamma v_\gamma + (L_{33})\Delta\mu \tag{1.29c}$$

where the tensorial character of the Onsager coefficients $L_{11}, L_{12}, L_{13}, L_{22}, L_{23}, L_{33}$ is yet to be determined. Note that since the time reversal signature of $\tilde{\sigma}^{d,s}_{\alpha\beta}$ and $\partial_\gamma v_\gamma$ are opposite, $L_{12} = L_{21}$ is a dissipative coupling, as per Onsager relations. Similarly, since the time reversal signature of $\tilde{\sigma}^{d,s}_{\alpha\beta}$, σ^d and $\Delta\mu$ are the same, $L_{31} = -L_{13}$ and $L_{32} = -L_{23}$ are reactive couplings. Curie principle forces $L_{12} = 0, L_{13} = 0$, as rotation symmetry must match on both sides. Then, L_{11}, L_{22} and L_{23} can be written as scalars, yielding the constitutive equations for an active compressible isotropic fluid:

$$\tilde{\sigma}^{d,s}_{\alpha\beta} = 2\eta\tilde{v}_{\alpha\beta} \tag{1.30a}$$

$$\sigma^d = \eta_v\partial_\gamma v_\gamma + \zeta\Delta\mu \tag{1.30b}$$

$$r = -\zeta\partial_\gamma v_\gamma + \Lambda\Delta\mu \tag{1.30c}$$

where the shear viscosity η and bulk viscosity η_v have been introduced as the Onsager coefficients. ζ describes the generation of active stress by ATP hydrolysis, while Λ describes diffusion of ATP and its hydrolysis products. The stress tensor $\sigma_{\alpha\beta}$ can be then written as:

$$\sigma_{\alpha\beta} = \tilde{\sigma}^{d,s}_{\alpha\beta} + \sigma^d\delta_{\alpha\beta} - p\delta_{\alpha\beta} = \eta\left(\partial_\beta v_\alpha + \partial_\alpha v_\beta\right) + \left(\eta_v - \frac{2\eta}{d}\right)\partial_\gamma v_\gamma\delta_{\alpha\beta} + (\zeta\Delta\mu - p)\delta_{\alpha\beta} \tag{1.31}$$

Equation 1.31 can be used in Equation 1.5 to obtain the dynamic equation for the flow velocity $\vec{v}$:

$$\rho\left(\partial_t v_\alpha + v_\beta\partial_\beta v_\alpha\right) = \partial_\alpha(\zeta\Delta\mu - p) + \eta\partial_\beta\partial_\beta v_\alpha + \left(\frac{d-2}{d}\eta + \eta_v\right)\partial_\alpha\partial_\beta v_\beta \tag{1.32}$$

Some features of the above derivation may now be recognized. First, note that the coupling between stress and chemical activity in Equation 1.30 only exists if the fluid exhibits isotropic stress – that is, if σ^d is not assumed zero throughout. Such a coupling indicates that stresses generated due to fuel consumption lead to expansion or contraction of the volume elements, not shear, in the case of active isotropic fluid. Second, note that the coupling is two-directional – that is, the reaction rate r is also dependent on the local expansion rate $\partial_\gamma v_\gamma$ by the same coefficient ζ. As one is typically interested only in the stress tensor $\sigma_{\alpha\beta}$, this effect in the reaction rate is usually not considered. Third, in the specific case of the actomyosin cortex, since the ATP hydrolysis is catalysed by myosin motors, the active stress $\zeta\Delta\mu$ is typically considered a function of the local myosin concentration on the cortex.

Finally, consider the case of a bulk 3-dimensional ($d = 3$) passive fluid ($r = 0, \Delta\mu = 0$). In this case, Equation 1.32 reduces to:

$$\rho\left(\partial_t v_\alpha + v_\beta \partial_\beta v_\alpha\right) = -\partial_\alpha p + \eta \partial_\beta \partial_\beta v_\alpha + \left(\frac{1}{3}\eta + \eta_v\right)\partial_\alpha \partial_\beta v_\beta \tag{1.33}$$

For an incompressible fluid passive fluid, $\partial_\beta v_\beta = 0$ yields:

$$\rho\left(\partial_t v_\alpha + v_\beta \partial_\beta v_\alpha\right) = -\partial_\alpha p + \eta \partial_\beta \partial_\beta v_\alpha \tag{1.34}$$

Both of these equations may be recognized as the well-known Navier-Stokes equation of fluid dynamics of a compressible or an incompressible fluid respectively.

1.2.4 Constitutive equations of active nematic fluids

Following the principles outlined in this section, constitutive equations for incompressible active nematic fluids have been derived in [85]. In particular, the thermodynamic fluxes are identified as (note that the notation followed here is from [85]):

1. Symmetric traceless part of the deviatoric stress
   Here, deviatoric stress $\sigma^d_{\alpha\beta}$ is defined as the excess stress from the equilibrium (or Ericksen) stress $\sigma^e_{\alpha\beta}$. Such an equilibrium stress arises in nematic fluids due to the free energy $f_0 = f_0(Q_{\alpha\beta}, \partial_\gamma Q_{\alpha\beta})$ for nematic ordering. The symmetric traceless part of this deviatoric stress is written as:

   $$\tilde{\sigma}^{d,s}_{\alpha\beta} = \sigma_{\alpha\beta} - (\sigma^{e,s}_{\alpha\beta} - P\delta_{\alpha\beta}) - (Q_{\alpha\gamma}H_{\beta\gamma} - H_{\alpha\gamma}Q_{\beta\gamma}) \tag{1.35}$$

   where superscript s denotes symmetric part and $\sim$ indicates traceless. $\sigma^{e,s}_{\alpha\beta}$ is the symmetric part of the equilibrium stress, P is the pressure, and $Q_{\alpha\gamma}H_{\beta\gamma} - H_{\alpha\gamma}Q_{\beta\gamma}$ is an antisymmetric stress that arises due to rotational invariance of the free energy in nematic fluids. As indicated before, this antisymmetric component of the stress will be ignored in the theoretical description of the cortex described in chapter 2. $H_{\alpha\beta}$ is the molecular field conjugate to the nematic order parameter $Q_{\alpha\beta}$.

2. Convected co-rotationed time derivative of the nematic tensor
   Convected co-rotationed time derivative is a material derivative taken in a reference frame that is convected and co-rotated with the center of mass of the local volume element [110]. It is defined here as:

   $$\frac{DQ_{\alpha\beta}}{Dt} = \partial_t Q_{\alpha\beta} + v_\gamma \partial_\gamma Q_{\alpha\beta} + \omega_{\alpha\gamma}Q_{\gamma\beta} + \omega_{\beta\gamma}Q_{\alpha\gamma} \tag{1.36}$$

   where $\omega_{\alpha\beta}$ is the vorticity of the fluid, defined as:

   $$\omega_{\alpha\beta} = \frac{\partial_\alpha v_\beta - \partial_\beta v_\alpha}{2} \tag{1.37}$$

3. Reaction rate r of ATP hydrolysis

and the thermodynamic forces are identified as:

1. Symmetric traceless part of the Strain rate
   The Symmetric traceless part of the Strain rate $\tilde{v}_{\alpha\beta}$ is defined as:
   $$\tilde{v}_{\alpha\beta} = \frac{\partial_\alpha v_\beta + \partial_\beta v_\alpha}{2} - \frac{1}{d}\partial_\gamma v_\gamma \delta_{\alpha\beta} \tag{1.38}$$
   where d is the number of space dimensions of the fluid.
2. Molecular field conjugate to the nematic tensor
   As noted earlier, $H_{\alpha\beta}$ is the molecular field conjugate to the nematic order parameter $Q_{\alpha\beta}$. It is defined as ($F_0 = \int f_0 \, \mathrm{d}V$):
   $$H_{\alpha\beta} = -\frac{\delta F_0}{\delta Q_{\alpha\beta}} = -\frac{\partial f_0}{\partial Q_{\alpha\beta}} + \partial_\gamma \frac{\partial f_0}{\partial(\partial_\gamma Q_{\alpha\beta})} \tag{1.39}$$
3. Chemical potential difference $\Delta\mu$ for ATP hydrolysis
   Note that the difference between the chemical potential of ATP and its hydrolysis products remains constant throughout the fluid due to the action of fuel reservoirs, which keep the same concentration of fuel (that is, ATP) and its products throughout the fluid.

The conjugate pairs of thermodynamic forces and fluxes are listed in Table 1.2.

Flux J_n	Force F_n	Time reversal signature $\epsilon(J_n), \epsilon(F_n)$	Rotation symmetry
$\tilde{\sigma}^{d,s}_{\alpha\beta}$	$\tilde{v}_{\alpha\beta}$	1,-1	Traceless symmetric tensor
$\frac{DQ_{\alpha\beta}}{Dt}$	$H_{\alpha\beta}$	-1,1	Traceless symmetric tensor
r	$\Delta\mu$	-1,1	Scalar

Table 1.2: Conjugate thermodynamic fluxes and forces for active nematic fluid. Adapted from [85]

The constitutive equations for the incompressible active nematic fluid are then written as:

$$\tilde{\sigma}^{d,s}_{\alpha\beta} = 2\eta\tilde{v}_{\alpha\beta} + \nu H_{\alpha\beta} + \zeta Q_{\alpha\beta}\Delta\mu \tag{1.40a}$$

$$\frac{DQ_{\alpha\beta}}{Dt} = -\nu\tilde{v}_{\alpha\beta} + \frac{1}{\bar{\gamma}}H_{\alpha\beta} + \lambda Q_{\alpha\beta}\Delta\mu \tag{1.40b}$$

$$r = -\zeta Q_{\alpha\beta}\tilde{v}_{\alpha\beta} + \lambda Q_{\alpha\beta}H_{\alpha\beta} + \Lambda\Delta\mu \tag{1.40c}$$

Here, $\eta, \nu, \zeta, \bar{\gamma}, \lambda, \Lambda$ are phenomenological constants that are material properties of the fluid. Their values are specific to each fluid. Hydrodynamic equations for the fluid can be found by using these equations in the conservation equations such as Equation 1.4.

In the actomyosin cortex, the ATP hydrolysis is catalysed by myosin motors to generate mechanical forces (see subsection 1.1.1). Given the role of myosin as a catalyst for ATP hydrolysis, the reaction rate r should be dependent on the local concentration of myosin. Such a supposition yields ζ, λ and Λ as dependent on myosin concentration. Note also that the ζ and λ terms are associated with the nematic tensor, and contribute to deviatoric stress and local change in the nematic tensor respectively. Since the nematic order of the actomyosin cortex is primarily imparted to it by the actin filaments [88], ζ captures the mechanical stress generated by action of myosin motors onto actin filaments and λ captures the myosin-driven local alignment of actin filaments. In chapter 2 this discussion is further expanded on, in the context of AP axis alignment.

1.3 *C. elegans* as a model organism

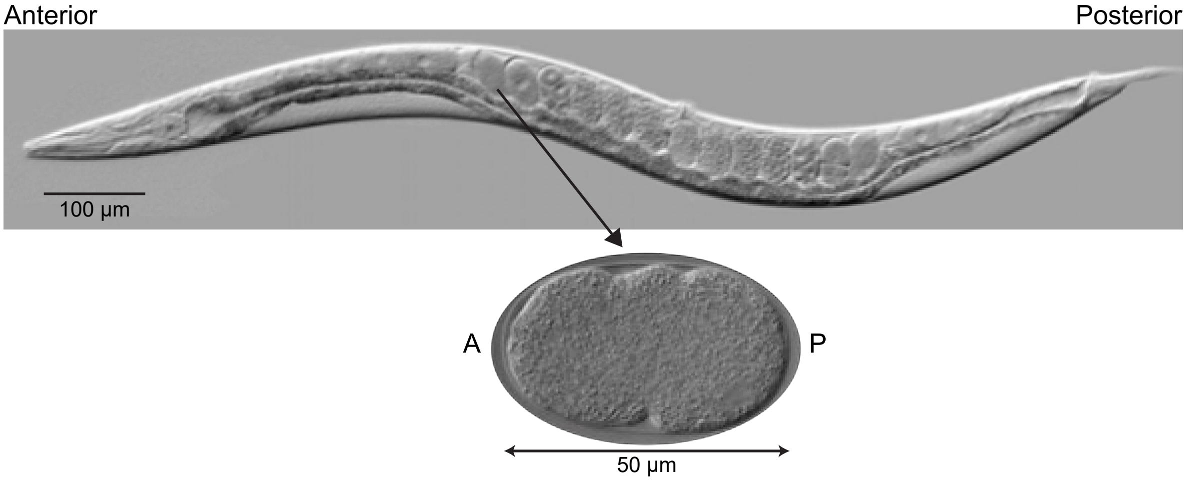

Figure 1.5: Microscope picture of *C. elegans* worm (top) and one-cell stage embryo (bottom), by M. Leaver (used with permission). A and P mark the anterior and posterior of the developing embryo. Typical location of the one-cell embryo in the gonad of the worm, and its length (approx. 50 µm) is marked

Caenorhabditis elegans (*C. elegans*) was first considered as a potential model organism by Sydney Brenner over 50 years ago – for studies in developmental biology and neuroscience [111–113]. *C. elegans* is a free-living self-fertilizing transparent nematode, typically found in temperate climate around the world. It is typically a self-fertilizing hermaphrodite with rare spontaneous males (less than 0.2% of worms [114, 115]) [112]. It feeds on bacteria, typically *Escherichia coli* (*E. coli*) on the surface of agarose plates when cultured in lab [112]. In lab conditions, *C. elegans* worms grow from initial larval stage (0.25 mm long) to final adult stage (1 mm long) in around 3 days at 20 °C, although this time can vary with temperature and food available [112, 115, 116]. It is a simple organism in both anatomy and genome. It has a fixed, genetically determined, number of cells at the adult stage, with adult hermaphrodite at 959 somatic cells and adult male at 1033 cells [117, 118]. One of most prominent features of *C. elegans* is its invariant cell lineage: every worm follows the same pattern of cell divisions and results in the same number of cells, i.e. the developmental fate of every somatic cell is invariant. This has enabled tracing the fate of cell during development, giving rise to a complete map of cell lineage [117–119]. Today, there are more than thousand research groups that use *C. elegans* as a model organism, due to the above ease of maintenance and the multitude of biological tools available for study and manipulation of *C. elegans* worms, in various fields such as neuroscience, development, ecology and cell biology [115].

Hermaphrodites and males differ in their adult morphology, with males being a bit thinner and shorter, and possess a distinctive tail [115]. The primary method of reproduction in *C. elegans* is via self-fertilization: hermaphrodites produce both sperms and oocytes, which fertilize each other. A hermaphrodite typically lays about 300 eggs. Males can also fertilize the hermaphrodites, allowing for a form of sexual reproduction. The young worms hatch and subsequently go through four larval stages (L1-L4) before adulthood. These adults are fertile for about 3 days, and have an average lifespan of about 2–3 weeks [115]. In harsh conditions, larval development can be paused – these worms can survive several months in a special state called dauer arrest [120].

The above properties of *C. elegans* make it very convenient to use as a model organism for development [112, 115]. It is easy to maintain and grow in bulk due to the large number of progeny and rapid life cycle. Worms can be easily frozen for years and revived later when needed. Individual worms can be easily observed at the level of single cells under the microscope due to their transparency. Its small size allows complete anatomical description even at the electron microscope level. Self-fertilization means a single worm can generate an entire population of its clones, while the rare males, which can be maintained, enable transfer of genetic markers between populations. *C. elegans* is also the first multi-cellular organism with a completely sequenced genome, containing about 18000 predicted genes [121]. Together with the simple feeding method of double stranded RNA mediated interference (RNAi) in *C. elegans* [122], all these properties of *C. elegans* make genetic perturbations in *C. elegans* worms a simple and efficient process. Using fluorescent proteins such as Green Fluorescent Protein (GFP) to tag the proteins in the embryo allows in-depth study of its development [123, 124].

1.3.1 Early embryogenesis in *C. elegans*

C. elegans embryogenesis begins when a mature oocyte, arrested in meiosis I, is fertilized by a sperm [127, 128] – see Figure 1.6a. As discussed more extensively later, the site of sperm entry defines the future posterior end of the embryo [6] (also, see Figure 1.1a). Prior to fertilization, the oocyte is fairly symmetric [129–131]. Thus, sperm entry represents the first event in which symmetry is broken in the oocyte. At fertilization, the sperm donates its genetic material – the male pronucleus – to the embryo, along with centrosomes [132–134]. After fertilization, meiosis is completed with the extrusion of two polar bodies, usually located at the anterior end. A rigid ovoid-shaped chitin eggshell is secreted by the newly formed embryo after fertilization – which provides the embryo with its ellipsoidal shape [135].

Events in the one-cell stage of the *C. elegans* embryo – called the P0 stage – can be divided into two phases: establishment phase and maintenance phase [129]. Establishment phase is initiated by the centrosomes near the male pronucleus. These centrosomes organize microtubule asters, which lead to triggering the establishment of the AP axis (discussed later). In the establishment phase, large-scale flows in the actomyosin cortex (directed away from the male pronucleus) and cytoplasm (directed towards the male pronucleus) are observed (which gives the establishment phase its other name – flow phase). Towards the end of establishment phase, the female pronucleus migrates towards and meets with the male pronucleus, concomitant with a characteristic constriction at the mid of the embryo – called the pseudocleavage furrow [88, 129, 136]. This migration is powered by the microtubules connecting the two pronuclei late in the establishment phase [137]. Pronuclear meeting indicates the end of establishment phase and start of the maintenance phase.

In the maintenance phase, the AP axis orientation is maintained – no flows in the actomyosin cortex or cytoplasm are observed. P granules, which play a role in determining germline fate, localize towards the posterior end, as dictated by the established AP axis [138, 139]. The mitotic spindle is set up in the center of the embryo, but elongates towards the posterior end following pronucleus envelope breakdown [44]. The spindle is observed to rock, i.e. oscillate

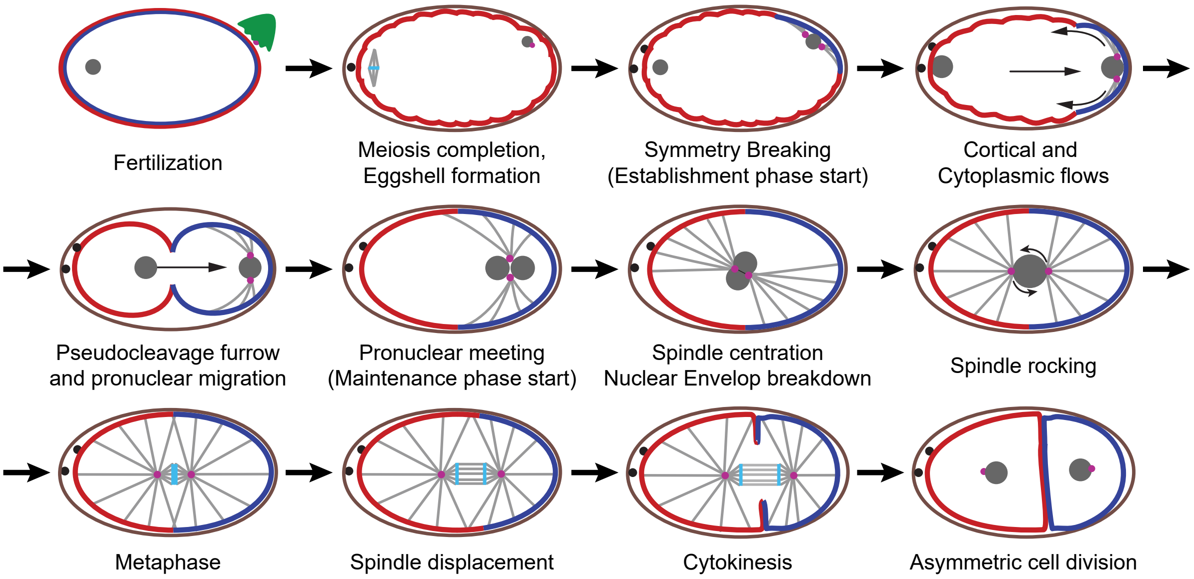

(a) Chronological sequence of events in the one-cell stage embryo, from fertilization until the first cell division. See subsection 1.3.1 and subsection 1.4.2 for further details. Anterior is to the left, posterior to the right. Grey circles represent pronuclei and nuclei, black circle extruded polar bodies, purple circle centrosomes. Microtubules are denoted in light grey, arrows illustrate movement. Blue represents pPARs, red represents aPARs. Adapted from [125]. Also see [126].

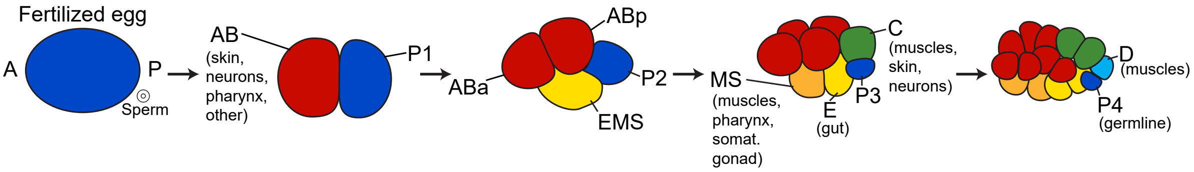

(b) Sketch depicting early embryogenesis in *C. elegans* embryo. The one-cell stage embryo, after fertilization, undergoes an asymmetric division, forming the larger, anterior AB cell and smaller, posterior P1 cell. AB gives rise to somatic cells only. P1 divides further, generating somatic blastomeres EMS (which divides into E and MS), C and D, and the germline progenitor P4. Tissues that the blastomeres give rise to are indicated next to them. Adapted from [125]. Also see [17].

Figure 1.6: Early embryogenesis in *C. elegans* embryo

[45]. Towards the end of maintenance phase, the P0 cell divides asymmetrically (due to the eccentric location of the mitotic spindle). This results in a large cell towards the anterior and a smaller cell at the posterior, termed AB and P1 respectively.

These cells divide further as the embryo develops, as depicted in Figure 1.6b. The established AP axis is however retained by the distribution of P granules as the embryo develops, as the P granules segregate into the germline precursor cells: P1, P2, P3, P4 [17, 127]. The P4 cell is the primodial germ cell – all sperms and oocytes generated in the new worm originate from this P4 cell [127, 140].

1.4 AP axis establishment in *C. elegans*

In this section, the mechanism of AP axis establishment in *C. elegans* is described. As noted before, the AP axis is established during the establishment phase at the one-cell stage during *C. elegans* embryogenesis [127]. AP axis is established via a cell polarization event mediated by PAR polarity proteins [139, 141, 142]. In this section, the PAR polarity system – a conserved system of proteins involved in cell polarization in many eukaryotic cells [139] – is first described. Next, the AP axis establishment process is described, detailing the role of the actomyosin cortex and the centrosomal trigger from the male pronucleus. Finally, the phenomenon of AP axis alignment is introduced. Mechanisms proposed for AP axis alignment by previous studies and considered in this thesis are also described.

1.4.1 PAR polarity system

Partitioning defective (PAR) proteins are a conserved set of proteins in eukaryotes, functioning to control asymmetric cell division and partitioning of components in many cell types [143, 144], and crucial in cell polarity establishment [143]. PAR proteins were first identified in the *C. elegans* embryos, as a result of genetic mutations that cause symmetric division of the one-cell embryo [145, 146].

PAR proteins help establish the AP axis in *C. elegans* via polarization of the one-cell stage embryo. PAR proteins can be classified into three groups based on their localization in this polarized embryo: PAR-4 and PAR-5 remain uniformly distributed on the cortex, PAR-1, PAR-2, LGL-1 (Posterior PAR proteins (pPARs)) localize to the posterior half of the cortex and PAR-3, PAR-6, PKC-3 (Anterior PAR proteins (aPARs)) localize to the anterior half of the cortex [141]. Importantly, this localization is specific to the cortex (but not absolute) - PAR proteins are uniformly distributed in the cytoplasm [139, 141].

Experiments using Fluorescent Recovery After Photo-bleaching and Fluorescent Correlation Spectroscopy have revealed that PAR proteins can exchange between the cortex and the cytoplasm, and also diffuse laterally on the cortex [139, 147–149]. Extensive mixing between the aPARs and pPARs on the cortex is prevented by the mutual inhibition between the two groups: aPARs inhibit the binding of pPARs to the cortex occupied by aPARs, and vice versa [139, 141]. The behaviour of PAR proteins on the cortex can be modelled as a reaction-diffusion system, with characteristics similar to those observed *in vivo* [139]. Importantly, PAR proteins can interact with the actomyosin cortex – aPARs can reduce the dissociation rate of NMY-2 from the cortex [1], while flows in the cortex can advect the PAR proteins [150].

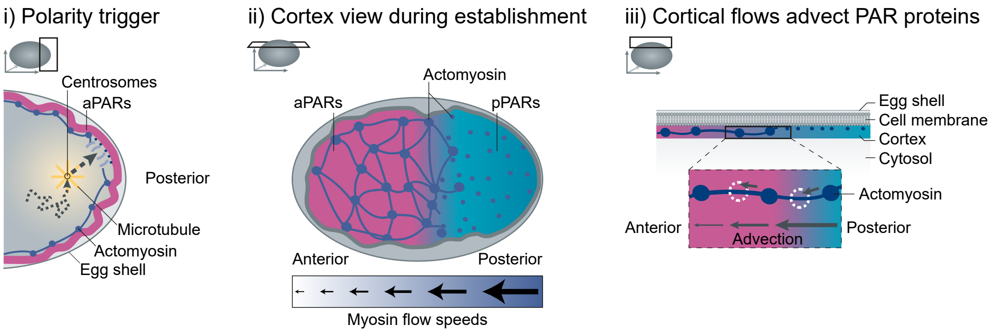

(a) Schematics depicting the major events that occur in AP axis establishment in one-cell *C. elegans* embryo. i) Polarity trigger is provided by the centrosome towards the future posterior end of the embryo, via microtubules and other diffusive components [139]. This trigger displaces the aPARs and down-regulate the actomyosin cortex near the trigger [1, 139]. ii) View onto the cell Cortex during AP axis establishment. Actomyosin cortex is less cross-linked and less dense in the posterior domain (indicated by pPARs) compared to anterior domain (indicated by aPARs). The cortex also shows anisotropic tension [77], with cortical flow directed towards the anterior. Flow speeds are larger in the posterior compared to anterior. iii) Cross-section of the cell cortex. Cortical flows passively transport the PAR proteins by advection [150]. Adapted from [139]

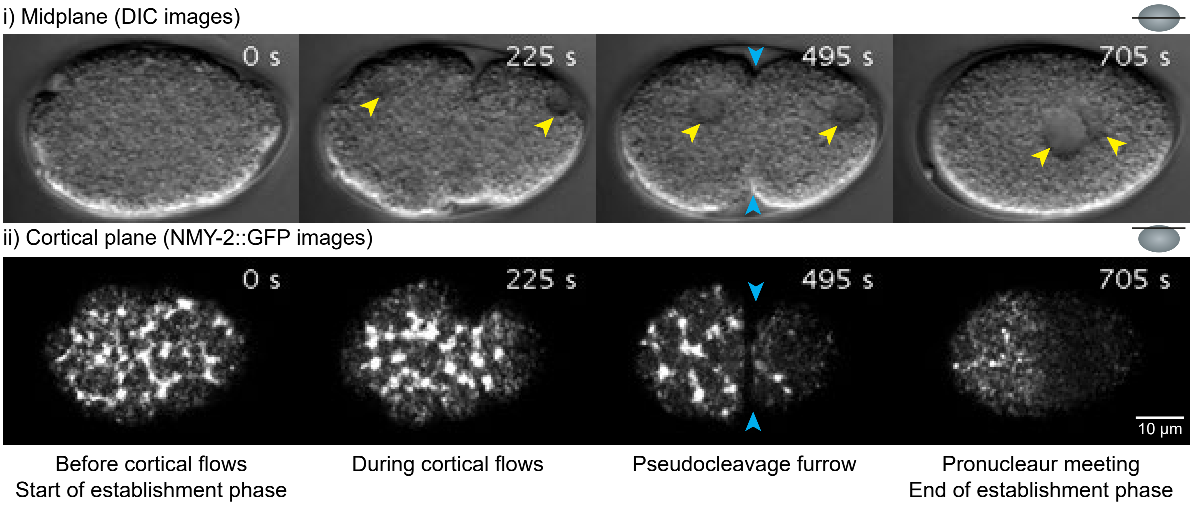

(b) Cortical activity during AP axis establishment. Top: DIC images taken in the midplane of the embryo. Bottom: NMY-2::GFP images taken at the surface of the embryo; that is, in the cortical plane. Anterior is to the left, posterior to the right. $T = 0\,\mathrm{s}$ indicates start of establishment phase, with myosin forming foci-like structures uniformly in the cortex. After polarization is triggered near the male pronucleus, anterior-directed cortical flows cause the cortex to retrace from the posterior end (ex: $T = 225\,\mathrm{s}$). The cortex completely retracts by the time the pseudocleavage furrow forms ($T = 495\,\mathrm{s}$), and the two domains have formed. Establishment phase ends at pronuclear meeting ($T = 705\,\mathrm{s}$), with myosin foci disappearing from the cortex. Yellow arrows indicate pronuclei (female on the left, male on the right) and blue arrows represent the ingression formed by the pseudocleavage furrow. Scale: 10 µm. Adapted from [151]

Figure 1.7: Mechanism of AP axis establishment in one-cell stage *C. elegans* embryo

1.4.2 Mechanism of AP axis establishment

AP axis establishment starts around 30 min after fertilization, by the polarity trigger provided by the centrosomes associated with the male pronucleus [132–134, 152]. Before the polarization trigger, the PAR polarity network is primed [153–156], resulting in an initially unpolarized one-cell embryo with aPARs uniformly enriched on the cortex [129–131].

As the male pronucleus approaches the cortex, the associated centrosome provides the polarity trigger to break this symmetric distribution and initiate AP axis establishment [133, 139, 157] – see Figure 1.7a. This polarity trigger loads the pPARs onto the cortex near the centrosome, and thus near the male pronucleus [1, 133, 134]. This nascent domain of pPARs, or the posterior domain, is protected from mutual inhibition from aPARs by microtubules from the centrosome [158]. Additionally, the polarity trigger inhibits actomyosin contractility near the male pronucleus by local down-regulation of NMY-2 [159]. This generates an unequal distribution of myosin motors within the cortex, leading to active stresses in the cortex, and generating flows in the actomyosin cortex towards the future anterior end of the embryo and pointing away from the male pronucleus [77, 160]. Cortical flows transport the PAR proteins towards the anterior end via advection – expanding the posterior domain [150]. Difference in the NMY-2 dissociation rates between the posterior and anterior domains [1] further drives the unequal distribution of myosin motors on the cortex, and thus promotes cortical flows. Modification of the actomyosin cortex, and thus cortical flows, can be observed in NMY-2::GFP labelled movies of the *C. elegans* embryo, see Figure 1.7b.

Additional to PAR protein transport, cortical flows also generate cytoplasmic flows due to the drag between the cortex and the cytoplasm; with cytoplasmic flows being directed towards the male pronucleus due to the incompressible nature of the cytoplasm and embryo geometry [137]. Thus, the male pronucleus is pushed into the cortex – ensuring robust polarization of the embryo [161].

Polarization of the embryo thus proceeds via a self-organized mechanochemical feedback loop between the PAR polarity system and cortical flows guided by the polarity trigger from the centrosome [1, 3, 84]. PAR proteins control the flows in the cortex [1] and cortical flows control the size of the PAR domains [150, 160]. Altogether, this process continues until the one-cell embryo is transformed from an initially unpolarized state to a polarized state. The polarization thus set up at the end of establishment phase establishes the AP axis – with the eventual anterior and posterior domains denoting the anterior and posterior end of the embryo.

Converting this polarization into the AP axis is accomplished by processes downstream of the PAR proteins. PAR domains on the cortex induce a cytoplasmic gradient of MEX-5 [148], which drives the segregation of P granules and various other “determinants” towards the posterior end [139]. Differential contractility of the actomyosin cortex in the posterior and anterior domains also sets up the stage for the asymmetric division of the one-cell embryo [44]. Together, these processes ensure that the AP axis established at the one-cell stage is realized as the embryo develops.

Note that in the following sections and chapters, unless specifically mentioned, the centrosome is always considered attached to the male pronucleus, and thus the actions of the centrosome are attributed to the male pronucleus as a shorthand.

1.4.3 AP axis alignment

In the description of AP axis establishment, the orientation of the AP axis with respect to the ellipsoidal-like geometry of the embryo has so far not been considered. The ellipsoidal-like shape is imposed on the embryo by the eggshell surrounding it, which it secretes shortly after fertilization [135]. The embryo has one long axis about 50 µm in length, and two short axes about 30 µm in length [128, 162]. The AP axis in *C. elegans* always forms along the long axis of the ellipsoidal embryo [6]. How then are the AP axis and the geometric long axis aligned?

In the typical case, the sperm enters the embryo near long axis of the embryo. Thus, in the typical case, the male pronucleus and the centrosome are located near to the long axis – ensuring that the AP axis already establishes along the long axis. However, as described in [6], the AP axis will always form along the long axis – even if the male pronucleus is initially away from the long axis. In this untypical case, which occurs due to lateral sperm entry (sperm entry away from the long axis), the AP axis actively re-orient to align with the long axis. As shown in Figure 1.8a, this is observed as the movement of PAR domains to align correctly with the long axis, along with the migration of the male pronucleus with the posterior domain and towards the closest tip [6]. This migration of the male pronucleus is called here as posteriorisation. The mechanism(s) that drive(s) the alignment of AP axis with the long axis is not currently understood.

Multiple mechanisms have been proposed in the past to explain AP axis alignment. Observing that the cytoplasmic flows in the embryo are directed towards the male pronucleus, [6] suggested that these cytoplasmic flows could drive the posteriorization. It was proposed that these flows could push onto the male pronucleus [163], and owning to the geometry of the embryo in which the flows operate, push the male pronucleus towards the closest tip in the untypical case [6] – see Figure 1.8b. Experiments with artificially generated cytoplasmic flows in maintenance phase indicate that cytoplasmic flows can influence the orientation of the AP axis [164]. Thus, in this mechanism, cytoplasmic flows act as a geometry-sensor. This proposed mechanism of AP axis alignment is referred to as the cytoplasmic flow-dependent mechanism.

In this work, another mechanism for AP axis alignment is proposed. In addition to cytoplasmic flows, cortical flows also lead to the formation of the pseudocleavage furrow – a contractile ring-like structure that forms at the boundary between the two PAR domains late in the establishment phase [88, 136]. Previous studies have found the pseudocleavage furrow to be not essential for AP axis establishment [165], but indicate that it may play a role in the dynamics of AP axis establishment [166]. Here, it is proposed that the pseudocleavage furrow may play a role in AP axis alignment. In the untypical case, the pseudocleavage furrow is not perpendicular to the long axis of the embryo. Akin to an elastic rubber-band on an ellipsoid, the pseudocleavage furrow could rotate to minimize its circumference and position itself perpendicular to the long axis, forcing the cortex to reposition such that the AP axis aligns with the long axis – see Figure 1.8b. This proposed mechanism of AP axis alignment is referred to as the pseudocleavage furrow-dependent mechanism.

Other mechanisms proposed are concerned with the distribution of PAR proteins, instead of the mechanics-based mechanisms considered above. [167] proposes that the reaction-diffusion system constituted by the PAR proteins on the ellipsoidal surface of the embryo is sufficient to attain the alignment of AP axis with the long axis. However, this mechanism explicitly is

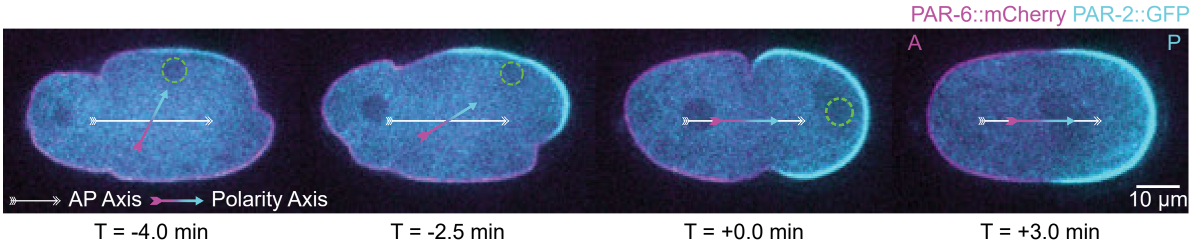

(a) AP axis alignment in *C. elegans* embryo, labelled with PAR-2::GFP, PAR-6::mCherry. In the untypical case where the AP axis establishment is triggered away from the long axis of the embryo, the AP axis – defined as the orientation of the PAR domains – reorients towards the long axis of the ellipsoidal embryo. In this micrograph, PAR-2::GFP (in cyan) denotes the posterior domain (pPARs), and PAR-6::mCherry (in magenta) denotes the anterior domain (aPARs). $T = 0\,\text{min}$ denotes the timepoint when the domains are fully established, and the male pronucleus moves away from the cortex. Green dashed circle denotes the male pronucleus. Instantaneous AP axis (polarity axis) is denoted by arrow colored cyan to magenta, long axis of embryo is denoted by white arrow. Anterior is to the left, posterior to the right. The timepoints are depicting, in order, the start of establishment phase ($T = -4.0\,\text{min}$), an intermediate snapshot during cortical flows ($T = -2.5\,\text{min}$), formation of pseudocleavage furrow ($T = 0.0\,\text{min}$), and pronuclear meeting ($T = 3.0\,\text{min}$). Note the movement of the posterior PAR domain along with the male pronucleus towards the right tip of the embryo – such that the AP axis aligns with the long axis. Images taken by Peter Gross [1] (used with permission)

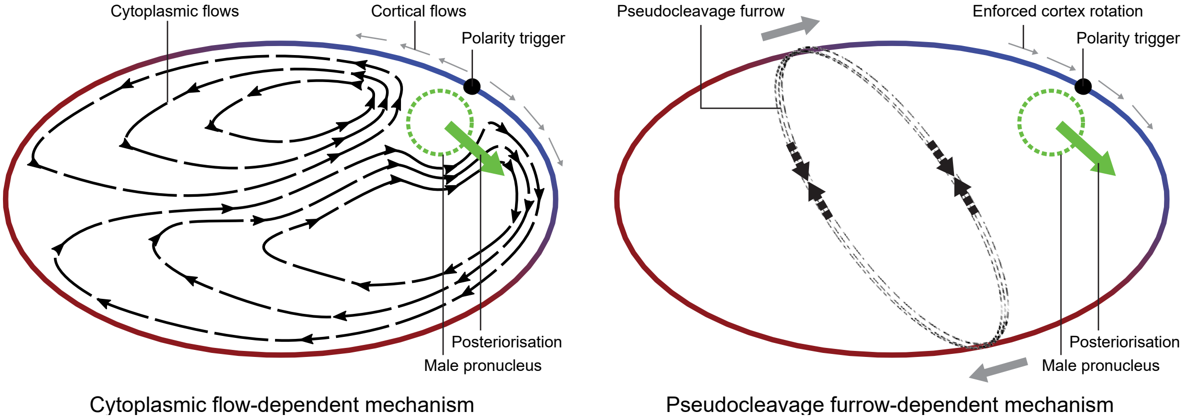

(b) Possible mechanisms for AP axis alignment, driven by cortical flows. Cortical flows can drive flows in the cytoplasm (left) [137] and lead to the formation of a contractile ring of actin around the embryo – called the pseudocleavage furrow (right) [88]. Cytoplasmic flow-dependent mechanism (left): In the untypical case where the male pronucleus (green dashed circle) is not on the long axis of the embryo, the polarity trigger (black circle) generates cortical flows (grey arrows) asymmetrically. These leads to asymmetric cytoplasmic flows (black dashed), which can then advect the male pronucleus towards the closest tip (posteriorisation denoted by green block arrow). Pseudocleavage furrow-dependent mechanism (right): In the untypical case where the male pronucleus is not on the long axis of the embryo, the pseudocleavage furrow is generated not perpendicular to the long axis of the embryo. As this contractile ring (black dashed arrows denote contraction) rotates to attain a configuration with minimal length (denoted by grey block arrows), it forces the rotation of the cortex (denoted by grey thin arrows). This forces the male pronucleus towards the closest tip.

Figure 1.8: AP axis aligns to the long axis in one-cell stage *C. elegans* embryo. Possible mechanisms of AP axis alignment.

considered in the absence of any activity of the actomyosin cortex – and therefore explains any correction of the AP axis during the later maintenance phase, not the alignment in the establishment phase. In fact, previous studies indicate that AP axis alignment cannot occur during the establishment phase in the absence of any cortical activity [158, 168, 169]. Additionally, [156] has indicated that binding and unbinding of PAR proteins to the cortex could be curvature sensitive – which could also play a role in the geometry sensing required for AP axis alignment.

1.5 Overview

The aim of this work is to elucidate the mechanism that drives AP axis alignment in the one-cell stage *C. elegans* embryo. This is accomplished in the following way: An active nematic fluid description of the actomyosin cortex present on the 2D surface of the embryo, which can incorporate both the cytoplasmic flow-dependent and pseudocleavage furrow-dependent mechanisms, is first introduced. This theoretical model of AP axis alignment, in conjunction with experiments that remove the pseudocleavage furrow, is then used to show that the pseudocleavage furrow-dependent mechanism is the predominant mechanism driving AP axis alignment in *C. elegans*, with cytoplasmic flow-dependent mechanism a minor contributor. Furthermore, relation between AP axis alignment and embryo geometry is explored. Experimental modifications to the embryo geometry are used to show that embryo geometry can influence AP axis alignment process in a manner consistent with both the theoretical description of the cortex and a simplified model of the pseudocleavage furrow-dependent mechanism.

The structure of the thesis is as follows. In chapter 2 the theoretical model of AP axis alignment is introduced, developed by combining the descriptions of the cortex from [1] and [88]. Details on the numerical simulations and selection of parameters of the theoretical model are also briefly described. In chapter 3, the experimental methods of the work presented in this thesis are detailed, alongwith discussing the worm strains used and genetic perturbations made. Details of acquiring movies of *C. elegans* embryos undergoing AP axis alignment, and their subsequent analysis to obtain relevant measurements are also discussed. In chapter 4, the tools introduced in chapter 3 are used to test various hypotheses experimentally and compare their results to simulation results from the theoretical model discusses in chapter 2, in order to elucidate the mechanism of AP axis alignment. In chapter 5, the results presented in this thesis are summarised and discussed in context of results from previous studies.

Chapter 2

A theoretical model for AP axis alignment

In this chapter, the theoretical model for AP axis alignment is described. The chapter is divided into three sections. The first section reviews the model of AP axis establishment described in [1], which utilizes a reaction-diffusion-advection system to describe the distribution of PAR proteins and NMY-2. The second section reviews the model of the formation of pseudocleavage furrow via compressive alignment of actin filaments due to flows in the actomyosin cortex, as described in [88]. The third section describes the theoretical model of AP axis alignment used in this thesis, by combining the two models discussed in the sections before. It also describes the details of the numerical simulations of the theoretical model, and how the parameters of the model were calibrated using experimental data. The theoretical model was developed in collaboration with M. Nestler and A. Voigt, with numerical simulations and calibration done by M. Nestler – further details on the model are described in [170].

2.1 A model of AP axis establishment in *C. elegans*

As discussed in section 1.4, the centrosomes associated with the male pronucleus guide the establishment of AP axis. In [1], the authors propose a model to investigate the centrosome-guided AP axis establishment. In particular, the following components are included in the model proposed in [1]:

- Mutual antagonism between aPARs and pPARs [139] is captured via a mass-conserved Turing-like system [150, 171, 172]
- Mechanochemical feedback between the PAR polarity system and actomyosin cortex is captured via coupling this Turing-like system to an active isotropic fluid description of the cortex [77, 84]
- Spatiotemporal cues provided by the centrosomes associated with the male pronucleus (for loading of pPARs and depletion of myosin on the cortex) are captured as two distinct guiding cues – pPARs stabilization cue and actomyosin cue, with the latter having two components.

This section describes this model of AP axis establishment introduced in [1]. This model assumes that the male pronucleus is always present at the posterior end, and thus assumes rotational symmetry around the long axis of the embryo. This simplifies the model to a 1-dimensional model of length L with periodic boundary conditions, along the boundary of the cross-section at the midplane of the embryo [1]. The posterior end is considered to be at the center of the domain $x \in [-\frac{L}{2}, \frac{L}{2}]$ – that is, at $x = 0$ (see Figure 2.1). Note that the curvature of the embryo boundary is neglected in this model.

2.1.1 Turing-like system for PAR polarity system

Three proteins are considered in the model discussed in this section: aPARs, pPARs and myosin. Each protein has a membrane-bound fraction and a cytoplasmic fraction, with exchange between the two fractions throughout the cortex. It is assumed that the sum total of its membrane-bound fraction c and cytoplasmic fraction c_{cyto} is a constant c_{tot} throughout the AP axis establishment. Here c can either be A, P or M – representing aPARs, pPARs or myosin respectively. This constraint of limited protein pool can be written as:

$$c_{tot}V = \int_{\text{cortex}} c \, \mathrm{d}S + \int_{\text{cytoplasm}} c_{cyto} \, \mathrm{d}V \tag{2.1}$$

where V is the volume of the embryo and c, c_{cyto} are volumetric concentrations while c is surface concentration of the protein considered. It is further assumed that the cytoplasmic concentrations are fairly homogeneous (therefore, $\int_{\text{cytoplasm}} c_{cyto} \, \mathrm{d}V \approx c_{cyto}V$) – due to the large diffusion coefficients in the cytoplasm [147]. Altogether, this leads to the following expression for the concentration of the cytoplasmic fraction c_{cyto}:

$$c_{cyto} = c_{tot} - \frac{1}{V} \int_{\text{cortex}} c \, \mathrm{d}S \tag{2.2}$$

In the model discussed in this section, rotational symmetry has been used to reduce the cortex to a 1-dimensional surface along the embryo boundary at the mid-plane cross-section. In this scenario, the above reduces to:

$$c_{cyto} = c_{tot} - \frac{\psi}{L} \int_{-\frac{L}{2}}^{\frac{L}{2}} c(x,t) \, \mathrm{d}S \tag{2.3}$$

where ψ is the surface-to-volume ratio for the ellipsoidal geometry of the embryo.

The spatiotemporal dynamics of the surface concentrations c are considered next. The continuity equation for c can be written as (from Equation 1.6):

$$\partial_t c(x,t) + \partial_x J^{(c)} = r^{(c)} \tag{2.4}$$

where $J^{(c)}$ is the flux of proteins c and $r^{(c)}$ the rate of generation of c from all the reactions that affect c. As before, $J^{(c)} = cv + j^{(c)}$ can be split into a advective flux (due to advection with cortical flow velocity $\vec{v}(x,t)$) and relative flux $j^{(c)}$. In the model discussed here, the relative flux $j^{(c)}$ arises due to passive diffusion – thus, $j^{(c)} = -D_c \partial_x c$ from Fick's law of diffusion, for diffusion constant D_c. Altogether, the dynamics of $c(x,t)$ is given by:

$$\partial_t c(x,t) = -\partial_x(cv) + D_c \partial_x^2 c + r^{(c)} \tag{2.5}$$

for c being either A, P or M. Equation 2.5 includes three physical processes: advective transport by cortical flows $-\partial_x(cv)$, passive diffusion on the cortex $D_c \partial_x^2 c$ and chemical reactions amongst the surface-bound molecules and their cytoplasmic counterparts. The reaction terms $r^{(c)}$ are considered next.

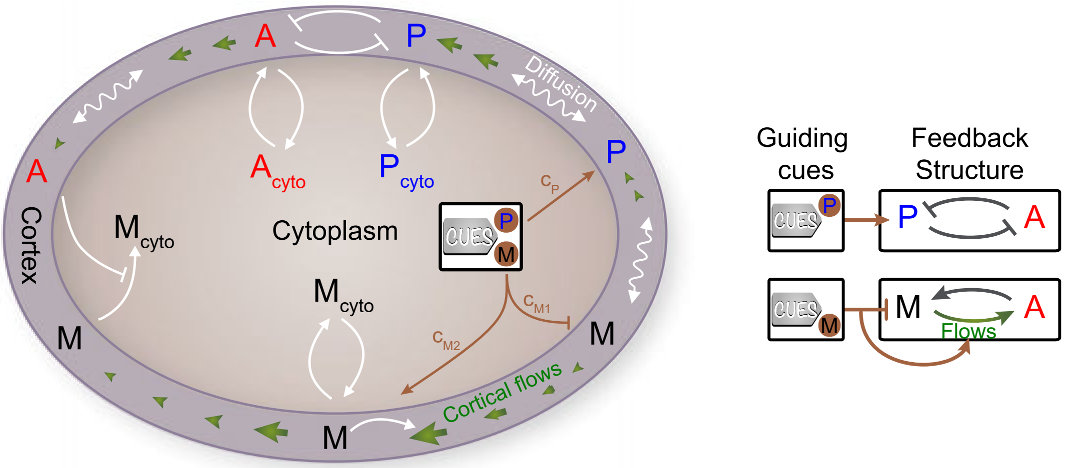

(a) Schematic depicting the Turing-like system for aPARs A, pPARs P and myosin M. These proteins are either located in the cytoplasm (denoted using the *cyto* subscript) or at the cortex, where they are subjected to lateral diffusion and advective transport by cortical flows. The following reactions are considered: spontaneous association with and dissociation from the cortex, mutual antagonism between aPARs and pPARs when associated to the cortex, and aPARs regulated dissociation of myosin from the cortex. Two guiding cues are provided by the centrosomes and steer the AP axis establishment process: pPARs domain stabilisation cue (denoted by c_P) and actomyosin cue with two components – one depleting myosin at the cortex (denoted by c_{M1}) and the other regulating contractility (denoted by c_{M2}. See section 2.1 for details.

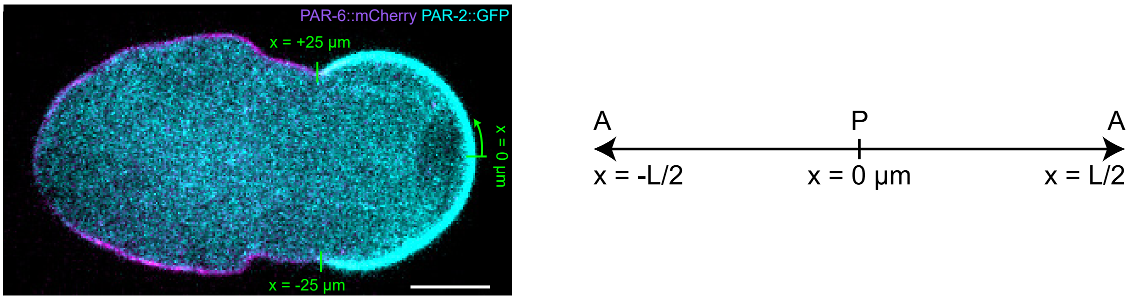

(b) Left: Mid-plane section of the *C. elegans* embryo, labelled with PAR-2::GFP (posterior domain, in cyan) and PAR-6::mCherry (anterior domain, in magenta). The model discussed in section 2.1, using the rotational symmetry around the long axis, is reduced to a 1-dimensional model along the boundary of this mid-plane section, endowned with the arclength variable x. x is annotated in green – $x = 0$ denotes the posterior pole. Scale bar: 10 µm. Note that the positive and negative "arm" of the boundary is flipped compared to that in [1] following the convention followed in this thesis. Right: Boundary of the cross-section at the midplane of the embryo reduced to a 1-dimensional line with periodic boundary conditions. $x = 0$ is at the posterior pole (denoted by P), and $x = \pm L/2$ at the anterior (denoted by A).

Figure 2.1: Schematic representing the 1-dimensional model of AP axis establishment described in [1], and visualization of the arclength axis used in the model. Figure adapted froim [1], see section 2.1 for details

For myosin, two reactions are considered: exchange of cortical myosin with the cytoplasm, and regulation of the dissociation rate (from the cortex) by aPARs [1]. The reaction rate $r^{(M)}$ can then be written as:

$$r^{(M)} = k_{on,M} M_{cyto} - \left[k_{off,M} - k_{AM} A\right] M \tag{2.6}$$

where $k_{on,M}$ and $k_{off,M}$ are myosin association (to the cortex) and dissociation (from the cortex) rates – governing the exchange between the cortical and cytoplasmic myosin. k_{AM} represents the regulation of the dissociation rate of myosin by aPARs.

For aPARs and pPARs, two reactions are considered: exchange with cytoplasmic bulk fraction, and mutual antagonism on the cortex between aPARs and pPARs [139]. For aPARs, this antagonism occurs in the form of regulation of the cortical association rate of aPARs by the pPARs protein complex [173, 174]. For pPARs, this antagonism instead occurs in the form of regulation of the cortical dissociation rate of pPARs by the aPARs protein complex [150]. Thus, including both exchange with the cytoplasm and mutual antagonism in the PAR polarity system, the reaction rates $r^{(A)}$ and $r^{(P)}$ can be written as:

$$r^{(A)} = \frac{k_{on,A}}{1 + k_{AP} P^{s_P}} A_{cyto} - k_{off,A} A \tag{2.7a}$$

$$r^{(P)} = k_{on,P} P_{cyto} - \left[k_{off,P} + k_{PA} A^{s_A}\right] P \tag{2.7b}$$

where $k_{on,A}$ and $k_{off,A}$ are association and dissociation rates for aPARs, and similarly $k_{on,P}$ and $k_{off,P}$ are association and dissociation rates for pPARs. These govern the exchange between the cortical and cytoplasmic fractions of the PAR proteins. k_{AP} and k_{PA} represents the mutual antagonism between aPARs and pPARs proteins, and s_A and s_P are stoichiometric coefficients.

2.1.2 Active isotropic description of actomyosin cortex

In the model described in this section, the actomyosin cortex is considered as an active isotropic fluid, with an additional frictional drag force on the cortex due to the surrounding cell membrane, eggshell and cytoplasm [77]. In other words, the momentum balance in this model is written as:

$$\partial_\beta \sigma_{\alpha\beta} - \gamma v_\alpha = 0 \tag{2.8}$$

where γ is the frictional drag coefficient. As the flows in the actomyosin cortex may be considered to in the low-reynolds number regime, the inertial term $\rho(\partial_t v_\alpha + v_\beta \partial_\beta v_\alpha)$ from Equation 1.5 can be neglected.

Furthermore, the stress is separated into a passive viscous stress and an active actomyosin-generated stress. Namely, Equation 1.31 may be re-written as (for the 2-dimensional cortex):

$$\sigma_{\alpha\beta} = \left[2\eta \left(\frac{\partial_\beta v_\alpha + \partial_\alpha v_\beta}{2} - \frac{1}{2}\partial_\gamma v_\gamma \delta_{\alpha\beta}\right) + \left(\eta_v \partial_\gamma v_\gamma - p\right)\delta_{\alpha\beta}\right] + \zeta \Delta\mu \delta_{\alpha\beta} = \sigma^{(passive)}_{\alpha\beta} + \sigma^{(active)}_{\alpha\beta} \tag{2.9}$$

where $\sigma^{(passive)}_{\alpha\beta} = 2\eta\left(\frac{\partial_\beta v_\alpha + \partial_\alpha v_\beta}{2} - \frac{1}{2}\partial_\gamma v_\gamma \delta_{\alpha\beta}\right) + \left(\eta_v \partial_\gamma v_\gamma - p\right)\delta_{\alpha\beta}$ contains all the viscous terms in the stress and $\sigma^{(active)}_{\alpha\beta} = \zeta\Delta\mu\delta_{\alpha\beta}$ is the active stress generated by myosin motors. Here, η and η_v are shear and bulk viscosity coefficients, p is the pressure, $\Delta\mu$ the difference in chemical potential for ATP hydrolysis and ζ is a phenomenological coefficient that denotes the stress generated by myosin motors. Note that rotational symmetry has not been utilized till now, in the description of the cortex.

Following [85], the passive viscous stress may be written as:

$$\sigma_{\alpha\beta}^{(passive)} = 2\eta\left(\frac{\partial_\beta v_\alpha + \partial_\alpha v_\beta}{2} - \frac{1}{2}\partial_\gamma v_\gamma \delta_{\alpha\beta}\right) + (\eta_v \partial_\gamma v_\gamma - p)\,\delta_{\alpha\beta} \tag{2.10}$$

where $\bar{\eta}$ is effective 2-D bulk viscosity of the cortex. In the the model described here, this effective bulk viscosity is neglected – thus, only the shear stress related term is retained. Rotational symmetry around the long axis implies that gradients survive only along the x-axis, thus reducing the passive viscous stress to:

$$\sigma^{(passive)} = \eta \partial_x v \tag{2.11}$$

The active stress $\sigma^{(active)}$ is assumed to be of the following form:

$$\sigma^{(active)} = C_* \frac{M}{M + M_*} \tag{2.12}$$

where C_* indicates the strength of cortical contractility, M is the local concentration of myosin and M_* is a Hill coefficient. Note that M_* controls the sensitivity of active stress to myosin concentration – if $M >> M_*$, $\sigma^{(active)} \approx C_*$, while if $M << M_*$, $\sigma^{(active)} \approx \frac{C_*}{M_*}$. In other words, a myosin rich patch of cortex generates an active stress closer to C_*, while a myosin poor patch generates a much smaller active stress closer to $\frac{C_*}{M_*}$.

2.1.3 Guiding cues for AP axis establishment

Before the dynamical equations for the concentrations $c(x, t) = A, P, M$ and cortical velocity $v(x, t)$ are written, the guiding cues provided by the centrosome need to be considered. Since in the model described in this section, it is assumed that the male pronucleus is at the posterior end, these cues are provided at the posterior pole – that is, at $x = 0$. Two guiding cues are provided by the centrosomes – a cue to the pPARs domain, and a cue to the actomyosin cortex. Additionally, the cue to the actomyosin cortex contains two components. Altogether, these cues are:

- pPARs domain stabilisation cue, due to the microtubule-mediated local inhibition of removal of pPARs from the cortex by aPARs [158]. This cue is incorporated in the model by modifying the reaction rate for pPARs $r^{(P)}$ as:

  $$r^{(P)} = k_{on,P} P_{cyto} - \left[k_{off,P} + k_{PA} A^{s_A} (1 - \kappa_P F_P(x) f_P(t))\right] P \tag{2.13}$$

  where κ_P is the (dimensionless) strength of the pPARs domain stabilisation cue. $F_P(x)$ localizes the cue near the posterior pole – and selected to be a gaussian $F_p(x) = \exp\left(-\frac{x^2}{d_P^2}\right)$ with characteristic length d_P. $f_P(t)$ captures the temporal characteristics of the cue, and is set to $f_P(t) = \frac{1}{2}\left[\tanh\left(\frac{t}{\tau_{P,on}}\right) + 1\right]$. $f_P(t)$ describes a smooth transition from zero at $t = 0$ to one on the time-scale $\tau_{on,P}$. The pPARs domain stabilisation cue thus starts at $t = 0$ and remains on.

- Myosin depletion component of the actomyosin cue, acting via an unknown mechanism [159]. This cue is incorporated in the model by modifying the reaction rate for myosin $r^{(M)}$ as:
  $$r^{(M)} = k_{on,M}M_{cyto} - \left[k_{off,M}(1 + \kappa_M F_M(x) f_M(t)) - k_{AM}A\right] M \tag{2.14}$$
  where κ_M is the (dimensionless) strength of the actomyosin cue. $F_M(x)$ localizes the cue near the posterior pole – and selected to be a gaussian $F_M(x) = \exp\left(-\frac{x^2}{d_M^2}\right)$ with characteristic length d_M. $f_M(t)$ captures the temporal characteristics of the cue, and is set to $f_M(t) = \frac{1}{2}\left[\tanh\left(\frac{t}{\tau_{M,on}}\right) - \tanh\left(\frac{t-T_M}{\tau_{M,off}}\right)\right]$. $f_M(t)$ describes a smooth transition from zero at $t = 0$ to one on the time-scale $\tau_{on,M}$, and subsequently from one to zero after $t = T_M$ on a time-scale $\tau_{off,M}$. The myosin depletion component of the actomyosin cue thus starts at $t = 0$ and remains active until $t = T_M$, after which it shuts off.

- Contractility component of the actomyosin cue, due to the up-regulation of myosin contractility briefly after centrosomes trigger polarity establishment [169]. This cue is incorporated in the model by modifying the active stress $\sigma^{(active)}$ as:
  $$\sigma^{(active)} = C_* f_C(t) \frac{M}{M + M_*} \tag{2.15}$$
  where $f_C(t)$ captures the temporal characteristics of the cue, and is set to $f_C(t) = \frac{1}{2}\left[1 - \tanh\left(\frac{t-T_M}{\tau_{M,off}}\right)\right]$. $f_C(t)$ describes a smooth transition from one to zero after $t = T_M$ on a time-scale $\tau_{off,M}$. The contractility component of the actomyosin cue thus turns off after $t = T_M$.

2.1.4 Full model of AP axis establishment in [1]

Combining all these together, the full set of dynamic equations for the concentrations $A(x,t), P(x,t), M(x,t)$ (for aPARs, pPARs and myosin respectively) are given by:

$$\partial_t A = -\partial_x(vA) + D_A\partial_x^2 A + \frac{k_{on,A}}{1 + k_{AP}P^{s_P}} A_{cyto} - k_{off,A}A \tag{2.16a}$$
$$\partial_t P = -\partial_x(vP) + D_P\partial_x^2 P + k_{on,P}P_{cyto} - \left[k_{off,P} + k_{PA}A^{s_A}(1 - \kappa_P F_P(x) f_P(t))\right] P \tag{2.16b}$$
$$\partial_t M = -\partial_x(vM) + D_M\partial_x^2 M + k_{on,M}M_{cyto} - \left[k_{off,M}(1 + \kappa_M F_M(x) f_M(t)) - k_{AM}A\right] M \tag{2.16c}$$

where $v(x,t)$ is the cortical flow velocity, and the rest of the terms are defined as in subsection 2.1.1 and subsection 2.1.3. The cytoplasmic concentrations $A_{cyto}, P_{cyto}, M_{cyto}$ are found using Equation 2.3.

The dynamical equation for cortical flow velocity $v(x,t)$ is written using the momentum balance (Equation 2.8) and the definitions of active (Equation 2.15) and passive stresses (Equation 2.11) as:

$$\eta\partial_x^2 v - \gamma v = -C_* f_C(t)\partial_x\left(\frac{M}{M + M_*}\right) \tag{2.17}$$

where η is the viscosity of the cortex and γ the frictional drag coefficient. C_* and M_* are defined in subsection 2.1.2, and $f_C(t)$ in subsection 2.1.3.

2.2 A model of pseudocleavage furrow formation in *C. elegans*

In [88], the authors investigate the role of cortical flows in the formation of contractile rings in the *C. elegans* embryo, such as the pseudocleavage furrow or the cytokinetic ring. The pseudocleavage furrow, as mentioned in section 1.4, is a contractile ring-like structure that appears late in the establishment phase which appears as a furrow in the middle of the embryo [88, 136]. The cytokinetic ring is a contractile ring that forms much later during the first cell division in the embryo, and divides the one-cell P0 embryo into a larger AB cell and a smaller P1 cell (see section 1.3). The discussion here focuses on the pseudocleavage furrow only.

In [88], the authors show that the contractile ring that is the pseudocleavage furrow forms as a result of cortical flow-driven compressive alignment of actin filaments in the actomyosin cortex. For this purpose, the authors in [88] propose a model of the actomyosin cortex as an active nematic fluid, which is discussed in this section. The nematic tensor $Q_{\alpha\beta}$ quantifies the average orientation of actin filaments in the cortex at the micrometer scale – see the discussion on coarse-grained variables in section 1.2. The model considers the case where the male pronucleus is at the posterior pole of the embryo – that is, when the AP axis is aligned with the long axis of the embryo. Thus, the model assumes rotational symmetry around the long axis of the embryo, as was the case in the previous section. Additionally, the curvature of the embryo is neglected, allowing a description of the cortex in an effective Cartesian coordinate system (see Figure 2.2).

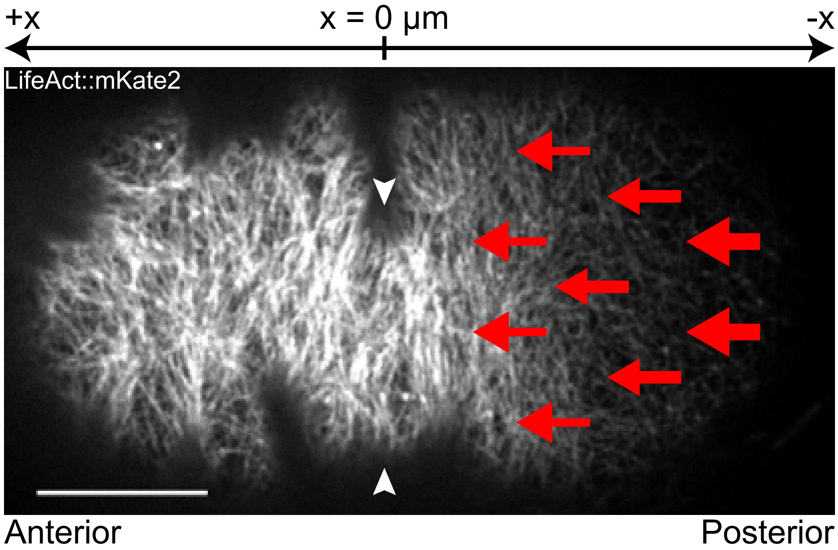

Figure 2.2: Cortical section of the *C. elegans* embryo, labelled with LifeAct::mKate2 (white), to depict the organisation of actin filaments at onset of pseudocleavage furrow (white arrows). Red arrows depict anterior-directed cortical flows observed during pseudocleavage furrow onset. The x axis used in section 2.2 are also depicted, with $x = 0\,\mu m$ at the pseudocleavage furrow, and the posterior (anterior) on the negative (positive) x end. y axis is along the vertical edge of the image. Scale bar: 10 μm. Adapted from [88]

2.2.1 Dynamics of Actin alignment

Following the discussion in section 1.2, the constitutive equation that governs the rate of change in the nematic tensor for an active nematic fluid may be written from Equation 1.40 as:

$$\frac{DQ_{\alpha\beta}}{Dt} = -\nu\tilde{v}_{\alpha\beta} + \frac{1}{\bar{\gamma}}H_{\alpha\beta} + \lambda Q_{\alpha\beta}\Delta\mu \tag{2.18}$$

where $\frac{DQ_{\alpha\beta}}{Dt} = \partial_t Q_{\alpha\beta} + v_\gamma \partial_\gamma Q_{\alpha\beta} + \omega_{\alpha\gamma}Q_{\gamma\beta} + \omega_{\beta\gamma}Q_{\alpha\gamma}$ is the corotational and comoving derivative of $Q_{\alpha\beta}$ (see Equation 1.36), $\tilde{v}_{\alpha\beta} = \frac{\partial_\alpha v_\beta + \partial_\beta v_\alpha}{2} - \frac{1}{2}\partial_\gamma v_\gamma \delta_{\alpha\beta}$ is the traceless symmetric part of the velocity gradient (written for a 2-dimensional cortex, see Equation 1.38), $\omega_{\alpha\beta} = \frac{\partial_\alpha v_\beta - \partial_\beta v_\alpha}{2}$ is the antisymmetric part of the velocity gradient (see Equation 1.37), $H_{\alpha\beta} = -\frac{\delta F_0}{\delta Q_{\alpha\beta}}$ is the molecular field conjugate to the nematic tensor $Q_{\alpha\beta}$ for the instrinsic free energy F_0 (see Equation 1.39) and $\Delta\mu$ is the chemical potential difference for ATP hydrolysis. Note that the corotational and comoving derivative $\frac{DQ_{\alpha\beta}}{Dt}$ includes the effect of advection on $Q_\alpha\beta$.

The phenomenological coefficient ν captures the change in nematic tensor $Q_{\alpha\beta}$ due to the velocity gradient $\tilde{v}_{\alpha\beta}$ – thus capturing the compressive alignment of actin filaments driven by flows in the actomyosin cortex. The phenomenological coefficient λ couples the activity of myosin motors (which catalyse the hydrolysis of ATP) to the change in nematic tensor $Q_{\alpha\beta}$ – thus capturing the active alignment of actin filaments by myosin motors. The phenomenological coefficient $\bar{\gamma}$ captures the relaxation of the actin alignment to the equilibrium state. For the free energy F_0, the following form is assumed:

$$F_0 = K\int \left[\frac{1}{2}Q_{\alpha\beta}Q_{\alpha\beta} + \frac{l^2}{2}\partial_\gamma Q_{\alpha\beta}\partial_\gamma Q_{\alpha\beta}\right] \mathrm{d}S \tag{2.19}$$

where the integral is taken over the whole cortex, K characterises the tendency of actin filaments to relax to isotropic orientation ($K > 0$), and l is the characteristic length scale below which filaments are coherently aligned. This form of F_0 yields $H_{\alpha\beta}$ as:

$$H_{\alpha\beta} = -\frac{\delta F_0}{\delta Q_{\alpha\beta}} = K[l^2\partial_\gamma\partial_\gamma Q_{\alpha\beta} - Q_{\alpha\beta}] \tag{2.20}$$

Finally, it is noted in [88] that the active alignment of actin filaments by myosin motors plays an insignificant role in the formation of the pseudocleavage furrow. Thus, λ is set to zero. This yields the following equation for the dynamics of $Q_{\alpha\beta}$:

$$\frac{DQ_{\alpha\beta}}{Dt} = -\nu\tilde{v}_{\alpha\beta} + \frac{1}{\bar{\gamma}}H_{\alpha\beta} = -\nu\tilde{v}_{\alpha\beta} + \frac{Kl^2}{\bar{\gamma}}\partial_\gamma\partial_\gamma Q_{\alpha\beta} - \frac{K}{\bar{\gamma}}Q_{\alpha\beta} \tag{2.21}$$

As the model assumes the AP axis is aligned with the long axis, the rotational symmetry around the long axis can be utilized to neglect derivatives in directions perpendicular to the long axis. Additionally, the component of the cortical flow velocity perpendicular to the long axis is also ignored. This simplifies Equation 2.21 into:

$$\partial_t Q_{xx} + v_x\partial_x Q_{xx} = -\frac{\nu}{2}\partial_x v_x + \frac{Kl^2}{\bar{\gamma}}\partial_x^2 Q_{xx} - \frac{K}{\bar{\gamma}}Q_{xx} \tag{2.22a}$$

$$\partial_t Q_{xy} + v_x\partial_x Q_{xy} = \frac{Kl^2}{\bar{\gamma}}\partial_x^2 Q_{xy} - \frac{K}{\bar{\gamma}}Q_{xy} \tag{2.22b}$$

where x denotes the direction along the long axis and y perpendicular to it, on the cortex (see Figure 2.2). Note that the curvature of the embryo is not considered in these equations. The nematic tensor is given by:

$$Q_{\alpha\beta} = \begin{bmatrix} Q_{xx} & Q_{xy} \\ Q_{xy} & -Q_{xx} \end{bmatrix} \tag{2.23}$$

Thus, given the cortical flow velocity v_x, Equation 2.22 governs the dynamics of the nematic tensor $Q_{\alpha\beta}$ and consequently the alignment of actin filaments in the cortex. At steady state, as assumed in [88], $\partial_t Q_{xx}$ and $\partial_t Q_{xy}$ are set to zero.

2.2.2 Active stress generated by alignment of actin filaments

In [88], the following form for the stress tensor is proposed:

$$\sigma_{\alpha\beta} = \eta \tilde{v}_{\alpha\beta} + \eta_v \partial_\gamma v_\gamma \delta_{\alpha\beta} + \zeta \delta_{\alpha\beta} + \sigma_{\alpha\beta}^{(nematic)} \tag{2.24}$$

where η and η_v are shear and bulk viscosity of the cortex respectively. ζ represents the isotropic part of the active contractile stresses generated by myosin motors in the actomyosin cortex. $\sigma_{\alpha\beta}^{(nematic)}$ is the part of the active tension that depends on the nematic stress tensor $Q_{\alpha\beta}$ – such a component encodes the anisotropic active stress generated due to the interaction between the myosin motors and aligned actin filaments [88]. For the purposes of this discussion, the curvature of the embryo is neglected as the primary interest is in the form of the stress tensor. [88] considers a differential geometry description of the stress tensor, which does include curvature.

The following form of $\sigma_{\alpha\beta}^{(nematic)}$ is proposed:

$$\sigma_{\alpha\beta}^{(nematic)} = \frac{\Psi}{2}\left[\frac{1}{\sqrt{2}}\sqrt{Q_{\gamma\nu}Q_{\nu\gamma}}\delta_{\alpha\beta} + Q_{\alpha\beta}\right] \tag{2.25}$$

where Ψ is a phenomenological coefficient that controls the strength of the nematic component of the stress. Note that $\sqrt{Q_{\gamma\nu}Q_{\nu\gamma}}$ is the Frobenius norm of $Q_{\alpha\beta}$. The above form is selected to ensure that the nematic stress is along the local orientation of actin filaments. This can be observed by writing Equation 1.10 for the 2-dimensional cortex – with the unit vector $\vec{n}$ denoting the local nematic director (and thus the local orientation of actin filaments):

$$\begin{aligned}
Q_{\alpha\beta} &= S\left(n_\alpha n_\beta - \frac{1}{2}\delta_{\alpha\beta}\right); \quad n_\alpha n_\alpha = 1 \\
Q_{\alpha\beta}Q_{\beta\alpha} &= S^2\left(n_\alpha n_\beta - \frac{1}{2}\delta_{\alpha\beta}\right)\left(n_\beta n_\alpha - \frac{1}{2}\delta_{\beta\alpha}\right) = \frac{S^2}{2} \implies \sqrt{Q_{\alpha\beta}Q_{\beta\alpha}} = \frac{S}{\sqrt{2}} \\
\sigma_{\alpha\beta}^{(nematic)} &= \frac{\Psi}{2}\left[\frac{1}{\sqrt{2}}\sqrt{Q_{\gamma\nu}Q_{\nu\gamma}}\delta_{\alpha\beta} + Q_{\alpha\beta}\right] = \frac{\Psi}{2}\left[\frac{S}{2}\delta_{\alpha\beta} + Q_{\alpha\beta}\right] = \frac{S\Psi}{4}n_\alpha n_\beta
\end{aligned}$$

which implies that the stress $\sigma_{\alpha\beta}^{(nematic)}$ will always generate force along the local nematic director $\vec{n}$, never perpendicular to it.

One may also compare the stress tensor used in this section (Equation 2.24) to those used in the model proposed in [1] (Equation 2.9) and obtained in the generic theory of active nematic fluids (Equation 1.40):

- Comparing to model proposed in [1] and discussed in section 2.1
  On comparison with Equation 2.9, one may note that the stress tensor in Equation 2.24 is essentially the same as that in Equation 2.9 plus an additional active term $\sigma_{\alpha\beta}^{(nematic)}$ that arises from the nematic nature of the cortex considered in this section. Note however that the model proposed in [1] ignores the bulk viscosity related terms in the stress, while those are considered here.

- Comparing to generic constitutive equations for an active incompressible nematic fluid [85] discussed in subsection 1.2.4
  On comparison with Equation 1.40, one may note that the stress tensor in Equation 2.24 shares the shear viscosity related term $\eta\tilde{v}_{\alpha\beta}$ with the symmetric deviatoric stress tensor in Equation 1.40. Additionally, the model discussed here contains the bulk viscosity term $\eta_v \partial_\gamma v_\gamma \delta_{\alpha\beta}$ and active isotropic stress generated by myosin motors $\zeta\delta_{\alpha\beta}$ not considered in Equation 1.40. However such terms are compatible with the generic hydrodynamic theory of active nematic fluid – as can be observed by comparing the stress tensor for an active isotropic fluid Equation 1.31 and active nematic incompressible fluid Equation 1.40. Note that any coupling between isotropic stress and nematic tensor is ignored here. Another difference is the absence of the terms coupling the stress to the molecular field $H_{\alpha\beta}$ and $Q_{\alpha\beta}$ in Equation 1.40 – instead, they are replaced by $\sigma_{\alpha\beta}^{(nematic)}$ in the model discussed in this section. Finally, the equilibrium stress and antisymmetric component of the stress generated in nematic fluids – as written in Equation 1.35 – are ignored here (thus the symmetric traceless deviatoric stress in Equation 1.40 is the full stress tensor in Equation 2.24).

2.3 A model of AP axis alignment in *C. elegans*

In the previous sections, the two models for the actomyosin cortex proposed in [1] and [88] are discussed. Both studies discussed aspects of the actomyosin cortex during AP axis establishment in the one-cell *C. elegans* embryo – the first discussing the guidance of AP axis establishment via centrosomes and the second discussing the formation of the pseudocleavage furrow. In both cases, the AP axis is always assumed to be aligned with the long axis of the ellipsoidal embryo. However, as discussed in subsection 1.4.3, the AP axis may not always be aligned with the long axis – in fact, the AP axis actively re-orients to align with the long axis if it is not aligned before. In this section, the theoretical model for this AP axis alignment is described – obtained by combining elements of the two models discussed in section 2.1 and section 2.2. This theoretical model is the one used in this thesis for comparison with experimental observations of AP axis alignment under different conditions – see chapter 4 for details. This theoretical model of AP axis alignment was developed in collaboration with Michael Nestler and Prof. Axel Voigt from the Technische Universität Dresden. The text follows the description in [170].

In the derivation of this theoretical model of the AP axis alignment, it is assumed that the fluid flow in the cortex and cytoplasm is laminar – that is, in the low Reynolds number regime. In this scenario, the inertial terms in the momentum balance for the cortex and cytoplasm can be ignored – thus, the momemtum balance in the cortex is described by Equation 2.8, and in the cytoplasm by the Stokes equation. Additionally, it is assumed that the cortical dynamics is fast enough that the AP axis alignment may be considered to be a quasi-steady state process. That is, for a given position of the male pronucleus (and thus the centrosomal cues), the concentration of myosin in the cortex and the cortical flow velocity are instantly defined, and can be obtained by the steady state approximation. In effect, the theoretical model of AP axis alignment takes as input the given position of the male pronucleus, and calculates as output the velocity of the male pronucleus. In chapter 4, the position of the male pronucleus is recorded as its "Angular Position": the angle between the long axis and the line connecting the center of the ellipsoidal embryo to the center of the male pronucleus; and its velocity is recorded as the "Posteriorisation velocity": the component of the velocity of the male pronucleus locally parallel to the cortex.

This section is organised as follows. First, the actomyosin cortex is described as an active nematic surface fluid, on the fixed surface of an ellipsoid. This is achieved in two steps. A bulk description of the cortex as an active nematic compressible fluid is presented – illustrating the elements of the two models discussed before that are combined here. This bulk description is then converted into a surface description by a thin film limit – yielding the description of the cortex as an active nematic surface fluid. Note that this description of the cortex takes into account the curvature of the ellipsoid, unlike the two models described in the sections above. Second, the description of the cytoplasmic bulk and transport of the male pronucleus is presented: the cytoplasmic bulk being treated as a Stokes fluid [137] and the male pronucleus as being advected by both cytoplasmic and cortical flows. This description of the cytoplasmic bulk and male pronucleus together with the description of the cortex as an active nematic surface fluid consititutes the theoretical model of AP axis alignment considered in this thesis. Finally, the details of the numerical simulations of the theoretical model are presented – including the details on the calibration of model parameters using experimental data. These numerical simulations were performed by Michael Nestler [170].

2.3.1 A thin film active nematic description of the cortex

Before considering the description of the actomyosin cortex as considered in the theoretical model of AP axis alignment, the general constitutive equations for an active compressible nematic fluid can be derived. The description of the actomyosin cortex used in the theoretical model then can be obtained as a special case.

Constitutive equations for a generic active compressible nematic fluid

Following the discussion in subsection 1.2.4 and [85], the constitutive equations for the active nematic compressible fluid may be written down. In particular, the entropy production rate may be identified as:

$$T\theta = \tilde{\sigma}^{d,s}_{\alpha\beta}\tilde{v}_{\alpha\beta} + \sigma^d \partial_\gamma v_\gamma + r\Delta\mu + \frac{DQ_{\alpha\beta}}{Dt}H_{\alpha\beta} \tag{2.26}$$

where

- The stress tensor $\sigma_{\alpha\beta}$ is decomposed into a symmetric traceless part $\tilde{\sigma}^{d,s}_{\alpha\beta}$ and an isotropic stress σ^d:

$$\begin{aligned}
\sigma_{\alpha\beta} &= \tilde{\sigma}^{d,s}_{\alpha\beta} + \sigma^d \delta_{\alpha\beta} \\
\tilde{\sigma}^{d,s}_{\alpha\beta} &= \sigma_{\alpha\beta} - \frac{1}{3}\sigma_{\gamma\gamma}\delta_{\alpha\beta} \\
\sigma^d &= \frac{1}{3}\sigma_{\gamma\gamma}
\end{aligned}$$

Note that the stress tensor is assumed to be symmetric. Additionally, comparison with Equation 1.35 indicates that the equilibrium stress (along with pressure) and the antisymmetric stress $Q_{\alpha\gamma}H_{\beta\gamma} - H_{\alpha\gamma}Q_{\beta\gamma}$ are ignored, following [88] (see subsection 2.2.2).

- The velocity gradient $\partial_\beta v_\alpha$ is decomposed into a symmetric traceless part $\tilde{v}_{\alpha\beta}$, an antisymmetric part $\omega_{\alpha\beta}$ and an isotropic part $\partial_\gamma v_\gamma$ ($\vec{v}$ is the cortical flow velocity):

$$\begin{aligned}
\partial_\beta v_\alpha &= \tilde{v}_{\alpha\beta} + \omega_{\alpha\beta} + \frac{1}{3}\partial_\gamma v_\gamma \delta_{\alpha\beta} \\
\tilde{v}_{\alpha\beta} &= \frac{\partial_\beta v_\alpha + \partial_\alpha v_\beta}{2} - \frac{1}{3}\partial_\gamma v_\gamma \delta_{\alpha\beta} \\
\omega_{\alpha\beta} &= \frac{\partial_\beta v_\alpha - \partial_\alpha v_\beta}{2}
\end{aligned}$$

- r is the reaction rate and $\Delta\mu$ the difference in chemical potential for the ATP hydrolysis reaction
- $H_{\alpha\beta} = -\frac{\delta F_0}{\delta Q_{\alpha\beta}}$ is the molecular field conjugate to the nematic tensor $Q_{\alpha\beta}$ (see Equation 1.39), and $\frac{DQ_{\alpha\beta}}{Dt}$ is the corotational and comoving derivative of $Q_\alpha\beta$ (see Equation 1.36).

Flux J_n	Force F_n	Time reversal signature $\epsilon(J_n), \epsilon(F_n)$	Rotation symmetry
$\tilde{\sigma}^{d,s}_{\alpha\beta}$	$\tilde{v}_{\alpha\beta}$	1,-1	Traceless symmetric tensor
σ^d	$\partial_\gamma v_\gamma$	1,-1	Scalar
$\frac{DQ_{\alpha\beta}}{Dt}$	$H_{\alpha\beta}$	-1,1	Traceless symmetric tensor
r	$\Delta\mu$	-1,1	Scalar

Table 2.1: Conjugate thermodynamic fluxes and forces for active compressible nematic fluid. Adapted from [85]

The conjugate thermodynamic fluxes and forces are identified in Table 2.1. Using the Onsager relations and Curie symmetry principle discussed in subsection 1.2.3, the constitutive equations for the active compressible nematic fluid may be written:

$$\tilde{\sigma}^{d,s}_{\alpha\beta} = 2\eta\tilde{v}_{\alpha\beta} + \chi Q_{\alpha\beta}\partial_\gamma v_\gamma + \nu H_{\alpha\beta} + \zeta_1 Q_{\alpha\beta}\Delta\mu \tag{2.27a}$$

$$\sigma^d = \chi Q_{\alpha\beta}\tilde{v}_{\alpha\beta} + \eta_v \partial_\gamma v_\gamma + \epsilon Q_{\alpha\beta}H_{\alpha\beta} + \zeta_2\Delta\mu \tag{2.27b}$$

$$\frac{DQ_{\alpha\beta}}{Dt} = -\nu\tilde{v}_{\alpha\beta} - \epsilon Q_{\alpha\beta}\partial_\gamma v_\gamma + \frac{1}{\gamma}H_{\alpha\beta} + \lambda Q_{\alpha\beta}\Delta\mu \tag{2.27c}$$

$$r = -\zeta_1 Q_{\alpha\beta}\tilde{v}_{\alpha\beta} - \zeta_2\partial_\gamma v_\gamma + \lambda Q_{\alpha\beta}H_{\alpha\beta} + \Lambda\Delta\mu \tag{2.27d}$$

where $\eta, \eta_v, \bar{\gamma}, \Lambda, \chi, \nu, \zeta_1, \epsilon, \zeta_2, \lambda$ are phenomenological coefficients. η and η_v are the shear and bulk viscosity of the fluid, $\bar{\gamma}$ characterises the relaxation of the local nematic ordering to equilibrium state and Λ describes diffusion. ζ_1 and ζ_2 represent active stresses in the fluid – ζ_1 represnting active nematic stress and ζ_2 representing active isotropic stress. λ represents the effect of activity on the nematic tensor – such as the active alignment of actin filaments by myosin motors [88] (see subsection 2.2.1). ν represents the change in nematic tensor due to flows in the fluid – such as the compressive alignment of actin filaments in the cortex [88] (see subsection 2.2.1). χ and ϵ are additional coefficients that appear in the case of the compressible active nematic fluid, both representing the additional passive stresses generated due to local nematic ordering.

Bulk description of the actomyosin cortex in the theoretical model of AP axis alignment

Equation 2.27 provides the general constitutive equations that a compressible active nematic fluid follows. However, in the case of the actomyosin cortex, simplifications can be made, following the models described in section 2.1 and section 2.2. Note that only the relations related to the stress ($\tilde{\sigma}^{d,s}_{\alpha\beta}$, σ^d) and nematic tensor ($\frac{DQ_{\alpha\beta}}{Dt}$) are of interest here.

Consider the corotational and comoving derivative of $Q_{\alpha\beta}$ first. As described in [88] (see subsection 2.2.1), the nematic tensor $Q_{\alpha\beta}$ arises due to the alignment of actin filaments. In [88], it was shown that for the description of the nematic tensor $Q_{\alpha\beta}$ – and thus actin alignment – during the formation of the pseudocleavage furrow, active alignment of actin filaments plays an insignificant role. Thus, λ is set to 0. Additionally, [88] considers an incompressible cortex – thus implying that ϵ should also be set to 0. $\frac{DQ_{\alpha\beta}}{Dt}$ is then given by:

$$\frac{DQ_{\alpha\beta}}{Dt} = -\nu\tilde{v}_{\alpha\beta} + \frac{1}{\bar{\gamma}}H_{\alpha\beta} \tag{2.28}$$

The form of the intrinsic free energy density F_0 is obtained from [88]. Thus, as discussed in subsection 2.2.1, the molecular field $H_{\alpha\beta}$ is given by:

$$H_{\alpha\beta} = K[l^2\partial_\gamma\partial_\gamma Q_{\alpha\beta} - Q_{\alpha\beta}] \tag{2.29}$$

Furthermore, it is observed that the advection terms in $\frac{DQ_{\alpha\beta}}{Dt}$ only lead to a slight shift in the position of the pseudocleavage furrow. For sake of simplicity, it is assumed here that this advection term can be ignored. In steady state therefore,

$$\frac{DQ_{\alpha\beta}}{Dt} = 0 \implies H_{\alpha\beta} = K[l^2\partial_\gamma\partial_\gamma Q_{\alpha\beta} - Q_{\alpha\beta}] = \nu\bar{\gamma}\tilde{v}_{\alpha\beta} \tag{2.30}$$

This is then the equation (specifically, its surface equivalent, which is discussed later) that governs the dynamics of the nematic tensor $Q_{\alpha\beta}$ in the theoretical model of AP axis alignment.

Consider now the isotropic stress σ^d. Note that the nematic tensor $Q_{\alpha\beta}$ arises due to the local ordering of actin filaments – and thus the terms $\chi Q_{\alpha\beta}\tilde{v}_{\alpha\beta}$ and $\epsilon Q_{\alpha\beta}H_{\alpha\beta}$. In here, it is assumed that the isotropic stresses – that cause expansion or contraction of the local volume elements of the cortex – are generated solely by myosin motors. Thus, χ is also set to 0 ($\epsilon = 0$ from the previous discussion on dynamics of $Q_{\alpha\beta}$). These assumptions yield:

$$\sigma^d = \eta_v\partial_\gamma v_\gamma + \zeta_2\Delta\mu \tag{2.31}$$

The total stress $\sigma_{\alpha\beta}$ can then be written as:

$$\sigma_{\alpha\beta} = \tilde{\sigma}^{d,s}_{\alpha\beta} + \sigma^{d}\delta_{\alpha\beta} = [2\eta\tilde{v}_{\alpha\beta} + \eta_v \partial_\gamma v_\gamma \delta_{\alpha\beta} + \nu H_{\alpha\beta}] + [\zeta_1 Q_{\alpha\beta}\Delta\mu + \zeta_2 \Delta\mu \delta_{\alpha\beta}] = \sigma^{(passive)}_{\alpha\beta} + \sigma^{(active)}_{\alpha\beta} \tag{2.32}$$

where $\sigma^{(passive)}_{\alpha\beta} = 2\eta\tilde{v}_{\alpha\beta} + \eta_v \partial_\gamma v_\gamma \delta_{\alpha\beta} + \nu H_{\alpha\beta}$ contains the passive terms in the stress and $\sigma^{(active)}_{\alpha\beta} = \zeta_1 Q_{\alpha\beta}\Delta\mu + \zeta_2 \Delta\mu \delta_{\alpha\beta}$ contains the active terms.

Consider now the passive stress $\sigma^{(passive)}_{\alpha\beta}$. Using Equation 2.30 to simplify $\sigma^{(passive)}_{\alpha\beta}$ yields:

$$H_{\alpha\beta} = \nu\bar{\gamma}\tilde{v}_{\alpha\beta} \implies \sigma^{(passive)}_{\alpha\beta} = (2\eta + \nu^2\bar{\gamma})\tilde{v}_{\alpha\beta} + \eta_v \partial_\gamma v_\gamma \delta_{\alpha\beta} \tag{2.33}$$

Thus, the stress generated due to compressive alignment of actin filaments $\nu H_{\alpha\beta}$, under the steady state condition assumed in the theoretical model, reduces to an effective renormalization of the viscosity of the cortex. Following [1], the bulk viscosity is ignored – that is, η_v is set to 0. Then, denoting this effective viscosity as $\tilde{\eta} = \eta + \frac{\nu^2\bar{\gamma}}{2}$, $\sigma^{(passive)}_{\alpha\beta}$ can be written as:

$$\sigma^{(passive)}_{\alpha\beta} = 2\tilde{\eta}\tilde{v}_{\alpha\beta} \tag{2.34}$$

Consider now the active stress $\sigma^{(active)}_{\alpha\beta}$. Following [1], the active stress could be written as:

$$\zeta_2\Delta\mu = \xi \frac{M}{M + M_*} \tag{2.35}$$

$$\zeta_1 Q_{\alpha\beta}\Delta\mu = \xi_N \frac{M}{M + M_*} Q_{\alpha\beta} \tag{2.36}$$

$$\sigma^{(active)}_{\alpha\beta} = \left[\frac{M}{M + M_*}\right](\xi\delta_{\alpha\beta} + \xi_N Q_{\alpha\beta}) \tag{2.37}$$

where ξ represents the active isotropic stress generated by the cortex, and ξ_N the active anisotropic stress dependent on the local alignment of actin filaments. Here, the dependence of the active stresses on the myosin concentration M is borrowed from [1] – with ξ and ξ_N playing the role of C_* in Equation 2.12. Additionally, it is assumed that both isotropic and anisotropic active stress share the same Hill coefficient M_*.

In [1], the dynamics of the myosin concentration M is considered in the context of the reaction-advection-diffusion system of PAR proteins (see section 2.1). In the theoretical model of AP axis alignment considered here, this is simplified to consider only the dynamics of M on the cortex. Specifically, from Equation 2.14, the term $k_{AM}AM$ that represents the regulation of dissociation of myosin from the cortex by aPARs is not considered here, nor are the dynamics of aPARs and pPARs in Equation 2.16. As the theoretical model considers only steady state, the time component of the centrosomal cue is ignored. Furthermore, the time derivative of M in Equation 2.16 is ignored. Similar to nematic tensor $Q_{\alpha\beta}$, the advection term for M is also ignored. With these assumptions, the following equation for the dynamics of myosin at the cortex is obtained:

$$-D_M \partial_\gamma \partial_\gamma M = k_{on,M} M_{cyto} - k_{off,M} M - k_{off,M} \kappa_M F_M(\vec{r}_{nucl}) M \tag{2.38}$$

where M_{cyto} is obtained in a similar fashion to Equation 2.3, and $F_M(\vec{r}_{nucl}) = -\exp\left(-\frac{(\vec{r}-\Pi[\vec{r}_{nucl}])^2}{d_M^2}\right)$ models the centrosomal cue that depletes myosin near the male pronucleus with characteristic length d_M. $\vec{r}_{nucl}$ refers to the location of the male pronucleus, and $\Pi[\vec{r}_{nucl}]$ is the point on the cortex closest to the male pronucleus.

The total stress $\sigma_{\alpha\beta}$ is then given by:

$$\sigma_{\alpha\beta} = \sigma_{\alpha\beta}^{(passive)} + \sigma_{\alpha\beta}^{(active)} = 2\tilde{\eta}\tilde{v}_{\alpha\beta} + \xi\left(\frac{M}{M+M_*}\right)\delta_{\alpha\beta} + \xi_N\left(\frac{M}{M+M_*}\right)Q_{\alpha\beta} \tag{2.39}$$

Momentum balance is taken in the Low-Reynolds number regime, following [1], with a frictional drag coefficient γ. Thus, Equation 2.8 implies $-\partial_\beta\sigma_{\alpha\beta} + \gamma v_\alpha = 0$, which yields:

$$-\tilde{\eta}\left[\partial_\beta\partial_\beta v_\alpha + \frac{1}{3}\partial_\alpha\partial_\beta v_\beta\right] + \gamma v_\alpha = \xi\partial_\alpha\left(\frac{M}{M+M_*}\right) + \xi_N\partial_\beta\left[\left(\frac{M}{M+M_*}\right)Q_{\alpha\beta}\right] \tag{2.40}$$

Dividing throughout by γ yields:

$$-\lambda_H\left[\partial_\beta\partial_\beta v_\alpha + \frac{1}{3}\partial_\alpha\partial_\beta v_\beta\right] + v_\alpha = \lambda_A\partial_\alpha\left(\frac{M}{M+M_*}\right) + \lambda_N\partial_\beta\left[\left(\frac{M}{M+M_*}\right)Q_{\alpha\beta}\right] \tag{2.41}$$

where hydrodynamic length $\lambda_H = \frac{\tilde{\eta}}{\gamma}$, active force relaxation $\lambda_A = \frac{\xi}{\gamma}$ and nematic stress relaxation $\lambda_N = \frac{\xi_N}{\gamma}$ have been introduced. A similar modification can be done for Equation 2.30, yielding:

$$l^2\partial_\gamma\partial_\gamma Q_{\alpha\beta} - Q_{\alpha\beta} = \nu\tau\tilde{v}_{\alpha\beta} \tag{2.42}$$

where $\tau = \frac{\bar{\gamma}}{K}$ is the characteristic relaxation time for the nematic tensor $Q_{\alpha\beta}$.

Altogether, the equations Equation 2.38, Equation 2.41 and Equation 2.42 constitute the set of dynamical equations that comprise the bulk description of the cortex in the theoretical model. Under the thin film limit discussed next, these equations will be converted into their surface counterparts. Note that the stress induced by nematic ordering in Equation 2.39 – $\xi_N\left(\frac{M}{M+M_*}\right)Q_{\alpha\beta}$ – is not the same as that was introduced in [88]. This will be replaced with the nematic stress introduced in Equation 2.25 after the thin film limit is applied to obtain a 2-dimensional surface description of the cortex, to ensure that the forces induced by the actin alignment are only along the local orientation of the actin filaments.

Thin film limit: Description on the surface of an ellipsoid

The previous section describes the description of the cortex in bulk – that is, assuming that the cortex is a bulk fluid. However, the actomyosin cortex resides only near the cell membrane – thus a surface description is needed for the cortex. To transform the bulk description into the relevant surface description, a thin film limit is utilised as described in [175]. Let $\mathcal{E}$ denote the surface of the ellipsoidal embryo, and $\hat{\mathcal{E}}$ its interior. Note that the ellipsoidal surface is considered fixed in shape – the "ruffling" of the cortex is not considered here. The idea of the thin film limit is to consider a tubular extension $\mathcal{E}_h$ of the surface $\mathcal{E}$ of constant thickness h. The bulk description of the cortex considered above is then used in this thin ellipsoidal shell of thickness h. By applying proper boundary conditions on this volume $\mathcal{E}_h$ and taking $h \to 0$, a covariant surface description of the cortex can be obtained.

Denote the outward normal to the surface $\mathcal{E}$, along which the shell $\mathcal{E}_h$ has been extended, as $\vec{n}$. Additionally, in this section tensors will be denoted in boldface. The boundary conditions of the thin shell $\mathcal{E}_h$ are selected as below [176–178]:

- No additional flux of Myosin normal to the cortex beyond what is already considered in the reaction term: $(\nabla M) \cdot \vec{n} = 0$.
- No cortical flow along the normal to $\mathcal{E}$, and thus the boundary of $\mathcal{E}_h$: $\vec{v} \cdot \vec{n} = 0$.
- No variation in cortical flow velocity along the normal to $\mathcal{E}$, and thus between the outer and inner boundary of $\mathcal{E}_h$: $(\vec{n} \cdot \nabla)\vec{v} = 0$.
- No nematic ordering in the direction normal to $\mathcal{E}$: $\vec{n} \cdot \mathbf{Q} \cdot \vec{n} = 0$. Additionally, it is assumed that $(\nabla \mathbf{Q}) \cdot \vec{n} = 0$, to ensure continous values for $\mathbf{Q}$ as $h \to 0$ [176].
- Normal components of the stress do not contain tangential parts and vice-versa: $\sigma \cdot \vec{n}$ is a vector along $\vec{n}$. Under this condition, the tangential and normal (to the surface $\mathcal{E}$) parts of the stress decouple. Note that this also implies that only the tangential parts of the stress tensor are considered in the theoretical model.

Note that since $h \to 0$, it has been assumed that the normal vector to the surface of $\mathcal{E}_h$ does not vary much from the corresponding normal vector to the surface $\mathcal{E}$.

With these considerations, the dynamic equations of the theoretical model – Equation 2.38, Equation 2.41 and Equation 2.42 – can be converted into a covariant surface form after applying the thin film limit. Here, only the tangential parts of the corresponding tensors in the bulk description are considered. Additionally, the covariant gradient and divergence operations on the surface $\mathcal{E}$ are denoted by grad and div respectively. Here, the surface equations are directly reported – the reader is referred to [170] for details.

The dynamics of myosin concentration M on the cortex is governed by:

$$-D_M \text{div grad}\, M = k_{on,M} M_{cyto} - k_{off,M} M - k_{off,M} \kappa_M F_M(\vec{r}_{nucl}) M \tag{2.43}$$

where $M_{cyto} = M_{tot} - \frac{\psi}{|\mathcal{E}|} \int_{\mathcal{E}} M \, \mathrm{d}\mathcal{E}$ – as in Equation 2.3 and $F_M(\vec{r}_{nucl}) = -\exp\left(-\frac{s(\vec{r}, \Pi[\vec{r}_{nucl}])^2}{d_M^2}\right)$ where s is the geodesic distance measure on $\mathcal{E}$ and $\Pi[\vec{r}_{nucl}]$ is the closest point on the cortex with respect to the male pronucleus center. $\mathbf{g}$ denotes the metric of the ellipsoid surface $\mathcal{E}$.

The dynamics of the nematic tensor $\mathbf{Q}$ on the cortex is governed by [175]:

$$l^2[\text{div grad}\, \mathbf{Q} - \|\mathbf{B}\|^2 \mathbf{Q}] - \mathbf{Q} = \nu \tau \tilde{\mathbf{v}} \tag{2.44}$$

where $\mathbf{B} = -\Pi[\nabla \vec{n}]$ is the shape operator of $\mathcal{E}$ – that is, the projection (to the tangent space of $\mathcal{E}$, denoted by Π) of the gradient of the normal vector $\vec{n}$ of $\mathcal{E}$. $\mathbf{Q}$ is the nematic tensor and $\tilde{\mathbf{v}} = \frac{1}{2}[\text{grad}\, \vec{v} + (\text{grad}\, \vec{v})^T - (\text{div}\, \vec{v})\mathbf{g}]$ is the symmetric traceless strain rate, both tangential to the surface $\mathcal{E}$. Note that the determinant of the shape operator $\mathbf{B}$ is the gaussian curvature $\mathcal{K}$.

The momentum balance for the cortex in this surface description reads:

$$-\lambda_H \left[\text{div grad}\, \vec{v} + \mathcal{K}\vec{v} + \frac{1}{3}\text{grad div}\, \vec{v}\right] + \vec{v} = \lambda_A \text{grad} \left(\frac{M}{M + M_*}\right) + \lambda_N \text{div} \left[\left(\frac{M}{M + M_*}\right) \mathbf{Q}\right]$$

where $\vec{v}$ is the cortical flow velocity and the rest are defined in Equation 2.41. As noted before, the form of the stress induced by actin alignment is not in the form presented in Equation 2.25. Replacing the nematic stress here to that from Equation 2.25 yields:

$$\left(\frac{M}{M+M_*}\right)\mathbf{Q} \to \left(\frac{M}{M+M_*}\right)\left[\frac{1}{2\sqrt{2}}\|\mathbf{Q}\|\mathbf{g} + \frac{1}{2}\mathbf{Q}\right]$$

$$\begin{aligned} &- \lambda_H \left[\text{div grad}\, \vec{v} + \mathcal{K}\vec{v} + \frac{1}{3}\text{grad div}\, \vec{v}\right] + \vec{v} \\ &\qquad = \lambda_A \text{grad} \left(\frac{M}{M+M_*}\right) + \lambda_N \text{grad} \left[\left(\frac{M}{M+M_*}\right)\left(\frac{1}{2\sqrt{2}}\|\mathbf{Q}\|\mathbf{g} + \frac{1}{2}\mathbf{Q}\right)\right] \end{aligned} \tag{2.45}$$

where $\mathbf{g}$ is the metric of the ellipsoid surface $\mathcal{E}$.

Altogether, the equations Equation 2.43, Equation 2.44 and Equation 2.45 constitute the set of dynamical equations that comprise the surface description of the cortex – the description of the cortex that is used in the theoretical model of AP axis alignment.

A note may be made on the parameters λ_H, λ_A and λ_N in Equation 2.45. These parameters characterise the strength of the passive and active stresses in the cortex relative to frictional drag – with λ_H characterising the passive viscous stress, λ_A characterising the active isotropic stress and λ_N characterising the active anisotropic stress generated by the local alignment of actin filaments. As discussed in [88], this anisotropic stress generated by alignment of actin filaments gives rise to the contractile ring-like nature of the pseudocleavage furrow that forms during the late establishment phase. The active isotropic stress characterised by λ_A cannot generate such a ring-like structure. Furthermore, as discussed in [137], this active isotropic stress can capture the cytoplasmic flows observed in the cytoplasm. Thus, λ_N controls the strength of active anisotropic stress generated in the cortex by the pseudocleavage furrow; while λ_A controls the strength of the isotropic active stress in the cortex. In other words, λ_N controls the strength of the pseudocleavage furrow-dependent mechanism, while λ_A controls the strength of the cytoplasmic flow-dependent mechanism discussed in subsection 1.4.3.

2.3.2 Description of the Cytoplasm and Male pronucleus

Flows in the cytoplasmic bulk

Following the results of [137], the cytoplasmic bulk can be modelled as an incompressible Newtonian fluid in the Stokes regime, with flows in it driven by flows at the cortex. Specifically, the flow in the cytoplasmic bulk $\hat{\mathcal{E}}$ is given by the Stokes equation:

$$\nabla \cdot (\eta_{cyto} \nabla \vec{v}_{cyto}) - \nabla p = 0; \quad \nabla \cdot \vec{v}_{cyto} = 0 \quad \text{in } \hat{\mathcal{E}} \tag{2.46}$$

where η_{cyto} is cytoplasmic viscosity, $\vec{v}_{cyto}$ is the flow velocity of the cytoplasm and p is the pressure in the cytoplasm.

Following the approach in [179], the male pronucleus itself is treated as a colloidal particle in the cytoplasm. Specifically, the male pronucleus is modelled as a region $\phi(\vec{r})$ with a large viscosity $\omega_{nucl}\eta_{cyto}$ in the cytoplasm to ensure homogeneous flow field inside the pronucleus region:

$$\phi(\vec{r}) = \frac{1}{2}\left[1 - \tanh\left(\frac{3\left(\|\vec{r} - \vec{r}_{nucl}\| - R_{nucl}\right)}{\bar{\epsilon}}\right)\right]; \quad \vec{r} \in \hat{\mathcal{E}} \tag{2.47}$$

where $\vec{r}_{nucl}$ is the center of the male pronucleus, R_{nucl} is the radius of the male pronucleus and $\bar{\epsilon}$ the width of transition of this function from 0 to 1 – usually selected to be small. The viscosity term in Equation 2.46 is then replaced $\eta_{cyto} \to \eta_{cyto}(1 + \omega_{nucl}\phi(\vec{r}))$ [179]. Dividing throughout by η_{cyto} and setting $\bar{p} = p/\eta_{cyto}$ yields the dynamical equations for the cytoplasmic flow velocity $\vec{v}_{cyto}$ as:

$$\nabla \cdot ((1 + \omega_{nucl}\phi(\vec{r}))\nabla\vec{v}_{cyto}) - \nabla\bar{p} = 0 \quad \text{in } \hat{\mathcal{E}} \tag{2.48a}$$

$$\nabla \cdot \vec{v}_{cyto} = 0 \quad \text{in } \hat{\mathcal{E}} \tag{2.48b}$$

$$\vec{v}_{cyto} = \vec{v} \quad \text{on } \partial\hat{\mathcal{E}} = \mathcal{E} \tag{2.48c}$$

where the last equation specifics the no-slip boundary condition for the cytoplasmic flow velocity at the cortex.

Posteriorisation velocity of the male pronucleus

The velocity of the male pronucleus is then calculated from two contributions: advective transport by cytoplasmic flows and drag on the pronucleus due to local movement of the cortex. To obtain the first contribution, the cytoplasmic flow velocity $\vec{v}_{cyto}$ observed in the domain of the pronucleus $\phi(\vec{r})$ is averaged.

$$\vec{v}^{(cyto)}_{nucl} = \frac{\int_{\hat{\mathcal{E}}} \phi(\vec{r})\vec{v}_{cyto}\, \mathrm{d}\hat{\mathcal{E}}}{\int_{\hat{\mathcal{E}}} \phi(\vec{r})\, \mathrm{d}\hat{\mathcal{E}}}$$

The second contribution is obtained by averaging the cortical flow velocity $\vec{v}$ over a domain $\mathcal{N}$ matching the projection of the male pronucleus, centered around the point $\Pi[\vec{r}_{nucl}]$ on $\mathcal{E}$ – the point on the cortex closest to the center of the male pronucleus $\vec{r}_{nucl}$.

$$\mathcal{N} = \{\vec{r} \in \mathcal{E} : s(\vec{r}, \Pi[\vec{r}_{nucl}]) \leq R_{nucl}\}; \quad \vec{v}^{(crtx)}_{nucl} = \frac{\int_{\mathcal{N}} \vec{v}\, \mathrm{d}\mathcal{N}}{|N|}$$

where s is the geodesic distance measure on $\mathcal{E}$, $\Pi[\vec{r}_{nucl}]$ is the closest point on the cortex with respect to the male pronucleus center and R_{nucl} is the radius of the male pronucleus.

The total velocity of the male pronucleus is then given by:

$$\vec{v}_{nucl} = \vec{v}^{(cyto)}_{nucl} + d\,\vec{v}^{(crtx)}_{nucl} \tag{2.49}$$

where $d \in [0, 1]$ is a phenomenological coefficient that characterises the strength of the drag on the pronucleus due to local movement of the cortex. The posteriorisation velocity $\vec{v}^{(post)}_{nucl}$ is then obtained as the component of $\vec{v}_{nucl}$ parallel to $\mathcal{E}$, using the unit normal vector $\vec{n}$ to $\mathcal{E}$ at $\Pi[\vec{r}_{nucl}]$:

$$\vec{v}^{(post)}_{nucl} = \vec{v}_{nucl} - (\vec{v}_{nucl} \cdot \vec{n})\vec{n} \tag{2.50}$$

2.3.3 Numerical simulations of the theoretical model

The previous paragraphs describe the development of the theoretical model of AP axis alignment, which will be used in chapter 4 to compare against and make predictions about experimentally observed AP axis alignment in *C. elegans* embryos. Conceptually, this model describes how flows in the actomyosin cortex drive flows in the cytoplasm and the subsequent displacement of the male pronucleus. As discussed in section 1.4, the male pronucleus acts as the organiser of AP axis establishment (via the centrosomes associated with the male pronucleus). Thus, the theoretical model captures how cortical flows drive the re-orientation of the AP axis as it aligns with the long axis of the ellipsoidal embryo.

In this theoretical model, dynamics of the actomyosin cortex is described by integrating elements from the models proposed in [1] and [88] into a generic hydrodynamic theory of active nematic compressible fluid; and then made into a surface description using a thin film limit [175]. For a given position of the male pronucleus $\vec{r}_{nucl}$ in the cytoplasm $\hat{\mathcal{E}}$, the spatial pattern of myosin concentrations M on the cortex $\mathcal{E}$ is determined by Equation 2.43 – where $F_M(\vec{r}_{nucl}) = -\exp\left(-\frac{s(\vec{r},\Pi[\vec{r}_{nucl}])^2}{d_M^2}\right)$ represents the polarisation cue from the centrosomes associated with the male pronucleus. Given these concentrations, the coupled equations Equation 2.44 and Equation 2.45 determine the cortical flow velocity $\vec{v}$ and nematic tensor $\mathbf{Q}$ characterising the local state of alignment of actin filaments in the cortex. Myosin dynamics, centrosomal cue and dependence of active stresses on myosin concentration are borrowed from [1]. Active stress generated by nematic tensor (included in Equation 2.45) – and therefore the alignment of actin filaments – and the compressive alignment of actin filaments (included in Equation 2.44) are borrowed from [88]. These cortical flow determine the flows in the cytoplasm via a no-slip boundary condition at the interface between the cortex and the cytoplasm in Equation 2.48, in which the cytoplasm is assumed to be a Newtonian fluid in the Stokes regime. The effect of the flows in the bulk cytoplasm on the cortex are captured already in the frictional drag in Equation 2.45. Finally, the velocity of the male pronucleus is calculated as a summation of two contributions from Equation 2.49 – one due to advection by cytoplasmic flows, and the other due to drag with the moving cortex. Thus, the theoretical model describes a feedback loop between the position of the male pronucleus and its velocity, which is governed by the geometry of the embryo via its effect on the cortical and cytoplasmic flow fields.

The numerical simulations of the theoretical model use the "one-way" description of the previous paragraph, in effect calculating the velocity of the male pronucleus for a given position of the male pronucleus. Specifically, the numerical simulations take as input the angular position α of the male pronucleus – the angle made between the long axis of the ellipsoidal embryo and line connecting the center of the male pronucleus and the center of the embryo. Assuming a constant distance between the cortex and male pronucleus $\|\vec{r}_{nucl} - \Pi[\vec{r}_{nucl}]\| = 3.5\,\mu\mathrm{m}$ and a nucleus radius $R_{nucl} = 3\,\mu\mathrm{m}$, the corresponding $\vec{r}_{nucl}$ can be recovered from the angular position α. Angular positions α are selected between 0–20 deg. For each angular position, the corresponding cortical flow velocity $\vec{v}$ and nematic tensor $\mathbf{Q}$ are calculated by solving Equation 2.43, Equation 2.44 and Equation 2.45 using surface finite element methods for tangential vector and tensor quantities [180]. The corresponding cytoplasmic flow velocity $\vec{v}_{cyto}$ are calculated using standard finite element methods, with boundary conditions on the cytoplasm imposed using a diffuse domain approach [181]. Using these, the velocity of the male pronucleus $\vec{v}_{nucl}$, and thus the posteriorisation velocity $\vec{v}_{nucl}^{(post)}$ using Equation 2.50, can be calculated for each angular position α. All finite element methods are implemented and solved using the AMDiS toolbox.

Calibrating model parameters

One may observe that there are several parameters whose values are required before the numerical simulations outlined above can be performed. Specifically, the following model parameters are required:

- Parameters for myosin concentration (Equation 2.43): $D_M; k_{on,M}; k_{off,M}; \kappa_M; d_M$. These parameters can be directly obtained from [1].
- Parameters for actin alignment (Equation 2.44): $l; \nu\tau$. These can be obtained from [88].
- Parameters for cortical flow velocity (Equation 2.45): M_*;λ_H;λ_N;λ_A. Of these only M_* can be obtained, from [1].
- Parameters for cytoplasmic flow velocity (Equation 2.48): $\omega_{nucl}; \bar{\epsilon}; R_{nucl}$. Note that $\omega_{nucl}; \bar{\epsilon}$ are numeric parameters – with no physical relevance. ω_{nucl} is only required to be $\omega_{nucl} >> 1$ to ensure the required behaviour of a homogeneous flow field inside the pronucleus region $\phi(\vec{r})$; $\bar{\epsilon}$ is only required to be $\bar{\epsilon} << R_{nucl}$ to ensure a sharp transition between the pronucleus and cytoplasm. Here, $R_{nucl} = 3\,\mu\text{m}$, $\bar{\epsilon} = 0.25\,\mu\text{m}$ and $\omega_{nucl} = 100$ is chosen.
- Parameters for pronucleus velocity (Equation 2.49): d

Thus, most of the model parameters are already determined in [1] and [88] – see Table 2.2 for the their values. Only 4 parameters need to be determined: λ_H, λ_N, λ_A and d. Of these, the first three – λ_H, λ_N and λ_A– are determined by matching the cortical flows calculated by the theoretical model with those observed in experiments. This "calibration" of the model is described next. d is determined by fitting the observed posteriorisation velocity as a function of angular position for the unperturbed embryos only – see subsection 4.3.2 for details.

To determine the values of λ_H, λ_N and λ_A, the calibration procedure matches the calculated cortical flows in the numerical simulations to those observed in experiments. These experimental cortical flow fields are measured from the midplane images of the embryo – thus available only on a planar slice $\mathcal{P}$ – for a range of different angular positions of the male pronucleus (see subsection 3.4.3 and section 3.5). The experimental cortical flow velocity is described as a function of arclength s along this planar slice $\mathcal{P}$, with the posterior end designated as the origin and oriented along the counter-clockwise direction (represented by the tangent vector $\vec{t}$ pointing counter-clockwise). For calibration, the experiment cortical flows are shifted to have the closest point to the male pronucleus on $\mathcal{P}$ as the origin.

One may observe that the cortical velocity $\vec{v}$ and nematic tensor $\mathbf{Q}$ in Equation 2.45 scale with λ_A– that is, $\tilde{C}\lambda_A \to (\tilde{C}\vec{v}, \tilde{C}\mathbf{Q})$. Using this, λ_A can be independently fit by matching the kinetic energy of the calculated and experimental cortical flows. With this, the calibration then proceeds in two steps:

Model Parameter	Physical revelance	Parameter Value	Source
D_M	Myosin diffusion constant on cortex	$0.054\,\mu\mathrm{m}^2\,\mathrm{s}^{-1}$	[1]
$k_{on,M}$	Myosin association rate with cortex	$0.20\,\mu\mathrm{m}\,\mathrm{s}^{-1}$	[1]
$k_{off,M}$	Myosin dissociation rate from cortex	$0.12\,\mathrm{s}^{-1}$	[1]
κ_M	Strength of polarity cue (myosin depletion)	4.9	[1]
d_M	Characteristic length for polarity cue (myosin depletion)	$15.9\,\mu\mathrm{m}$	[1]
M_*	Hill coefficient for contractility	$8.0\,\mu\mathrm{m}^{-2}$	[1]
l	Length scale below which actin filaments are coherently aligned	$4.72\,\mu\mathrm{m}$	[88]
$\nu\tau$	Compressive alignment of actin filaments	$0.63\,\mathrm{min}$	[88]
ω_{nucl}	Numeric parameter	100	See [179]
$\bar{\epsilon}$	Numeric parameter	$0.25\,\mu\mathrm{m}$	-
R_{nucl}	Radius of Male pronucleus	$3\,\mu\mathrm{m}$	[182]

Table 2.2: Values of model parameter used in the theoretical model which are not obtained by calibration. Both ω_{nucl} and $\bar{\epsilon}$ are numeric parameters that do not have physical relevance. See text for explanation. For R_{nucl}, also see section 3.4

1. Equation 2.43, Equation 2.44 and Equation 2.45 are solved for different values of λ_H and λ_N while keeping λ_A^* fixed. This solution yields the myosin concentration M, and scaled version of the cortical flow velocity $\vec{v}^*$ and nematic tensor $\mathbf{Q}^*$. To obtain the proper scaling, the kinetic energy $\mathbb{E}^{\mathcal{P}}(\vec{v}) = \int_{\mathcal{P}} \vec{v}^2 \,\mathrm{d}\mathcal{P}$ is fit across all angular positions:

$$\min_{S\in\mathbb{R}} \sum_{\alpha} \left[\mathbb{E}^{\mathcal{P}}(\vec{v}^{(\mathrm{expt})}) - \mathbb{E}^{\mathcal{P}}(S\vec{v}^*)\right] = S^*$$

   where the summation goes over all angular positions for which experimental cortical flows $\vec{v}^{(\mathrm{expt})}$ are available. As the scaled cortical flow velocity $\vec{v}^*$ are calculated for a selected value of λ_H and λ_N, S^* is thus a function of λ_H and λ_N. Therefore, for a given value of λ_H and λ_N, $\lambda_A = S^*\lambda_A^*$, $\vec{v} = S^*\vec{v}^*$ and $\mathbf{Q} = S^*\mathbf{Q}^*$ are obtained as best match to experimentally measured cortical flows.

2. To obtain the values of λ_H and λ_N that best match the experimentally measured cortical flows, a mixed calibration cost measure $E = L + \Theta R$ – combining a similarity measure L and an imbalance measure R with weighting factor Θ – is evaluated. The measures L

and R are defined as [170]:

$$
\begin{aligned}
L &= \sum_{\alpha} \sqrt{\frac{\mathbb{E}^{\mathcal{P}}(\vec{v}^{(\mathrm{expt})}) - \mathbb{E}^{\mathcal{P}}(\vec{v})}{\mathbb{E}^{\mathcal{P}}(\vec{v})}} \\
M^{+}(\vec{v}) &= -\frac{1}{2} \int_{\mathcal{P}} (-\vec{v} \cdot \vec{t} - |\vec{v} \cdot \vec{t}|) \, \mathrm{d}\mathcal{P} \\
M^{-}(\vec{v}) &= -\frac{1}{2} \int_{\mathcal{P}} (\vec{v} \cdot \vec{t} - |\vec{v} \cdot \vec{t}|) \, \mathrm{d}\mathcal{P} \\
R &= \sum_{\alpha} \left| \frac{M^{+}(\vec{v}^{(\mathrm{expt})})}{M^{-}(\vec{v}^{(\mathrm{expt})})} - \frac{M^{+}(\vec{v})}{M^{-}(\vec{v})} \right| \Bigg/ \left| \frac{M^{+}(\vec{v})}{M^{-}(\vec{v})} \right|
\end{aligned}
$$

where the summation goes over all angular positions for which experimental cortical flows $\vec{v}^{(\mathrm{expt})}$ are available. The similarity measure L penalizes the mismatch between the kinetic energy of the cortical flows calculated in simulations and experimentally measured cortical flows. M^{+} is the sum of magnitude of flow velocities pointed counter-clockwise, and M^{-} is the sum of magnitude of flow velocities pointed clockwise. The ratio M^{+}/M^{-} thus characterises the "imbalance" in the cortical flow field. The imbalance measure R penalizes the mismatch for this imbalance between the cortical flows calculated in simulations and experimentally measured cortical flows. Both L and R are considered relative to the calculated cortical flow velocity. This imbalance measure is motivated by the observation of a correlation between the angular position and the imbalance in the experimentally observed flow fields. Θ weighs the importance of matching the imbalance observed in experimental flow fields – and is set to $\Theta = 5$.

Evaluating male pronucleus trajectories

Trajectories of the male pronucleus – that is, the angular position as a function of time $\alpha(t)$ – are evaluated by integrating the calculated velocity of the male pronucleus Equation 2.50, for an initial angular position set at $\alpha = 45\,\mathrm{deg}$ and arbitrary time domain $t \in [0, 1000]$. For comparison with experimentally observed trajectories of the male pronucleus (see chapter 4), a temporal reference point $\hat{t}$ is introduced – separately defined for each experimental condition. For each experimental conditions, the experimentally obtained trajectories are binned temporally (using 100 bins). $\hat{t}$ is then selected using least square, to ensure best fit to experimentally observed trajectories:

$$
\min_{\hat{t} \in \mathbb{R}} \sum_{i=1}^{100} \left| \alpha^{(\mathrm{expt})}(t_i) - \alpha(t_i - \hat{t}) \right|^2 \to \hat{t}
$$

Chapter 3

Materials and Methods

3.1 Culture conditions, strains and worm handling

C. elegans worms were cultured on Nematode Growth Medium (NGM) agar plates seeded with OP50 *E. coli* (a slow-growing *E. coli* bacterial strain), and handled as described in [112]. Worms were maintained at 20 °C. The following strains were used in this work:

Strain	Fluorescent tags	Genotype
SWG070	NMY-2::GFP, phDomain::mCherry	nmy-2(cp7[nmy-2::gfp + LoxP unc-119(+) LoxP]) I; ltIs44 [pAA173 pie-1p-mCherry::PH(PLC1delta1) + unc-119(+)]
SWG057	Tubulin (TUB)::GFP, NMY-2::mKate	nmy-2(cp52 [nmy-2::mkate2 + LoxP unc-119(+) LoxP]) I; unc-119(ed3)III; ruIs57[pAZ147: pie-1p/GFP::C36E8.5] III
SWG228	NMY-2::GFP	nmy-2(cp8[nmy-2::GFP]) I; nop-1(it142) III

Table 3.1: *C. elegans* strains used in this study

The primary strain used in this work is a dual-color strain labelled with NMY-2::GFP and phDomain::mCherry, named SWG070. This transgenic strain labels NMY-2 myosin with Green Fluorescent Protein (GFP) and PH-domain (localized to the cell membrane [183]) with mCherry (a red fluorescent protein [184]). Thus, SWG070 enable visualization of the myosin distributions in the embryo and its cell membrane during its development. SWG228 is the *nop-1* mutant strain used primarily for the triple *air-1; mel-11* in *nop-1* mutant background (see subsection 4.5.2). For experiments with *goa-1; gpa-16* double RNAi (see subsection 4.5.3), SWG057 was used. This strain labels tubulin with GFP and NMY-2 myosin with mCherry. This allows visualization of the centrosomes in this condition, required for evaluating if the double RNAi was successful.

3.2 Genetic perturbations by RNAi

In order to achieve specific effects (example: embryos deficient in pseudocleavage furrow), expression of specific genes is reduced via RNA mediated interference (example: NOP-1). All RNA mediated interference (RNAi) experiments were performed via feeding, as previously described [122, 185]. For this process, RNAi feeding plates were generated by seeding NGM agar plates, containing 1 mM isopropyl-β-D-thiogalactoside and $50\,\mu g\,mL^{-1}$ ampicillin, with the bacterial expressing the Double-stranded RNA (dsRNA) targeting the gene of interest, and grown overnight. RNAi was then performed by transferring young L4 worms onto these RNAi feeding plates and incubating them for the specified time at 20 °C before imaging. See Table 3.2 for incubation times used. For single RNAi interference experiments, only the RNAi clone of interest was grown on the RNAi feeding plates. For double RNAi of *nop-1; mel-11* and double RNAi of *air-1; mel-11*, both RNAi clones were grown simultaneously on the RNAi feeding plates. For double RNAi of *goa-1; gpa-11*, sequences targeting both genes were integrated into a single bacterial clone, which was grown on the feeding plates.

RNAi condition	Strain	Feeding time
mlc-4	SWG070	22–24 hours
nop-1	SWG070	24–27 hours
nop-1; mel-11 (double)	SWG070	24–27 hours
ima-3	SWG070	20–24 hours
air-1	SWG070	24–27 hours
air-1; mel-11 (double)	SWG228	24–27 hours
goa-1; gpa-16 (double)	SWG057	24–27 hours

Table 3.2: Feeding times for RNAi conditions

All bacterial clones, except from *mlc-4* RNAi clone and *goa-1; gpa-16* double RNAi clone, were obtained from the Ahringer RNAi library (Source Bioscience) [122]. The *mlc-4* RNAi clone was obtained from the Hyman lab. The *goa-1; gpa-16* double RNAi clone was kindly provided by the Kotak lab [155].

3.3 Time-lapse microscopy

All movies of *C. elegans* embryos were obtained at room temperature, using a spinning-disk confocal microscope with Zeiss Axio Observer Z1 equipped with Yokogawa CSU-X1 scan head, a C-Apochromat 63X/1.2 NA Water objective, a Hamamatsu ORCA-Flash4.0 V2 CMOS camera (2048 pixel by 2048 pixel, pixel size of 0.105 µm), and operated using Micro-Manager [186]. The microscope is equipped with 488 nm and 561 nm solid-state imaging lasers.

To prepare a sample for imaging, adult worms (typically 2 per drop) were picked from agar plates and transferred in a drop (vol: 7 µL) of M9 buffer (22 mM KH_2PO_4, 42 mM Na_2HPO_4, 86 mM NaCl) placed on a cover slip. 20 µm polystyrene beads were added to the M9 buffer to act as spacers for imaging – ensuring the height of embryo after mounting is atleast 20 µm. To obtain one-cell stage embryos, these worms were dissected using a syringe tip to extract the embryos from the worm body into the M9 buffer.

The M9 droplet with embryos was mounted on a microscope slide, and transferred to the microscope. The sample is scanned using a 10X objective with transmitted light to find one-cell embryos before onset of AP axis establishment. Such embryos can be recognized by the smooth cytoplasm and lightly ruffled cell membrane. Once an embryo has been identified for imaging, the objective is changed to the 63X water objective. The focus is brought to the midplane of the embryo, and the image acquisition process is started.

3-channel time-lapse movies were acquired by taking three images at each time-point: one using transmitted light (denoted here as BrightField (BF)), one using 488 nm excitation laser (for imaging NMY-2::GFP) and one using 561 nm excitation laser (for imaging cell membrane) – see Figure 3.1a. All images are taken at the midplane of the imaged embryo. Movies were acquired at 3 s intervals between time-points, with 50 ms exposure time for transmitted light, 200 ms exposure time for GFP and 150 ms exposure time for mCherry. Embryos were imaged starting from the onset of cortical flows until pronuclear meeting. T = 0 s was selected at the end of posteriorization of the male pronucleus; that is, the time-point after which the male pronucleus moves away from the cortex and towards the female pronucleus. All movies were synchronized using this time-point.

For SWG057, a slight variation of the above process was followed – see Figure 3.1b. At each time-point, a BF image using transmitted light and a NMY-2 image using 561 nm excitation laser were taken at the midplane of the embryo. Additionally, a z-stack of 11 slices, with uniform spacing of 1 µm, was taken using the 488 nm excitation laser. This z-stack is used later to facilitate detection of embryo boundary. Movies were acquired at 5 s intervals between time-points, with 50 ms exposure time for transmitted light, 100 ms exposure time for each slice of the z-stack in GFP and 150 ms exposure time for mKate.

3.4 Image analysis

In this section, the general image analysis pipeline used to analyse the movies acquired from the microscope is described. The main focus is on movies generated using the SWG070 strain – the primary strain used in this thesis. However, the analysis pipeline itself can be used for movies from other strains, after certain modifications if needed. For SWG297, since the fluorescent tags are the same, the analysis pipeline can be used without modifications. For SWG057, the pre-processing stage is modified – as described later. Any specific details regarding the analysis of movies generated for a given experiment will be described in the respective sections in chapter 4.

The image analysis pipeline presented here is modified from image analysis pipelines from Mirna Kramer [182] and Peter Groß [1]. The following softwares were used in the image analysis pipeline: Fiji Is Just ImageJ (FIJI) [187, 188] for pre-processing, Python [189] for tracking the male pronucleus and setting up the inputs for measurements of cortical flows, and MATrix LABoratory (MATLAB) [190] for measurement of cortical and cytoplasmic flows using PIV and constructing averages of various quantities over the ensemble of embryos in each condition. A custom PowerShell script was used for automated batch processing of movies.

3.4.1 Pre-processing

Movies are pre-processed using a custom FIJI macro. For each movie, the following steps are performed in order:

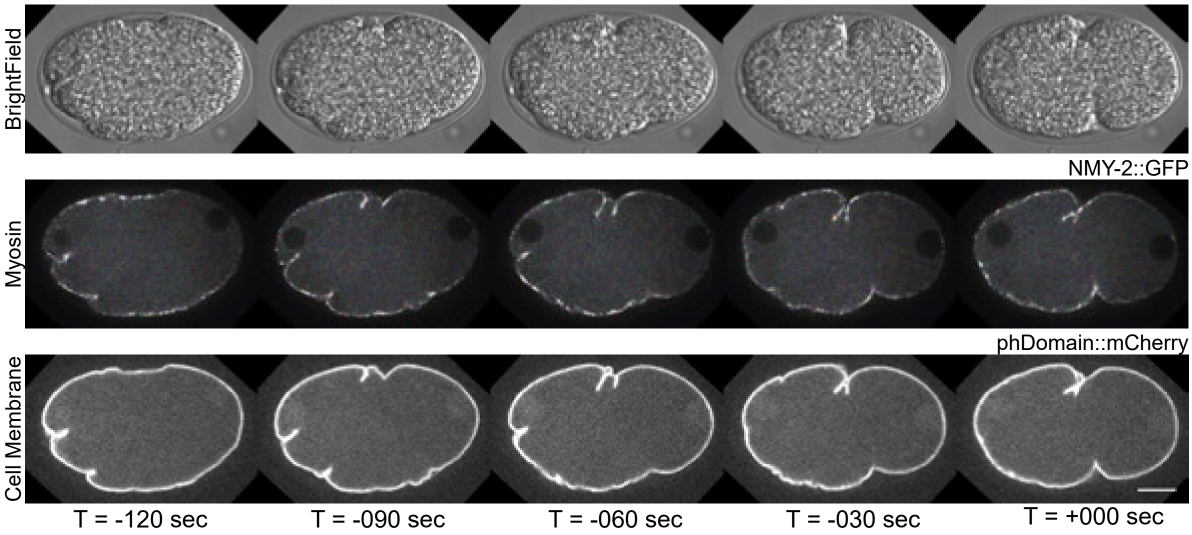

(a) Microscope images of an embryo of SWG070 strain acquired during time-lapse microscopy, depicting the three channels recorded. Top: Bright field, Middle: NMY-2::GFP (myosin), Bottom: phDomain::mCherry (boundary). The male pronucleus can be visualized as the dark circle in the myosin channel towards the posterior end (right). T = 0 s is set at the end of posteriorisation. Scale bar: 10 µm

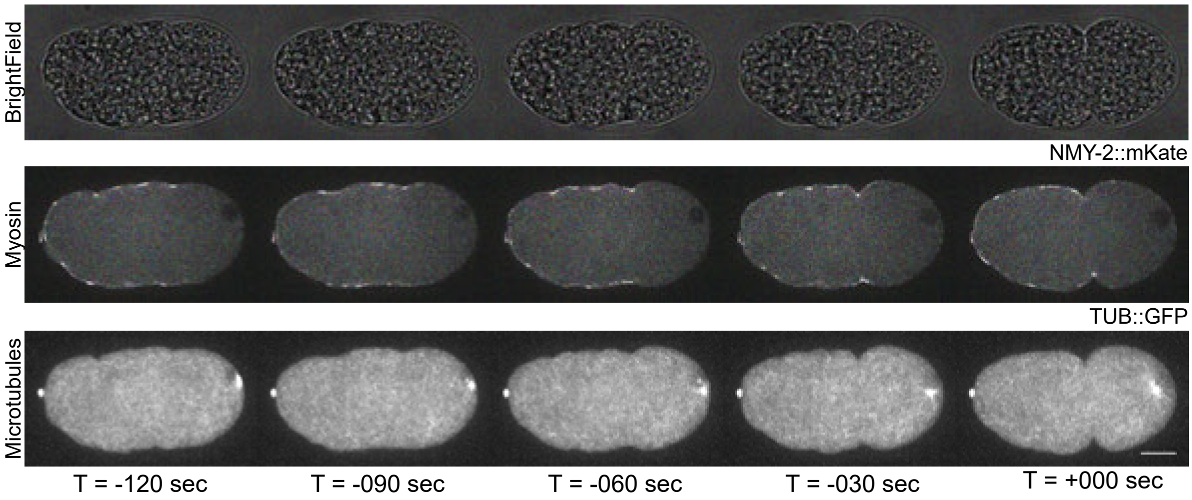

(b) Microscope images of an embryo of SWG057 strain acquired during time-lapse microscopy, depicting the three channels recorded. Top: Bright field, Middle: NMY-2::mKate (myosin), Bottom: TUB::GFP (microtubules - embryo boundary is extracted from this channel). The male pronucleus can be visualized as the dark circle in the myosin channel towards the posterior end (right). For microtubule channel, the max projection of the z-stack is shown (see Figure 3.3 for example of full z-stack). T = 0 s is set at the end of posteriorisation. Scale bar: 10 µm

Figure 3.1: Image acquisition during time-lapse microscopy for SWG070 and SWG057 strain. Images are rotated such that anterior and posterior ends are to the left and right respectively.

1. Each movie is cropped to ensure that only a single embryo is present in each frame. If other embryos are present in the cropped frame, they are cleared to black using the *Clear...* command in FIJI.
2. Anterior and posterior end of the embryo of interest are manually selected. Posterior side is identified by the depletion of NMY-2 on the posterior end of the cortex. The movie is rotated using bi-linear interpolation such that the anterior and posterior ends of the embryo of interest are on the left and right sides of the frame respectively (see Figure 3.2a).
3. The pronuclei can be seen as grey circles in the BF and dark circles in the NMY-2 channels, located in the cytoplasm. The male pronucleus is identified as the pronucleus towards the posterior end. The movie is flipped to ensure that the male pronucleus is located near the top side of the frame at the start of posteriorization. Any movies with both pronuclei on the same side are discarded (see Figure 3.2a).
4. The first frame in the movie at which the male pronucleus appears and the last frame before the male pronucleus moves away from the cortex were manually selected. Only frames between these two selected frames will be analysed (see Figure 3.2b).

For movies generated using SWG057 strain, step 1 of the pre-processing is modified – see Figure 3.3. z-stack collected in the GFP channel is used to detect the boundary of the embryo of interest in the frame. Kuwahara filter with window size 11 is used for noise reduction while still preserving edges [191]. The z-stack is thresholded using the default thresholding method used by FIJI [192]. Maximum projection of this binary stack is then used to generate embryo boundary. If multiple embryos are present, only the binary mask corresponding to the embryo of interest is retained. The BF images, NMY-2 images and embryo outlines are arranged together in the same channel arrangement as those used for SWG070 movies. After this modification, movies from SWG057 strain are processed in the same as movies from the SWG070 strain.

3.4.2 Tracking posteriorisation of the male pronucleus

To track the position of the male pronucleus as it posteriorises, processed movies were analysed using a custom Python script. Following external packages were used in this Python script: openCV [193], tifffile [194], scipy [195] and numpy [196]. This script expects the input movies to be a multipage tiff file with three channels – first for BF (which is not used in analysis), second for NMY-2 and third denoting embryo boundary (example – phDomain::mCherry in SWG070). These will be referred to as BF channel, the myosin channel, and the boundary channel respectively.

Segmenting the embryo boundary

For each time-point, the boundary channel frames are extracted and smoothed using a gaussian filter (with sigma = 2 pixel). Each frame are then thresholded using the 90th percentile of the intensity values in that frame as the threshold. A morphological closing operation (with disk element of size 17 pixel) is performed on the binary image thus constructed, to close any gaps in the boundary. To detect if the segmented embryo boundary is indeed closed, the inside of the boundary is filled using a binary fill holes operation. If the boundary is not filled, this operation

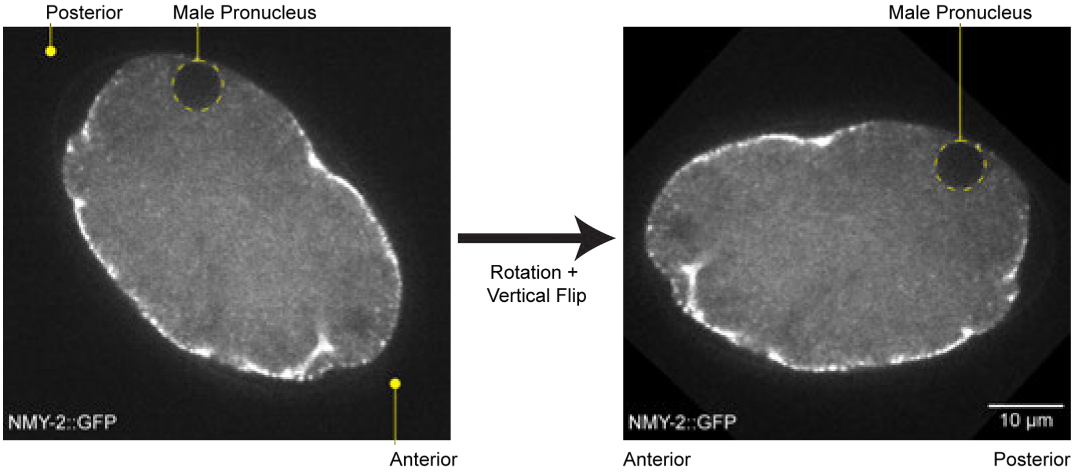

(a) Left image (myosin channel) demonstrates the manual annotation done during pre-processing. Posterior end is recognized by the the presence of the male pronucleus (yellow dotted circle) and the associated depletion of myosin on the cortex. Two points are then marked to denote the posterior and anterior ends respectively (yellow dots near the ends of the embryo). Right image shows the result – the image is rotated and then flipped (if necessary) to ensure that the anterior and posterior ends are on the left and right of the frame, and that the male pronucleus moves from the top of the embryo towards the posterior end. Scale bar: 10 µm

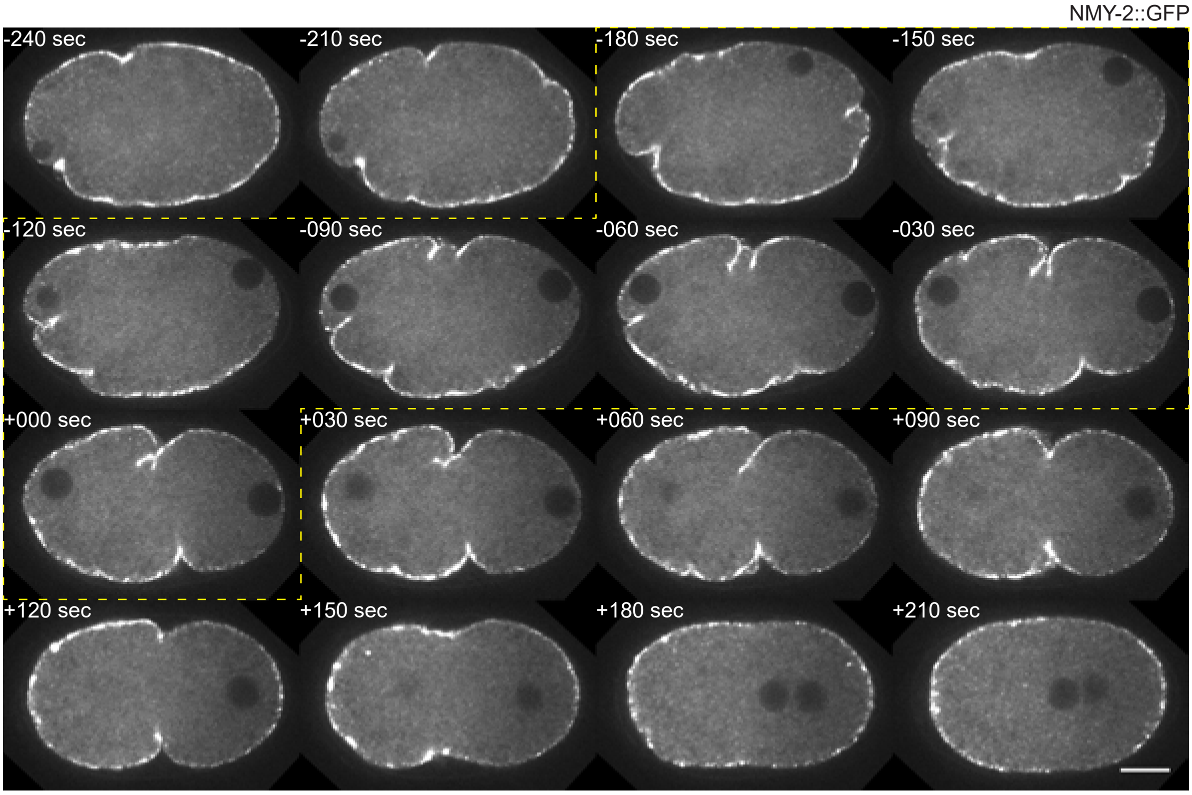

(b) Myosin frames at different time-points depicting the movement of the male pronucleus (after rotation and flip). The frame where the male pronucleus first appears is denoted as the first frame. The frame where the male pronucleus starts moving away from the cortex – and therefore the frame where posteriorisation ends – is denoted as the last frame. Only the time-points that lie between the first and last frame are analysed (indicated by yellow dotted line). Time-points are denoted in s, with T = 0 s selected as the last frame, i.e. end of posteriorisation. Scale bar: 10 µm

Figure 3.2: Pre-processing steps in the image analysis pipeline, for SWG070 strain. Anterior and posterior are to left and right respectively in all images.

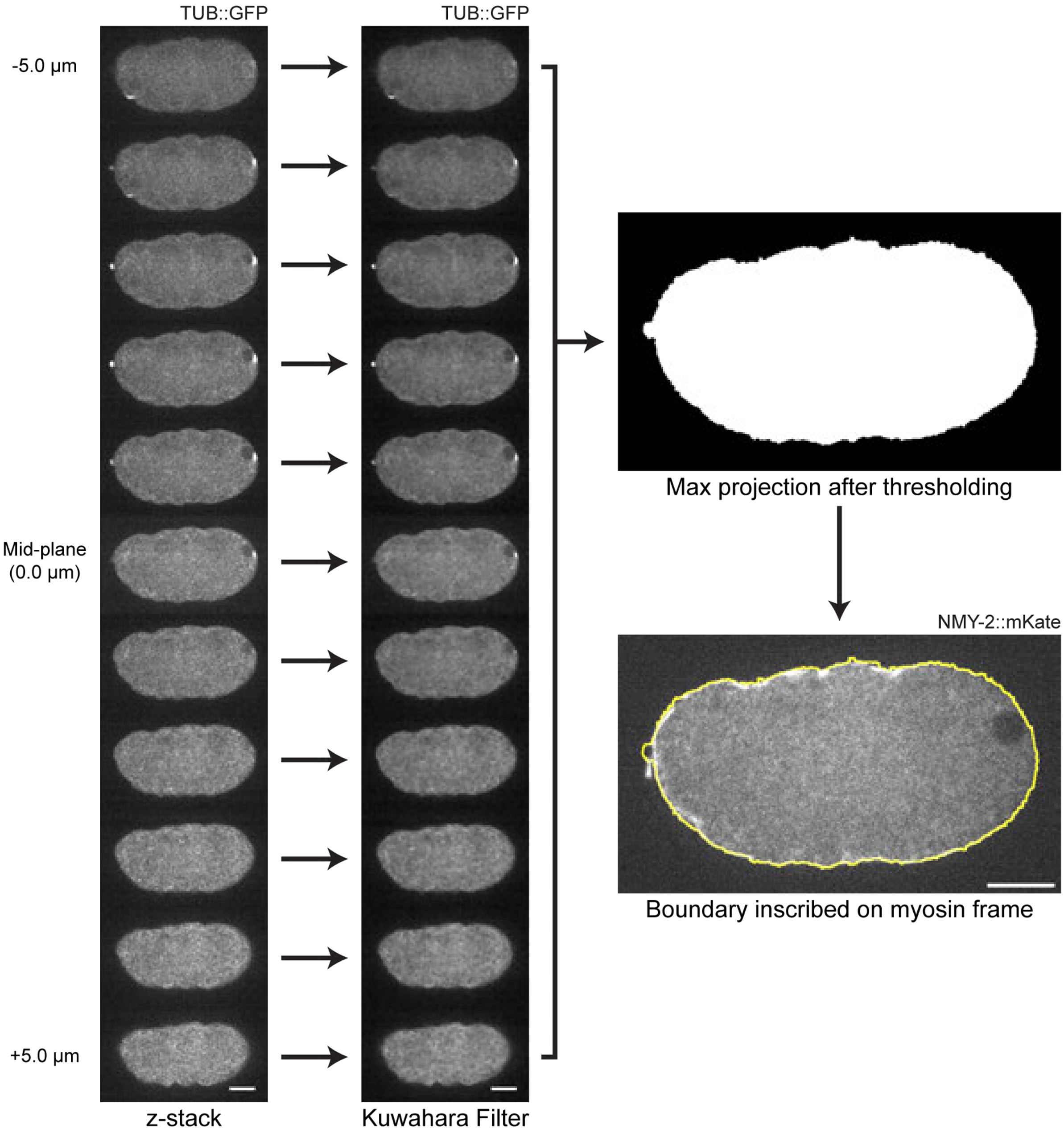

Figure 3.3: Modified pre-processing steps for SWG057 strain, to extract embryo boundary from microtubule z-stacks. At each time-point, the z-stack of 11 slices in the microtubule channel are filtered using the kuwahara filter, binarized and then max projected. The outline of the max projection is encoded as the boundary channel, mimicking the phDomain::mCherry channel of the SWG070 strain. This outline is shown here as the yellow boundary inscribed onto the myosin frame at the same time-point. Scale bars in all images: 10 µm. Anterior and posterior are to left and right respectively in all images.

will fill the whole frame instead. Thus, to detect if the boundary was closed, it is checked if more than 80% of the frame is filled. If less than 80% of the frame was filled, the boundary is closed – extracted as the contour of non-zero length enclosing the largest area in the frame. If more than 80% of the frame was filled, a morphological dilation (with disk element of size 18 pixel) of the binary frame is performed to attempt closing gaps again. If after the dilation, binary fill holes still leads to more than 80% of the frame being filled, boundary detection is considered to have failed for this time-point and the boundary segmented in the previous time-point is used instead. Otherwise, the contour of non-zero length enclosing the largest area in the frame after dilation is again considered as the boundary. Boundary segmented at the previous time-point is also used if the boundary segmented at the current frame has a length too different from the previous one.

For each time-point, the segmented boundary is fit to an ellipse and the long and short axes of the fitted ellipse are calculated. To obtain the average axes for the movie, the axes detected for each time-point are averaged. The average direction is found by averaging the unit vectors that denote the instantaneous directions of the axes in each time-point, and the average lengths by averaging the lengths of the instantaneous axes. See Figure 3.4 for an example.

Additionally, the myosin channel frames are also denoised using non-local means denoising [197], with the following parameters: Filter strength = 3 pixel, template window size = 4 pixel, search window size = 12 pixel.

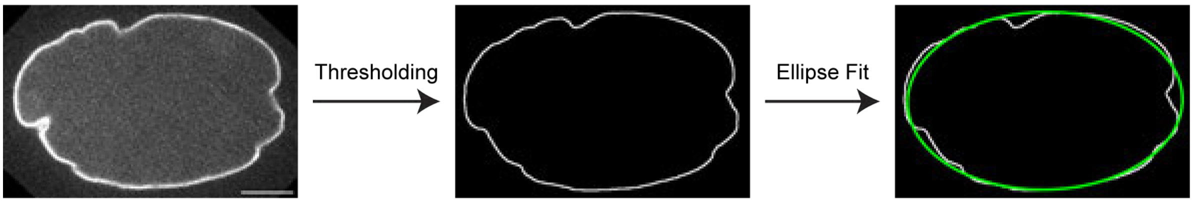

Figure 3.4: Boundary detection using the phDomain::mCherry channel in SWG070. At each time-point, the frame (left) is thresholded (middle, see Segmenting the embryo boundary for details). The thresholded image provides the segmented boundary. An ellipse is fit to this segmented boundary to obtain the instantenous long and short axes (right, yellow line indicates the fitted ellipse). The same process is carried out on movies generated using embryos from the SWG057 strain. Scale bar: 10 µm

Segmenting the male pronucleus

The denoised myosin channel frames are utilized for segmenting the male pronucleus. Only myosin frames for the time-points in the range selected in subsection 3.4.1 are considered. In these frames, the pronuclei can be identified as dark circles devoid of myosin in the cytoplasm. The male pronucleus is identified as the one present in the posterior half (steps in subsection 3.4.1 ensure this is always true). This difference in intensities between the cytoplasmic myosin and male pronucleus is utilized to segment the latter, using successive thresholding. The following steps are undertaken for each myosin frame (that is, at each time-point) to segment the male pronucleus (see Figure 3.5 for an example):

1. The segmented embryo boundary is used to create a mask of the interior of the embryo – in this way, the boundary segmentation is crucial for male pronucleus segmentation, as it allows separating the interior of the embryo from the whole frame.
2. The set of thresholds to use for successive thresholding is selected, ranging from the 5th to the 95th percentile of the non-zero intensity values in the embryo interior.
3. For each threshold in the selected range:
   a) The frame is thresholded using the selected threshold. Pixels with intensity values below the selected threshold are set to be white (= 1), and rest to black (= 0).
   b) All pixels to the left (or in the anterior half) of the embryo center (determined as the center of the ellipse fit to the boundary) are set to black (= 0). This ensures that only the male pronucleus is detected, which is present to the right (or in the posterior half). A morphological opening operation with disk element of size 5 pixel is performed to remove small regions of white pixels.
   c) The total number of white pixels for this threshold is recorded.
4. To detect the thresholds to use for male pronucleus segmentation, the "knee" of the Number of white pixels vs Thresholds graph is detected. This "knee" indicates the threshold above which which the number of white pixels for each threshold increase rapidly, indicating that the white pixels are "flooding" outside the dark circle that denotes the male pronucleus. To detect this "knee", at each threshold a cost function is calculated: the square root of the average of differences from the mean of the number of white pixels up until that threshold is calculated. The threshold for which this cost is the lowest is selected as the maximum threshold to be used for male pronucleus segmentation. See Figure 3.5a for an example.
5. All thresholds upto this maximum threshold calculated in the last step are considered. The male pronucleus is identified as a dark circle. To quantify how circular a segmentation is, circularity measure[1] $= 4\pi\frac{\text{Area}}{\text{Perimeter}^2}$, where Area and Perimeter are of the segmented section, is used. Circularity is a dimensionless measure that ranges from 0 to 1, with 1 being a perfect circle. From all segmentations generated by the thresholds considered in this step, the one that has the largest area and circularity is identified as the male pronucleus. See Figure 3.5b for an example.

Tracking the male pronucleus

Male pronucleus segmentations generated by the process outlined above are filtered to ensure the following:

- The centers of consecutive male pronucleus segmentations (consecutive as in two consecutive time-points) do not have a distance exceeding 13 pixel. This ensures that spurious detections which are far from the male pronucleus are ignored. Given that the cortex

---

[1] This measure is based on the isoperimeteric inequality: a geometric inequality that relates the surface area (perimeter for 2D) to the volume (area for 2D) of a region. In 2D, it states that the perimeter of any closed curve L is related to the enclosed area A as $L^2 >= 4\pi A$. Thus, in 2D, for all closed curves with the same perimeter, the one enclosing the most area is the circle.

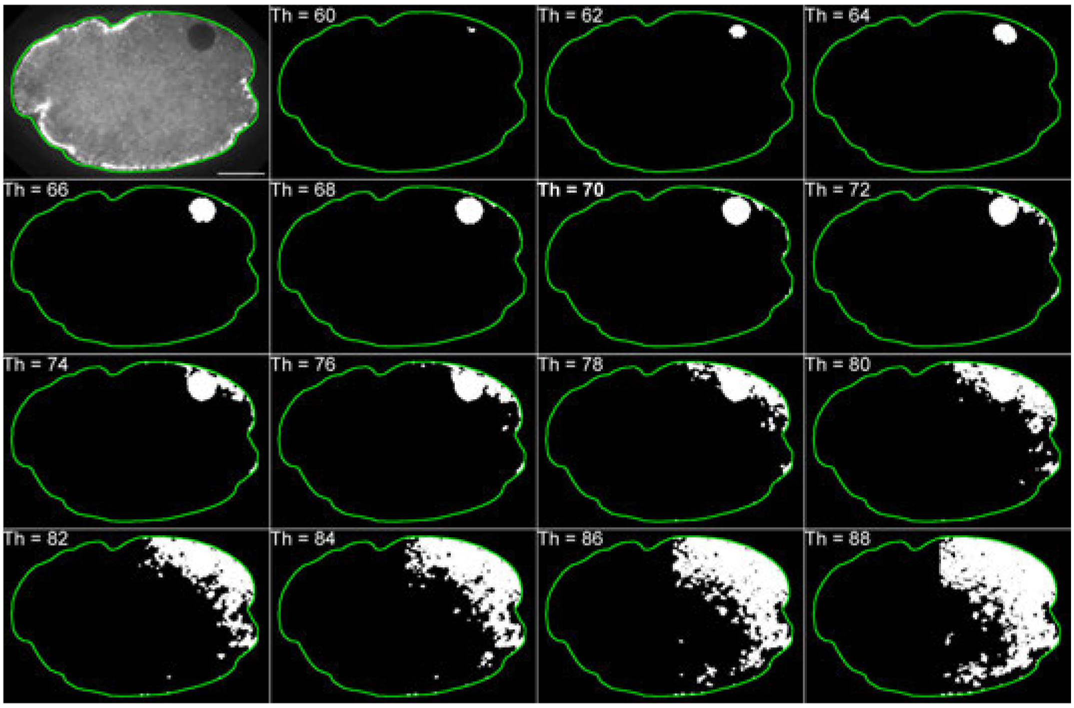

(a) Successive thresholding on myosin frame to segment male pronucleus. Top left image is the denoised myosin frame. All pixels outside this contour are ignored for the purposes of thresholding. Rest of the images show the result after thresholding at a specific threshold – White pixels have intensities below the selected threshold. Yellow contour indicates the segmented boundary for all images. Note that any white pixels in the left half (that is, anterior half) of the embryo are automatically discarded. Threshold = 70 is selected for this myosin frame – see Figure 3.5b. Scale bar: 10 µm

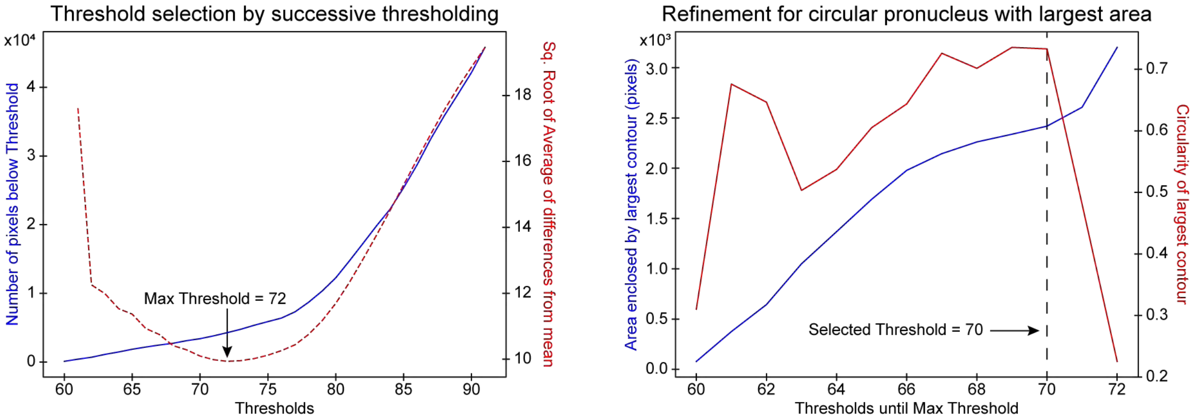

(b) Automatic threshold selectiong using successive thresholding (see Segmenting the male pronucleus). Left: Selecting Max Threshold. Blue curve (left y-axis) depicts the number of white pixels in the sense of Figure 3.5a for each threshold. Max Threshold is selected near the "knee" of this curve. Red dotted curve (right y-axis) depicts the cost function. Max Threshold is selected as the threshold with the minimum cost. Right: Selecting Threshold. All thresholds upto Max Threshold are considered. For each threshold, the area of the largest contour (that is, boundary of the largest connected component) is calculated (blue curve, left y-axis). Additionally, the circularity of this contour is calculated (red curve, right y-axis). Final selected threshold for this frame is where the area and circularity are both maximised. For this frame, the selected threshold is 70. See Segmenting the male pronucleus for definitions

Figure 3.5: Segmenting the male pronucleus by successive thresholding and automatic selection. Only a single time-point is considered throughout the figure. Anterior and posterior are to left and right respectively in all images.

and cytoplasm flow at speeds around 0–10 µm min^{-1} (see subsection 3.4.3) and the limitation here corresponds to a speed of 27.3 µm min^{-1} or more, no true segmentations are ignored.

- Segmentations which are too irregular – that is, with circularity less than 0.7 – are ignored.
- Segmentations which are very small – that is, with area less than 200 pixel^2 – are ignored.

For frames where the segmentations are ignored, an estimate is generated by linearly interpolating between the two closest "good" frames, where the segmentations were not ignored. This is only done for gaps of 5 frames or less, and is not done at the edges of the set of frames selected for nucleus segmentation. The set of male pronucleus segmentations thus generated, as a function of time-points of each frame, constitute the detected trajectory of the male pronucleus in this movie.

Both the male pronucleus trajectory and the embryo boundary detected using the above analyses are manually verified – see Figure 3.6. If a movie fails to detect any embryo boundary, or fails to detect the male pronucleus in more than 30% of frames selected, the movie is discarded.

Following attributes of the trajectory are calculated for each frame (see Figure 3.7 and Figure 3.8):

Pronucleus position

Calculated with respect to the embryo center, designated as origin. The x and y coordinates of the center of the pronucleus, and the polar angle between the long axis and the line connecting the center of the embryo to the center of the pronucleus are stored. This angle is referred to as the "Angular Position of the male pronucleus".

Pronucleus Size

Calculated as the total number of pixels in the male pronucleus segmentation at each time-point.

Distance from cortex

Calculated as the distance between the center of the male pronucleus and the closest point on the embryo boundary (cortex).

Pronucleus velocity

Calculated as the gradient of the position of the male pronucleus. The component of the velocity along the x and y axes are stored. Additionally, components of the velocity parallel and perpendicular to the embryo boundary are also calculated. This component of the pronucleus velocity parallel to the embryo boundary is referred to as the "Posteriorisation velocity".

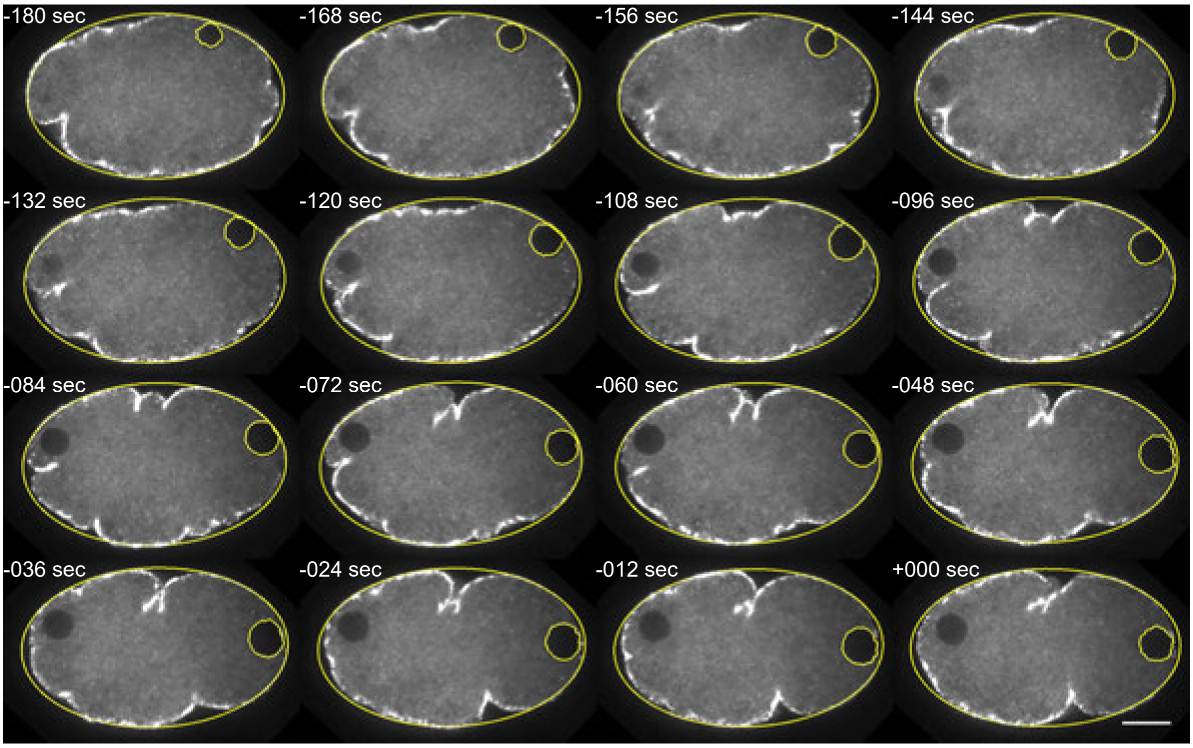

Figure 3.6: Validating the results of the segmentations, for different time-points. In each image, the outer yellow contour denotes the fitted ellipse to the segmented boundary, and the inner yellow contour denotes the segmented male pronucleus. Scale bar: 10 µm. Anterior is to the left and posterior to the right in all images. T = 0 s denotes end of posteriorisation.

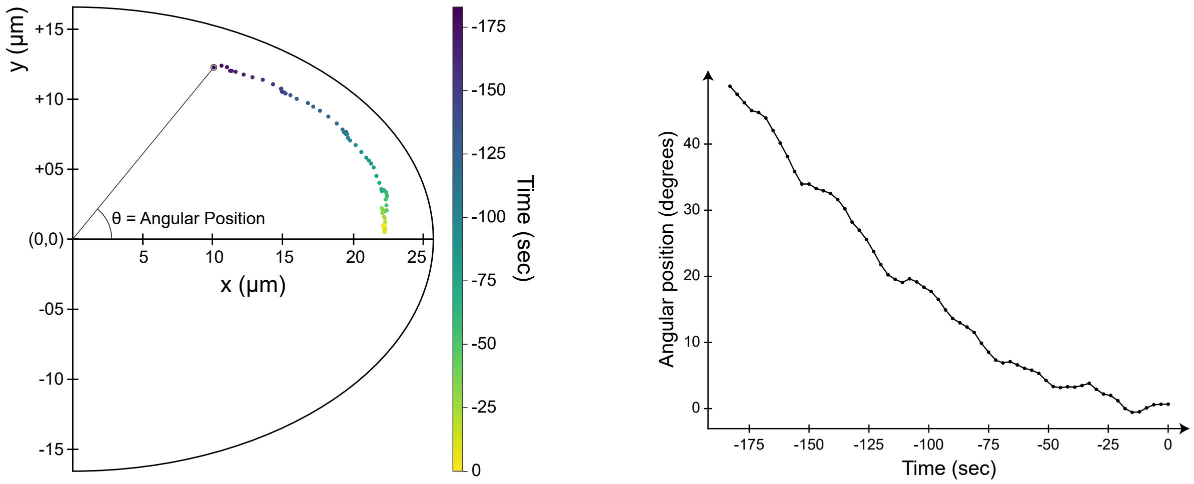

(a) Trajectory of the male pronucleus – denoted by the coordinates of its center – as it posteriorises over time. Color represents time. x- and y-axes lie along the long and short axes of the ellipse fitted to the embryo boundary. Angular position is defined as the angle between the long axis and line connecting the centers of the male pronucleus and embryo.

(b) Plot of Angular position of the male pronucleus (y-axis) as a function of time (x-axis).

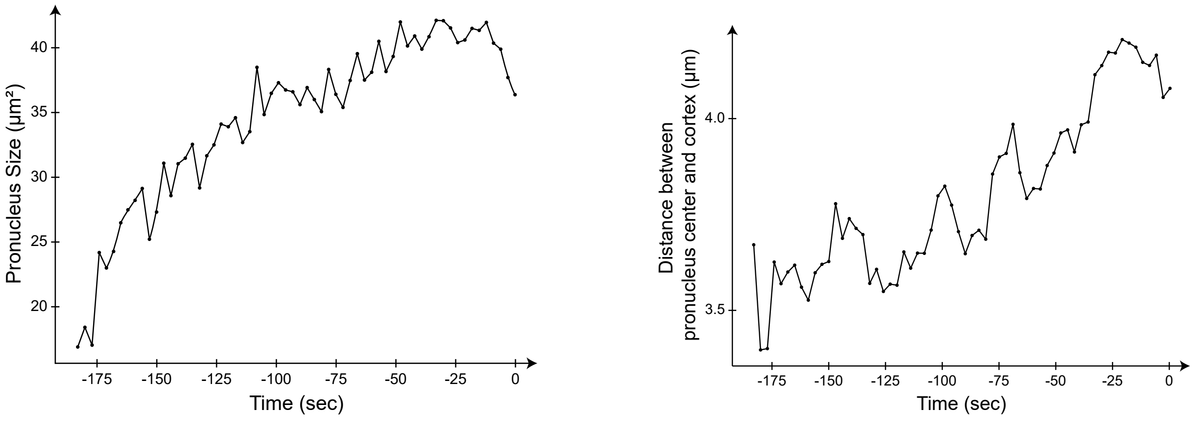

(c) Plot of the size of the male pronucleus (y-axis) as a function of time (x-axis). Size is measured as the area enclosed by the contour denoting the male pronucleus segmentation.

(d) Plot of Distance between the center of male pronucleus and closest point on cortex (y-axis) as a function of time (x-axis).

Figure 3.7: Trajectory of the male pronucleus obtained using the image analysis pipeline. For all plots, T = 0 s denotes the end of posteriorisation. All plots are obtained from a single movie of an embryo of SWG070 strain – same embryo depicted in Figure 3.1, Figure 3.2, Figure 3.4, Figure 3.5 and Figure 3.6

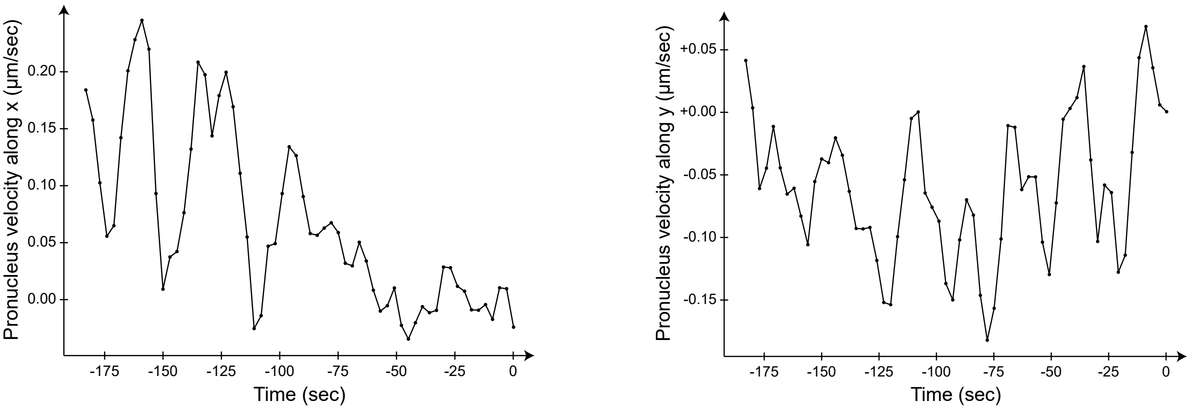

(a) Plot of component of the velocity of the male pronucleus along the long axis (y-axis) as a function of time (x-axis). Positive velocity indicates movement towards posterior.

(b) Plot of component of the velocity of the male pronucleus along the short axis (y-axis) as a function of time (x-axis). Positive velocity indicates movement towards the top of the embryo.

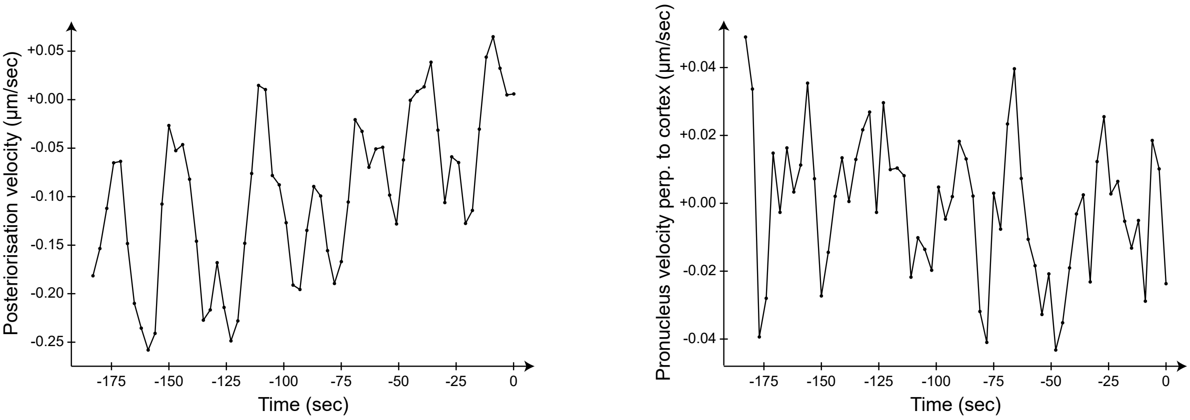

(c) Plot of the posteriorisation velocity of the male pronucleus (y-axis) as a function of time (x-axis). Posteriorisation velocity is defined as the component of the velocity of the male pronucleus parallel to the cortex. Positive velocity indicates movement towards posterior.

(d) Plot of the component of the velocity of the male pronucleus perpendicular to the cortex (y-axis) as a function of time (x-axis). Positive velocity indicates movement towards the cortex.

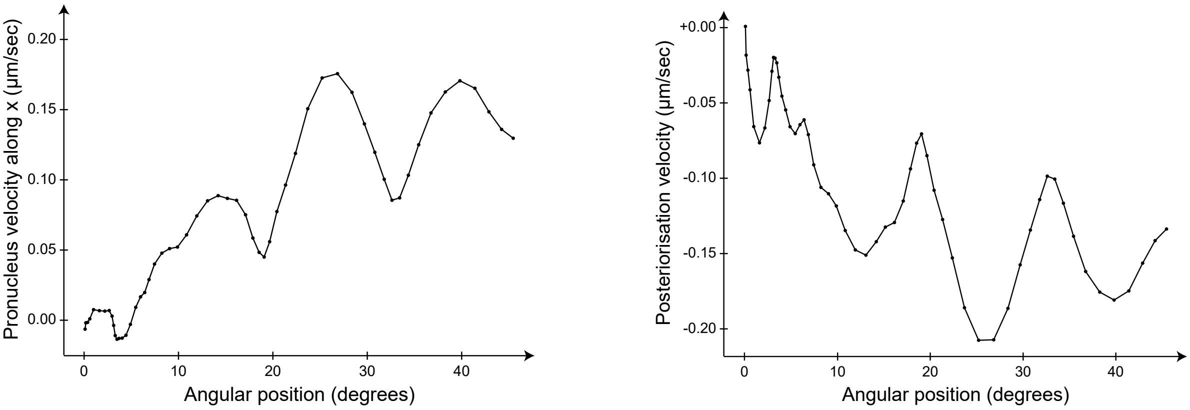

(e) Plot of component of the velocity of the male pronucleus along the long axis (y-axis) as a function of angular position (x-axis). Values have been smoothed using a sliding average with window of 7 frames. Positive velocity indicates movement towards posterior.

(f) Plot of posteriorisation velocity of the male pronucleus (y-axis) as a function of angular position (x-axis). Values have been smoothed using a sliding average with window of 7 frames. Positive velocity indicates movement towards posterior.

Figure 3.8: Velocities obtained using the image analysis pipeline. For plots against time, T = 0 s denotes the end of posteriorisation. All plots are obtained from a single movie of an embryo of SWG070 strain – same embryo depicted in Figure 3.1, Figure 3.2, Figure 3.4, Figure 3.5 and Figure 3.6

Measuring NMY-2 concentrations

Myosin concentrations in the cytoplasm and cortex can be measured using the boundary segmentations and denoised myosin frames obtained from the Python script. Myosin concentration are measured in intensity per pixel units, where intensity is measured in arbitrary units corresponding to the readings from the camera used to record the movies. A region 15 pixels wide below the segmented boundary is considered as being at the cortex, while the cytoplasm is considered as the interior region, left after the cortical region is removed. Myosin concentration in each region is estimated as the average intensity per pixel in the corresponding region, averaged over 7 consecutive frames (sliding window).

3.4.3 Measuring cortical flows

Cortical flows were measured from the denoised myosin frames using a custom MATLAB script, following [1] (MATLAB script written by Peter Groß). The script takes as input the boundary segmentations and the denoised myosin frames generated by the Python script, and performs two steps:

1. Using the boundary segmentations already made by the Python script, the MATLAB script generates a kymograph of the cortical layer in the myosin frames. The cortical layer is identified as the region starting from the boundary of the embryo and stretching 30 pixel deep inwards.
2. These kymographs are then used to measure the flow velocity of the cortex as a function of position along the cortex, using Particle Image Velocimetry (PIV) [198].

See Figure 3.9 for output kymographs and cortical flows, for the example movie considered in this chapter.

Creating kymographs

For a given myosin frame, its corresponding boundary segmentation (generated by the Python script) is converted into a composite Bézier curve: a series of Bézier curves joined end to end. This converts the discrete pixel positions of the boundary segmentation into a smooth curve that represents the embryo boundary. The point on this curve that is on the embryo's long axis and at the posterior end are identified. Starting from this point, additional points are sampled at one pixel size distance between adjacent points on both ends of the curve. Denoting the initial point on the posterior as zero, these points denote the integer distances along the curve, that is integer arclengths. Thus, the composite Bézier curve is used to define the distance along the cortex – the arclength axis.

At each point sampled on the curve, the normal to the curve pointing towards the embryo interior is found. Points are sampled along each normal at one pixel size distance between adjacent points on a normal upto a distance of 30 pixel, and pixel values are interpolated to obtain the estimated intensities at these points. This can be folded out into a thin rectangular "band"[2] of points along the embryo boundary. This "band" is identified as a folded out version of the cortex, calculating for the frame of interest. The long edge of this band is along the arclength axis, while the short edge is perpendicular.

---

[2] The change in length between the outermost points at the boundary and innermost points towards the embryo interior are ignored, as the length of the embryo boundary is much larger than 30 pixel

By taking the maximum intensity value along this perpendicular axis for each point on the arclength axis (maximum projection), and stacking the resultant 1D representations of myosin distributions for each frame in order of time vertically, a visualization known as the kymograph can be generated – see Figure 3.9a and Figure 3.9b. This kymograph allows visualization of the changes in myosin distributions as a function of time at each position on the cortex.

Particle Image Velocimetry (PIV)

PIV is a method of visualizing flow in fluids and measuring instantaneous flow velocities [198, 199]. Under this method, the fluid is seeded with tracer particles which can be illuminated with light. These tracer particles are small enough that they can be assumed to faithfully follow the fluid dynamics. Time-lapse movies of the fluid flow, with the tracer particles illuminated, are taken. Instead of tracking individual particles, the flow field at a given time-point is calculated by cross-correlating sections of the frame at this time-point with the frame at the next section. In detail, the frame at the current time-point is divided into templates of defined sizes. Each template is cross-correlated with the frame at the next time-point by displacing the template upto a maximum distance from its location in the current time-point. Displacement with the largest cross-correlation, divided by the time elapsed between the two frames, is the measured velocity of the fluid at the location of the template. Here a multi-pass PIV algorithm is used, which uses templates of different sizes to measure fluid flow at finer resolutions; along with Gaussian fitting of the peak in the cross-correlation to obtain subpixel accuracy. See [199] for a detailed discussion.

In the case of the cortex, since myosin motors are fluorescently labelled, tracer particles are not required – fluorescent tags take the role of the tracer particles. To calculate cortical flow velocities along the arclength axis, the cortical “bands” extracted for each frame are used for the cross-correlations instead. A multi-pass (4 passes) PIV was utilized, with initial template size of 24 pixel and step size of 4 pixel. Max displacement of each template during cross-correlation was limited to 7 pixel. See Figure 3.9c for the measured cortical flows in the example movie considered for this chapter.

3.4.4 Measuring cytoplasmic flows

Cytoplasmic flows in the embryos were measured using the BF frames in the embryo movies (see section 3.4). A MATLAB implementation of PIV [198] was used to calculate the flow fields in the cytoplasm from the BF frames (see subsection 3.4.3 for general introduction to PIV), with the boundary segmentations (see subsection 3.4.2) used to exclude the exterior of the embryo. Yolk granules in the cytoplasm serve the role of the tracer particles in the cytoplasm. A multi-pass (4 passes) PIV was utilized, with initial template size of 24 pixel and step size of 4 pixel. Max displacement of each template during cross-correlation was limited to 7 pixel.

3.5 Data analysis

This section describes the methods used to analyse the data – male pronucleus trajectories and cortical flows measured for each embryo – to obtain ensemble averages for a given experiment. Average posteriorisation velocity as a function of angular position of the male pronucleus is used as the primary measure of AP axis alignment. Average cortical flows as a function of angular position of the male pronucleus are used as the input for the calibration process

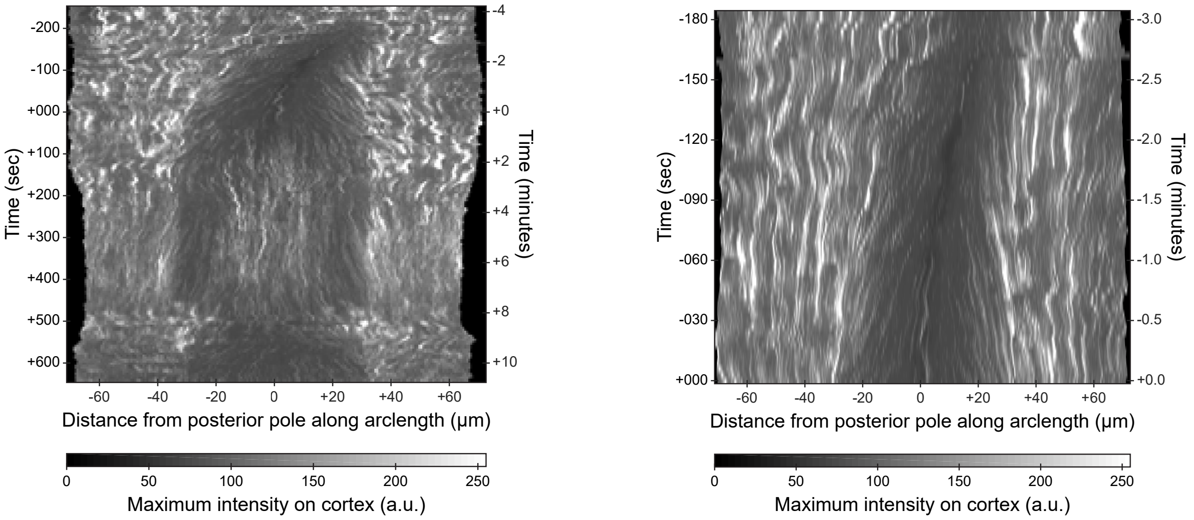

(a) Kymograph depicting intensities along the cortex (arclength axis along x-axis) as a function of time (along y-axis), for the full movie. Colorbar indicates the maximum intensity value on the cortex at the given position and time.

(b) Kymograph depicting intensities along the cortex (arclength axis along x-axis) as a function of time (along y-axis), only for time-points used to analyze posteriorisation. Colorbar indicates the maximum intensity value on the cortex at the given position and time.

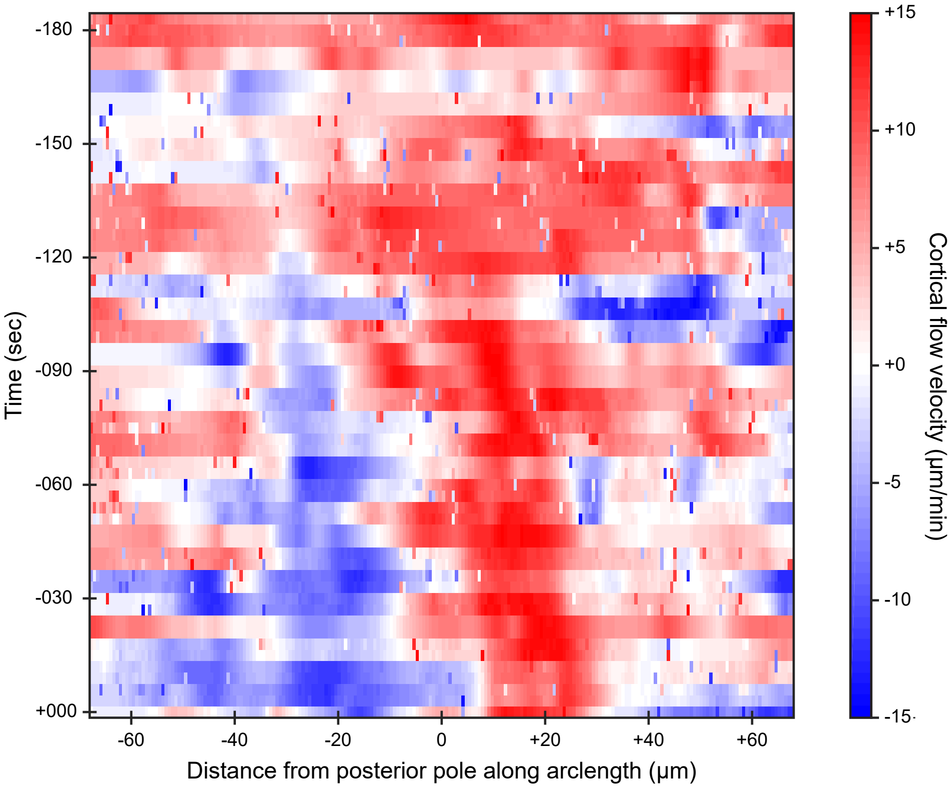

(c) Cortical flow velocity (colorbar) measured for the time-points used to analyse posteriorization, as a function of time (y-axis) and position along the cortex (x-axis). Positive/Negative flow velocity, depicted in red/blue, indicate movement towards/away from positive end of the arclength axis (x-axis).

Figure 3.9: Measuring cortical flows. For all plots, T = 0 s on the y-axis denotes the end of posteriorisation, and s = 0 µm on the x-axis denotes the posterior pole. All plots are obtained from a single movie of an embryo of SWG070 strain – same embryo depicted in Figure 3.1, Figure 3.2, Figure 3.4, Figure 3.5 and Figure 3.6

described in chapter 2. For all experimental conditions, the average posteriorisation velocity and average cortical flows as a function of angular position are calculated. All data analysis is done using custom scripts written in MATLAB.

Short-term fluctuations in each male pronucleus trajectory are smoothed using a sliding average with a window of 7 frame for each movie separately. To calculate average posteriorization velocity as a function of angular position, posteriorization velocity and angular positions calculated for all embryos for a given experimental condition are combined together. Angular positions in this dataset are binned in 3 deg bins. Average posteriorization velocity for each angular position bin is calculated by averaging over all posteriorization velocities corresponding to the angular positions included in the bin. 95% confidence interval for the mean posteriorization velocities are calculated using a two-sided t-test. See Figure 3.10a for an example.

Cortical flows measured for all embryos for a given experimental condition are first aligned using the arclength axis. Cortical flows are then classified using the angular position of the male pronucleus, and binned together in angular position bins of 3 deg width each. Average cortical flows for each angular position bin are calculated by averaging all cortical flows within an angular position bin. Note that this averaging is done spatially: that is, measured flow velocities at the same position on the arclength axis corresponding to different frames are averaged together. The model described in chapter 2 uses these averaged cortical flows for calibration. See Figure 3.10b for an example.

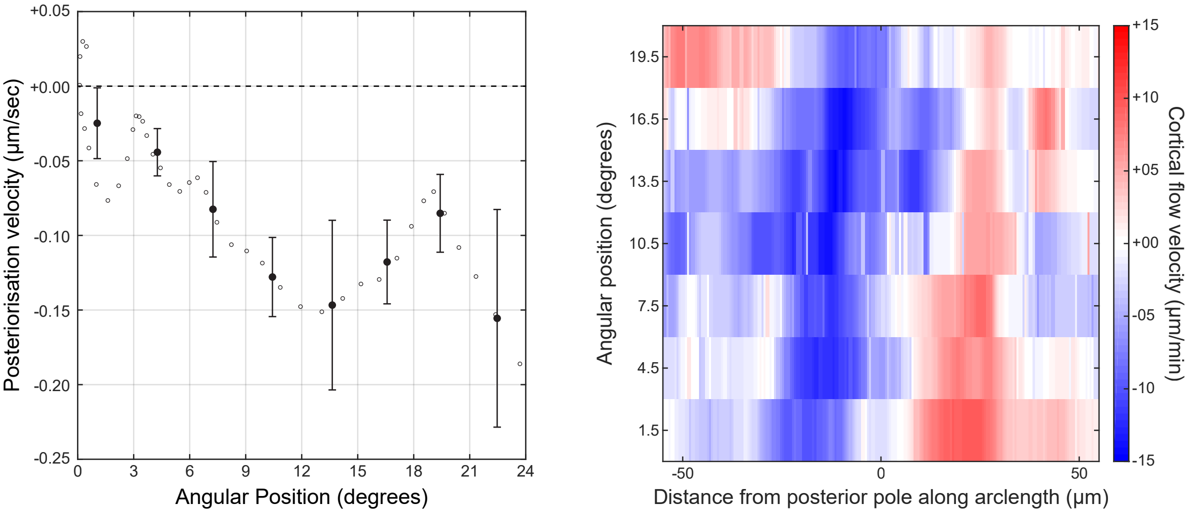

(a) Binning Posteriorization velocity (y-axis) vs Angular position (x-axis). Each angular position bin is of 3 deg width. For each bin, the mean posteriorization velocity (dark circles) and 95% confidence intervals of the mean (error bars) are depicted. Open circles denote the datapoints obtained after smoothing via sliding average (window: 7 frames). Dotted line indicates zero posteriorization velocity.

(b) Binning Cortical flow velocity (colorbar) using Angular position (y-axis). For each angular position bin (bin width 3 deg), the mean cortical flow at each position along the cortex (x-axis) is calculated – using all frames that fall within the angular position bin. Positive/Negative flow velocity, depicted in red/blue, indicate movement towards/away from positive end of the arclength axis (x-axis). s = 0 µm on the x-axis denotes the posterior pole.

Figure 3.10: Data analysis done for a single movie of an embryo of SWG070 strain, for illustrative purpose. Movie depicted in Figure 3.1, Figure 3.2, Figure 3.4, Figure 3.5 and Figure 3.6. This figure showcases the two main output graphs obtained from the data analysis.

Chapter 4

Experimental investigation of AP axis alignment

In this chapter, the results of various experiments conducted to investigate AP axis alignment in *C. elegans* embryo are reported, along with their comparison to the numerical simulations of the theoretical model of AP axis alignment described in section 2.3. This chapter follows [170] closely. Experiments described here were performed in collaboration with Peter Gross and Mirna Kramer from Technische Universität Dresden; with numerical simulations by Michael Nestler from Technische Universität Dresden.

4.1 Characterising AP axis alignment in unperturbed embryos

AP axis alignment is first characterised in unperturbed embryos. "Unperturbed" here refers to no genetic perturbations, such as no RNAi or mutations, apart from the addition of fluorescent tags. To this end, time-lapse microscopy of embryos from the SWG070 strain was undertaken, which is labelled with NMY-2::GFP and phDomain::mCherry – as described in section 3.3. In these embryos, the male pronucleus can be observed as a dark circle in the cytoplasm, in the NMY-2::GFP fluorescent channel – as cytoplasmic myosin is excluded from the proncleus. The posterior domain as the depletion of NMY-2 on the cortex near the male pronucleus. The AP axis alignment process is characterised by tracking the position of the male pronucleus as it undergoes posteriorisation. See section 3.4 for details on the image analysis methods used to track the male pronucleus.

Experimental Condition	Strain	No. of Embryos
Unperturbed	SWG070	57
mlc-4 RNAi	SWG070	10
nop-1 RNAi	SWG070	9
nop-1; mel-11 RNAi	SWG070	69
ima-3 RNAi	SWG070	35
air-1 RNAi	SWG070	23
air-1; mel-11 RNAi	SWG228	13
Unperturbed	SWG057	32
goa-1; gpa-16 RNAi	SWG057	30

Table 4.1: Number of embryos in various experimental conditions described in this chapter.

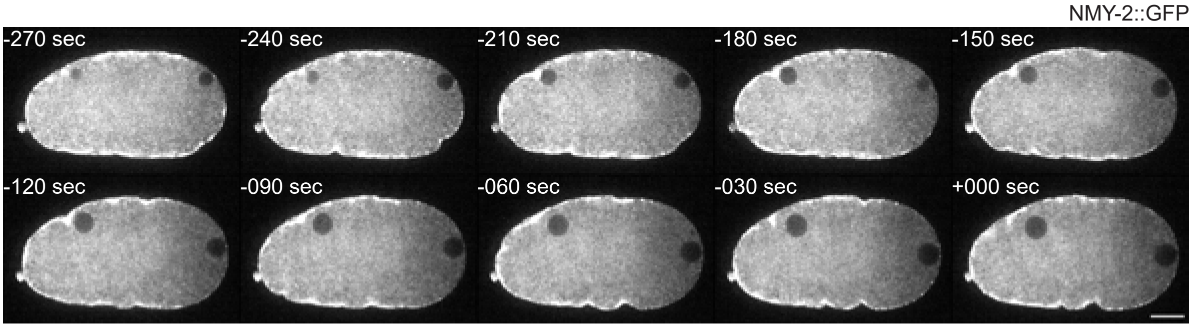

Figure 4.1: Representative unperturbed embryo of SWG070 strain, labelled with NMY-2::GFP (white), showing the posteriorisation of the male pronucleus and the concurrent movement of the myosin depletion (indicating the pPARs domain) towards the posterior end. The male pronucleus can be visualized as the dark circle in the myosin channel towards the posterior end (right). t = 0 s is set at the end of posteriorisation of the male pronucleus. Scale bar: 10 µm. Images are rotated such that anterior and posterior ends are to the left and right respectively.

Two aspects of the posteriorisation of the male pronucleus are quantified: its “angular position” and “posteriorisation velocity” (see section 3.4). Angular position refers to the angle made between the long axis and the line connecting the center of the male pronucleus to the center of the embryo. Posteriorisation velocity is the component of the velocity of the male pronucleus that is parallel to the cortex (at the given angular position). Negative posteriorisation velocities indicate movement in direction of decreasing angular positions and thus towards the posterior end, positive posteriorisation velocity in direction of increasing angular positions and thus away from the posterior end. End of posteriorisation is denoted as the zero time-point (t = 0 s), and all movies are synchronised using this time-point.

Plotting the angular position as a function of time, the angular positions were found to generally decrease towards 0 deg as time reaches closer to end of posteriorisation (t = 0 s). Specifically, in embryos where the AP axis is mis-aligned – that is, with initial angular position greater than 5 deg (33 out of 57 embryos) – the AP axis re-aligns back towards the long axis. Furthermore, this decay towards 0 deg was quantified by fitting an exponential $\alpha = \alpha_0 + \exp\left(-\frac{t}{t_0}\right)$ to the plotted angular positions, yielding a time constant $t_0 = 119 \pm 3\,\mathrm{s}$ and $\alpha_0 = -0.75 \pm 0.30\,\mathrm{deg}$. These observations confirm those made in [6] – the AP axis does align itself towards the long axis of the embryo, evidenced by the posteriorisation of the male pronucleus. Note that the exponential fit considered here is only phenomenological, and does not attempt to capture any physically relevant features of AP axis alignment – rather it allows for easier comparison of the decreasing angular positions in different experimental conditions considered in this chapter.

Plotting the posteriorisation velocity as a function of angular position (see section 3.5 for details on binning of angular positions), it is found that the male pronucleus is, on average, moving towards the posterior end (as indicated by the negative sign of the velocity) – with higher speed at higher angular positions (Figure 4.3). This can also be observed as increasing magnitude of slope of the angular position vs time plots for higher angular positions in Figure 4.2b. Based

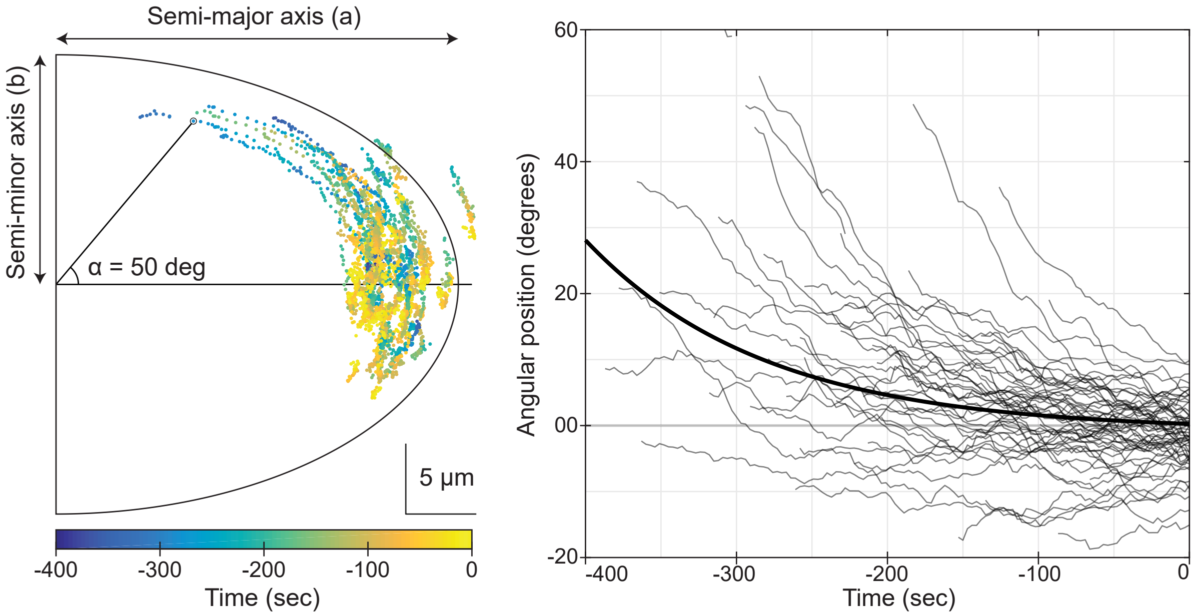

(a) Trajectories of the male pronucleus (denoted by the coordinates of its center) observed in unperturbed embryos. Color represents time. x- and y-axes lie along the long and short axes of an ellipse with semi-major axis $a = 28.9\,\mu\text{m}$ and semi-minor axis $b = 16.3\,\mu\text{m}$. Scale bar: $5\,\mu\text{m}$

(b) Angular position of the male pronucleus (on y-axis, in deg) plotted as a function of time (on x-axis, in s), in unperturbed embryos. Thin grey lines represent individual trajectories, thick black line represents a exponential fit to the average of these tracks: $\alpha = \alpha_0 + \exp\left(-\frac{t}{t_0}\right)$, with $t_0 = 119 \pm 3\,\text{s}$ and $\alpha_0 = -0.75 \pm 0.30\,\text{deg}$.

Figure 4.2: Experimentally observed trajectories of the male pronucleus during posteriorisation in unperturbed embryos of SWG070 strain (N = 57). See subsection 3.4.2 for details on male pronucleus tracking. Average semi-major and semi-minor axes lengths for unperturbed embryos of SWG070 strain are used in Figure 4.2a – see Table 4.11. Angular position is defined as the angle between the long axis and line connecting the centers of the male pronucleus and embryo, depicted in Figure 4.2a. t = 0 s denotes end of posteriorisation.

Angular positions (deg)	Posteriorisation velocity (1×10^{-1} µm/s)	No. of embryos
0–3	−0.15 (−0.18,−0.13)	37
3–6	−0.17 (−0.20,−0.14)	36
6–9	−0.27 (−0.30,−0.23)	31
9–12	−0.40 (−0.46,−0.35)	27
12–15	−0.46 (−0.52,−0.41)	20
15–18	−0.40 (−0.47,−0.34)	16
18–21	−0.49 (−0.58,−0.40)	13
21–24	−0.85 (−0.98,−0.72)	10
24–27	−1.12 (−1.26,−0.97)	8

Table 4.2: Posteriorisation velocity measured for each angular position bin in unperturbed embryos. Average posteriorisation velocity along with 95% confidence interval for the average are reported.

on this observation, it is concluded here that the rate of AP axis alignment is faster at higher angular positions: the male pronucleus moves faster towards the posterior end the further away from the posterior end it is.

Cortical flows are also measured in unperturbed embryos using the methodology described in section 3.4. Average cortical flow speed of 4.12 ± 0.59 µm/min is observed in unperturbed embryos. Average cortical flow fields are calculated by averaging over all embryos – obtaining the average flow field as a function of position of the cortex and time relative to end of posteriorisation (Figure 4.6). Average cortical flows fields for each angular position bin are also calculated by averaging over all frames in all embryos which have the corresponding angular position of the male pronucleus within said angular position bin (see section 3.5 and Figure 4.7). In the latter, it is observed that the point where the cortical flows change sign correlates with the angular position – which is expected from the role of the male pronucleus as the organiser of cortical flows during AP axis establishment, via the centrosomes associated with the male pronucleus. These observed cortical flows are later used by the model of AP axis alignment described in section 2.3 for calibration, to generate theoretical values of posteriorisation velocity as a function of angular positions – see subsection 4.3.2.

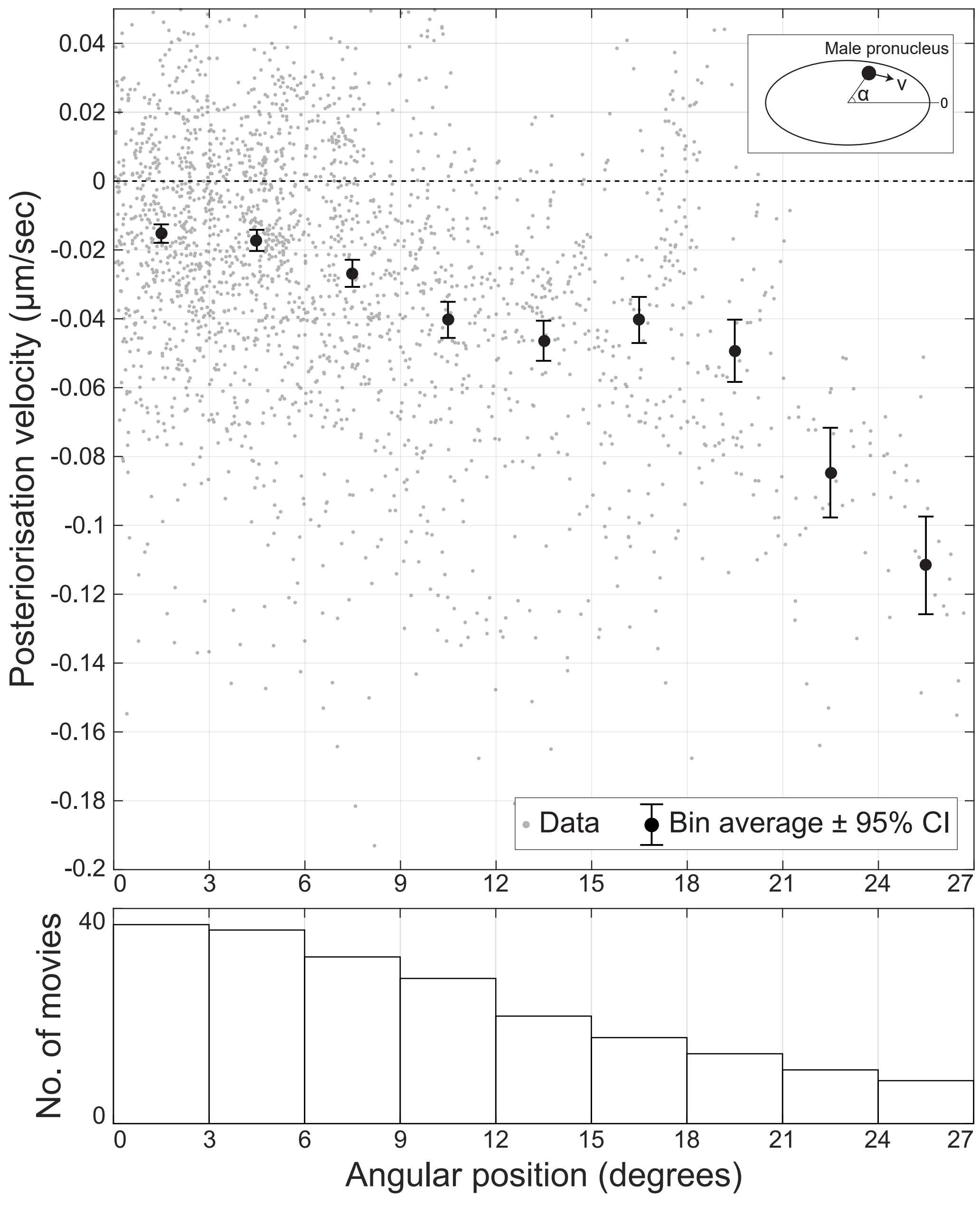

Figure 4.3: Top: Posteriorization velocity of the male pronucleus (along y-axis, in µm/s) plotted against its angular position, in unperturbed embryos of SWG070 strain (N = 57). Negative values of the posteriorisation velocity indicate movement towards the posterior end. Angular position is binned using a bin width of 3 deg. Black circles with errors bars denote the average posteriorization velocity with 95% confidence intervals in each angular position bin. Grey circles represent the data scatter – the measured posteriorization velocities for different angular positions in each embryo (see subsection 3.4.2). Bottom: Histogram of the number of movies (along y-axis) contributing to each angular position (along x-axis) bin. A movie is considered to contribute to an angular position bin if it has any frames with angular positions within that bin. Note that a movie can contribute to multiple bins, as it may contain frames spanning different angular positions.

4.2 Cortical flows are required for AP axis alignment

As discussed in section 1.4, cortical flows play an important role in proper AP axis establishment. A prime question to ask then is if cortical flows also play a role in AP axis alignment. The role of cortical flows in AP axis alignment could be understood by observing posteriorisation of the male pronucleus in embryos with impaired cortical flows. To generate embryos with reduced cortical flow velocity, RNAi of *mlc-4* on worms of SWG070 strain was performed for a feeding time of 24 hours (see section 3.2 for details on RNAi). MLC-4 is a conserved regulatory light chain present in NMY-2, and is required for the NMY-2 myosin motor to function [200]. Cortical flows were found to be indeed reduced in *mlc-4* RNAi embryos – an average cortical flow speed of 1.45 ± 0.30 µm/min in *mlc-4* RNAi embryos compared to 4.12 ± 0.59 µm/min in unperturbed control embryos was observed.

Next, AP axis alignment in the *mlc-4* RNAi embryos – in which cortical flows are impaired – is investigated. Specifically, the posteriorisation of the male pronucleus is quantified as described before – see Figure 4.8 and Figure 4.9. The male pronucleus in *mlc-4* RNAi embryos was manually tracked instead of being tracked using the image analysis pipeline described in section 3.4. Posteriorisation of the male pronucleus was observed to be suppressed in these *mlc-4* RNAi embryos: from 7 out of 10 RNAi embryos in which the male pronucleus has an initial angular position greater than 5 deg, all were observed to fail to posteriorise – see Figure 4.8. Furthermore, almost no change is observed in angular position of the male pronucleus in RNAi embryos over time. Fitting the exponential $\alpha = \alpha_0 + \exp\left(-\frac{t}{t_0}\right)$ to the plotted angular positions, as done for unperturbed embryos, results in a fit that does not converge. Instead, the best fit is found for the constant function $\alpha = \alpha_0$ with $\alpha_0 = 5.45 \pm 0.43$ deg (see Figure 4.8). Thus the migration of the male pronucleus is heavily suppressed in *mlc-4* RNAi embryos. Such an observation is strengthened by the very slow posteriorisation velocity observed in *mlc-4* RNAi embryos (see Figure 4.9 and Table 4.4) compared to those observed in unperturbed embryos (compare Figure 4.3 and Table 4.2). Altogether, these observations lead to the conclusion that cortical flows are essential for posteriorisation of the male pronucleus, and thus AP axis alignment.

Experimental Condition	Strain	Avg. cortical flow speed (µm/min)
Unperturbed	SWG070	4.12 ± 0.59
mlc-4 RNAi	SWG070	1.45 ± 0.30
nop-1 RNAi	SWG070	2.89 ± 0.65
nop-1; mel-11 RNAi	SWG070	3.34 ± 0.52
ima-3 RNAi	SWG070	3.99 ± 0.51
air-1 RNAi	SWG070	3.04 ± 0.84
Unperturbed	SWG057	2.84 +- 0.37
goa-1; gpa-16 RNAi	SWG057	2.62 +- 0.52

Table 4.3: Cortical flow speeds measured in different experimental conditions described in chapter 4. Average cortical flow speeds ± standard deviation are reported.

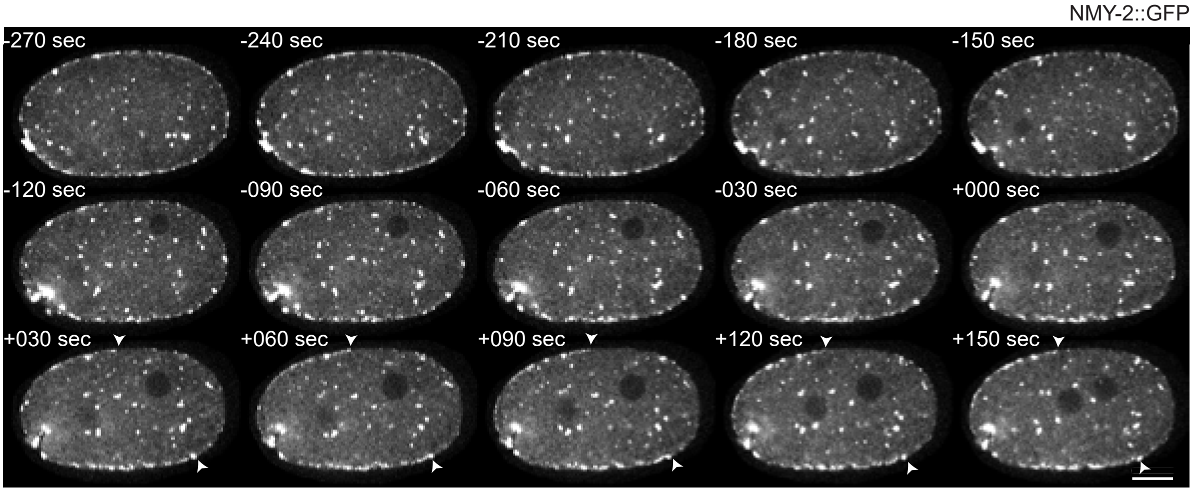

Figure 4.4: Representative *mlc-4* RNAi embryo of SWG070 strain, labelled with NMY-2::GFP (white), showing that male pronucleus does not posteriorise in *mlc-4* RNAi embryos, where cortical flows are impaired. White arrows denote the depletion of myosin at the pPARs domain, which does not re-orient towards the posterior end even after t = 0 s. The male pronucleus can be visualized as the dark circle in the myosin channel towards the posterior end (right). t = 0 s is set at the end of posteriorisation of the male pronucleus – as syncronised with the movies from unperturbed embryos of SWG070 strain. Scale bar: 10 µm. Images are rotated such that anterior and posterior ends are to the left and right respectively.

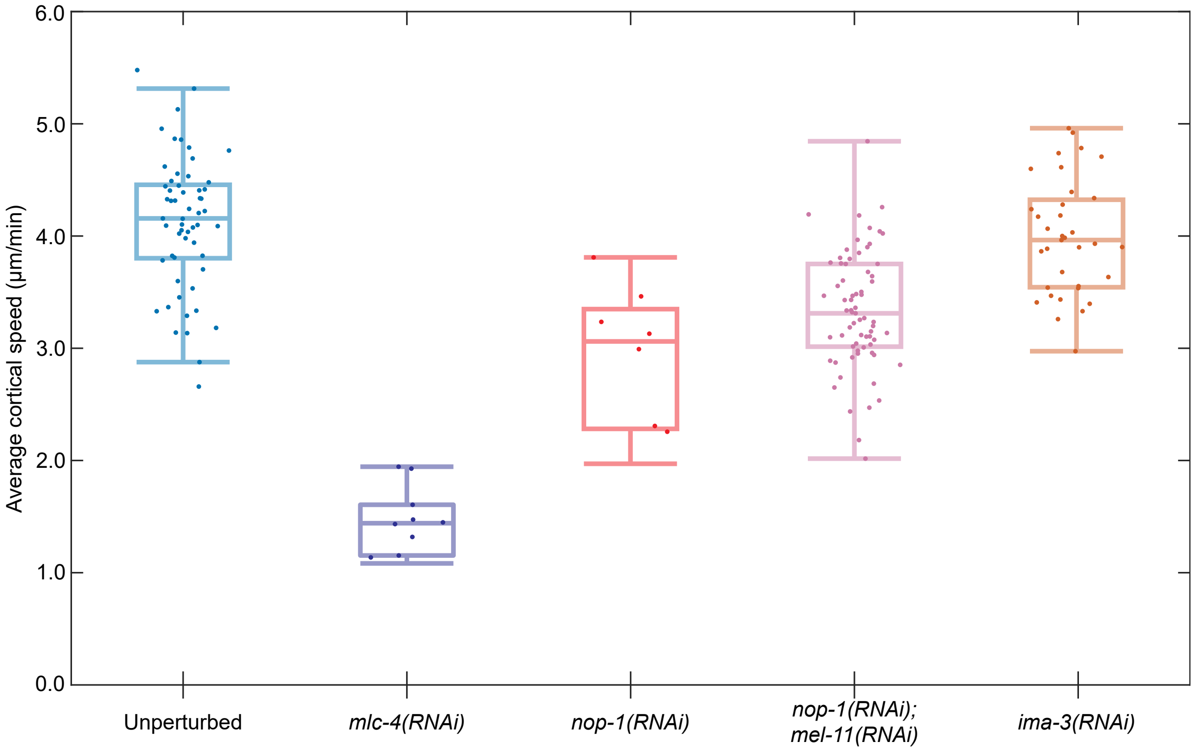

Figure 4.5: Average cortical flow speeds observed in different experimental conditions. Cortical flow speeds are averaged over all positions at all times for all embryos in given experimental condition. Also see Table 4.3

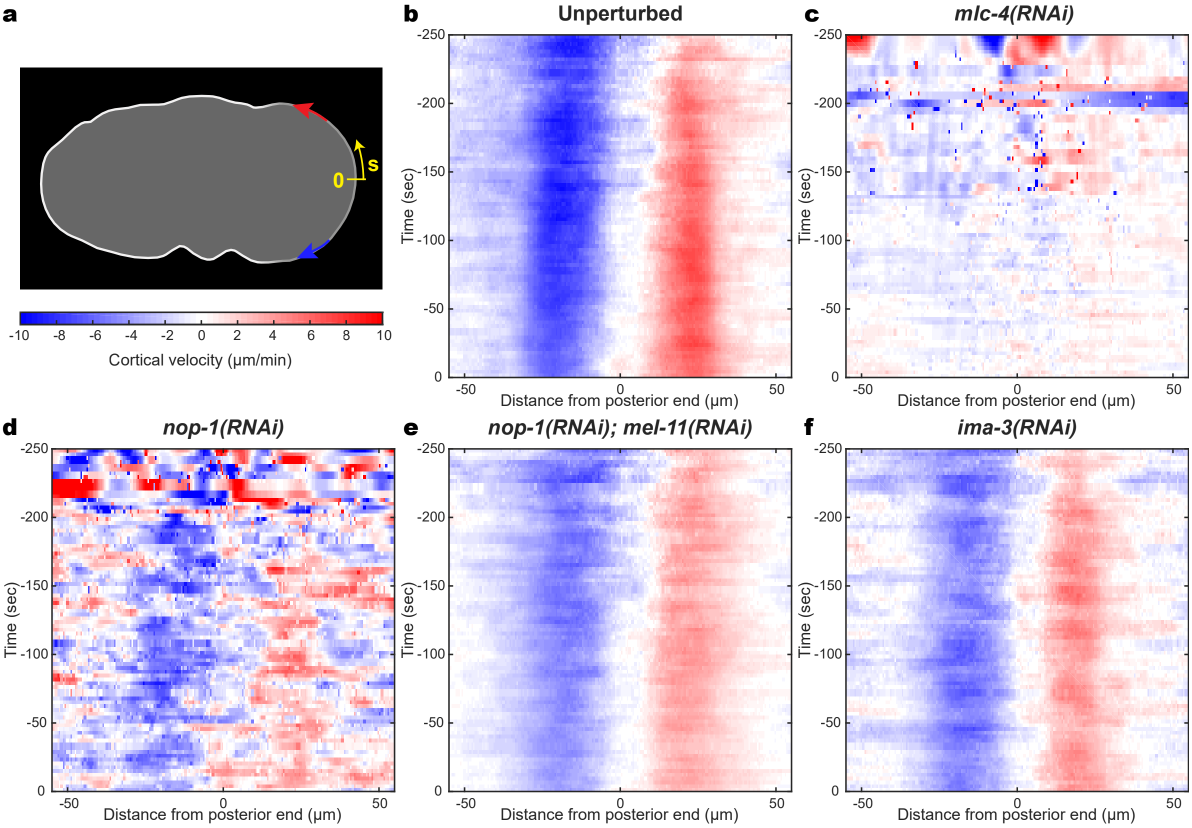

Figure 4.6: Average cortical flow velocity (color, in µm/min) plotted as a function of time (along y-axis, in s, t = 0 s denotes end of posteriorization) and position on the cortex (along x-axis, in µm, s=0 µm denotes posterior end), as observed in different experimental conditions. Average cortical flow velocity at a given time and position on the cortex is obtained by averaging over cortical flows measured in all embryos at the given time and position on the cortex – see section 3.5. a) Schematic. s denotes the position on the cortex, as measured along the arclength of the cortex from the posterior end (s=0 µm). Distances in the anti-clockwise direction are considered positive. Color bar maps the colors in the plots to cortical velocity in µm/min. Red shades indicates cortical flow pointing in the anti-clockwise direction (i.e. along the increasing direction of s, denoted as positive flow velocity), and blue shades in the clockwise direction (denoted as negative flow velocity). Cortical flows for (b) unperturbed embryos (N = 57), (c) *mlc-4* RNAi embryos (N = 10), (d) *nop-1* RNAi embryos (N = 9), (e) *nop-1; mel-11* RNAi embryos (N = 69), and (f) *ima3* RNAi embryos (N = 35) are plotted – all from SWG070 strain.

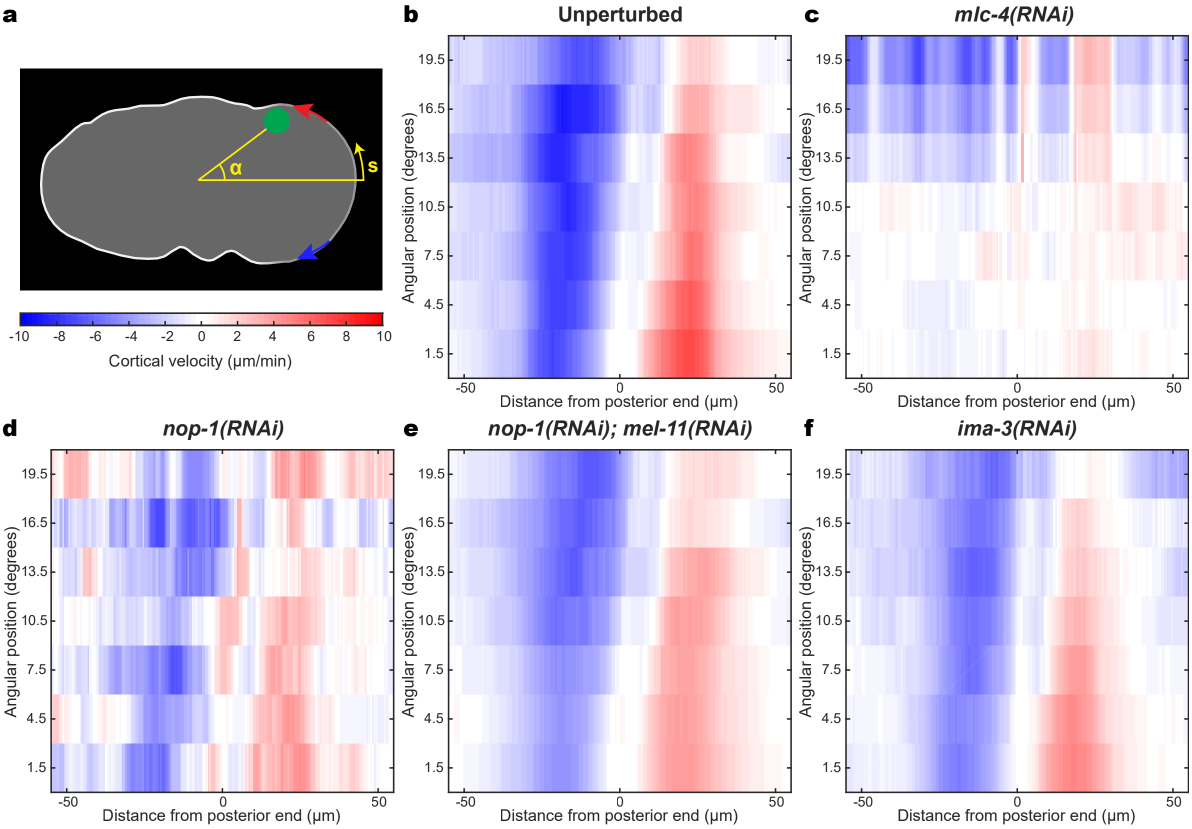

Figure 4.7: Average cortical flow velocity (color, in µm/min) plotted as a function of angular position of the male pronucleus (along y-axis, in deg) and position on the cortex (along x-axis, in µm, s=0 µm denotes posterior end), as observed in different experimental conditions. Angular positions are binned with bin width 3 deg. Average cortical flow velocity at a given angular position bin of the male pronucleus and position on the cortex is obtained by averaging over all frames that have the corresponding angular position lie in the given angular position, at the given position on the cortex – see section 3.5. a) Schematic. s denotes the position on the cortex, as measured along the arclength of the cortex from the posterior end (s=0 µm). Distances in the anti-clockwise direction are considered positive. α denotes the angular position of the male pronucleus. Color bar maps the colors in the plots to cortical velocity in µm/min. Red shades indicates cortical flow pointing in the anti-clockwise direction (i.e. along the increasing direction of s, denoted as positive flow velocity), and blue shades in the clockwise direction (denoted as negative flow velocity). Cortical flows for (b) unperturbed embryos (N = 57), (c) *mlc-4* RNAi embryos (N = 10), (d) *nop-1* RNAi embryos (N = 9), (e) *nop-1; mel-11* RNAi embryos (N = 69), and (f) *ima3* RNAi embryos (N = 35) are plotted – all from SWG070 strain.

Angular positions (deg)	Posteriorisation velocity (1×10^{-1} µm/s)	No. of embryos
0–3	−0.03 (−0.08,0.01)	4
3–6	−0.02 (−0.01,0.05)	5
6–9	−0.02 (−0.07,0.03)	3
9–12	−0.02 (−0.07,0.02)	2
12–15	−0.3 (−0.4,−0.17)	1

Table 4.4: Posteriorisation velocity measured for each angular position bin in *mlc-4* RNAi embryos. Average posteriorisation velocity along with 95% confidence interval for the average are reported.

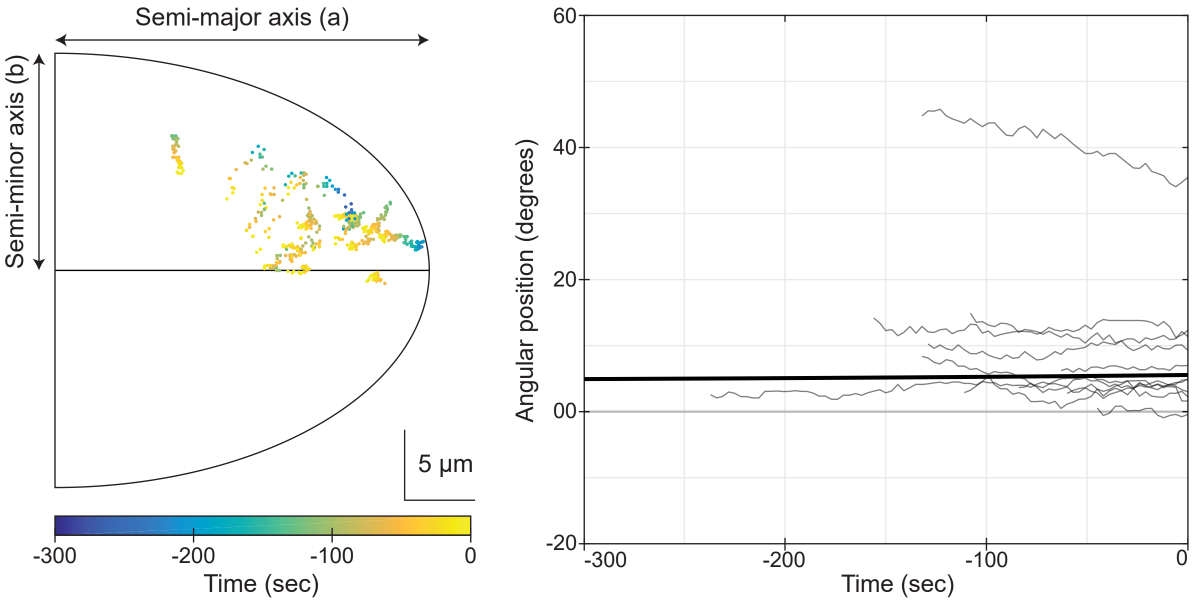

(a) Trajectories of the male pronucleus (denoted by the coordinates of its center) observed in *mlc-4* RNAi embryos. Color represents time. x- and y-axes lie along the long and short axes of an ellipse with semi-major axis $a = 26.40\,\mu\text{m}$ and semi-minor axis $b = 16.10\,\mu\text{m}$. Scale bar: 5 µm

(b) Angular position of the male pronucleus (on y-axis, in deg) plotted as a function of time (on x-axis, in s), in *mlc-4* RNAi embryos. Thin grey lines represent individual trajectories, thick black line represents a constant fit to the average of these tracks: $\alpha = \alpha_0$, with $\alpha_0 = 5.45 \pm 0.43\,\text{deg}$. Note that the fit excludes the outlier trajectory around 30 deg – however including the trajectory in the exponential or the constant fit does not qualitatively change the result.

Figure 4.8: Experimentally observed trajectories of the male pronucleus during posteriorisation in *mlc-4* RNAi embryos of SWG070 strain (N = 10). Male pronucleus is manually tracked in *mlc-4* RNAi embryos. Average semi-major and semi-minor axes lengths for *mlc-4* RNAi embryos of SWG070 strain are used in Figure 4.8a – see Table 4.11. Angular position is defined as the angle between the long axis and line connecting the centers of the male pronucleus and embryo. t = 0 s denotes end of posteriorisation.

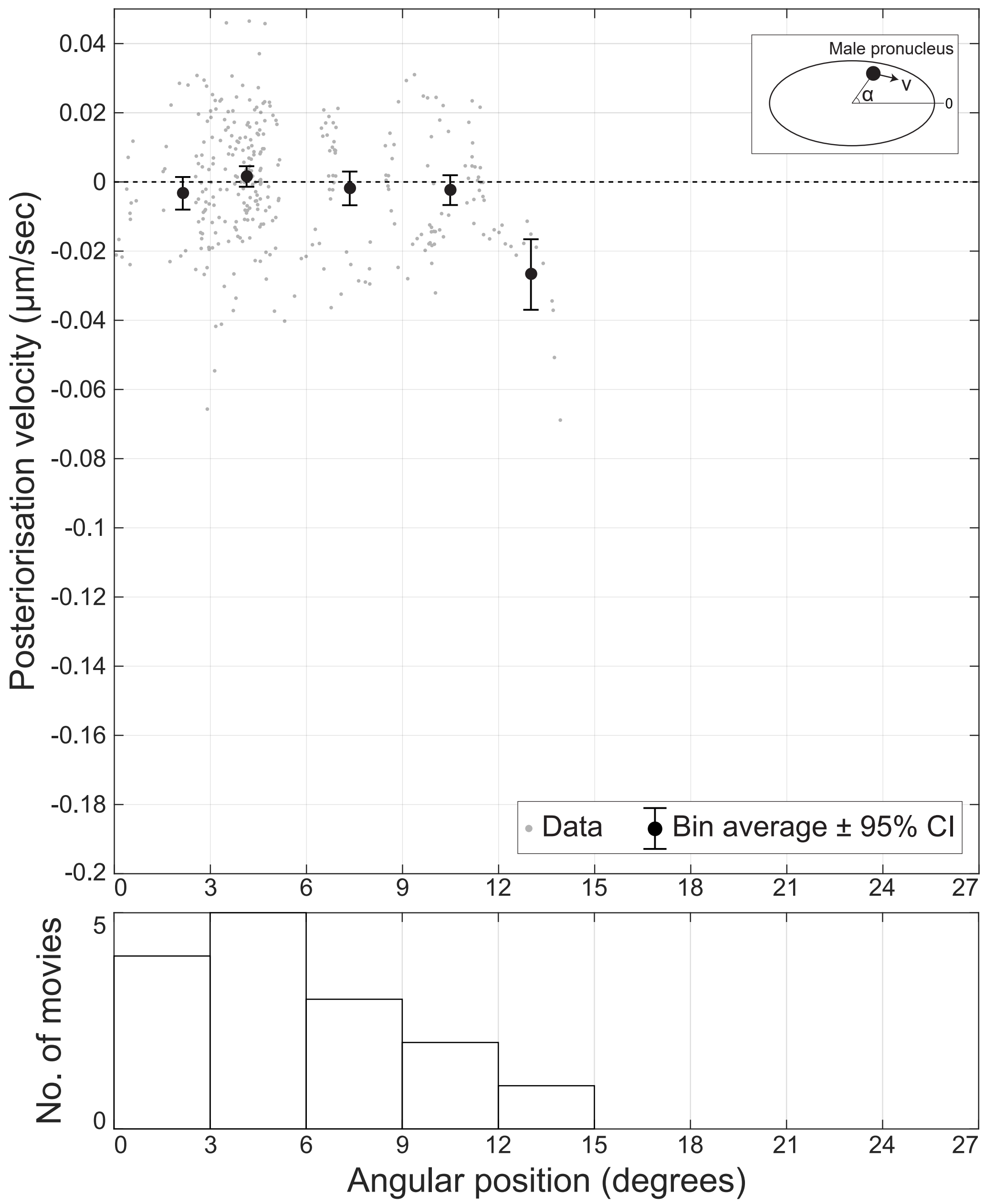

Figure 4.9: Top: Posteriorization velocity of the male pronucleus (along y-axis, in μm/s) plotted against its angular position, in *mlc-4* RNAi embryos of SWG070 strain (N = 10). Negative values of the posteriorisation velocity indicate movement towards the posterior end. Angular position is binned with bin width of 3 deg. Black circles with errors bars denote average posteriorization velocity with 95% confidence intervals in each angular position bin. Grey circles represent data scatter – measured posteriorization velocities for different angular positions in each embryo (calculated as described in subsection 3.4.2 after manual tracking). Bottom: Histogram of the number of movies (along y-axis) contributing to each angular position (along x-axis) bin. A movie contributes to an angular position bin if it has any frames with angular positions within that bin. Note that a movie can contribute to multiple bins, as it may contain frames spanning different angular positions. Data was only available until 15 deg

4.3 Role of Pseudocleavage furrow in AP axis alignment

As discussed in subsection 1.4.3, cortical flows during AP axis establishment can lead to two consequences – flows within the bulk cytoplasm [137] and formation of the pseudocleavage furrow [88]. Two different mechanisms of AP axis alignment – cytoplasmic flow-dependent mechanism and pseudocleavage furrow-dependent mechanism – that arise from each of the two consequence were discussed in subsection 1.4.3. In this section, the contributions of these two mechanisms is evaluated using experiments that remove the pseudocleavage furrow and corresponding numerical simulations of the theoretical model described in section 2.3.

4.3.1 Removing Pseudocleavage furrow via RNAi

To understand the role of the pseudocleavage furrow-dependent mechanism in AP axis alignment, posteriorisation of the male pronucleus was quantified in embryos lacking a pseudocleavage furrow. Such embryos were generated via RNAi of *nop-1* on worms of SWG070 strain for a feeding time of 24 hours (see section 3.2 for details on RNAi). NOP-1 modulates activity of the small GTPase RHO-1, which is a major regulator of the activity of the actomyosin cortex in the *C. elegans* embryo [169]. Embryos generated by worms which are mutant for NOP-1 (that is, possess a non-functional form of NOP-1) have been observed to lack a pseudocleavage furrow [165]. While it was observed that *nop-1* RNAi embryos do indeed lack a pseudocleavage furrow (8 out of 9 embryos), these embryos also showed reduced cortical flow speeds, with average cortical flow speed of $2.89 \pm 0.65\,\mu\text{m/min}$ in *nop-1* RNAi embryos compared to $4.12 \pm 0.59\,\mu\text{m/min}$ observed in unperturbed embryos (see Table 4.3, Figure 4.5, Figure 4.6 and Figure 4.7).

To generate pseudocleavage furrow-deficient embryos with cortical flows comparable to those observed in unperturbed embryos (which do possess a pseudocleavage furrow), a double RNAi of *nop-1* and *mel-11* was performed on worms of SWG070 strain for a feeding time of 24 hours (see section 3.2 for details on double RNAi). MEL-11 is a myosin phosphatase [201] that suppresses the activity of myosin in the cortex [202]. The *nop-1; mel-11* RNAi embryos thus generated lack a pseudocleavage furrow (69 out of 69 embryos). Furthermore, experimental measurement of cortical flows in *nop-1; mel-11* RNAi embryos yields average cortical flow speed of $3.34 \pm 0.52\,\mu\text{m/min}$ in *nop-1; mel-11* RNAi embryos, comparable to the average cortical flow speed $4.12 \pm 0.59\,\mu\text{m/min}$ observed in unperturbed embryos (see Table 4.3, Figure 4.5, Figure 4.6 and Figure 4.7). Thus, the double RNAi of *nop-1* and *mel-11* leads to the required pseudocleavage furrow-deficient embryos with cortical flows comparable to those observed in unperturbed embryos.

Next, the AP axis alignment process in these *nop-1; mel-11* RNAi embryos – which lack a pseudocleavage furrow – is investigated. Specifically, the posteriorisation of the male pronucleus is quantified as described before – see Figure 4.11 and Figure 4.12, using the image analysis pipeline described in section 3.4. Angular positions in the pseudocleavage furrow-deficient embryos were generally observed to decrease towards 0 deg as time reaches closer to end of posteriorisation ($t = 0\,\text{s}$), albeit at a slower rate compared to that observed for unperturbed embryos (Figure 4.11). Specifically, this decay towards 0 deg was quantified by fitting an exponential $\alpha = \alpha_0 + \exp\left(-\frac{t}{t_0}\right)$ to the plotted angular positions, yielding a time constant $t_0 = 201 \pm 24\,\text{s}$ and $\alpha_0 = -0.75 \pm 0.30\,\text{deg}$ (Figure 4.11). Note that the time constant

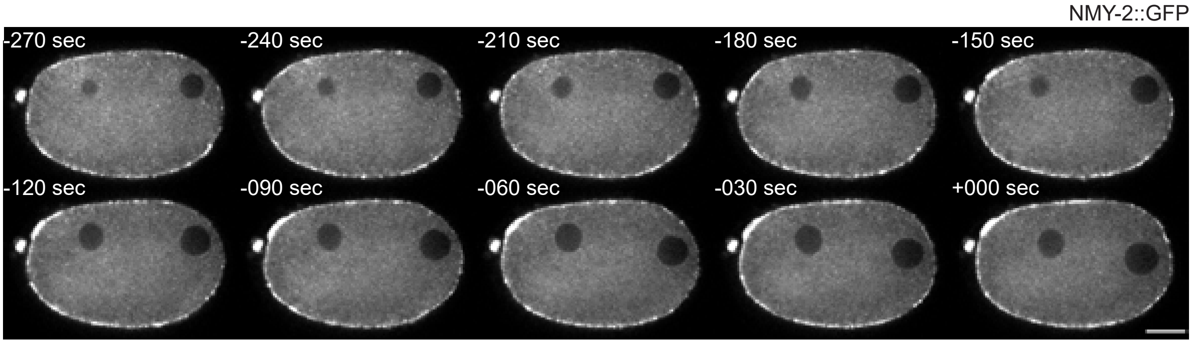

(a) Representative *nop-1* RNAi embryo of SWG070 strain, labelled with NMY-2::GFP (white), showing the lack of pseudocleavage furrow in *nop-1* RNAi embryos.

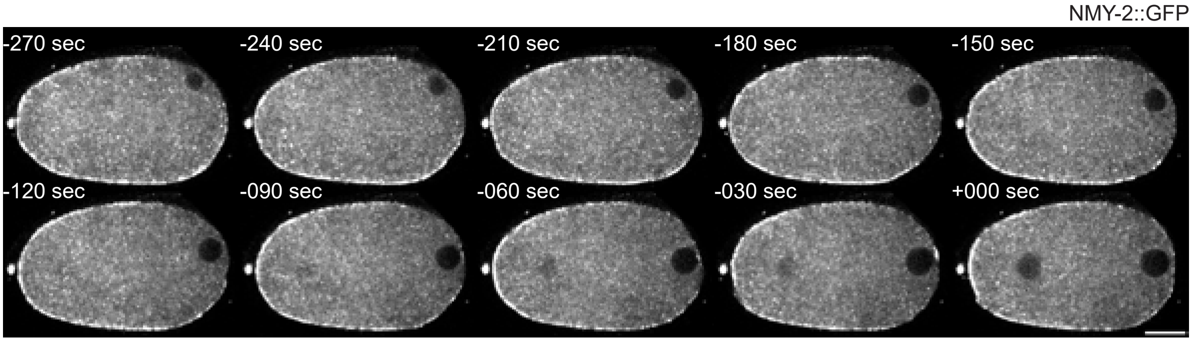

(b) Representative *nop-1; mel-11* double RNAi embryo of SWG070 strain, labelled with NMY-2::GFP (white), showing the lack of pseudocleavage furrow in *nop-1; mel-11* RNAi embryos.

Figure 4.10: Representative *nop-1* RNAi embryo and *nop-1; mel-11* double RNAi embryo of SWG070 strain, labelled with NMY-2::GFP (white), showing the lack of pseudocleavage furrow in both *nop-1* RNAi and *nop-1; mel-11* RNAi embryos. Compare to representative unperturbed embryo depicted in Figure 4.1 and pseudocleavage furrow depicted in Figure 1.8. The male pronucleus can be visualized as the dark circle in the myosin channel towards the posterior end. $t = 0\,\mathrm{s}$ is set at the end of posteriorisation of the male pronucleus. Scale bar: 10 µm in each. Images are rotated such that anterior and posterior ends are to the left and right respectively.

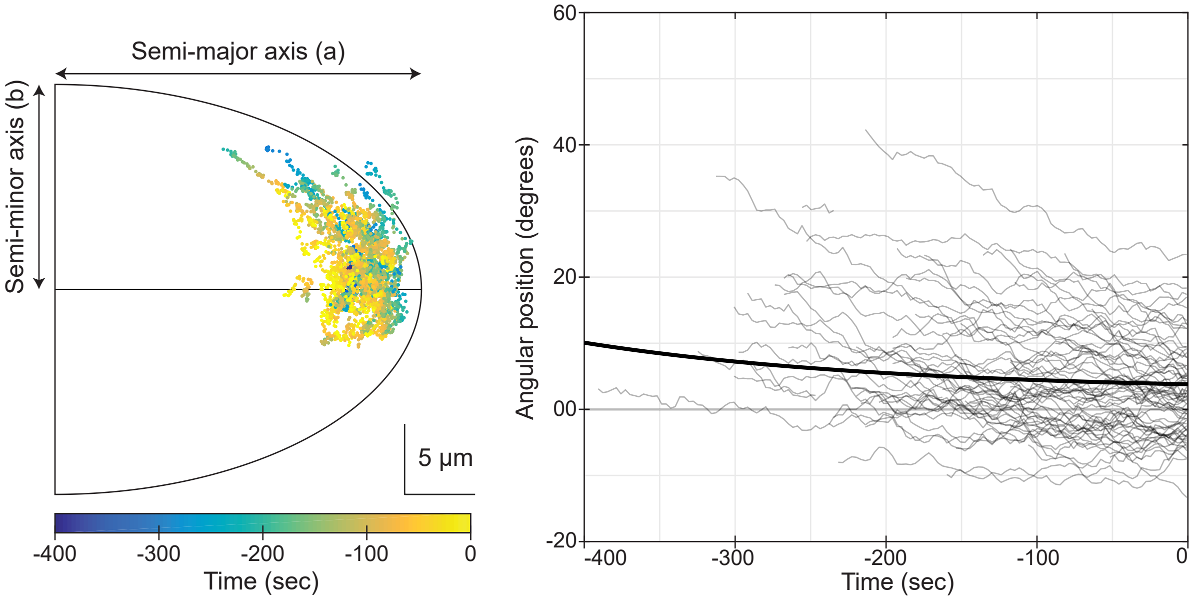

(a) Trajectories of the male pronucleus (denoted by the coordinates of its center) observed in *nop-1; mel-11* RNAi embryos. Color represents time. x- and y-axes lie along the long and short axes of an ellipse with semi-major axis $a = 26.4\,\mu\text{m}$ and semi-minor axis $b = 16.1\,\mu\text{m}$. Scale bar: 5 µm

(b) Angular position of the male pronucleus (on y-axis, in deg) plotted as a function of time (on x-axis, in s), in *nop-1; mel-11* RNAi embryos. Thin grey lines represent individual trajectories, thick black line represents a exponential fit to the average of these tracks: $\alpha = \alpha_0 + \exp\left(-\frac{t}{t_0}\right)$, with $t_0 = 201 \pm 24\,\text{s}$ and $\alpha_0 = -0.75 \pm 0.30\,\text{deg}$.

Figure 4.11: Experimentally observed trajectories of the male pronucleus during posteriorisation in *nop-1; mel-11* embryos of SWG070 strain (N = 69). See subsection 3.4.2 for details on male pronucleus tracking. Average semi-major and semi-minor axes lengths for *nop-1; mel-11* embryos of SWG070 strain are used in Figure 4.11a – see Table 4.11. Angular position is defined as the angle between the long axis and line connecting the centers of the male pronucleus and embryo. t = 0 s denotes end of posteriorisation.

$t_0 = 201 \pm 24\,\text{s}$ for the pseudocleavage furrow-deficient embryos is larger than that found for the unperturbed embryos $t_0 = 119 \pm 3\,\text{s}$ – indicating a slower posteriorisation of the male pronucleus in the pseudocleavage furrow-deficient embryos compared to that observed in unperturbed embryos.

Posteriorisation velocity of the male pronucleus in the pseudocleavage furrow-deficient embryos, plotted as a function of angular position (see section 3.5 for details on binning of angular positions), demonstrate that the male pronucleus is, on average, moving towards the posterior end (as indicated by the negative sign of the velocity) – with higher speed at higher angular positions (Figure 4.12, Table 4.5). This is qualitatively similar to the observations made for the unperturbed embryos (Figure 4.3, Table 4.2). However, on comparison with the posteriorisation velocity observed in the latter, it is observed that the posteriorisation velocity of the male pronucleus observed in the pseudocleavage furrow-deficient embryos are consis-

Angular positions (deg)	Posteriorisation velocity (1×10^{-1} µm/s)	No. of embryos
0–3	−0.10 (−0.12,−0.08)	37
3–6	−0.14 (−0.17,−0.11)	36
6–9	−0.14 (−0.17,−0.11)	29
9–12	−0.17 (−0.21,−0.13)	19
12–15	−0.17 (−0.21,−0.13)	19
15–18	−0.20 (−0.25,−0.16)	13
18–21	−0.20 (−0.25,−0.16)	12
21–24	−0.36 (−0.44,−0.29)	8
24–27	−0.10 (−0.15,−0.05)	3

Table 4.5: Posteriorisation velocity measured for each angular position bin in *nop-1; mel-11* RNAi embryos. Average posteriorisation velocity along with 95% confidence interval for the average are reported.

tently slower that those observed in the unperturbed embryos, with larger difference between the two at higher angular positions.

Altogether, these experimental observations indicate that the rate of AP axis alignment is diminished in the absence of the pseudocleavage furrow. In other words, experimental removal of pseudocleavage furrow via a double *nop-1; mel-11* RNAi indicates that the pseudocleavage furrow is important for the dynamics of AP axis alignment, and to ensure the alignment of the AP axis at the rate observed in the unperturbed embryos. However, the pseudocleavage furrow is not essential for AP axis alignment – embryos deficient in the pseudocleavage furrow can still exhibit AP axis alignment, albeit at a slower rate.

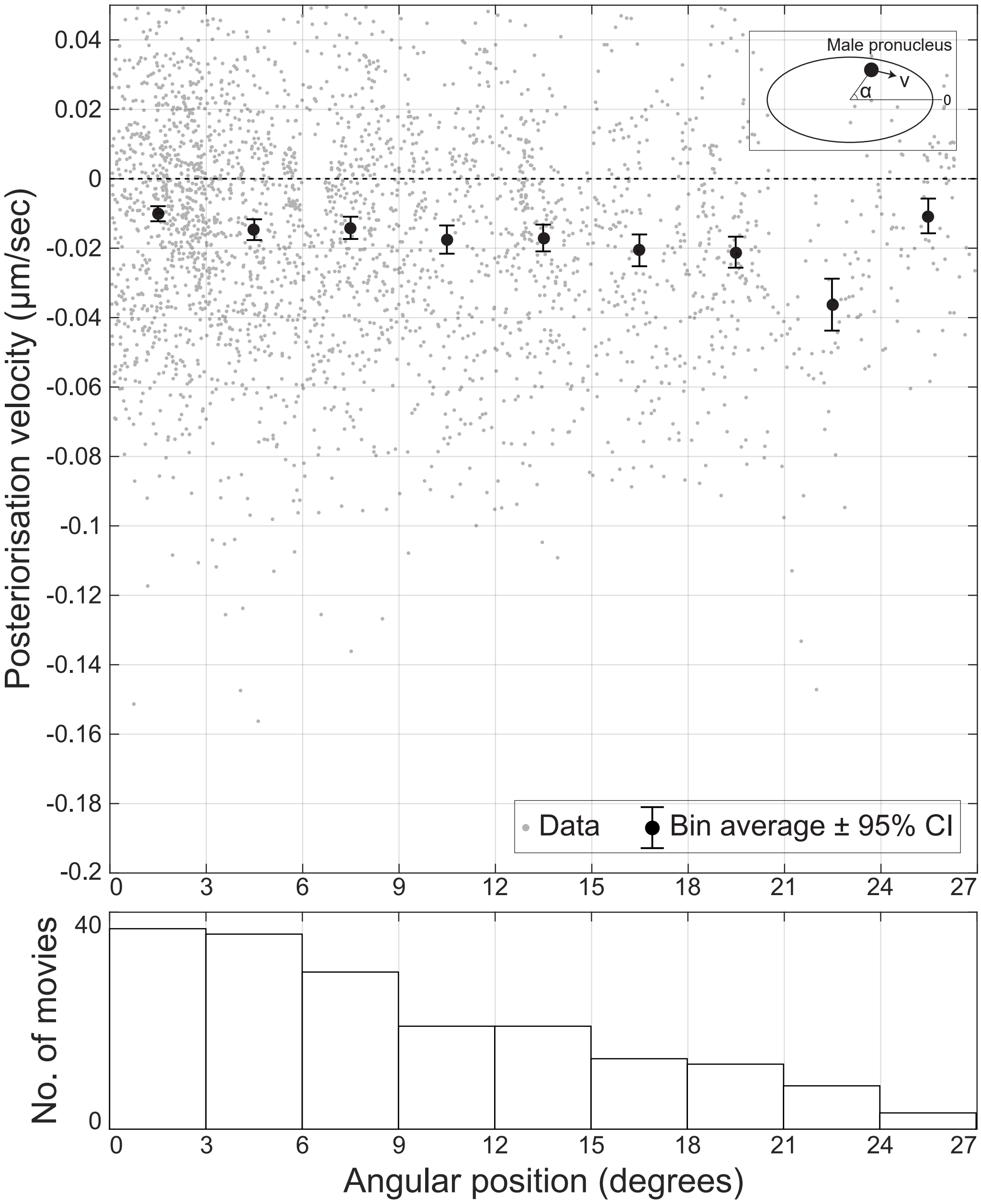

Figure 4.12: Top: Posteriorization velocity of the male pronucleus (along y-axis, in µm/s) plotted against its angular position, in *nop-1; mel-11* RNAi embryos of SWG070 strain (N = 69). Negative values of the posteriorisation velocity indicate movement towards the posterior end. Angular position is binned using a bin width of 3 deg. Black circles with errors bars denote the average posteriorization velocity with 95% confidence intervals in each angular position bin. Grey circles represent the data scatter – the measured posteriorization velocities for different angular positions in each embryo (see subsection 3.4.2). Bottom: Histogram of the number of movies (along y-axis) contributing to each angular position (along x-axis) bin. A movie is considered to contribute to an angular position bin if it has any frames with angular positions within that bin. Note that a movie can contribute to multiple bins, as it may contain frames spanning different angular positions.

4.3.2 Comparing numerical simulations to experimental results

Theoretical model accounts for AP axis alignment in unperturbed controls

To further probe the role of the pseudocleavage furrow in AP axis alignment, these experimental observations are compared to numerical simulations of the theoretical model of AP axis alignment. As described in section 2.3 and subsection 1.4.3, the theoretical model considers two possible mechanisms of AP axis alignment: cytoplasmic flow-dependent mechanism, and pseudocleavage furrow-dependent mechanism. Comparisons of experimental observations in unperturbed embryos – which possess a pseudocleavage furrow – and *nop-1; mel-11* RNAi embryos – which lack a pseudocleavage furrow with numerical simulations of the theoretical model could then yield insights into the contributions of the two mechanisms to AP axis alignment.

First, the theoretical model is compared with observations in the unperturbed embryo. Specifically, posteriorisation velocity of the male pronucleus as a function of its angular position, and the trajectory of the male pronucleus (that is, angular position as a function of time) are calculated (see section 2.3 for details) using the full theoretical model – that is, including the pseudocleavage furrow-dependent mechanism, as unperturbed embryos possess a pseudocleavage furrow. Quantities calculated from the the theoretical model are then compared to those observed in the experiments with unperturbed embryos.

Numerical simulations of the theoretical model requires calibration of model parameters using the experimentally measured cortical flows. Note that the model is evaluated (in this section) on an ellipsoid with the same axes lengths as the average axes lengths for the unperturbed embryos: $a = 28.9\,\mu\mathrm{m}$ (semi-major axis), $b = 16.4\,\mu\mathrm{m}$ – see Table 4.11. In brief, the calibration procedure varies the following model parameters: hydrodynamic length λ_H, active force relaxation λ_A and nematic stress relaxation λ_N. Cortical flows calculated using the varied parameters are then compared to those experimentally measured. This is done for a range of angular positions of the male pronucleus, using the average cortical flows observed for angular position bin (with bin width of 3 deg, shown in Figure 4.7 – see section 3.5 for details on methodology). Angular positions upto 21 deg only are considered for the calibration procedure, due to worse quality of data for higher angular positions as the number of movies contributing to those angular position bins decreases. The calibration procedure results in values of λ_H, λ_A and λ_N that ensure best match with experimentally measured cortical flows. A detailed discussion on the calibration process can be found in subsection 2.3.3.

For the experimentally measured cortical flows in unperturbed embryos, the calibration procedure yields the following model parameters: $\lambda_H = 10\,\mu\mathrm{m}$, $\lambda_A = 11.5\,\mu\mathrm{m}^2\,\mathrm{s}^{-1}$, $\lambda_N = 152.5\,\mu\mathrm{m}^2\,\mathrm{s}^{-1}$ – see Figure 4.13. In the theoretical model, bulk cytoplasmic flows are determined uniquely from the calculated cortical flows via the no-slip boundary condition (see subsection 2.3.2). Comparison of experimentally measured cortical and cytoplasmic flows (see subsection 3.4.3 and subsection 3.4.4 for methodology) with calculated cortical and cytoplasmic flows shows a good agreement between the two – see Figure 4.13 and Figure 4.14. Thus, the theoretical model can faithfully recapitulate the experimental cortical and cytoplasmic flows, for the selected set of model parameters.

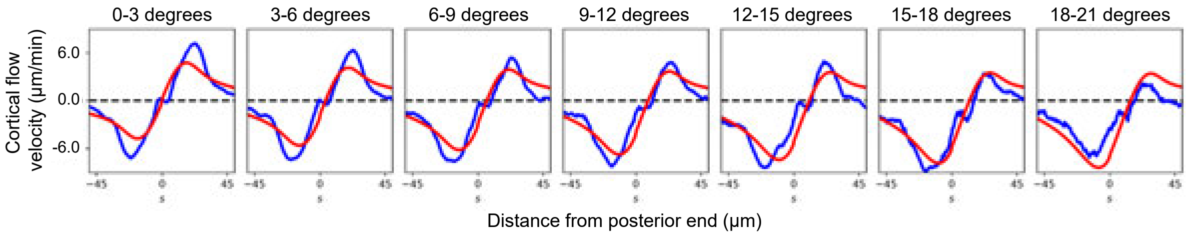

Figure 4.13: Comparison of observed cortical flows in unperturbed embryos of SWG070 strain to those calculated by the theoretical model of AP axis alignment. Blue line denotes the average cortical flow velocity observed in unperturbed embryos, plotted as a function of position along the cortex s in each angular position bin – also depicted in Figure 4.7. Red denotes the cortical flow velocity calculated by the theoretical model after calibration, with model parameters: $\lambda_H = 10\,\mu\mathrm{m}$, $\lambda_A = 11.5\,\mu\mathrm{m}^2\,\mathrm{s}^{-1}$, $\lambda_N = 152.5\,\mu\mathrm{m}^2\,\mathrm{s}^{-1}$.

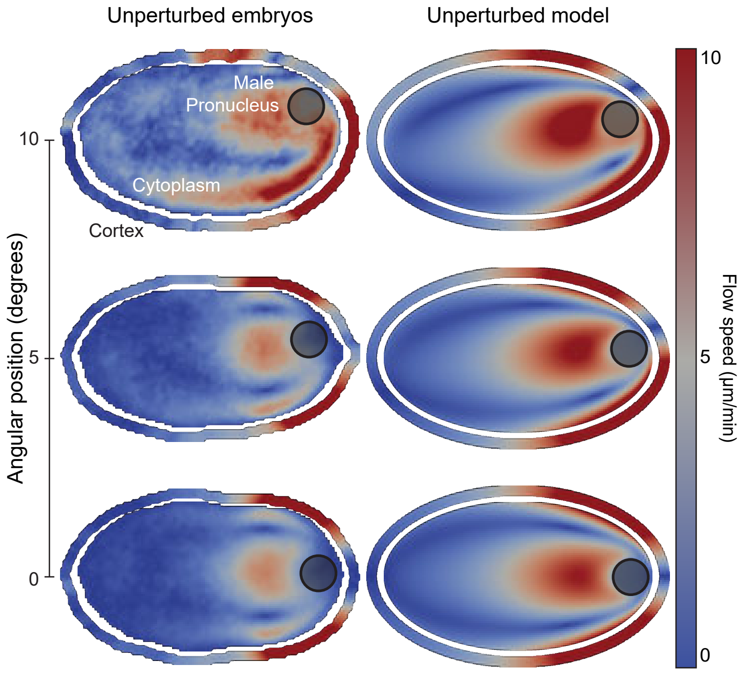

Figure 4.14: Comparison of observed cortical and cytoplasmic flows in unperturbed embryos of SWG070 strain (left) to those calculated by the theoretical model of AP axis alignment (right) with model parameters: $\lambda_H = 10\,\mu\mathrm{m}$, $\lambda_A = 11.5\,\mu\mathrm{m}^2\,\mathrm{s}^{-1}$, $\lambda_N = 152.5\,\mu\mathrm{m}^2\,\mathrm{s}^{-1}$ (referred to as the unperturbed model), for three angular positions (0 deg, 5 deg, 10 deg) of the male pronucleus (black shaded circle).In each panel, ellipse interior represents cytoplasmic flows, and outer ellipse represents cortical flows. See colorbar for magnitude of flow velocities.

Angular positions (deg)	Experimental post. velocity (1×10^{-1} µm/s)	Calculated post. velocity (1×10^{-1} µm/s)
0–3	−0.15 (−0.18,−0.13)	−0.09
3–6	−0.17 (−0.20,−0.14)	−0.22
6–9	−0.27 (−0.30,−0.23)	−0.30
9–12	−0.40 (−0.46,−0.35)	−0.38
12–15	−0.46 (−0.52,−0.41)	−0.45
15–18	−0.40 (−0.47,−0.34)	−0.47
18–21	−0.49 (−0.58,−0.40)	−0.48
21–24	−0.85 (−0.98,−0.72)	−0.47

Table 4.6: Experimentally observed posteriorisation velocity for each angular position bin in unperturbed embryos compared with those calculated by the unperturbed model (theoretical model evaluated with model parameters: $\lambda_H = 10\,\mu\text{m}$, $\lambda_A = 11.5\,\mu\text{m}^2\,\text{s}^{-1}$, $\lambda_N = 152.5\,\mu\text{m}^2\,\text{s}^{-1}$, $d = 0.61$). Experimental Post. velocity: Average posteriorisation velocity along with 95% confidence interval for each angular position bin observed in unperturbed embryos (see Table 4.2 and Figure 4.3. Calculated Post. velocity: Posteriorisation velocity calculated at center of angular position bin by theoretical model with model parameters: $\lambda_H = 10\,\mu\text{m}$, $\lambda_A = 11.5\,\mu\text{m}^2\,\text{s}^{-1}$, $\lambda_N = 152.5\,\mu\text{m}^2\,\text{s}^{-1}$, $d = 0.61$.

Comparison of the experimentally observed posteriorisation velocity of the male pronucleus with those calculated using the model fix the final model parameter d. This parameter captures the direct interactions between the male pronucleus and the cortex (see subsection 2.3.2). For the set of model parameters obtained via calibration for the unperturbed embryos, $d = 0.61$ to ensure that the calculated posteriorisation velocity best match the observed posteriorization velocity as a function of angular position of the male pronucleus – see Figure 4.15a and Table 4.6. With these model parameters, the calculated posteriorisation velocity agrees with experimentally observed average posteriorisation velocity in unperturbed embryos, for angular positions upto 21 deg. For higher angular positions, average posteriorisation velocity observed in experiments is faster compared to calculated posteriorisation velocity for the same angular position. By integrating the calculated posteriorisation velocity (as a function of angular position), the calculated trajectory of the male pronucleus – referring to the calculated angular position of the male pronucleus as a function of time relative to end of posteriorisation – can also be obtained (see subsection 2.3.3), which is observed to agree well with the experimentally observed trajectories of the male pronucleus – see Figure 4.15b.

The sensitivity of the calculated posteriorisation velocity to the calibrated model parameters was also investigated. Specifically, λ_H and λ_N were separately varied to ±50% of their calibrated values – see Figure 4.16, Table 4.7 and Table 4.8. As discussed in subsection 2.3.3, λ_A scales with the cortical flow velocity, and therefore is set separately. Posteriorisation velocity of the male pronucleus is then calculated using the varied model parameters and then compared again to those experimentally measured in unperturbed embryos. It is observed that the calculated posteriorisation velocity still retain similar qualitative features as those experimentally measured in unperturbed embryos: Posteriorisation velocity calculated after model parameter variation remain comparable to the average posteriorisation velocity observed in

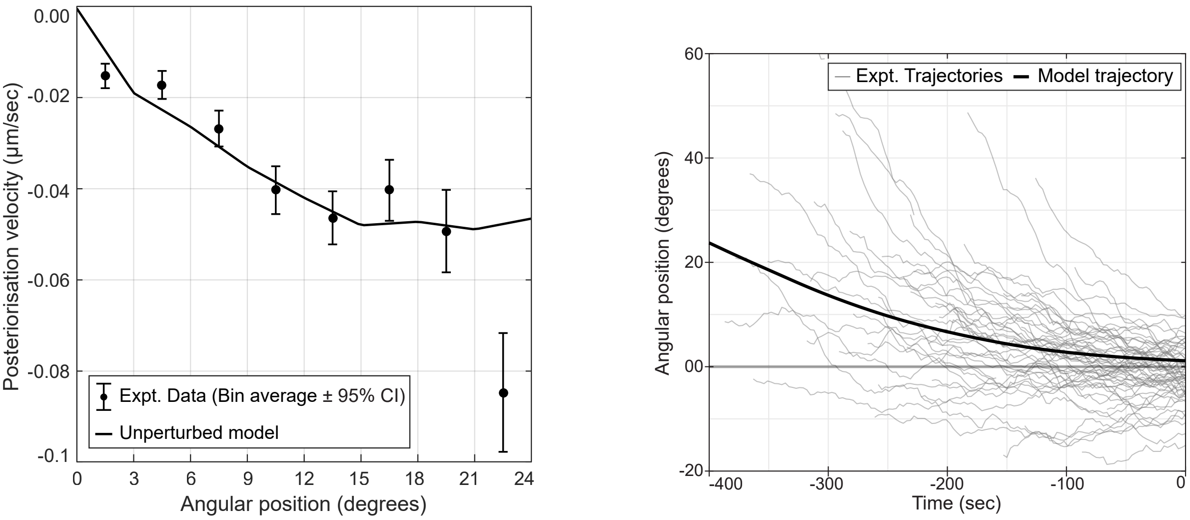

(a) Comparing average posteriorisation velocity of the male pronucleus (black circles with error bars, 95% confidence interval) in unperturbed embryos (from Figure 4.3) with that calculated by unperturbed model (black line), both plotted against angular position of the male pronucleus. Posteriorisation velocity is on y-axis (in µm/s, negative velocity indicate movement towards posterior end), and angular position on x-axis (in deg).

(b) Comparing angular positions of the male pronucleus (y-axis, in deg) observed in unperturbed embryos (thin grey lines, from Figure 4.2) with the calculated trajectory of the male pronucleus (thick black line) from unperturbed model, both plotted against time (on x-axis, in s, t = 0 s denotes end of posteriorisation).

Figure 4.15: Comparing experimentally observed posteriorisation of the male pronucleus in unperturbed embryos of the SWG070 strain with that calculated by the unperturbed model. Unperturbed model refers to the theoretical model of AP axis alignment evaluated with the following model parameters: $\lambda_H = 10\,\mu\text{m}$, $\lambda_A = 11.5\,\mu\text{m}^2\,\text{s}^{-1}$, $\lambda_N = 152.5\,\mu\text{m}^2\,\text{s}^{-1}$, $d = 0.61$. $d = 0.61$ is selected to best match the average posteriorisation velocity observed in unperturbed embryos of the SWG070 strain, depicted in Figure 4.15a.

Angular positions (deg)	Calculated posteriorisation velocity (1×10^{-1} µm/s)	
	$\lambda_H := 1.5\lambda_H$	$\lambda_H := 0.5\lambda_H$
0–3	−0.08	−0.11
3–6	−0.18	−0.25
6–9	−0.25	−0.34
9–12	−0.32	−0.43
12–15	−0.38	−0.50
15–18	−0.40	−0.53
18–21	−0.40	−0.53
21–24	−0.40	−0.52

Table 4.7: Posteriorisation velocity calculated (at center of angular position bin) using unperturbed model after varying λ_H, for different angular positions. Unperturbed model refers to theoretical model evaluated with model parameters: $\lambda_H = 10\,\mu\text{m}$, $\lambda_A = 11.5\,\mu\text{m}^2\,\text{s}^{-1}$, $\lambda_N = 152.5\,\mu\text{m}^2\,\text{s}^{-1}$, $d = 0.61$. Second column uses $\lambda_H = 15\,\mu\text{m}$ instead, and third column $\lambda_H = 5\,\mu\text{m}$ instead.

experiments for angular positions upto 21 deg. Thus, the calculated posteriorisation velocity is robust to variations in the calibration procedure.

Of note also is the hydrodynamic length λ_H, whose value have been measured in previous studies [76, 77]. Here, a hydrodynamic length of $\lambda_H = 10\,\mu\text{m}$ is observed for the unperturbed embryo, which is close to the previous measurements of the hydrodynamic length ($\sim$14 µm [76, 77]). Additionally, the model parameter variation considered before indicates that the calculated posteriorisation velocity is robust towards variation in λ_H. Thus, the calibrated hydrodynamic length used in theoretical model here is in agreement with the previously observed measurements of the hydrodynamic length of the cortex.

Therefore, the full model (with both mechanisms included) can – both qualitatively and quantitatively – recapitulate the observed AP axis alignment process in the unperturbed embryos, using the set of model parameters selected here: $\lambda_H = 10\,\mu\text{m}$, $\lambda_A = 11.5\,\mu\text{m}^2\,\text{s}^{-1}$, $\lambda_N = 152.5\,\mu\text{m}^2\,\text{s}^{-1}$, $d = 0.61$. The model evaluated with this set of model parameters will be referred to as the unperturbed model.

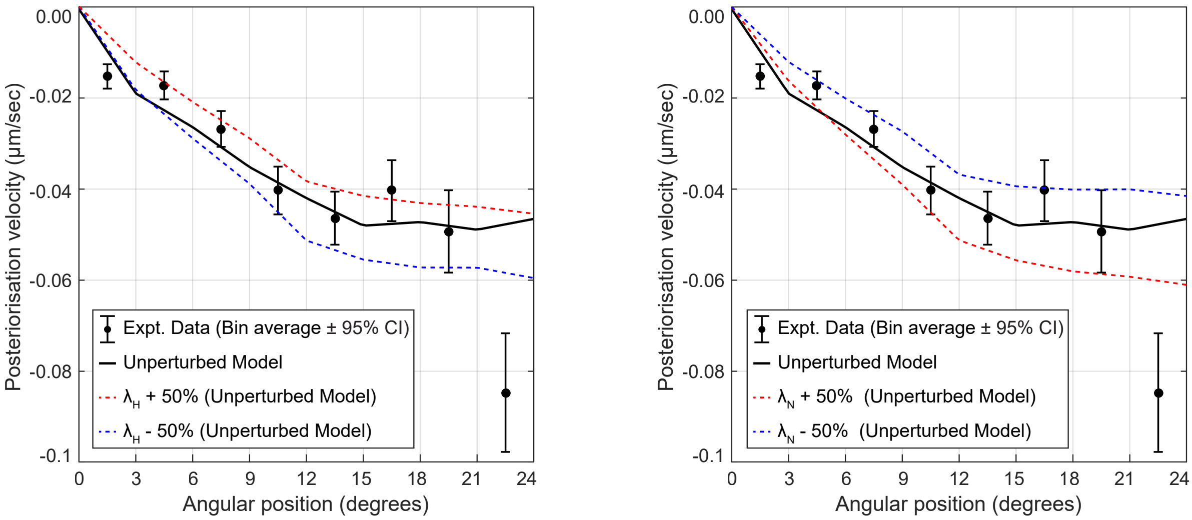

(a) Varying λ_H between [5 µm,15 µm]. Increasing λ_H leads to slower posteriorisation velocity.

(b) Varying λ_N between [76.25 µm,228.75 µm]. Increasing λ_N leads to faster posteriorisation velocity.

Figure 4.16: Posteriorisation velocity of the male pronucleus calculated by the unperturbed model (theoretical model evaluated with model parameters: $\lambda_H = 10\,\mu\text{m}$, $\lambda_A = 11.5\,\mu\text{m}^2\,\text{s}^{-1}$, $\lambda_N = 152.5\,\mu\text{m}^2\,\text{s}^{-1}$, $d = 0.61$) is robust to variation in λ_H and λ_N. Comparison of the calculated posteriorisation velocity using calibrated model parameters (black line), calculated posteriorisation velocity with $\lambda_H := 1.5\lambda_H$ (Figure 4.16a, red dashed line) or $\lambda_N := 1.5\lambda_N$ (Figure 4.16b, red dashed line), calculated posteriorisation velocity with $\lambda_H := 1.5\lambda_H$ (Figure 4.16a, blue dashed line) or $\lambda_N := 0.5\lambda_N$ (Figure 4.16b, blue dashed line), and average posteriorisation velocity observed in unperturbed embryos (black circles with error bars, 95% confidence interval). Posteriorisation velocity is plotted on the y-axis in µm/s against angular position on the x-axis in deg.

Angular positions (deg)	Calculated posteriorisation velocity (1×10^{-1} µm/s)	
	$\lambda_N \coloneqq 1.5\lambda_N$	$\lambda_N \coloneqq 0.5\lambda_N$
0–3	−0.10	−0.08
3–6	−0.25	−0.18
6–9	−0.34	−0.24
9–12	−0.43	−0.30
12–15	−0.50	−0.36
15–18	−0.54	−0.37
18–21	−0.54	−0.37
21–24	−0.54	−0.37

Table 4.8: Posteriorisation velocity calculated (at center of angular position bin) using unperturbed model after varying λ_N, for different angular positions. Unperturbed model refers to theoretical model evaluated with model parameters: $\lambda_H = 10\,\mu\text{m}$, $\lambda_A = 11.5\,\mu\text{m}^2\,\text{s}^{-1}$, $\lambda_N = 152.5\,\mu\text{m}^2\,\text{s}^{-1}$, $d = 0.61$. Second column uses $\lambda_N = 228.75\,\mu\text{m}$ instead, and third column $\lambda_N = 76.25\,\mu\text{m}$ instead.

Eliminating role of pseudocleavage furrow-dependent mechanism in model explains the slower AP axis alignment in pseudocleavage furrow-deficient embryos

Next, the theoretical model is compared with observations in the pseudocleavage furrow-deficient embryos generated by *nop-1; mel-11* double RNAi. To mimic the experimental removal of the pseudocleavage furrow in the model, λ_N– the model parameter that controls the contribution of the pseudocleavage-furrow dependent mechanism in the model (see subsection 2.3.3) – is fixed to $0\,\mu\text{m}^2\,\text{s}^{-1}$. Due to this, and since the cortical flows in these embryos are similar but not identical to those observed in unperturbed embryos, the model is recalibrated to ensure cortical flows observed in the *nop-1; mel-11* RNAi embryos are captured by the model. In this recalibration, only λ_A is varied. Doing so yields the following model parameters: $\lambda_H = 10\,\mu\text{m}$, $\lambda_A = 7\,\mu\text{m}^2\,\text{s}^{-1}$, $\lambda_N = 0\,\mu\text{m}^2\,\text{s}^{-1}$. The value for the drag coefficient $d = 0.61$ as determined for the unperturbed embryos is retained here. The model evaluated with this set of model parameters will be referred to as the pseudocleavage furrow-deficient model.

Before a comparison with experimental data is made, the posteriorisation velocity calculated using the unperturbed model and the pseudocleavage-deficient model are compared (compare Figure 4.18a with Figure 4.15a). At each angular position, the pseudocleavage furrow-deficient model calculates slower posteriorisation velocity compared to the unperturbed model – with the difference larger for higher angular positions. This is qualitatively similar to what was observed experimentally observed – pseudocleavage furrow-deficient embryos (generated using *nop-1; mel-11* RNAi) exhibit slower average posteriorisation velocities compared to unperturbed embryos at all angular positions observed in experiments – with larger difference at higher angular positions (compare Figure 4.3 to Figure 4.12). Direct comparison between the calculated posteriorisation velocity from the pseudocleavage furrow-deficient embryo to the experimental posteriorisation velocity observed in pseudocleavage furrow-deficient embryos (gen-

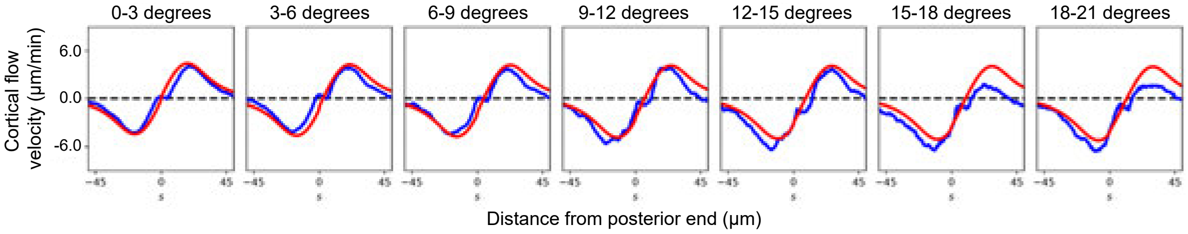

Figure 4.17: Comparison of observed cortical flows in pseudocleavage furrow-deficient embryos generated using *nop-1; mel-11* RNAi in SWG070 strain to those calculated by the theoretical model of AP axis alignment, with setting $\lambda_N = 0\,\mu\mathrm{m}^2\,\mathrm{s}^{-1}$. Blue line denotes the average cortical flow velocity observed in *nop-1; mel-11* RNAi embryos, plotted as a function of position along the cortex s in each angular position bin – also depicted in Figure 4.7. Red denotes the cortical flow velocity calculated by the theoretical model after calibration, with model parameters: $\lambda_H = 10\,\mu\mathrm{m}$, $\lambda_A = 7\,\mu\mathrm{m}^2\,\mathrm{s}^{-1}$, $\lambda_N = 0\,\mu\mathrm{m}^2\,\mathrm{s}^{-1}$.

erated using *nop-1; mel-11* RNAi) reveals that the calculated posteriorisation velocity broadly match the experimentally observed ones in the pseudocleavage furrow-deficient embryos – see Figure 4.18a and Table 4.9. Specifically, the pseudocleavage furrow-deficient model calculates posteriorisation velocity which are slightly slower, but still comparable to those observed in the pseudocleavage furrow-deficient embryos. As before, the calculated posteriorisation velocity may be integrated over to obtain a calculated trajectory of the male pronucleus using the pseudocleavage furrow-deficient model (see subsection 2.3.3). Comparison with experimentally observed trajectories in the pseudocleavage furrow-deficient embryo shows that the calculated trajectory agrees well with the experimentally observed trajectories of the male pronucleus observed in pseudocleavage furrow-deficient embryos – see Figure 4.18b.

Therefore, the pseudocleavage furrow-deficient model – where λ_N is set to $0\,\mu\mathrm{m}^2\,\mathrm{s}^{-1}$ – can recapitulate the observed AP axis alignment process in the pseudocleavage furrow-deficient embryos generated using *nop-1; mel-11* RNAi embryos. The pseudocleavage furrow-deficient model here refers to theoretical model evaluated with the following model parameters: $\lambda_H = 10\,\mu\mathrm{m}$, $\lambda_A = 7\,\mu\mathrm{m}^2\,\mathrm{s}^{-1}$, $\lambda_N = 0\,\mu\mathrm{m}^2\,\mathrm{s}^{-1}$, $d = 0.61$.

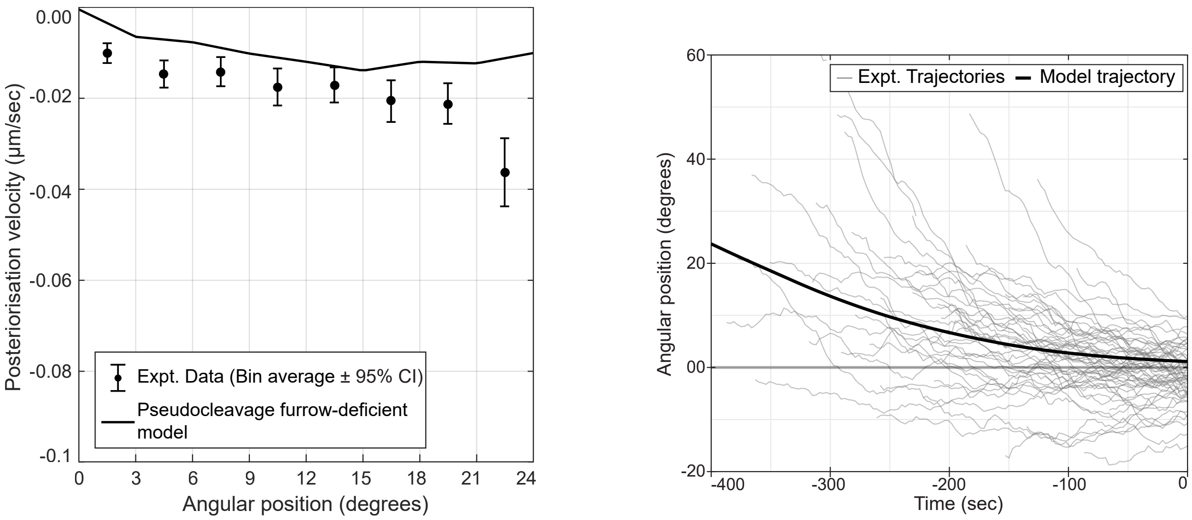

(a) Comparing average posteriorisation velocity of the male pronucleus (black circles with error bars, 95% confidence interval) in pseudocleavage furrow-deficient embryos (from Figure 4.12) with that calculated by pseudocleavage furrow-deficient model (black line), both plotted against angular position of the male pronucleus. Posteriorisation velocity is on y-axis (in µm/s, negative velocity indicate movement towards posterior end), and angular position on x-axis (in deg).

(b) Comparing angular positions of the male pronucleus (y-axis, in deg) observed in pseudocleavage furrow-deficient embryos (thin grey lines, from Figure 4.11) with the calculated trajectory of the male pronucleus (thick black line) from pseudocleavage furrow-deficient model, both plotted against time (on x-axis, in s, t = 0 s denotes end of posteriorisation).

Figure 4.18: Comparing experimentally observed posteriorisation of the male pronucleus in pseudocleavage furrow-deficient embryos generated by *nop-1; mel-11* RNAi in SWG070 strain with that calculated by the pseudocleavage furrow-deficient model. Pseudocleavage furrow-deficient model refers to the theoretical model of AP axis alignment evaluated with the following model parameters: $\lambda_H = 10\,\mu\mathrm{m}$, $\lambda_A = 7\,\mu\mathrm{m}^2\,\mathrm{s}^{-1}$, $\lambda_N = 0\,\mu\mathrm{m}^2\,\mathrm{s}^{-1}$, $d = 0.61$.

Angular positions (deg)	Experimental post. velocity (1×10^{-1} µm/s)	Calculated post. velocity (1×10^{-1} µm/s)
0–3	−0.10 (−0.12,−0.08)	−0.03
3–6	−0.14 (−0.17,−0.11)	−0.07
6–9	−0.14 (−0.17,−0.11)	−0.08
9–12	−0.17 (−0.21,−0.13)	−0.11
12–15	−0.17 (−0.21,−0.13)	−0.12
15–18	−0.20 (−0.25,−0.16)	−0.12
18–21	−0.20 (−0.25,−0.16)	−0.12
21–24	−0.36 (−0.44,−0.29)	−0.11

Table 4.9: Experimentally observed posteriorisation velocity for each angular position bin in pseudocleavage furrow-deficient embryos generated using *nop-1; mel-11* RNAi compared with those calculated by the pseudocleavage furrow-deficient model (theoretical model evaluated with model parameters: $\lambda_H = 10\,\mu\text{m}$, $\lambda_A = 7\,\mu\text{m}^2\,\text{s}^{-1}$, $\lambda_N = 0\,\mu\text{m}^2\,\text{s}^{-1}$, $d = 0.61$). Experimental Post. velocity: Average posteriorisation velocity along with 95% confidence interval for each angular position bin observed in *nop-1; mel-11* RNAi embryos (see Table 4.5 and Figure 4.12. Calculated Post. velocity: Posteriorisation velocity calculated at center of angular position bin by theoretical model with model parameters: $\lambda_H = 10\,\mu\text{m}$, $\lambda_A = 7\,\mu\text{m}^2\,\text{s}^{-1}$, $\lambda_N = 0\,\mu\text{m}^2\,\text{s}^{-1}$, $d = 0.61$.

Pseudocleavage furrow-dependent mechanism is the predominant mechanism for AP axis alignment in unperturbed embryos

A further comparison between the experimentally observed posteriorisation velocity in the unperturbed embryos and pseudocleavage furrow-deficient embryos generated using *nop-1; mel-11* RNAi embryos may now be made, by the plotting the two against each other. Specifically, the average posteriorisation velocities observed in a given angular position bin in the pseudocleavage furrow-deficient embryos are plotted against average posteriorisation velocities observed in the same angular position bin in the unperturbed embryos. Using this plot, the difference in the posteriorisation velocity between the two conditions at different angular positions may be visualized – see Figure 4.19a. A linear fit to this plot captures the trend observed in this plot, yielding a slope of $m = 0.34$ – implying that the average posteriorisation velocity observed in unperturbed embryos are about $\frac{1}{m} = 2.95$ times faster than those observed in the pseudocleavage furrow-deficient embryos.

Such a comparison may also made between the calculated posteriorisation velocity using the unperturbed model and the pseudocleavage furrow-deficient model, by plotting the calculated posteriorisation velocity from the pseudocleavage furrow-deficient model at a given angular position against the calculated posteriorisation velocity from the unperturbed model at the same angular position – see Figure 4.19b. A linear fit to this plot yields a slope of $m = 0.23$ – implying that the posteriorisation velocity calculated by the unperturbed model are about $\frac{1}{m} = 4.39$ times faster than those calculated by the pseudocleavage furrow-deficient model. Note that this factor is larger than that observed in the comparison of experimental posteriorisation velocities – such a discrepancy could be explained by the slightly slower posteriorisation

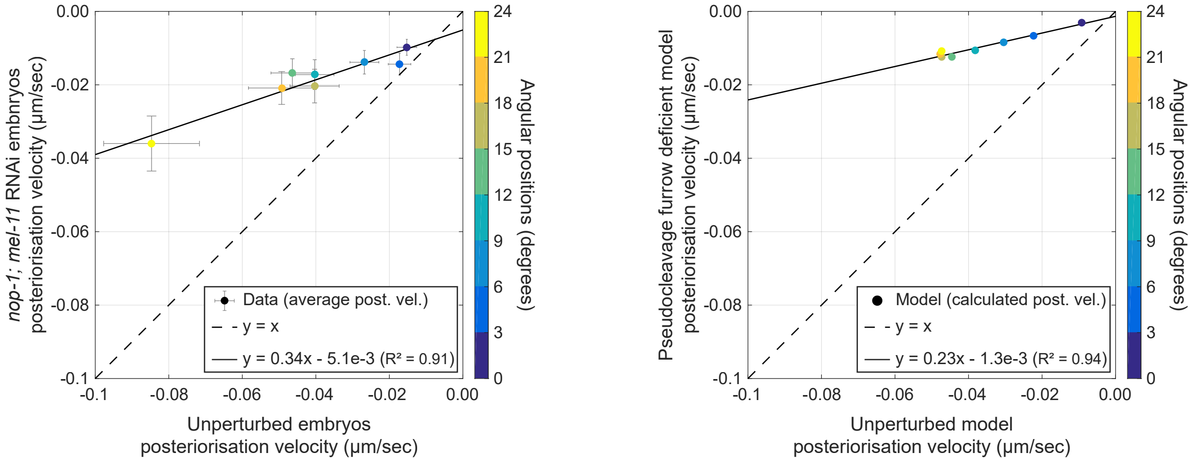

(a) Plotting average posteriorisation velocity (in µm/s) observed in *nop-1; mel-11* embryos (on y-axis) with those observed in the unperturbed embryos (on x-axis) at the same angular position bin – see Figure 4.12 and Figure 4.3.

(b) Plotting calculated posteriorisation velocity (in µm/s) from the pseudocleavage furrow-deficient model (on y-axis) with those calculated using the unperturbed model (on x-axis) at the same angular position bin – see Figure 4.18 and Figure 4.15.

Figure 4.19: Comparing pseudocleavage deficient condition with pseudocleavage present/unperturbed condition using experiments (Figure 4.19a) and theoretical model (Figure 4.19b). Color represents angular position bin for each datapoint. Dotted line indicates the $y = x$ line – the line along which the datapoints would lie if the posteriorisation velocities were similar at all angular positions. Black line is the fitted line $y = mx + c$ for the data scatter. In Figure 4.19a, error bars indicate the 95% confidence interval for the averages in both x- and y- axes.

velocity calculated by the pseudocleavage furrow-deficient model compared to those observed in the pseudocleavage furrow-deficient *nop-1; mel-11* RNAi embryos.

Therefore, the comparisons between the unperturbed embryos and pseudocleavage furrow-deficient embryos generated using *nop-1; mel-11* RNAi demonstrate that the pseudocleavage furrow plays an important role in the substantially ($\sim$ 3 times) faster dynamics of AP axis alignment observed in unperturbed embryos, but is not essential to ensure AP axis alignment occurs. Comparisons with numerical simulations using the theoretical model of AP axis alignment described in section 2.3 show that AP axis alignment in the two sets of embryos – unperturbed embryos and pseudocleavage furrow-deficient embryos – can be captured by the theoretical model, but with different model parameters Table 4.10. Of note is λ_N, which changes the most between the two sets of model parameters ($\lambda_N = 152.5\,\mu\text{m}^2\,\text{s}^{-1}$ for unperturbed model and $\lambda_N = 0\,\mu\text{m}^2\,\text{s}^{-1}$ for pseudocleavage furrow-deficient model). This difference in the λ_N also indicates a substantially ($\sim$ 4 times) faster dynamics in the unperturbed model compared to that calculated in the pseudocleavage furrow-deficient model. Note that λ_N is the model parameter that controls the contribution of the pseudocleavage furrow-dependent mechanism in the model (see section 2.3). Altogether, these observations lead to the conclusion that the pseudocleavage furrow-dependent mechanism provides the major contribution to

Model name	Compared to Expt.	Model parameters				Ellipsoid	
		λ_H (µm)	λ_A (µm^2 s^{-1})	λ_N (µm^2 s^{-1})	d	a (µm)	b (µm)
Unperturbed model	Unperturbed embryos	10	11.5	152.5	0.61	28.9	16.4
Pseudocleavage furrow-deficient model	*nop-1; mel-11* RNAi embryos	10	7	0	0.61	28.9	16.4
Unperturbed model	*ima-3* RNAi embryos	10	11.5	152.5	0.61	25.7	17.3

Table 4.10: Model parameters used for the theoretical model of AP axis alignment for comparison with and/or prediction for different experimental conditions. Model name refers to the name of the evaluation of the theoretical model at the corresponding set of model parameters.

the posteriorisation velocity observed in the unperturbed embryos, and thus is the predominant mechanism responsible for the proper AP axis alignment in the unperturbed embryos. Slow AP axis alignment in the pseudocleavage-furrow deficient embryos indicates that the other mechanism – the cytoplasmic flow-dependent mechanism – plays a minor role in AP axis alignment.

4.4 Role of embryo geometry in AP axis alignment

Given that the AP axis alignment process involves the alignment of the AP axis – defined by mechanochemical feedback between PAR proteins and actomyosin cortex (see section 1.4) – with the long axis of the embryo – determined by its geometry – a prime question to consider is the role of embryo geometry in AP axis alignment, which is done in this section. Specifically, the difference in the rate of AP axis alignment – measured as the posteriorisation velocity of the male pronucleus – between ellipsoidal embryos with differing aspect ratios is investigated. Aspect ratio of the embryo is defined as the ratio of the lengths of the long axis $2a$ and the two equal short axes $2b$ – aspect ratio $= a/b$.

4.4.1 Rounder embryos show slower AP axis alignment

Numerical simulations using the theoretical model described in section 2.3 are first used to investigate the influence of embryo geometry on AP axis alignment. Specifically, the theoretical model is evaluated with the same model parameters as those used for the unperturbed embryos (that is, $\lambda_H = 10\,\mu\text{m}$, $\lambda_A = 11.5\,\mu\text{m}^2\,\text{s}^{-1}$, $\lambda_N = 152.5\,\mu\text{m}^2\,\text{s}^{-1}$, and $d = 0.61$), but on ellipsoids with different aspect ratios (a/b = 1.10, 1.25, 1.35, 1.48, 1.58, 1.78) which retain the same volume as that used for the unperturbed model. Note that 1.78 is the aspect ratio of the ellipsoid used for the unperturbed model – corresponding to the average aspect ratio of unperturbed embryos (see Table 4.11). For each aspect ratio, the theoretical model then predicts posteriorisation velocity of the male pronucleus as a function of its angular position

Experimental Condition	Strain	Semi-major axis (a, µm)	Semi-major axis (b, µm)	Aspect ratio ($\frac{a}{b}$)
Unperturbed	SWG070	28.90 ± 1.64	16.30 ± 1.17	1.78 ± 0.15
mlc-4 RNAi	SWG070	26.90 ± 1.50	15.40 ± 0.74	1.75 ± 0.08
nop-1 RNAi	SWG070	26.90 ± 2.12	17.11 ± 0.59	1.58 ± 0.12
nop-1; mel-11 RNAi	SWG070	26.40 ± 1.43	16.10 ± 0.96	1.64 ± 0.09
ima-3 RNAi	SWG070	22.00 ± 2.27	14.70 ± 1.20	1.48 ± 0.18
air-1 RNAi	SWG070	28.90 ± 1.36	15.60 ± 1.08	1.87 ± 0.14
Unperturbed	SWG057	27.40 ± 1.36	16.20 ± 0.89	1.70 ± 0.14
goa-1; gpa-16 RNAi	SWG057	26.90 ± 1.08	15.60 ± 1.13	1.74 ± 0.16

Table 4.11: Quantification of embryo shape in various experimental conditions described in this thesis. Average value ± standard deviation are reported.

(see subsection 2.3.3). Comparing the predictions for different aspect ratios, it is observed that the posteriorisation velocity at a given angular position are generally faster for higher aspect ratio – Figure 4.20. This difference between posteriorisation velocity at different aspect ratios is larger at higher angular positions. Thus, the theoretical model predicts that the rate of AP axis alignment is influenced by aspect ratio of the ellipsoid, and therefore embryo geometry – with rounder embryos (that is, embryos with smaller aspect ratios) exhibiting slower AP axis alignment compared to more ellipsoidal ones (that is, embryos with larger aspect ratios). Note that such a prediction is consistent with the extreme case of a perfectly round (or spherical) embryo; since such a spherical embryo lacks any unique long axis, no AP axis alignment is expected in a spherical embryo.

To verify these predictions experimentally, embryos with aspect ratios smaller than those observed in unperturbed embryos were generated by performing a RNAi of *ima-3* on worms of SWG070 strain for a feeding time of 20 hours (see section 3.2 for details on RNAi). IMA-3 is a member of the importin α family of nuclear transport factors [203, 204]. It has been observed in previous studies that *ima-3* RNAi generates rounder and smaller embryos [204]. This observation is verified here by measuring the lengths of the semi-major a and semi-minor b axes and the aspect ratio of *ima-3* RNAi embryos and comparing them to those measured for the unperturbed embryos (see subsection 3.4.2 for details). The average axes lengths for the unperturbed embryos were measured to be $a = 28.7 \pm 1.6\,\mu\text{m}$ and $b = 16.2 \pm 1.1\,\mu\text{m}$, corresponding to an aspect ratio of $a/b = 1.78 \pm 0.20$. This is compared to the average axes lengths and aspect ratio measured for *ima-3* RNAi embryos, which were found to be $a = 20.9 \pm 2.2\,\mu\text{m}$, $b = 13.8 \pm 0.8\,\mu\text{m}$ and $a/b = 1.48 \pm 0.20$. It is also noted that the average volume (calculated for each embryo as the volume of the ellipsoid with the same axes lengths as those measured for the embryo) is smaller in *ima-3* RNAi embryos compared to unperturbed embryos – indicating *ima-3* RNAi embryos have a smaller volume compared to unperturbed embryos – see Figure 4.22. In summary, embryos generated using *ima-3* RNAi were observed to be smaller and rounder compared to unperturbed embryos, on average.

To ensure that the model parameters used in the unperturbed model can be used for com-

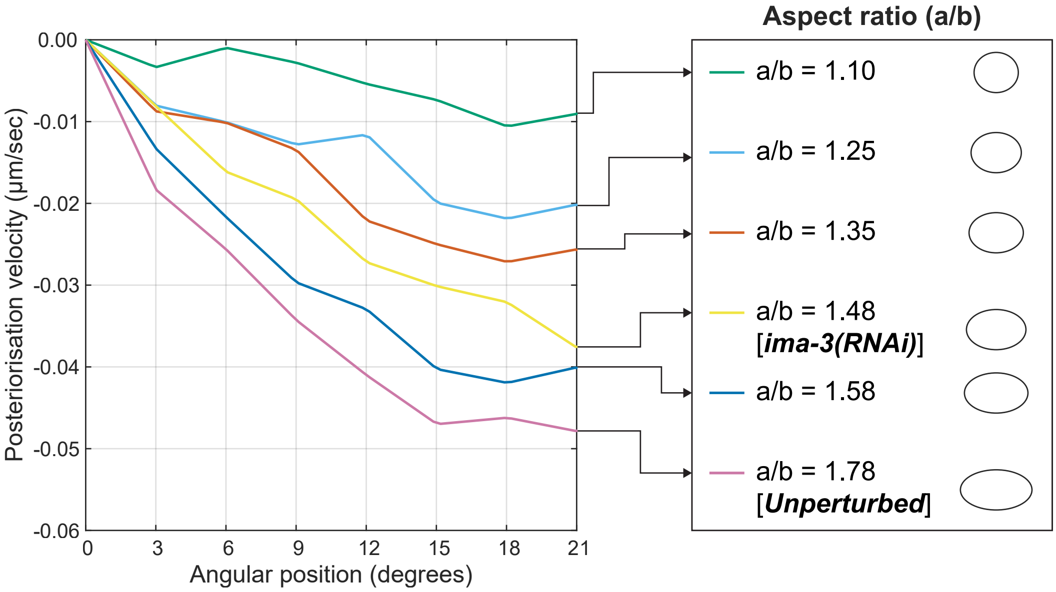

Figure 4.20: Posteriorisation velocity of the male pronucleus predicted by the theoretical model for embryos with different aspect ratios. Theoretical model is evaluated with the following model parameters: $\lambda_H = 10\,\mu\text{m}$, $\lambda_A = 11.5\,\mu\text{m}^2\,\text{s}^{-1}$, $\lambda_N = 152.5\,\mu\text{m}^2\,\text{s}^{-1}$, and $d = 0.61$), but on ellipsoids with different aspect ratios: a/b = 1.10, 1.25, 1.35, 1.48, 1.58, 1.78. Posteriorisation velocity is plotted on the y-axis (in µm/s) against angular position of the male pronucleus on the x-axis (in deg).

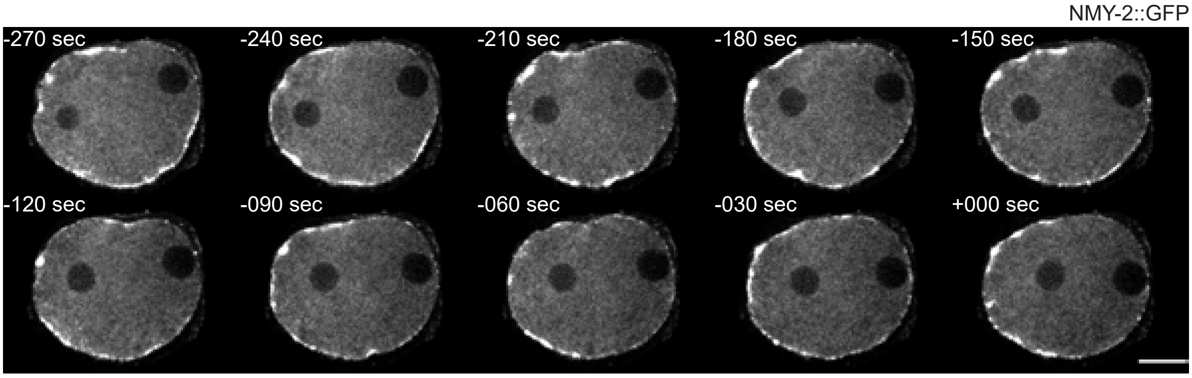

Figure 4.21: Representative *ima-3* RNAi embryo of SWG070 strain, labelled with NMY-2::GFP (white), showing the posteriorisation of the male pronucleus and the concurrent movement of the myosin depletion (indicating the pPARs domain) towards the posterior end. The male pronucleus can be visualized as the dark circle in the myosin channel towards the posterior end (right). T = 0 s is set at the end of posteriorisation of the male pronucleus. Scale bar: 10 µm. Images are rotated such that anterior and posterior ends are to the left and right respectively.

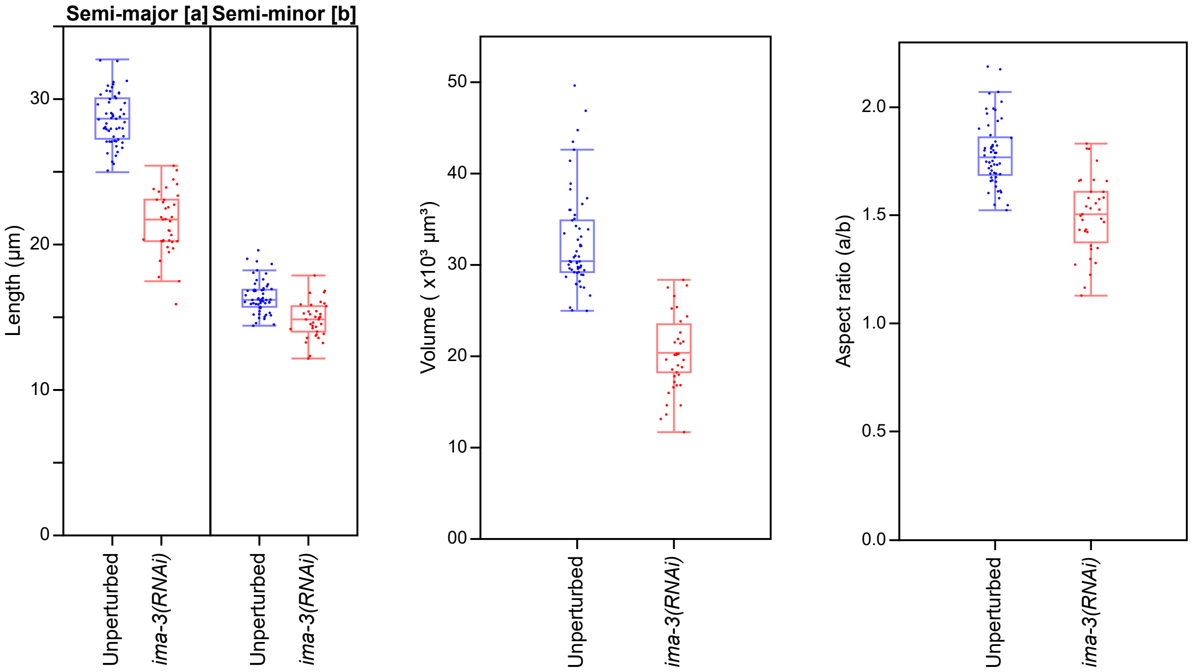

(a) Comparing embryo axes lengths. p-value $= 2.02 \times 10^{-18}$ for semi-major axis comparison, p-value $= 4.22 \times 10^{-8}$ for semi-minor axis comparison.

(b) Comparing embryo volumes. p-value $= 1.59 \times 10^{-6}$.

(c) Comparing embryo aspect ratios. p-value $= 1.48 \times 10^{-12}$

Figure 4.22: Comparison of embryo geometry between unperturbed embryos (N = 57, blue) and *ima-3* RNAi embryos (N = 35, red), both from the SWG070 strain. Semi-major a and semi-minor b axes lengths (Figure 4.22a), volume (calculated using measured semi-major and semi-minor axis lengths, Figure 4.22b) and aspect ratio (calculated using measured semi-major and semi-minor axis lengths, Figure 4.22c) are compared. Datapoints represent axes lengths, volume and aspect ratios measured for individual embryos in Figure 4.22a, Figure 4.22b and Figure 4.22c respectively. p-values are calculated using a two-sided t-test.

parison with *ima-3* RNAi embryos, myosin concentrations in the cytosol and cortex were measured and compared between the *ima-3* RNAi embryos and unperturbed embryos (see subsection 3.4.2 for methods); alongwith cortical flows. Myosin concentrations in the cytosol were measured to be 79.2 ± 4.3 AU/pixel in *ima-3* RNAi embryos, compared to 80.9 ± 13.8 AU/pixel in unperturbed embryos; myosin concentrations in the cortex were measured to be 80.3 ± 4.7 AU/pixel in *ima-3* RNAi embryos, compared to 76.2 ± 11.1 AU/pixel in unperturbed embryos; and average cortical flow speeds in the cortex were measured to be 3.99 ± 0.51 AU/pixel in *ima-3* RNAi embryos, compared to 4.12 ± 0.59 AU/pixel in unperturbed embryos. Thus, the AP axis alignment process in the *ima-3* RNAi embryos may be assumed to differ from that observed in the unperturbed embryos due to the difference in embryo geometry between the two sets of embryos – see Figure 4.23. Thus, the same model parameters as those used in the unperturbed model can be used for comparison with the rounder *ima-3* RNAi embryos.

To obtain the predicted posteriorisation velocity observed in rounder *ima-3* RNAi embryos, the theoretical model is therefore evaluated on the following model parameters: $\lambda_H = 10\,\mu\text{m}$, $\lambda_A = 11.5\,\mu\text{m}^2\,\text{s}^{-1}$, $\lambda_N = 152.5\,\mu\text{m}^2\,\text{s}^{-1}$, and $d = 0.61$, on an ellipsoid with semi-major axis $a = 25.7\,\mu\text{m}$ and semi-minor axes $b = 17.3\,\mu\text{m}$. Note that this yields an ellipsoid with aspect ratio $a/b = 1.48$ that matches the average aspect ratio observed in the *ima-3* RNAi embryos, but with the same volume as that observed in unperturbed embryos – therefore, the model prediction neglects the difference in volume between the *ima-3* RNAi embryos and unperturbed embryos. On comparison of the predicted posteriorisation velocity with the experimentally measured posteriorisation velocity in the *ima-3* RNAi embryos as a function of angular position (see Figure 4.26a), it is observed that predicted posteriorisation velocity agree with experimentally observed average posteriorisation velocity in RNAi embryos, for angular positions upto 24 deg. For higher angular positions, average posteriorisation velocity observed in experiments is faster compared to predicted posteriorisation velocity for the same angular position. By integrating the predicted posteriorisation velocity as a function of angular position (see subsection 2.3.3), a predicted trajectory of the male pronucleus in the rounder *ima-3* RNAi embryos is obtained, which agrees well with the experimentally observed trajectories of the male pronucleus in the *ima-3* RNAi embryos – see Figure 4.26b.

A direct comparison of the posteriorisation of the male pronucleus observed in *ima-3* RNAi embryos and unperturbed embryos is also made. Average posteriorisation velocity in each angular position bins observed in the rounder *ima-3* RNAi embryos were slower than those observed in the unperturbed embryos at the same angular position bins – with larger differences for higher angular positions (compare Figure 4.25 to Figure 4.3). As with unperturbed embryos, the angular positions were observed to decrease towards 0 deg in the rounder *ima-3* RNAi embryos – see Figure 4.24. Fitting an exponential $\alpha = \alpha_0 + \exp\left(\frac{t}{t_0}\right)$ to the angular positions observed in *ima-3* RNAi embryos yields a time constant $t_0 = 133 \pm 3\,\text{s}$ and $\alpha_0 = 1.68 \pm 0.29$ deg. Note that the time constant obtained for *ima-3* RNAi embryos ($t_0 = 133 \pm 3\,\text{s}$) is larger than that obtained for unperturbed embryos ($t_0 = 118 \pm 3\,\text{s}$). Altogether, these observations lead to the conclusion that the rounder *ima-3* RNAi embryos exhibit a slower rate of AP axis alignment compared to unperturbed embryos – matching the prediction of the theoretical model. Note also that while the posteriorisation velocity is slower in *ima-3* RNAi embryos compared to those observed in unperturbed embryos, but is faster than those observed in the pseudocleavage furrow-deficient embryos generated by the *nop-1; mel-11* RNAi – compare Figure 4.21,

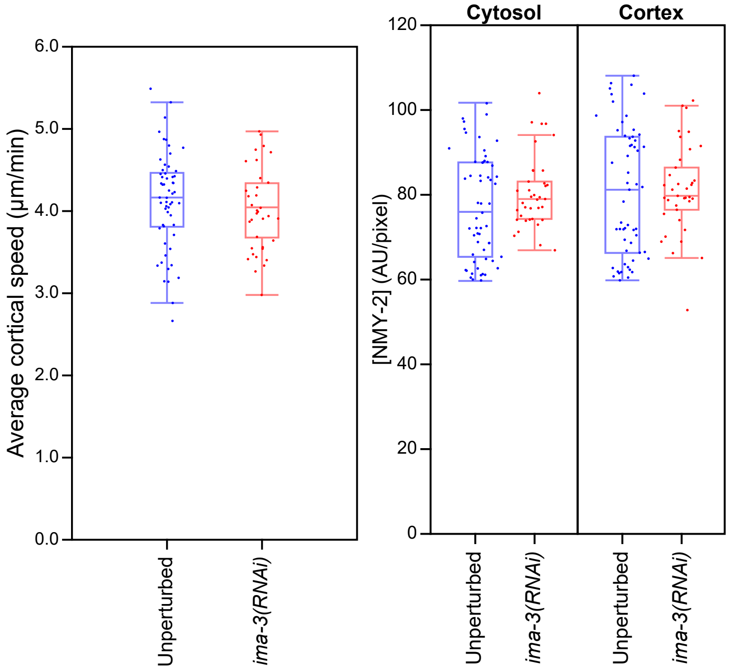

(a) Comparing average cortical speeds in embryos. p-value = 0.28

(b) Comparing myosin concentrations in embryos. p-value = 0.72 for myosin concentration in cortex, p-value = 0.19 for myosin concentration in cytosol.

Figure 4.23: Comparison of myosin concentrations and cortex flow speeds between unperturbed embryos (N = 57, blue) and *ima-3* RNAi embryos (N = 35, red), both from the SWG070 strain. Average cortical flow speeds (Figure 4.23a) and myosin concentrations in the cytosol and cortex (Figure 4.23b, see subsection 3.4.2) are compared. Datapoints represent average cortical flow speeds, myosin concentration in cytosol and cortex measured for individual embryos in Figure 4.23a and Figure 4.23b respectively. Myosin concentration is estimated as the average intensity of NMY-2::GFP per pixel in the cortex and cytosol. Intensity of NMY-2::GFP are measured in arbitrary units (AU). p-values are calculated using a two-sided t-test.

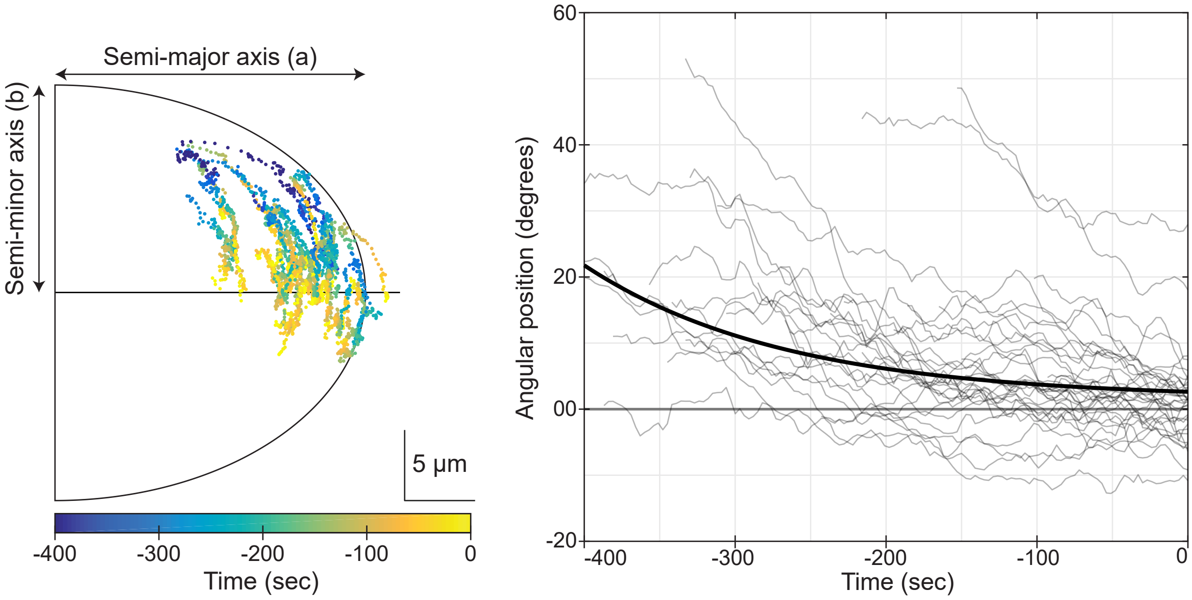

(a) Trajectories of the male pronucleus (denoted by the coordinates of its center) observed in *ima-3* RNAi embryos. Color represents time. x- and y-axes lie along the long and short axes of an ellipse with semi-major axis $a = 22.0\,\mu\text{m}$ and semi-minor axis $b = 14.7\,\mu\text{m}$. Scale bar: 5 µm

(b) Angular position of the male pronucleus (on y-axis, in deg) plotted as a function of time (on x-axis, in s), in *ima-3* RNAi embryos. Thin black lines represent individual trajectories, thick black line represents a exponential fit to the average of these tracks: $\alpha = \alpha_0 + \exp\left(-\frac{t}{t_0}\right)$, with $t_0 = 133 \pm 3\,\text{s}$ and $\alpha_0 = 1.68 \pm 0.29\,\text{deg}$.

Figure 4.24: Experimentally observed trajectories of the male pronucleus during posteriorisation in *ima-3* RNAi embryos of SWG070 strain (N = 35). See subsection 3.4.2 for details on male pronucleus tracking. Average semi-major and semi-minor axes lengths for *ima-3* RNAi embryos of SWG070 strain are used in Figure 4.24a – see Table 4.11. Angular position is defined as the angle between the long axis and line connecting the centers of the male pronucleus and embryo. T = 0 s denotes end of posteriorisation.

Figure 4.3 and Figure 4.12.

Altogether, these observations lead to the conclusion that rounder embryos do indeed show slower rate of AP axis alignment – as predicted by the theoretical model and confirmed experimentally. Since the diminished posteriorisation velocity observed in the rounder *ima-3* RNAi embryos match the posteriorisation velocity predicted by the model using the same aspect ratio as the average aspect ratio observed in *ima-3* RNAi embryos, the theoretical model captures this relation between embryo geometry and AP axis alignment in a quantitative manner. Additionally, the prediction for the *ima-3* RNAi embryos only takes into account the change in aspect ratio of the embryos, yet makes a prediction that matches the experimental observations – implying that the primary feature of embryo geometry that influences AP axis alignment is the aspect ratio of the embryo.

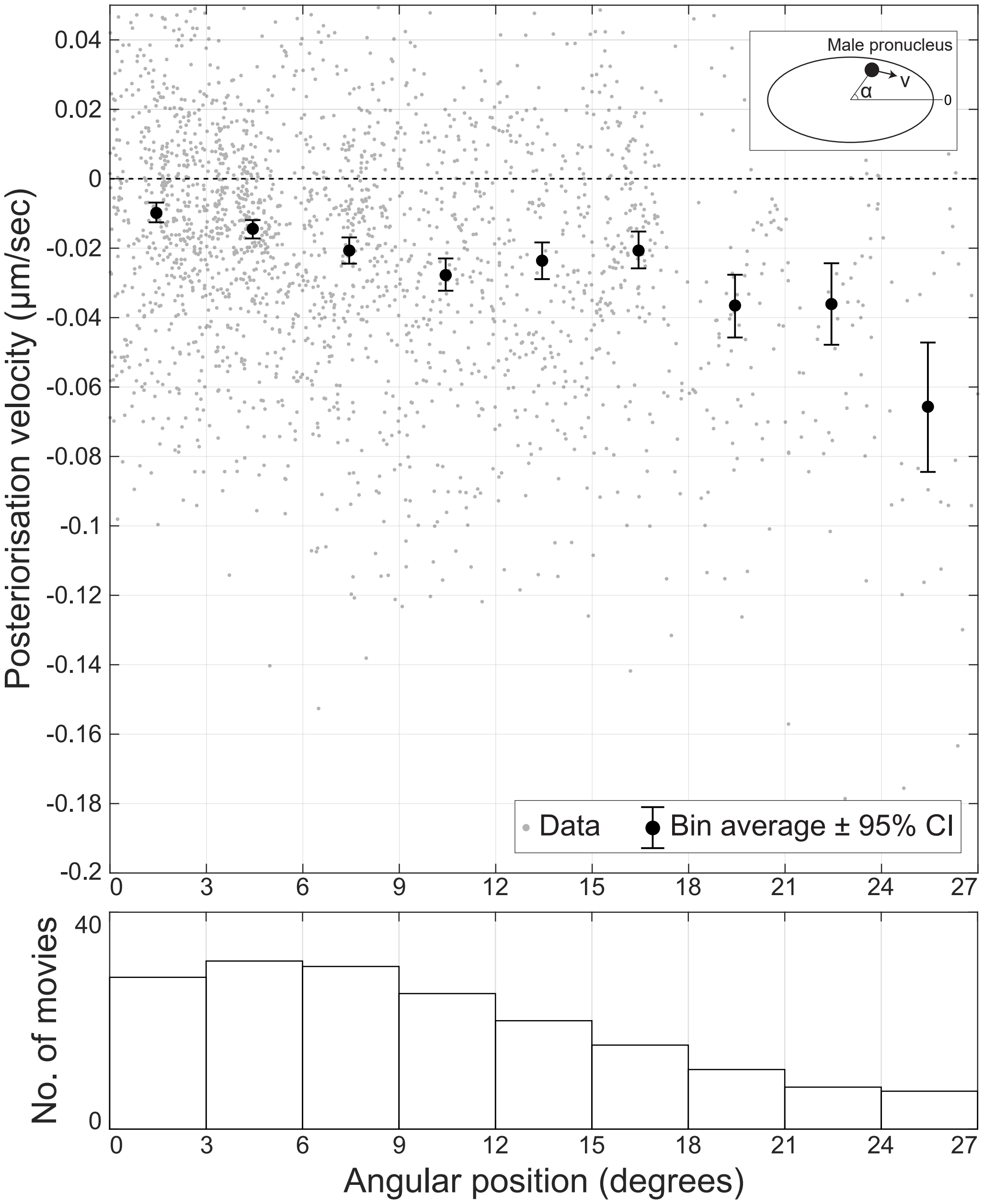

Figure 4.25: Top: Posteriorization velocity of the male pronucleus (along y-axis, in µm/s) plotted against its angular position, in *ima-3* RNAi embryos of SWG070 strain (N = 35). Negative values of the posteriorisation velocity indicate movement towards the posterior end. Angular position is binned using a bin width of 3 deg. Black circles with errors bars denote the average posteriorization velocity with 95% confidence intervals in each angular position bin. Grey circles represent the data scatter – the measured posteriorization velocities for different angular positions in each embryo (see subsection 3.4.2). Bottom: Histogram of the number of movies (along y-axis) contributing to each angular position (along x-axis) bin. A movie is considered to contribute to an angular position bin if it has any frames with angular positions within that bin. Note that a movie can contribute to multiple bins, as it may contain frames spanning different angular positions.

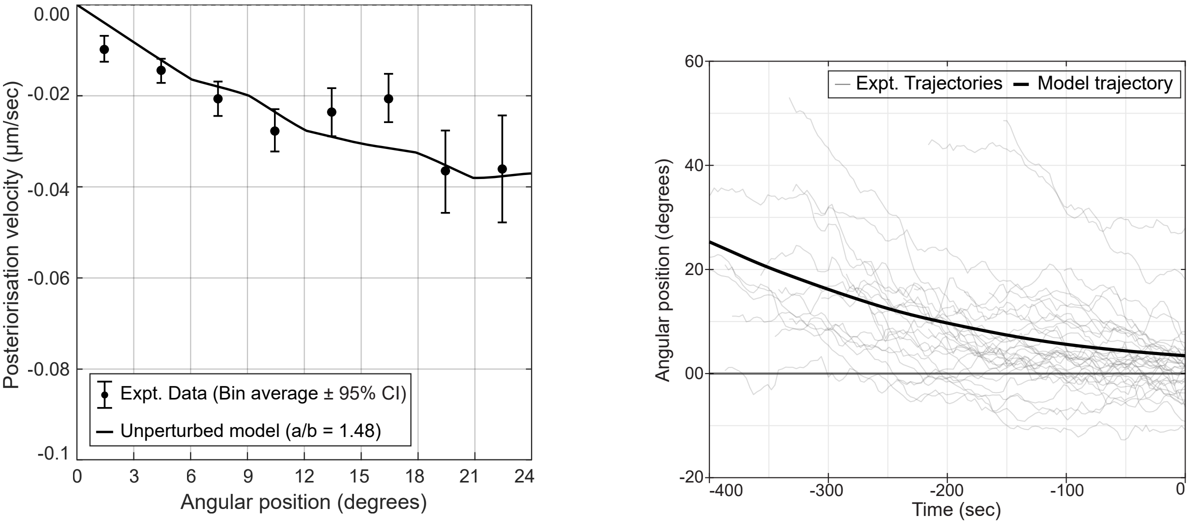

(a) Comparing average posteriorisation velocity of the male pronucleus (black circles with error bars, 95% confidence interval) in *ima-3* RNAi embryos (from Figure 4.25) with that predicted by unperturbed model on an ellipsoid with aspect ratio $a/b = 1.48$ (black line), both plotted against angular position of the male pronucleus. Posteriorisation velocity is on y-axis (in µm/s, negative velocity indicate movement towards posterior end), and angular position on x-axis (in deg).

(b) Comparing angular positions of the male pronucleus (y-axis, in deg) observed in *ima-3* RNAi embryos (thin grey lines, from Figure 4.24) with the predicted trajectory of the male pronucleus (thick black line) from unperturbed model on an ellipsoid with aspect ratio $a/b = 1.48$, both plotted against time (on x-axis, in s, t = 0 s denotes end of posteriorisation).

Figure 4.26: Comparing experimentally observed posteriorisation of the male pronucleus in *ima-3* RNAi embryos of the SWG070 strain with that predicted by the unperturbed model on an ellipsoid with aspect ratio $a/b = 1.48$. Unperturbed model refers to the theoretical model of AP axis alignment evaluated with the following model parameters: $\lambda_H = 10\,\mu\text{m}$, $\lambda_A = 11.5\,\mu\text{m}^2\,\text{s}^{-1}$, $\lambda_N = 152.5\,\mu\text{m}^2\,\text{s}^{-1}$, $d = 0.61$.

4.4.2 Relation between embryo geometry and AP axis alignment

Exploring the relation between aspect ratio and posteriorisation velocity

The predictions made using the theoretical model for embryos with different aspect ratios indicate a relation between the aspect ratio of the embryo and the rate of AP axis alignment (measured as the posteriorisation velocity of the male pronucleus): slower rate of AP axis alignment (that is, slower posteriorisation velocity at different angular positions) for smaller aspect ratios (that is, rounder embryos). To evaluate this relation experimentally, the following procedure is considered. Instead of considering the posteriorisation velocity of the male pronucleus as a function of angular position for a given average aspect ratio (as has been done until now), the posteriorization velocity are now considered as a function of aspect ratio, averaged over a range of angular positions. Experimental variation in the aspect ratios of both unperturbed (1.6–2.1) and *ima-3* RNAi embryos (1.1–1.7) enables evaluating the relation between aspect ratio and posteriorisation velocity over a broad range of aspect ratios (1.1–2.1) – see Figure 4.27. Since the difference in volume between the unperturbed embryos and RNAi embryos does not appear to be important for AP axis alignment, and that cortical flows and myosin concentrations are not significantly different between unperturbed embryos and *ima-3* RNAi embryos; these two sets of embryos can be combined into a single set which is now considered. In other words, the set of embryos considered in this subsection contains both the unperturbed embryos and *ima-3* RNAi embryos, with no distinction made between the two. This set of embryos will be referred to as the combined set of embryos.

To obtain the experimentally observed relation between the posteriorisation velocity of the male pronucleus and aspect ratio of the embryo from the combined set of embryos, the combined set is binned using aspect ratio with a bin width of 0.2. For each bin, the observed posteriorisation velocity included in this aspect ratio bin are averaged over all angular positions between 3–15 deg. This yields the average posteriorisation velocity (along with 95% confidence intervals calculated using two sided t-test) observed for each aspect ratio bin – thus yielding the experimentally observed relation between the two – see Figure 4.27.

From the numerical simulations done using ellipsoids with different aspect ratios, a similar relation between the posteriorisation velocity and aspect ratio can be predicted by the theoretical model. For each aspect ratio used in numerical simulations described before, the posteriorisation velocity are averaged for all angular positions between 3–15 deg. For aspect ratios in-between, linear interpolation is utilised. This yields the relation between the posteriorisation velocity and aspect ratio, as predicted using the theoretical model – see Figure 4.30. Comparing to the experimentally observed relation, the predicted relation agrees with the experimentally obtained one over a range of aspect ratios from 1.1–1.7.

Effective model of a contractile ring on an ellipsoid captures the relation between embryo geometry and AP axis alignment

How does this relation between the embryo geometry (characterised by aspect ratio) and AP axis alignment (characterised by posteriorisation velocity) arise? As shown in subsection 4.3.2, the predominant mechanism for AP axis alignment is the pseudocleavage furrow-dependent mechanism. The pseudocleavage furrow may effectively be considered as a contractile ring, rotating about the equator of an ellipsoid (representing the embryo) during AP axis alignment.

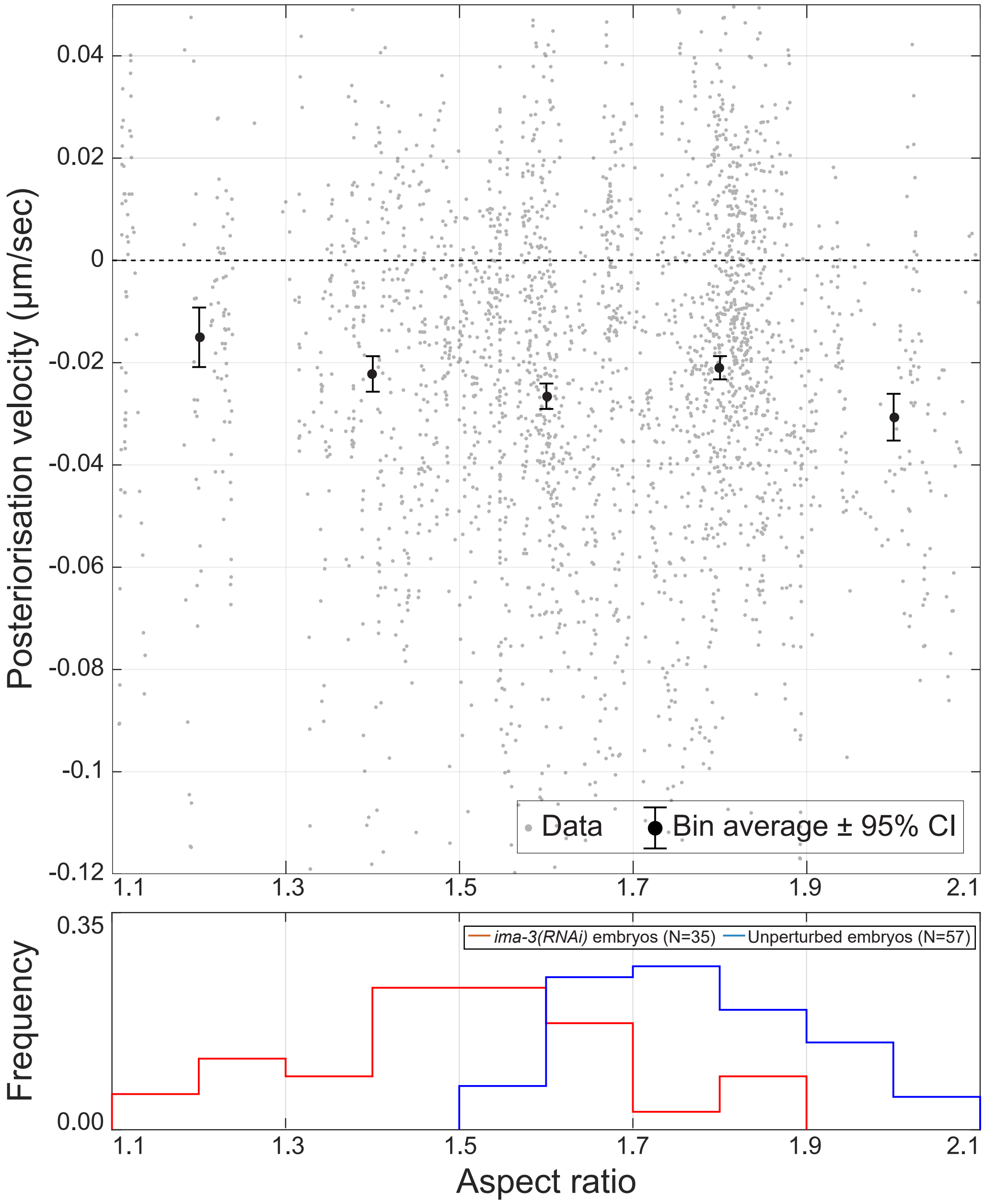

Figure 4.27: Top: Posteriorization velocity of the male pronucleus (along y-axis, in μm/s) plotted against aspect ratio of the embryo, in combined set embryos – comprised of unperturbed embryos and *ima-3* RNAi embryos. Negative values of the posteriorisation velocity indicate movement towards the posterior end. Aspect ratios is binned using a bin width of 0.2. Black circles with errors bars denote the average posteriorization velocity with 95% confidence intervals in each aspect ratio bin. Grey circles represent the data scatter – the measured posteriorization velocities for different aspect ratios in each embryo (see subsection 3.4.2). Bottom: Histogram of the frequency of movies (number of movies divided by total number of movies in the set, along y-axis) contributing to each aspect ratio (along x-axis) bin, for unperturbed embryos (blue) and *ima-3* RNAi embryos (red).

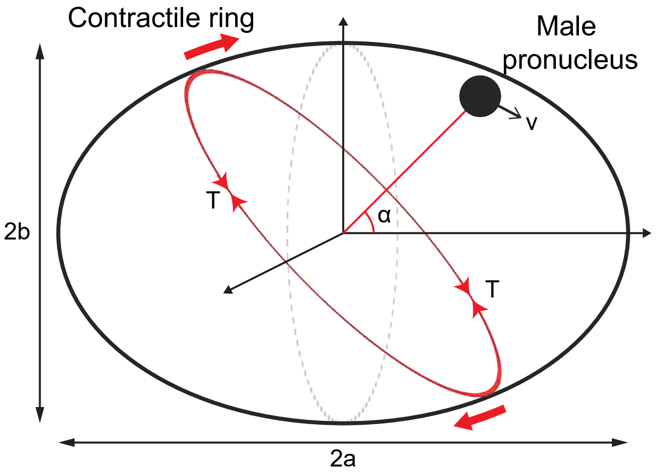

Figure 4.28: Schematic depicting effective model of a contractile ring (red ellipse) with fixed line tension (T) moving on an ellipsoid (black thick ellipse) with a long axis of length $2a$ and two short axes of length $2b$. x-axis is along the long axis of the ellipsoid. Both y- and z- axes are along the equal short axes of the ellipsoid (black dashed ellipse resides in the yz plane). The contractile ring is free to rotate about the z-axis (red block arrows), and its position is described by the angle α made between the plane of the contractile ring and the yz-plane. In the effective model, α also describes the angular position of the male pronucleus, considered to always be positioned along the normal to the plane of the contractile ring.

Can this effective model of a contractile ring on an ellipsoid be enough to capture the relation between aspect ratio of the embryo and posteriorisation velocity of the male pronucleus as observed in the combined set of embryos?

The effective model considers a fixed ellipsoid with one long axis (of length $2a$) and two equal short axes (of length $2b$ each) – see Figure 4.28. The long axis of the embryo defines the x-axis, while the two short axes define the y- and z- axes. On this ellipsoid, a contractile ring is considered to represent the pseudocleavage furrow. The center of the ring and the center of the ellipsoid are coincident (at the origin of the coordinate system). This ring rotates about the z-axis, representing the rotation of the pseudocleavage furrow during AP axis alignment. Thus, the contractile ring has only a sole degree of freedom: the angle α made between the normal to the plane of the contractile ring and the x-axis. Only small angles α are considered here (as angular positions between 3–15 deg only were considered for the experimentally obtained relation between aspect ration and posteriorisation velocity).

The following assumptions are made in the effective model, with regards to the dynamics of the contractile ring:

- The ring has a constant line tension T - independent of both the orientation of the ring (α) and the shape of the ellipsoid (a, b). Here, T has units of force.
- The frictional torque acting on the ring is controlled by a frictional coefficient γ, and is given by $\gamma \cdot \dot{\alpha}$

- No inertial terms in the momentum balance are considered: Torque generated by the ring is perfectly balanced by the torque generated by friction.

Under the above assumptions, the aim of the effective model is to calculate $\dot{\alpha}$ as a function of a, b and α – for small angles α.

Motion of contractile ring

Consider the mechanical energy stored in the contractile ring, which is given by:

$$E = TC(\alpha) \tag{4.1}$$

where $C(\alpha)$ is the total circumference of the ring.

To calculate the circumference of the ring for any given α, a description of the ring as an intersection of the ellipsoid with the plane in which the ring resides is written. This plane makes an angle of α with the yz plane, and passes through the origin. Thus, it can be described by the equation: $y = -x\cot\alpha$. The ellipsoid itself can be described as $\frac{x^2}{a^2} + \frac{y^2+z^2}{b^2} = 1$. On taking the intersection of the ring plane with the ellipsoid, the equation describing the ring can be obtained:

$$\begin{aligned}
\text{Plane: } & y = -x\cot\alpha \\
\text{Ellipsoid: } & \frac{x^2}{a^2} + \frac{y^2+z^2}{b^2} = 1 \\
\text{Intersection (Ellipse): } & \frac{x^2}{a^2} + \frac{x^2\cot^2\alpha + z^2}{b^2} = 1 \\
\implies & x^2\left(\frac{a^2\cot^2\alpha + b^2}{a^2b^2}\right) + \frac{z^2}{b^2} = 1; \quad y = -x\cot\alpha
\end{aligned}$$

Define $A = \frac{ab}{\sqrt{a^2\cot^2\alpha + b^2}}$. Then, the equation in the intersection part above can be written as: $\frac{x^2}{A^2} + \frac{z^2}{b^2} = 1$ - a form similar to the canonical form for an ellipse. Calling the parametric angle for this ellipse ϕ, the position vector describing the ring $\vec{r}$ can be written as:

$$\vec{r} = (A\cos\phi, -A\cot\alpha\cos\phi, b\sin\phi)\,; \quad A = \frac{ab}{\sqrt{a^2\cot^2\alpha + b^2}}$$

where $\phi \in [-\pi, \pi)$.

Note that the ring is an ellipse in its plane - since the intersection of an ellipsoid and a plane must be an ellipse. This can also be seen by the form by $\|\vec{r}\|^2$:

$$\|\vec{r}\|^2 = A^2(1 + \cot^2\alpha)\cos^2\phi + b^2\sin^2\phi$$

indicating that the contractile ring is an ellipse with semi-major a_{ring} and semi-minor b_{ring} axes, given by:

$$\begin{aligned}
a_{ring} &= A\sqrt{1 + \cot^2\alpha} = \frac{ab}{\sqrt{a^2\cot^2\alpha + b^2}}\sqrt{1 + \cot^2\alpha^2} = \frac{ab}{\sqrt{a^2\cos^2\alpha + b^2\sin^2\alpha}} \\
b_{ring} &= b \\
e_{ring} &= \sqrt{1 - \left(\frac{b_{ring}}{a_{ring}}\right)^2} = \sqrt{1 - \frac{a^2\cos^2\alpha + b^2\sin^2\alpha}{a^2}} = \sqrt{\sin^2\alpha - \frac{b^2}{a^2}\sin^2\alpha} = \sin\alpha\sqrt{1 - \frac{b^2}{a^2}}
\end{aligned}$$

where e_{ring} is the eccentricity of the ellipse formed by the ring. Note that since the ring rotates about the yz plane (i.e. the plane with the two short axes), the short axis of the ring is just b.

The circumference of the ring is then given by the circumference of this ellipse. The formula for the circumference of an ellipse is:

$$C(\alpha) = 4a_{ring} \int_0^{\frac{\pi}{2}} \sqrt{1 - e_{ring}^2 \sin^2 \phi}\, \mathrm{d}\phi \tag{4.2}$$

Torque generated by contractile ring

Using (4.1) and (4.2), the mechanical energy of the contractile energy is then:

$$\begin{aligned} E = TC(\alpha) &= 4Ta_{ring} \int_0^{\frac{\pi}{2}} \sqrt{1 - e_{ring}^2 \sin^2 \phi}\, \mathrm{d}\phi \\ &= 4T \frac{ab}{\sqrt{a^2 \cos^2 \alpha + b^2 \sin^2 \alpha}} \int_0^{\frac{\pi}{2}} \sqrt{1 - \left(1 - \frac{b^2}{a^2}\right) \sin^2 \alpha \sin^2 \phi\, \mathrm{d}\phi} \end{aligned}$$

The torque τ can then be expressed as:

$$\begin{aligned} \tau = -\frac{\mathrm{d}E}{\mathrm{d}\alpha} &= -4T \frac{\mathrm{d}}{\mathrm{d}\alpha} \left(\frac{ab}{\sqrt{a^2 \cos^2 \alpha + b^2 \sin^2 \alpha}} \int_0^{\frac{\pi}{2}} \sqrt{1 - \left(1 - \frac{b^2}{a^2}\right) \sin^2 \alpha \sin^2 \phi_{ring}}\, \mathrm{d}\phi_{ring} \right) \\ &= -4T \left[\frac{ab(a^2 - b^2) \cos \alpha \sin \alpha}{\left(a^2 \cos^2 \alpha + b^2 \sin^2 \alpha\right)^{3/2}} \int_0^{\frac{\pi}{2}} \sqrt{1 - \left(1 - \frac{b^2}{a^2}\right) \sin^2 \alpha \sin^2 \phi_{ring}}\, \mathrm{d}\phi_{ring} \right. \\ &\quad \left. + \frac{ab}{\sqrt{a^2 \cos^2 \alpha + b^2 \sin^2 \alpha}} \int_0^{\frac{\pi}{2}} \frac{-\left(1 - \frac{b^2}{a^2}\right) \sin \alpha \cos \alpha \sin^2 \phi_{ring}}{\sqrt{1 - \left(1 - \frac{b^2}{a^2}\right) \sin^2 \alpha \sin^2 \phi_{ring}}} \mathrm{d}\phi_{ring} \right] \\ &= -4T \frac{ab(a^2 - b^2) \sin \alpha \cos \alpha}{\sqrt{a^2 \cos^2 \alpha + b^2 \sin^2 \alpha}} \\ &\quad \times \int_0^{\frac{\pi}{2}} \left[\frac{1 - \left(1 - \frac{b^2}{a^2}\right) \sin^2 \alpha \sin^2 \phi_{ring}}{a^2 \cos^2 \alpha + b^2 \sin^2 \alpha} - \frac{\sin^2 \phi_{ring}}{a^2} \right] \frac{1}{\sqrt{1 - \left(1 - \frac{b^2}{a^2}\right) \sin^2 \alpha \sin^2 \phi_{ring}}} \mathrm{d}\phi_{ring} \\ &= -4T \frac{ab(a^2 - b^2) \sin \alpha \cos \alpha}{a^2 \sqrt{a^2 \cos^2 \alpha + b^2 \sin^2 \alpha}} \\ &\quad \times \int_0^{\frac{\pi}{2}} \left[\frac{a^2 - \left(a^2 - b^2\right) \sin^2 \alpha \sin^2 \phi_{ring}}{a^2 \cos^2 \alpha + b^2 \sin^2 \alpha} - \sin^2 \phi_{ring} \right] \frac{1}{\sqrt{1 - \left(1 - \frac{b^2}{a^2}\right) \sin^2 \alpha \sin^2 \phi_{ring}}} \mathrm{d}\phi_{ring} \\ &= -4T \frac{ab(a^2 - b^2) \sin \alpha \cos \alpha}{a^2 \sqrt{a^2 \cos^2 \alpha + b^2 \sin^2 \alpha}} \\ &\quad \times \int_0^{\frac{\pi}{2}} a^2 \left[\frac{1 - \sin^2 \phi_{ring}}{a^2 \cos^2 \alpha + b^2 \sin^2 \alpha} \right] \frac{1}{\sqrt{1 - \left(1 - \frac{b^2}{a^2}\right) \sin^2 \alpha \sin^2 \phi_{ring}}} \mathrm{d}\phi_{ring} \end{aligned}$$

$$\implies \tau = -4T\frac{ab(a^2-b^2)\sin\alpha\cos\alpha}{\left(a^2\cos^2\alpha+b^2\sin^2\alpha\right)^{3/2}}\int_0^{\frac{\pi}{2}}\frac{\cos^2\phi_{ring}}{\sqrt{1-\left(1-\frac{b^2}{a^2}\right)\sin^2\alpha\sin^2\phi_{ring}}}\,\mathrm{d}\phi_{ring}$$

Using the Taylor expansion around $\alpha = 0$, τ can be expanded to linear order in α as $\tau = \tau|_{\alpha=0} + \frac{\mathrm{d}\tau}{\mathrm{d}\alpha}\big|_{\alpha=0}\alpha + \mathcal{O}(\alpha^2)$. Note that on $\alpha = 0$, the torque also goes to zero. To obtain the linear order expansion, the derivative of the torque at $\alpha = 0$ is calculated:

$$\begin{aligned}
\left.\frac{\mathrm{d}\tau}{\mathrm{d}\alpha}\right|_{\alpha=0} &= -4T\frac{\mathrm{d}}{\mathrm{d}\alpha}\left.\left[\frac{ab(a^2-b^2)\sin\alpha\cos\alpha}{\left(a^2\cos^2\alpha+b^2\sin^2\alpha\right)^{3/2}}\int_0^{\frac{\pi}{2}}\frac{\cos^2\phi_{ring}}{\sqrt{1-\left(1-\frac{b^2}{a^2}\right)\sin^2\alpha\sin^2\phi_{ring}}}\,\mathrm{d}\phi_{ring}\right]\right|_{\alpha=0}\\
&= -4T\left[\left.\frac{\mathrm{d}}{\mathrm{d}\alpha}\left(\frac{ab(a^2-b^2)\sin\alpha\cos\alpha}{\left(a^2\cos^2\alpha+b^2\sin^2\alpha\right)^{3/2}}\right)\right|_{\alpha=0}\int_0^{\frac{\pi}{2}}\frac{\cos^2\phi_{ring}}{\sqrt{1-\left(1-\frac{b^2}{a^2}\right)(0)\sin^2\phi_{ring}}}\,\mathrm{d}\phi_{ring}\right.\\
&\quad\left.+\frac{ab(a^2-b^2)*0*1}{(a^2(1)+b^2(0))^{3/2}}\frac{\mathrm{d}}{\mathrm{d}\alpha}\left.\left(\int_0^{\frac{\pi}{2}}\frac{\cos^2\phi_{ring}}{\sqrt{1-\left(1-\frac{b^2}{a^2}\right)\sin^2\alpha\sin^2\phi_{ring}}}\,\mathrm{d}\phi_{ring}\right)\right|_{\alpha=0}\right]\\
&= -4T\left[\frac{ab(a^2-b^2)}{\left(a^2*1+b^2*0\right)^{3/2}}\right]\int_0^{\frac{\pi}{2}}\cos^2\phi_{ring}\,\mathrm{d}\phi_{ring} = -4T\frac{ab(a^2-b^2)}{a^3}\frac{\pi}{4}\\
\implies \left.\frac{\mathrm{d}\tau}{\mathrm{d}\alpha}\right|_{\alpha=0} &= -\pi Tb\left(1-\frac{b^2}{a^2}\right)
\end{aligned}$$

Thus, by Taylor expansion, the torque to linear order in α is:

$$\tau \approx \left.\frac{\mathrm{d}\tau}{\mathrm{d}\alpha}\right|_{\alpha=0}\alpha = -\pi Tb\left(1-\frac{b^2}{a^2}\right)\alpha \tag{4.3}$$

Torque balance for the contractile ring

Per the assumption of negligible inertial terms and the form of friction experienced by the ring, the torque balance of the ring can be written as:

$$\tau - \gamma\cdot\dot{\alpha} = 0$$

Putting in the expression for τ obtained before:

$$\dot{\alpha} \approx -\frac{\pi T}{\gamma}b\left[1-\frac{b^2}{a^2}\right]\alpha \tag{4.4}$$

Calculating posteriorization velocity of the male pronucleus

To get the posteriorization velocity of the male pronucleus v, an additional assumption is made: the angular position of the male pronucleus is the same as the angle α itself – see Figure 4.28. Effectively, the male pronucleus acts as if it is rigidly attached to the normal vector to the contractile ring. Then, the position of the male pronucleus is given by:

$$\begin{aligned}
\text{On ellipsoid:} \quad & \frac{x_{nucl}^2}{a^2} + \frac{y_{nucl}^2}{b^2} = 1 \\
\text{Angle with x-axis (long axis):} \quad & x_{nucl} = r_{nucl}\cos\alpha, \quad y_{nucl} = r_{nucl}\sin\alpha \\
\implies \quad & \frac{r_{nucl}^2\cos^2\alpha}{a^2} + \frac{r_{nucl}^2\sin^2\alpha}{b^2} = 1 \\
\implies r_{nucl} = \quad & \frac{ab}{\sqrt{a^2\sin^2\alpha + b^2\cos^2\alpha}}
\end{aligned}$$

The posteriorization velocity of the male pronucleus is then given by (for small angles α, velocity is almost parallel to the cortex, hence the full magnitude can be considered):

$$v \approx \sqrt{\left(\frac{\mathrm{d}x_{nucl}}{\mathrm{d}t}\right)^2 + \left(\frac{\mathrm{d}y_{nucl}}{\mathrm{d}t}\right)^2} = \sqrt{\dot{r}_{nucl}^2 + r_{nucl}^2\dot{\alpha}^2}$$

For small angle α, $r_{nucl} \approx a - \frac{a^3}{b^2}\alpha^2 + \mathcal{O}(\alpha^3)$ and $\dot{r}_{nucl} = -2\frac{a^3}{b^2}\alpha\dot{\alpha} + \mathcal{O}(\alpha^2)$. Thus,

$$v = \sqrt{\dot{r}_{nucl}^2 + r_{nucl}^2\dot{\alpha}^2} = \dot{\alpha}\sqrt{a^2 - 2\frac{a^4}{b^2}\alpha^2 + 4\frac{a^6}{b^4}\alpha^2 + \mathcal{O}(\alpha^3)} = \dot{\alpha}\left(a + \mathcal{O}(\alpha^2)\right)$$

Therefore, using (4.4), the following expression for the posteriorisation velocity v, to linear order in the angular position α, is obtained:

$$v \approx -\left[\frac{\pi T}{\gamma}\right]\left[ab\left(1 - \frac{b^2}{a^2}\right)\right]\alpha \tag{4.5}$$

where the negative sign ensures correspondence with observed posteriorisation velocity in experiments.

Estimating relation between aspect ratio and posteriorization velocity

To obtain a relation between the aspect ratio a/b and posteriorization velocity v for the combined set of embryos, the following procedure is used – see Figure 4.29:

1. Estimate $\kappa = \left[\frac{\pi T}{\gamma}\right]$ by fitting a straight line to the posteriorization velocity versus angular position graph for the unperturbed embryos
2. Use the average semi-minor axis length in the combined dataset to transform (4.5) into a relation between a/b and v.
3. Compare relation between aspect ratio and posteriorisation velocity from transformed (4.5) with those from the theoretical model and from experiments.

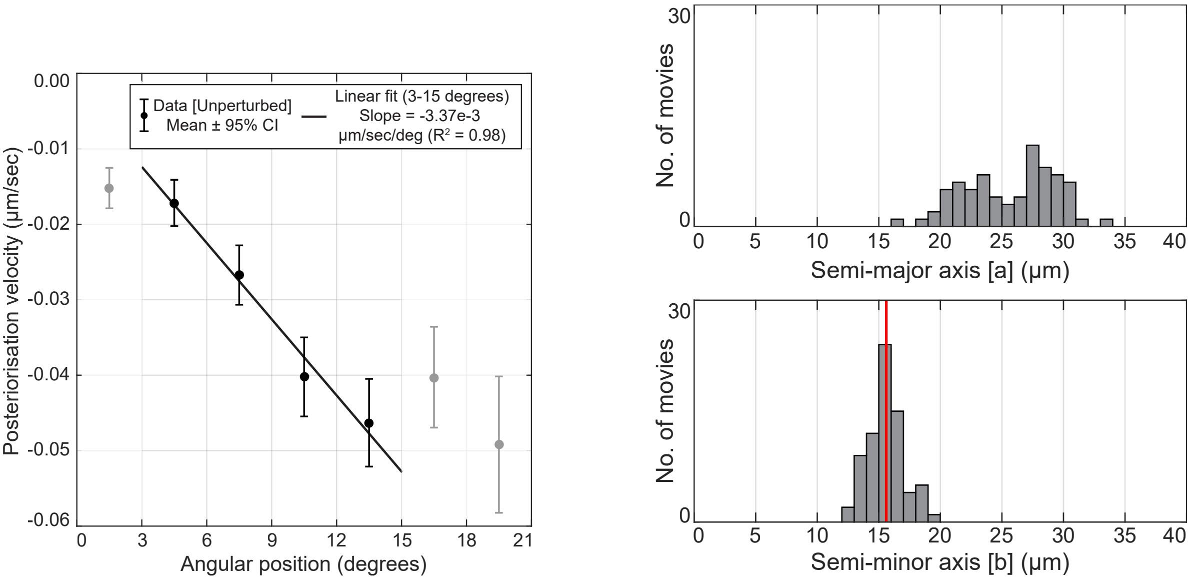

(a) Fitting a line to posteriorization velocity (on y-axis, in μm/s) vs angular position (on x-axis, in deg) plot for unperturbed embryos of SWG070 strain – see Figure 4.3. Black circles with error bars represent average posteriorisation velocity (with 95% confidence interval) in each angular position bin (of bin width 3 deg). Angular position bins from 3–15 deg are chosen for the linear fit, depicted by black line – with slope $m = -3.37 \times 10^{-3}\,\mu\text{m}\,\text{s}^{-1}\,\text{deg}^{-1}$ and intercept $c = 2.3 \times 10^{-3}\,\mu\text{m/s}$.

(b) Histograms of semi-major a (top, x-axis, in μm) and semi-minor b (bottom, x-axis, in μm) axis lengths in the combined (unperturbed and *ima-3* RNAi embryos, both of SWG070 strain) dataset. Bins of size 1 μm are used. Red line in bottom histogram denotes the average semi-minor axis length chosen for the effective model.

Figure 4.29: Procedure used to estimate relation between aspect ratio a/b and posteriorisation velocity v for the combined set of embryos. Figure 4.29a depicts line fit for posteriorisation velocity versus angular position in unperturbed embryos of SWG070 strain. Figure 4.29b depicts selection of average semi-minor axis $b = 15.6 \pm 1.5\,\mu\text{m}$ for the combined set (red line, bottom). Note the wide distribution of semi-major axis lengths a in the combined dataset (top).

To estimate $\kappa = \left[\frac{\pi T}{\gamma}\right]$, the set comprised only of unperturbed embryos is used. Plotting the average posteriorization velocity observed in these unperturbed embryos as a function of the angular position of the male pronucleus, a range of angular positions is chosen where the posteriorization velocity looks mostly linear with respect to the angular position – Figure 4.29a. Here, the following range of angular position is chosen: 3–15 deg. From the slope $m = -3.37 \times 10^{-3}\,\mu\text{m}\,\text{s}^{-1}\,\text{deg}^{-1}$ of the linear fit in the selected angular position range (3–15 deg), κ can be obtained using (4.5) as:

$$m = -\left[\frac{\pi T}{\gamma}\right]\left[a_{un}b_{un}\left(1-\frac{b_{un}^2}{a_{un}^2}\right)\right] = -\kappa\left[a_{un}b_{un}\left(1-\frac{b_{un}^2}{a_{un}^2}\right)\right] \implies \kappa = \frac{-m}{a_{un}b_{un}\left(1-\frac{b_{un}^2}{a_{un}^2}\right)} \tag{4.6}$$

where the subscript un refers to the average semi-major a_{un} and semi-minor b_{un} axes lengths for the unperturbed embryos. From Table 4.1, $a_{un} = 28.7 \pm 1.6\,\mu\text{m}$ and $b_{un} = 16.2 \pm 1.1\,\mu\text{m}$ are obtained. Using (4.6), κ is obtained to be:

$$\kappa = \frac{-(-3.37e-3)}{(28.7)(16.2)\left(1-\frac{(16.2)^2}{(28.7)^2}\right)} = 1.06 \times 10^{-5}\,\text{s}^{-1}\,\text{deg}^{-1}\,\mu\text{m}^{-1} \tag{4.7}$$

To then transform (4.5) into a relation between a/b and v, the distribution of semi-major a and semi-minor b axes length in the combined set of embryos is examined – see Figure 4.29b. While the combined set exhibits a wide range of a, b are mostly concentrated around the average value of $15.6 \pm 1.5\,\mu\text{m}$. Therefore, b is considered to be fairly constant throughout the combined set. This can be used to transform (4.5) as:

$$v \approx -\left[\frac{\pi T}{\gamma}\right]\left[ab\left(1-\frac{b^2}{a^2}\right)\right]\alpha = [\kappa b^2\alpha]\left(\frac{a}{b}\left(1-\frac{b^2}{a^2}\right)\right) = C\left(\frac{a}{b}\left(1-\frac{b^2}{a^2}\right)\right) \tag{4.8}$$

where $C = -\kappa b^2\alpha$ is treated as a constant when considering the relation between a/b and v alone. α is set to 9 deg – the average of the angular positions in 3–15 deg.

Therefore, C can be calculated as:

$$C = -\kappa b^2\alpha = (1.06 \times 10^{-5}\,\text{s}^{-1}\,\text{deg}^{-1}\,\mu\text{m}^{-1})(15.6\,\mu\text{m})^2(9\,\text{deg}) = -2.32 \times 10^{-2}\,\mu\text{m/s} \tag{4.9}$$

Using this in Equation 4.8, the relation between a/b and posteriorisation velocity v can be calculated from the effective model. Comparison between the relation between a/b and posteriorisation velocity obtained using the effective model with that obtained from experimental observations demonstrates that the effective model recapitulates the experimentally observed relation to a reasonable extent – see Figure 4.30. Thus, the effective model – comprising only of two features from the theoretical model: ellipsoidal geometry of the embryo and contractile ring (pseudocleavage furrow) – does indeed capture the relation between embryo geometry and AP axis alignment.

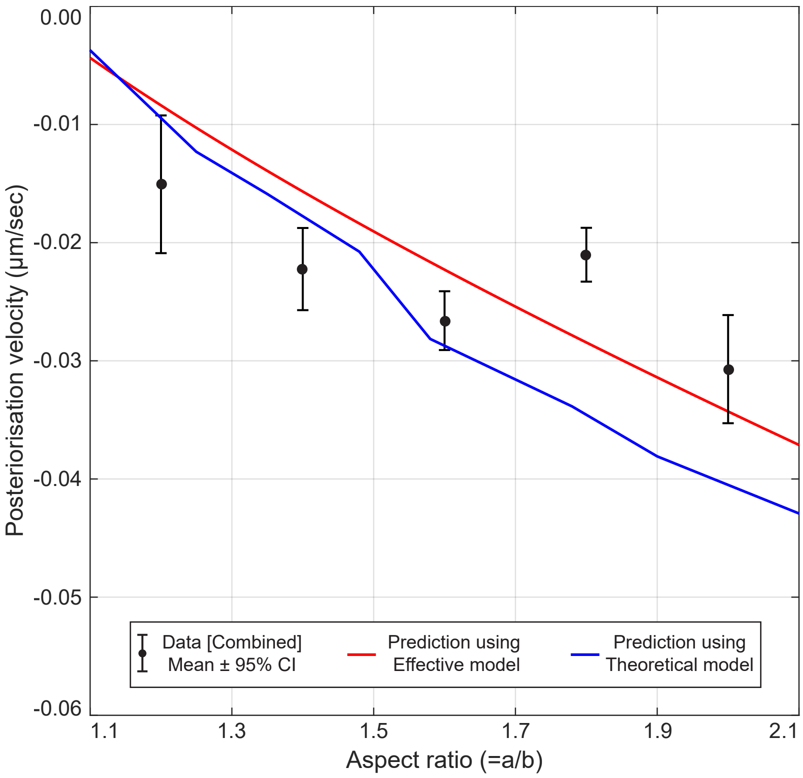

Figure 4.30: Posteriorization velocity in the combined dataset (along y-axis) as a function of aspect ratio (along x-axis) of the embryo, averaged for all angular positions in 3–15 deg. Black circles with error bars represent the average posteriorization velocities (with 95% confidence interval) observed in each aspect ratio bin in the combined dataset. Red line is the prediction obtained using the effective model, and blue line using the full mathematical model.

4.5 Additional experiments

This section describes additional experiments conducted during the course of the work presented here, and their results.

4.5.1 Exploring relation between embryo geometry and AP axis alignment in *ima-3* RNAi embryos

In section 4.4, it was observed that AP axis alignment observed rounder and smaller embryos generated using *ima-3* RNAi is slower compared to that observed in unperturbed embryos – by comparing both posteriorisation velocity of the male pronucleus as a function of its angular position, and angular position of the male pronucleus as a function of time. In that section, the difference between the embryo volume in the two sets of embryos was ignored; only comparison with respect to aspect ratio of the embryo were made.

In this subsection, the distribution of aspect ratios in *ima-3* RNAi embryos (a/b = 1.1–1.9) is leveraged to generate subsets of the set of *ima-3* RNAi embryos with similar volumes but different average aspect ratios. Specifically, *ima-3* RNAi embryos are classified into two subsets based on the aspect ratio of each embryo: round ($a/b < 1.5$) and elliptical ($a/b > 1.5$). The average axes lengths for the round *ima-3* RNAi embryos are found to be $a = 20.8 \pm 2.1\,\mu\text{m}$, $b = 15.3 \pm 1.2\,\mu\text{m}$; and that for the elliptical *ima-3* RNAi embryos are found to be $a = 23.2 \pm 1.8\,\mu\text{m}$, $b = 14.2 \pm 1.0\,\mu\text{m}$. Average volume of embryos in these two subsets are found to not be significantly different: $20.7 \pm 4.5 \times 10^3\,\mu\text{m}^3$ in round embryos compared to $19.8 \pm 3.8 \times 10^3\,\mu\text{m}^3$ in elliptical embryos. The volume for each embryo is calculated using the length of long ($2a_{emb}$) and short ($2b_{emb}$) axes measured for that embryo – its volume is calculated as the volume of an ellipsoid with a long axis of the same length as the long axis of the embryo and two equal short axes of the same length as the short axis of the embryo (volume = $4\pi/3\ a_{emb}b_{emb}^2$). Cortical flows between the two subsets are also found to be comparable. Specifically, average cortical speed of $4.23 \pm 0.50\,\mu\text{m/min}$ for round embryos compared to $3.77 \pm 0.40\,\mu\text{m/min}$ for elliptical embryos was observed. To then compare the AP axis alignment process between the two subsets, average posteriorisation velocity as a function of angular position observed in the round embryos are compared to those observed in the elliptical embryos. In general, it is observed that round embryos exhibit slower average posteriorisation velocity compared to those observed in elliptical embryos, with larger differences at higher angular positions. Specifically, it is observed that round and elliptical embryos exhibit similar average posteriorisation velocity for angular positions upto 9 deg; for higher angular positions, round embryos have slower average posteriorisation velocity compared to elliptical ones. However, note that the difference between the average posteriorisation velocity observed in round and elliptical embryos is not as large as that observed between the *ima-3* RNAi embryos (as a whole) and unperturbed embryos.

Altogether, these observations reconfirm the result from subsection 4.4.1 – rounder embryos indeed show diminished AP axis alignment. These observations also indicate that the relevant parameter related to embryo geometry that influences AP axis alignment is the aspect ratio of the embryo, while differences in embryo volume may be neglected for the relation between embryo geometry and AP axis alignment.

ima-3 RNAi subset	No. of Embryos	Semi-Major axis a (µm)	Semi-Minor axis b (µm)	Cortical flow speed (µm/min)	Volume (1×10^3 µm^3)
Round ($a/b < 1.5$)	17	20.8 ± 2.1	15.3 ± 1.2	4.23 ± 0.50	20.7 ± 4.5
Elliptical ($a/b > 1.5$)	18	23.2 ± 1.8	14.2 ± 1.0	3.77 ± 0.40	19.8 ± 3.8

Table 4.12: Properties of embryos in each subset created by a/b in *ima-3* RNAi embryos.

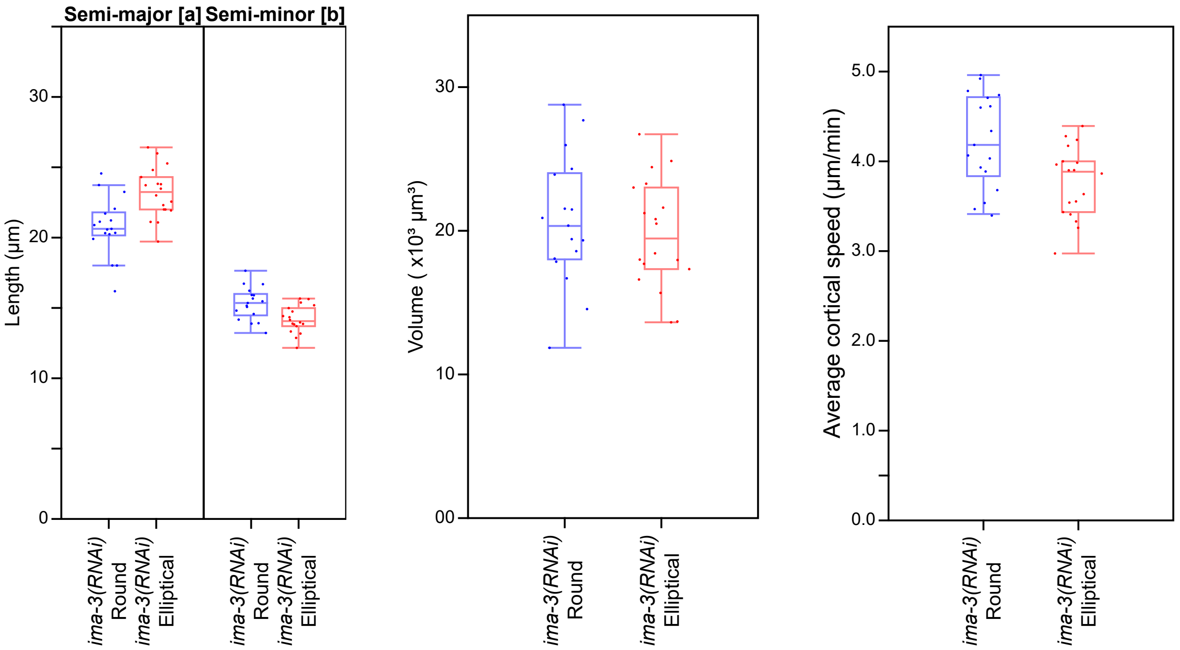

(a) Comparing embryo axes lengths. p-value $= 7.52 \times 10^{-4}$ for semi-major axis comparison, p-value $= 3.5 \times 10^{-3}$ for semi-minor axis comparison.

(b) Comparing embryo volumes. p-value = 0.52.

(c) Comparing average cortical speeds in embryos. p-value $= 6.3 \times 10^{-3}$.

Figure 4.31: Comparing embryo geometry and cortical flow speeds between round and elliptical *ima-3* RNAi embryos. Semi-major a and semi-minor b axes lengths (Figure 4.31a), volume (calculated using measured semi-major and semi-minor axis lengths, Figure 4.31b) and average cortical flow speed (Figure 4.31c) are compared. Datapoints represent axes lengths, volume and average cortical flow speed measured for individual embryos in Figure 4.31a, Figure 4.31b and Figure 4.31c respectively. p-values are calculated using a two-sided t-test.

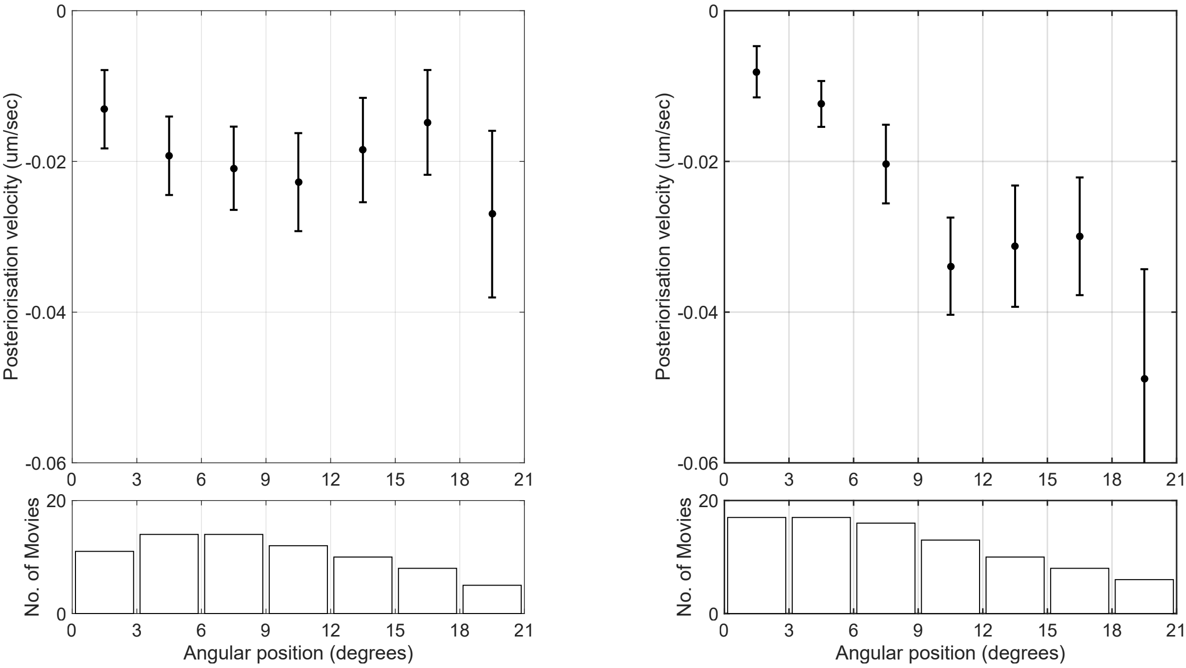

(a) Posteriorisation velocity observed in round *ima-3* RNAi embryos

(b) Posteriorisation velocity observed in elliptical *ima-3* RNAi embryos

Figure 4.32: Top: Posteriorization velocity of the male pronucleus (along y-axis, in µm/s) plotted against its angular position, in round (N = 17, Figure 4.32a) and elliptical (N = 18,Figure 4.32b) embryos of SWG070 strain. Negative values of the posteriorisation velocity indicate movement towards the posterior end. Angular position is binned using a bin width of 3 deg. Black circles with errors bars denote the average posteriorization velocity with 95% confidence intervals in each angular position bin. Bottom: Histogram of the number of movies (along y-axis) contributing to each angular position (along x-axis) bin. A movie is considered to contribute to an angular position bin if it has any frames with angular positions within that bin. Note that a movie can contribute to multiple bins, as it may contain frames spanning different angular positions.

4.5.2 Are pseudocleavage furrow-dependent and cytoplasmic flow-dependent mechanisms sufficient to explain AP axis alignment?

Decoupling positions of male pronucleus and polarisation trigger via *air-1* RNAi

In section 1.4, the mechanism of AP axis establishment, and the role of polarisation trigger provided by the centrosomes anchored to the male pronucleus during this process, are discussed. Given this anchoring between the male pronucleus and centrosomes [205], the position of the male pronucleus has been used in previous sections as a proxy to the position of the polarisation trigger, and thus the instantaneous orientation of the AP axis. Here, it is investigated if this link between the position of the male pronucleus and polarisation trigger could be broken, and the effect on AP axis alignment.

To do so, an RNAi of *air-1* is performed on worms of SWG070 strain for a feeding time of 24 hours (see section 3.2 for details on RNAi). AIR-1 (or Aurora Kinase A) is a serine/theronine kinase that is essential for centrosome maturation [206], among other functions related to mitotis and cytokinesis [155]. Previous studies have observed that RNAi-mediated depletion of *air-1* leads to embryos with multiple pPARs domains instead of a single one observed in unperturbed embryos, along with two pseudocleavage furrows [155, 156]. Additionally, in these RNAi embryos the centrosome is dispensible for positioning of the AP axis [155, 156].

Observations made here in *air-1* RNAi are found to be consistent with those made in these previous studies [155, 156]. Specifically, *air-1* RNAi embryos were observed to typically exhibit two pseudocleavage furrows, alongwith two domains where myosin is depleted – representing the two pPARs domains. Interestingly, the two myosin depletion domains form on the opposite ends of the embryo – that is, always aligned along the long axis of the embryo. Cortical flows observed in the RNAi embryos were found to be slower but comparable to those observed in unperturbed embryos: average cortical flow speed in RNAi embryos was measured to be 3.04 ± 0.84 µm/min compared to 4.12 ± 0.59 µm/min in unperturbed embryos – see Figure 4.35. However, no decay towards 0 deg is observed in the angular position of the male pronucleus with time, and very slow posteriorisation velocities are observed for all angular positions – see Figure 4.34 and Figure 4.36. Thus, the male pronucleus does not posteriorise in the *air-1* RNAi embryos, indicating that the RNAi embryos do not need the male pronucleus to "guide" the positioning of pPARs domain(s) (guidance here refers to centrosomes anchored to the male pronucleus – see [1]). This is consistent with the results of [156] and [155], which show that the centrosomes are dispensable for positioning of the AP axis in *air-1* RNAi embryos. However, even with no guidance from the centrosomes, polarisation in *air-1* RNAi embryos is observe to align with the long axis of the embryo.

	No. of embryos
Polarisation aligned with long axis	23
Two pseudocleavage furrows observed	14
Total number of embryos	23

Table 4.13: Number of embryos with different features in *air-1* RNAi embryos of SWG070 strain.

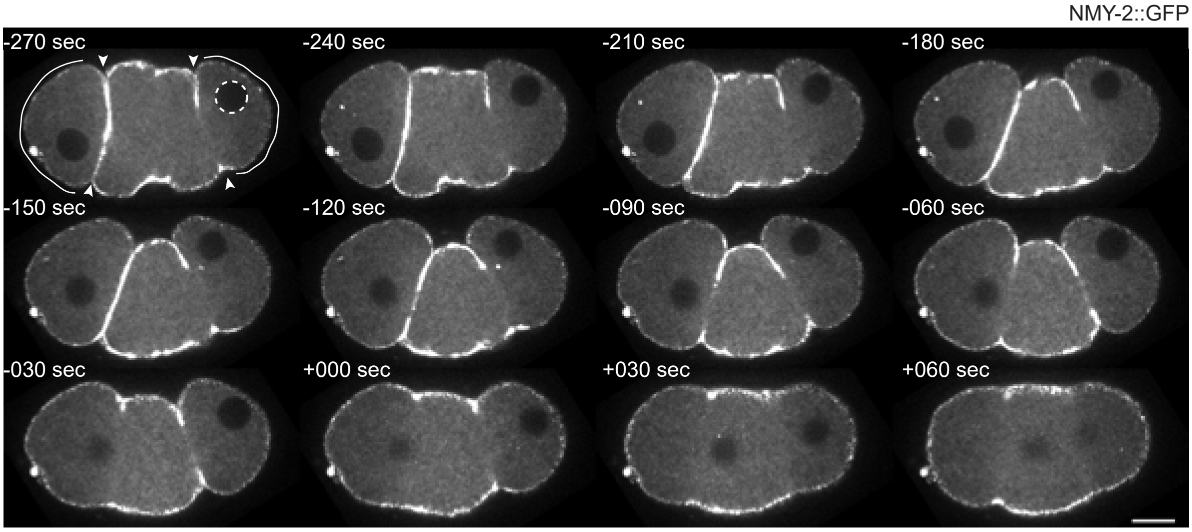

Figure 4.33: Representative *air-1* RNAi embryo of SWG070 strain, labelled with NMY-2::GFP (white), showing the 2 pseudocleavage furrows (white arrows) and 2 myosin depletion domains (white lines) that form on the anterior and posterior end. Note that the anterior and posterior myosin depletion domains form along the long axis of the embryo. Male pronucleus is indicated by white dashed circle. T = 0 s is set at the end of posteriorisation of the male pronucleus. Scale bar: 10 µm. Images are rotated such that anterior and posterior ends are to the left and right respectively.

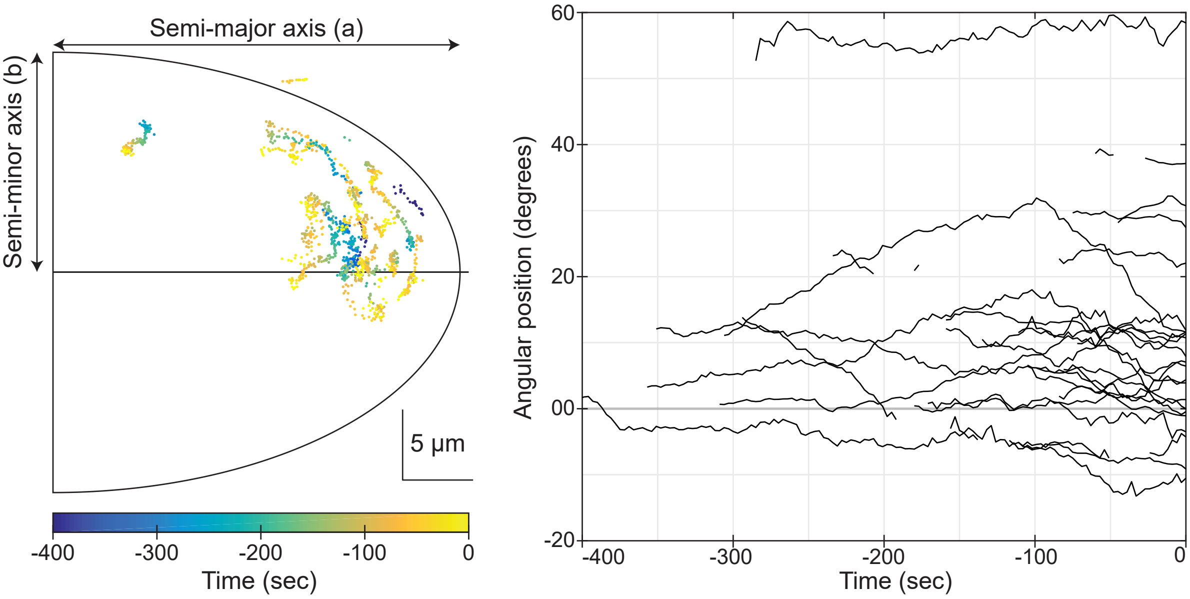

(a) Trajectories of the male pronucleus (denoted by the coordinates of its center) observed in *air-1* RNAi embryos. Color represents time. x- and y-axes lie along the long and short axes of an ellipse with semi-major axis $a = 28.9\,\mu m$ and semi-minor axis $b = 15.6\,\mu m$. Scale bar: 5 µm

(b) Angular position of the male pronucleus (on y-axis, in deg) plotted as a function of time (on x-axis, in s), in *air-1* RNAi embryos. Black lines represent individual trajectories.

Figure 4.34: Experimentally observed trajectories of the male pronucleus in *air-1* RNAi embryos of SWG070 strain (N = 23). See subsection 3.4.2 for details on male pronucleus tracking. Average semi-major and semi-minor axes lengths for *air-1* RNAi embryos of SWG070 strain are used in Figure 4.34a – see Table 4.11. Angular position is defined as the angle between the long axis and line connecting the centers of the male pronucleus and embryo. T = 0 s denotes end of posteriorisation.

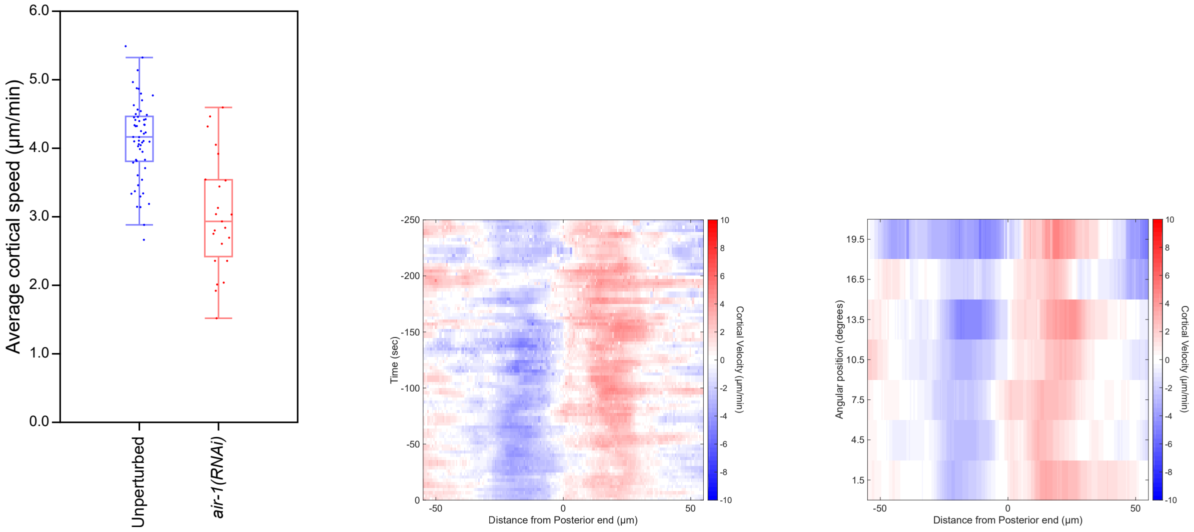

(a) Comparison of average cortex flow speeds between unperturbed embryos (N = 57, blue) and *air-1* RNAi embryos (N = 23, red), both from the SWG070 strain. Datapoints represent average cortical flow speeds measured for individual embryos.

(b) Average cortical flow velocity (color, in µm/min) plotted as a function of time (along y-axis, in s, t = 0 s denotes end of posteriorization) and position on the cortex (along x-axis, in µm, s=0 µm denotes posterior end), as observed in *air-1* RNAi embryos. See Figure 4.6 for details and comparison.

(c) Average cortical flow velocity (color, in µm/min) plotted as a function of angular position of the male pronucleus (along y-axis, in deg) and position on the cortex (along x-axis, in µm, s=0 µm denotes posterior end), as observed in *air-1* RNAi embryos. Angular positions are binned with bin width 3 deg. See Figure 4.7 for details and comparison.

Figure 4.35: Experimentally observed cortical flows in *air-1* RNAi embryos of SWG070 strain (N = 23). See subsection 3.4.3 for details on measuring cortical flows.

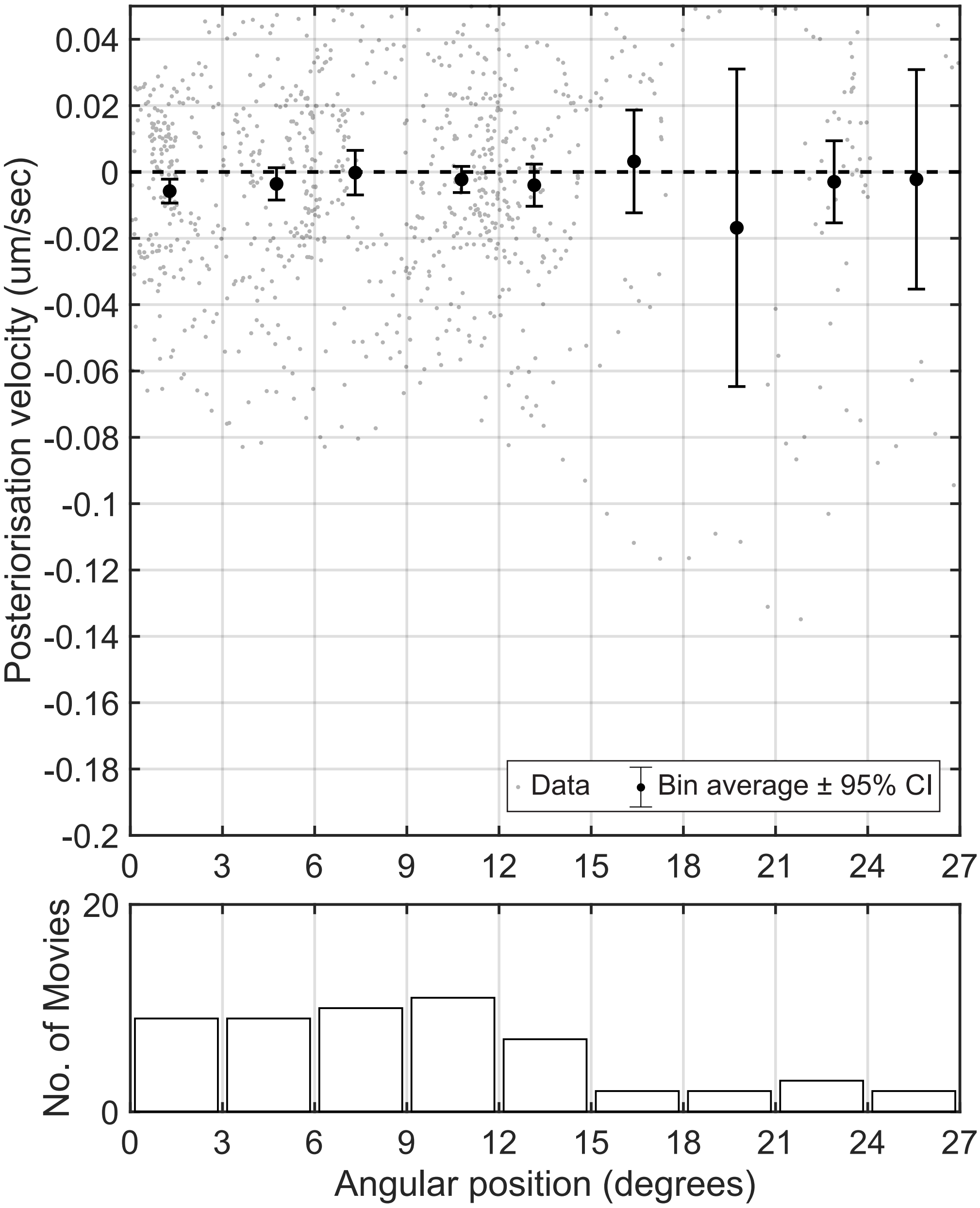

Figure 4.36: Top: Posteriorization velocity of the male pronucleus (along y-axis, in µm/s) plotted against its angular position, in *air-1* RNAi embryos of SWG070 strain (N = 23). Negative values of the posteriorisation velocity indicate movement towards the posterior end. Angular position is binned using a bin width of 3 deg. Black circles with errors bars denote the average posteriorization velocity with 95% confidence intervals in each angular position bin. Grey circles represent the data scatter – the measured posteriorization velocities for different angular positions in each embryo (see subsection 3.4.2). Bottom: Histogram of the number of movies (along y-axis) contributing to each angular position (along x-axis) bin. A movie is considered to contribute to an angular position bin if it has any frames with angular positions within that bin. Note that a movie can contribute to multiple bins, as it may contain frames spanning different angular positions.

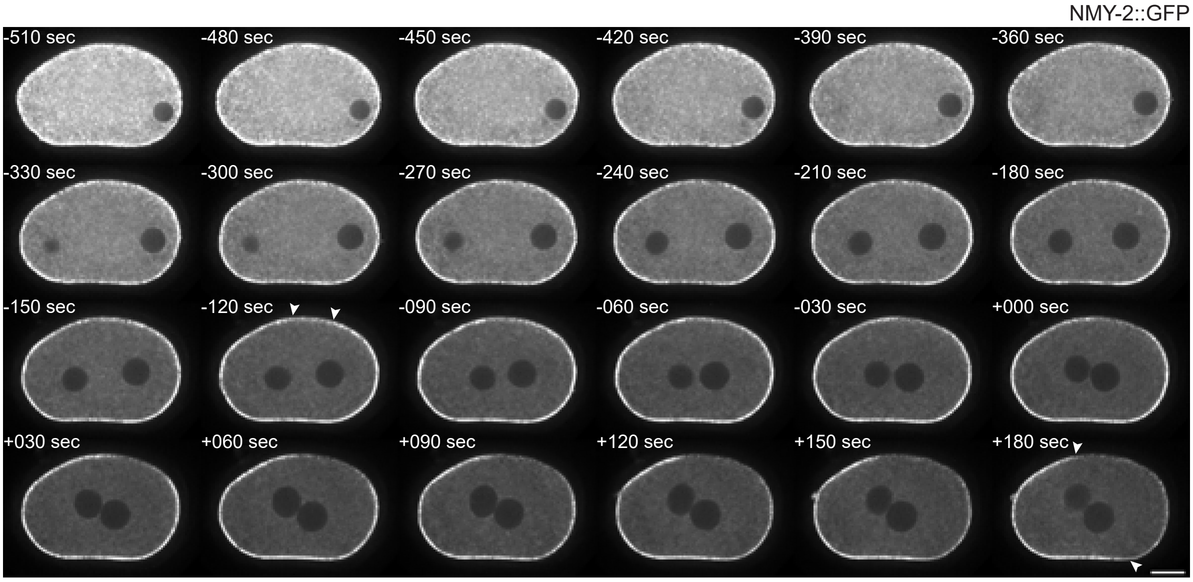

Figure 4.37: Representative *air-1; mel-11* RNAi in *nop-1* mutant embryo of SWG228 strain, labelled with NMY-2::GFP (white). Note the lack of pseudocleavage furrow. White arrows indicate the myosin depletion domain (indicating the pPARs domain) which initiates away from the male pronucleus. Note that this domain is not along the long axis of the embryo. Scale bar: 10 µm. Images are rotated such that anterior and posterior ends are to the left and right respectively.

In the theoretical model, the male pronucleus is advected by flows in the cytoplasm – see chapter 2. If however the male pronucleus is no longer coupled to the polarisation trigger, as seems to be case in *air-1* RNAi embryos, then one may expect that the advection of the male pronucleus by cytoplasmic flows should have no effect on embryo polarisation. Thus, in *air-1* RNAi embryos, cytoplasmic flow-dependent mechanism is unlikely to play a role in the alignment of the AP axis observed in *air-1* RNAi embryos. The pseudocleavage furrow-dependent mechanism enforces a rotation in the cortex itself, and thus should be less impacted by the broken coupling between the male pronucleus and polarisation trigger in *air-1* RNAi embryos. Thus, *air-1* RNAi may be a possible genetic perturbation to disable the cytoplasmic flow-dependent mechanism for AP axis alignment.

Suppressing both mechanisms via *air-1; mel-11* RNAi in *nop-1* mutant

To test if the AP axis still aligns with the long axis after both the cytoplasmic-flow dependent and pseudocleavage furrow-dependent mechanism are disabled, a double RNAi of *air-1; mel-11* is performed on *nop-1* mutant worms from the SWG228 strain for a feeding time of 24 hours (see section 3.2 for details on RNAi). This combines the two conditions we considered before: RNAi of *air-1* to disable cytoplasmic flow-dependent mechanism, and RNAi of *mel-11* in *nop-1* mutant background to disable the pseudocleavage furrow-dependent mechanism. *nop-1* mutant worms were chosen due to the difficulty in performing a triple RNAi condition and since *nop-1* mutation is not lethal.

As expected from observations in *nop-1; mel-11* RNAi embryos, no pseudocleavage furrows are

	No. of embryos
Myosin depletion domain starts away from poles	7
AP axis alignment fails	6
Total number of embryos	13

Table 4.14: AP axis alignment in *air-1; mel-11* RNAi in *nop-1* mutant embryos of SWG228 strain.

observed in *air-1; mel-11* RNAi in *nop-1* mutant embryos (13 out of 13 embryos). However, the domain where myosin is depleted (indicating the pPARs domain) is observed to not re-align back towards the tip of the embryo (6 out of 13 embryos), in the few embryos that start with a myosin depletion domain away from the poles of the embryos (7 out of 13 embryos) – see Table 4.14. These preliminary experiments seem to suggest that AP axis alignment is heavily suppressed in *air-1; mel-11* RNAi in *nop-1* mutant embryos – however, additional experimental data are needed for a conclusive result.

4.5.3 Role of microtubules in AP axis alignment

In section 1.4, the mechanism of AP axis establishment is discussed, including the polarity trigger provided by the centrosomes associated with the male pronucleus that initiate AP axis establishment. Microtubule asters emanating from these centrosomes play a key role in the AP axis establishment process, by protecting the nascent pPARs domain that forms on the cortex near the male pronucleus [1, 133]. In the investigation of the mechanism(s) driving AP axis alignment so far, any role of the astral microtubules emanating from the centrosomes have been neglected. A possible way in which these microtubules could influence the posteriorisation of the male pronucleus is via forces generated by dynein motors anchored at the cortex that pull on the astral microtubules abutting the cortex. As discussed in subsection 1.1.1, dynein motors are one of two families of motor proteins that bind to microtubules. They are (-)-end directed motor proteins [205]. Previous studies have explored the role of dynein motors in the positioning of centrosomes. Especially, dynein motors anchored to the cortex have been found to be influential in positioning the mitotic spindle, by pulling onto astral microtubules [205, 207–209]. Here, it is investigated if such pulling forces generated at the cortex by cortical dynein motors could influence the posteriorisation of the male pronucleus observed during AP axis alignment.

In this subsection, embryos from the SWG057 strain are used – instead of the SWG070 strain that has been used so far. SWG057 strain is labelled with TUB::GFP – which labels tubulin monomers that form the microtubules – and NMY-2::mKate. Thus this strain allows visualisation of both the microtubules and the centrosomes, and cortical myosin – while still allowing tracking of the position of the male pronucleus as a dark circle in the myosin channel – see section 3.4 for details on how movies generated with embryos from SWG057 were analysed. As with the SWG070, time-lapse microscopy movies of one-cell stage embryos generated from SWG057 strain were taken – see section 3.3 for details on microscopy.

The rate of AP axis alignment in unperturbed embryos of the SWG057 strain is characeterised by measuring the posteriorisation velocity of the male pronucleus as a function of angular position of the male pronucleus in these embryos. In unperturbed embryos, the male

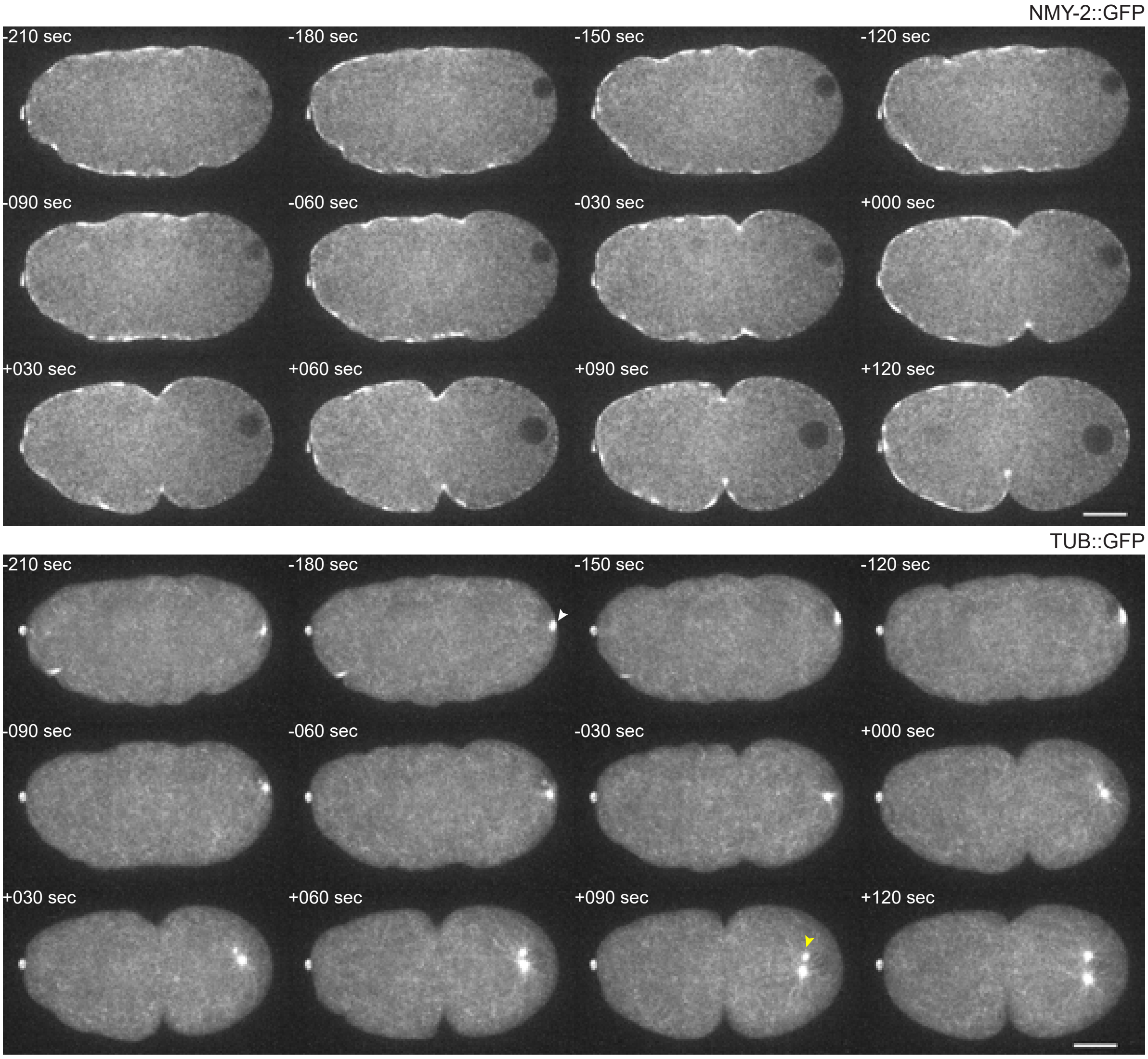

Figure 4.38: Representative unperturbed embryo of SWG057 strain, labelled with NMY-2::mKate (top) and TUB::GFP (bottom), showing the posteriorisation of the male pronucleus. Bottom: White arrow indicates centrosomes, yellow arrow indicates the separation of centrosomes during pronuclear meeting. Scale bar: 10 µm. Images are rotated such that anterior and posterior ends are to the left and right respectively.

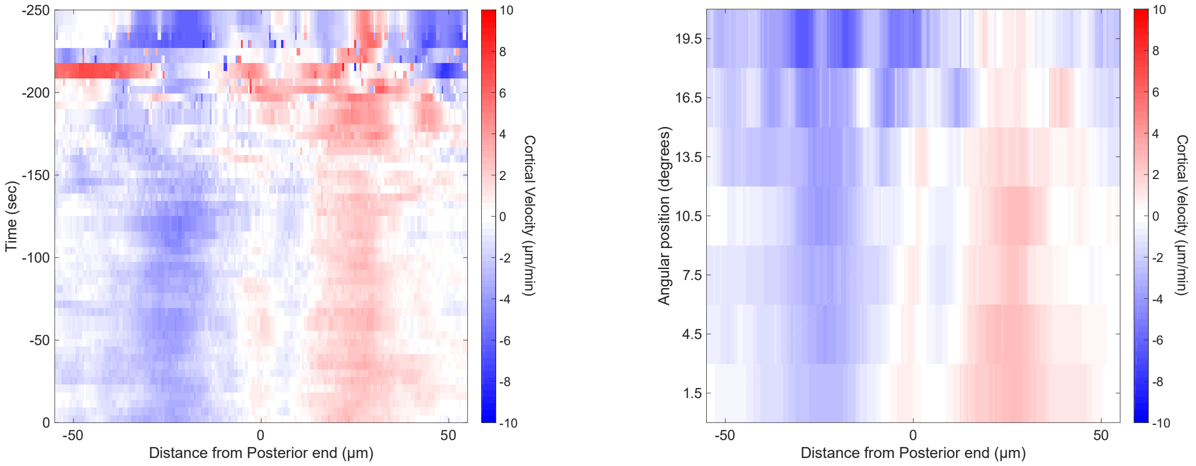

(a) Average cortical flow velocity (color, in µm/min) plotted as a function of time (along y-axis, in s, t = 0 s denotes end of posteriorization) and position on the cortex (along x-axis, in µm, s=0 µm denotes posterior end), as observed in unperturbed embryos of SWG057 strain. See Figure 4.6 for details and comparison.

(b) Average cortical flow velocity (color, in µm/min) plotted as a function of angular position of the male pronucleus (along y-axis, in deg) and position on the cortex (along x-axis, in µm, s=0 µm denotes posterior end), as observed in unperturbed embryos of SWG057 strain. Angular positions are binned with bin width 3 deg. See Figure 4.7 for details and comparison.

Figure 4.39: Experimentally observed cortical flows in unperturbed embryos of SWG057 strain (N = 32). See subsection 3.4.3 for details on measuring cortical flows.

pronucleus is observed to move, on average, towards the posterior end – with faster posteriorisation velocity at higher angular positions – see Figure 4.42a. Cortical flows in unperturbed embryos from SWG057 strain were also measured – see section 3.4 for methods – yielding an average cortical speed of $2.84 \pm 0.37\,\mu\text{m/min}$ for the unperturbed embryos of SWG057 strain – see Figure 4.39. Observed cortical flows are binned using angular positions of the male pronucleus – see section 3.5. The point where the cortical flows change sign is observed to correlate with the angular position. Given that these observations are similar to those made for the unperturbed embryos from the SWG070 strain (see section 4.1), it is concluded that the unperturbed embryos from SWG057 exhibit similar AP axis alignment characteristics as compared to unperturbed embryos from SWG070. Note however that the cortical flows observed in unperturbed embryos of the SWG057 strain are slower compared to those observed in the unperturbed embryos of the SWG070 strain.

To test if cortically anchored dynein motors pulling on astral microtubules influence AP axis alignment, the proteins that anchor the dynein motors to the cortex are suppressed. Specifically, a double RNAi of *goa-1* and *gpa-16* is performed on worms of SWG057 strain for a feeding time of 24 hours (see section 3.2 for details on double RNAi). GOA-1 and GPA-16 are heterotrimeric Gα proteins that, along with GPR-1/2 and LIN-5, help anchor dynein at the cortex [205, 208, 209]. Thus, their reduction via the double RNAi leads to depletion of cortically anchored dynein motors [205]. Cortical flows measured in *goa-1; gpa-16* RNAi embryos are compared with those observed in unperturbed embryos, both of the SWG057 strain. On comparison, the cortical flows in the two sets of embryos are found to not be significantly different, with a measured average cortical speed of $2.62 \pm 0.52\,\mu\text{m/min}$ in *goa-1; gpa-16* RNAi embryos compared to $2.84 \pm 0.37\,\mu\text{m/min}$ in unperturbed embryos – see Figure 4.41. Finally, the posteriorisation velocity observed in *goa-1; gpa-16* RNAi embryos are compared to those observed in unperturbed embryos, for different angular positions – finding not much difference between the two, for all angular positions considered (0–21 deg), and therefore implying that the posteriorisation of the male pronucleus does not differ significantly between *goa-1; gpa-16* RNAi embryos and unperturbed embryos – see Figure 4.42. These observations indicate that the double RNAi *goa-1; gpa-16* does not significantly affect either the cortical flow or the posteriorisation of the male pronucleus. Altogether, these observations lead to the conclusion that the forces generated by cortical dynein as they pull on astral microtubule do not play an significant role in AP axis alignment.

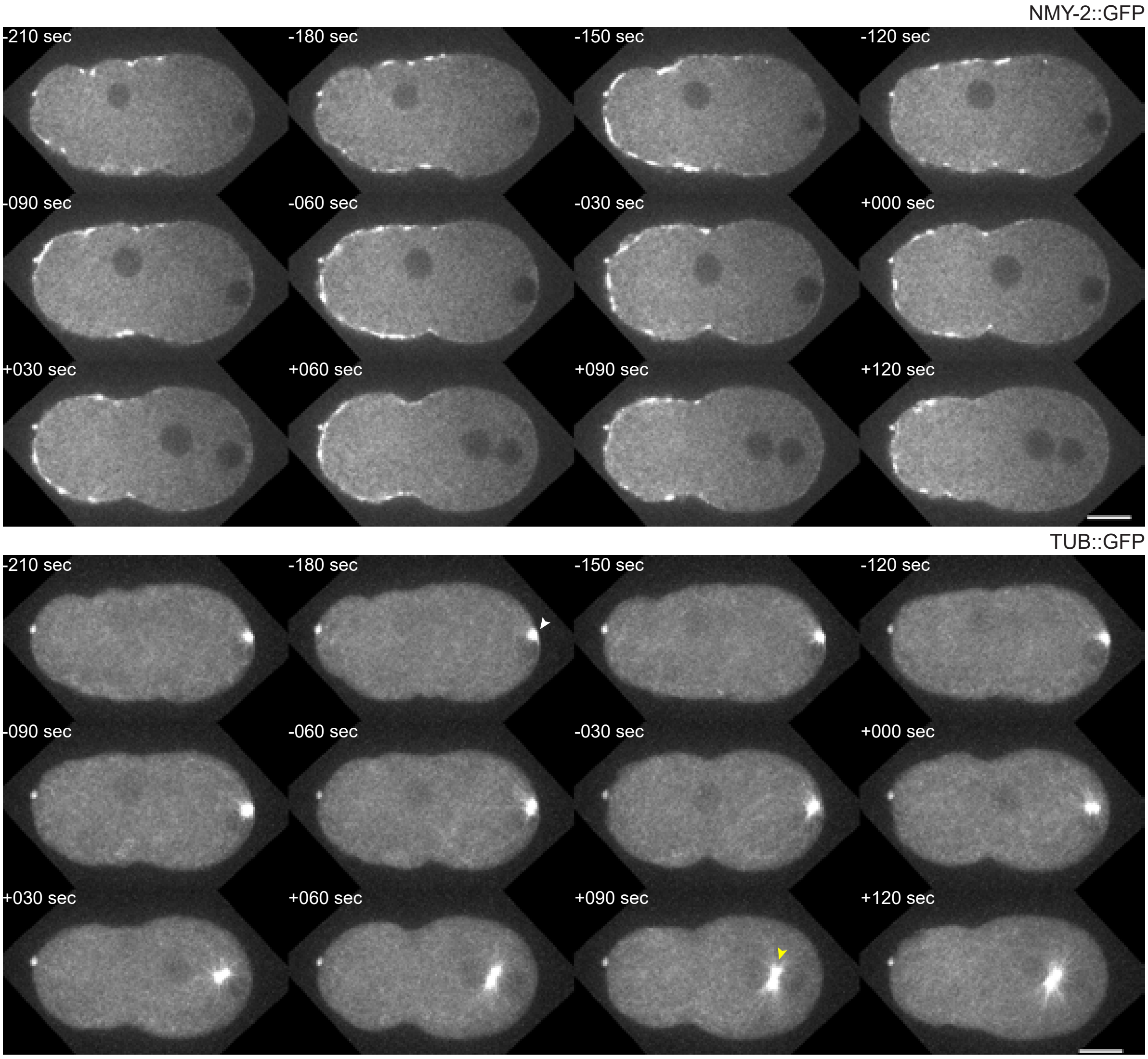

Figure 4.40: Representative *goa-1; gpa-16* RNAi embryo of SWG057 strain, labelled with NMY-2::mKate (top) and TUB::GFP (bottom), showing the posteriorisation of the male pronucleus. Bottom: White arrow indicates centrosomes, yellow arrow indicates the separation of centrosomes during pronuclear meeting. Compare to Figure 4.38 – *goa-1; gpa-16* RNAi embryos exhibit smaller separation between centrosomes [205]. Scale bar: 10 µm. Images are rotated such that anterior and posterior ends are to the left and right respectively.

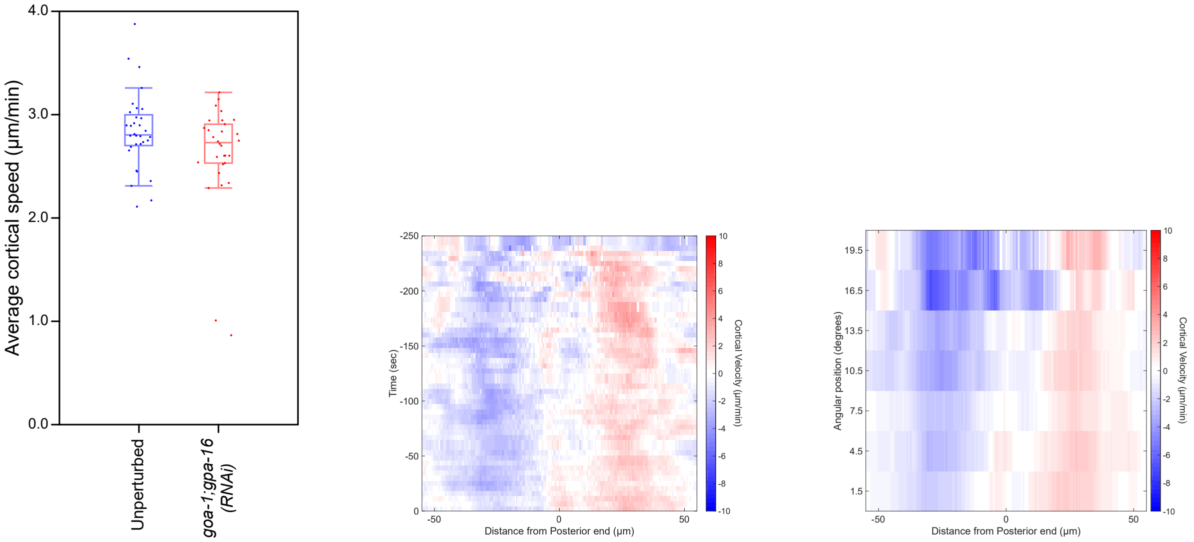

(a) Comparison of average cortex flow speeds between unperturbed embryos (N = 32, blue) and *goa-1; gpa-16* RNAi embryos (N = 30, red), both from the SWG057 strain. Datapoints represent average cortical flow speeds measured for individual embryos.

(b) Average cortical flow velocity (color, in µm/min) plotted as a function of time (along y-axis, in s, t = 0 s denotes end of posteriorization) and position on the cortex (along x-axis, in µm, s=0 µm denotes posterior end), as observed in *goa-1; gpa-16* RNAi embryos of SWG057 strain. See Figure 4.6 for details and comparison.

(c) Average cortical flow velocity (color, in µm/min) plotted as a function of angular position of the male pronucleus (along y-axis, in deg) and position on the cortex (along x-axis, in µm, s=0 µm denotes posterior end), as observed in *goa-1; gpa-16* RNAi embryos of SWG057 strain. Angular positions are binned with bin width 3 deg. See Figure 4.7 for details and comparison.

Figure 4.41: Experimentally observed cortical flows in *goa-1; gpa-16* RNAi embryos of SWG057 strain (N = 30). See subsection 3.4.3 for details on measuring cortical flows. p-value = 0.14 for comparison between average cortical flow speeds in Figure 4.41a, after removing outliers. p-value calculated via a two-sided t-test.

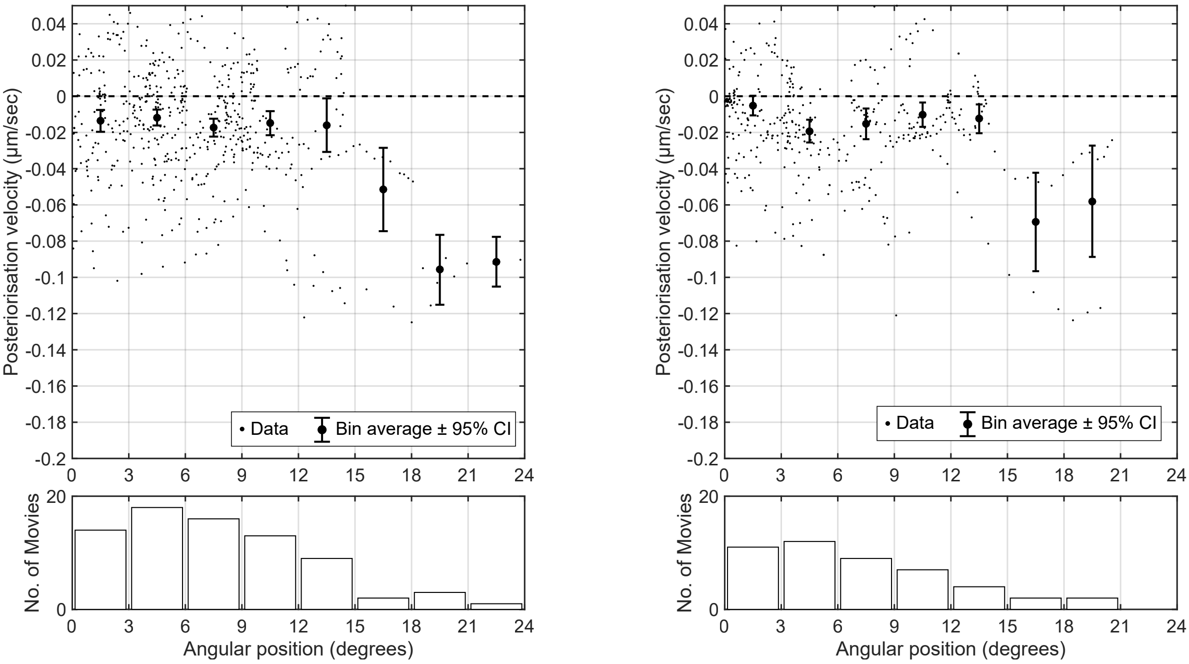

(a) Posteriorisation velocity observed in unperturbed embryos of SWG057 strain

(b) Posteriorisation velocity observed in *goa-1; gpa-16* RNAi embryos of SWG057 strain

Figure 4.42: Top: Posteriorization velocity of the male pronucleus (along y-axis, in µm/s) plotted against its angular position, in unperturbed (N = 32, Figure 4.42a) and *goa-1; gpa-16* RNAi (N = 30,Figure 4.42b) embryos of SWG057 strain. Negative values of the posteriorisation velocity indicate movement towards the posterior end. Angular position is binned using a bin width of 3 deg. Black circles with errors bars denote the average posteriorization velocity with 95% confidence intervals in each angular position bin. Black circles represent the data scatter – the measured posteriorization velocities for different angular positions in each embryo (see subsection 3.4.2). Bottom: Histogram of the number of movies (along y-axis) contributing to each angular position (along x-axis) bin. A movie is considered to contribute to an angular position bin if it has any frames with angular positions within that bin. Note that a movie can contribute to multiple bins, as it may contain frames spanning different angular positions. Data only available until 21 deg for *goa-1; gpa-16* RNAi embryos.

Chapter 5

Conclusions and Outlook

In the *C. elegans* embryo, the AP axis is established at the one-cell stage. It has been observed that the AP axis always forms along the long axis of the embryo, and that the former re-orients to align with the latter [6]. The aim of the work presented in this thesis was to elucidate the mechanism behind this AP axis alignment in the *C. elegans* embryo. Two possible mechanisms of AP axis alignment, arising as a consequence of flows in the actomyosin cortex of the *C. elegans* embryos, were considered in this thesis (as depicted in Figure 1.8):

Cytoplasmic flow-dependent Mechanism

Cortical flows at the embryo surface drive flows in the bulk cytoplasm [137]. The cytoplasmic flows thus generated have been observed to be directed towards the male pronucleus as it posteriorises [6]. It was proposed that these flows could push onto the male pronucleus [163], and owning to the geometry of the embryo in which the flows operate, push the male pronucleus towards the closest tip [6]. This mechanism was proposed in [6].

Pseudocleavage furrow-dependent Mechanism

Cortical flows also lead to the formation of the pseudocleavage furrow by compressive alignment of actin filaments in the cortex. The pseudocleavage furrow is a contractile ring-like structure that forms at the boundary of the PAR that specify the AP axis – and thus perpendicular to the instanteous AP axis. It was proposed in this thesis that the rotation of the pseudocleavage furrow as it minimizes its circumference would drive the rotation of the cortex and re-orient the AP axis towards the long axis of embryo.

In chapter 2, a theoretical model of AP axis alignment was described that incorporates these two mechanisms. This quasi-steady state theoretical model consists of the description of the cortex as an active nematic fluid on the surface of a fixed ellipsoid that represents the embryo, the description of the cytoplasm as a Newtonian fluid filling the bulk of the ellipsoid (following [137]) and the description of the transport of the male pronucleus via advection by cytoplasmic flows and drag with the cortex. The description of the cortex in the theoretical model is constructed by integrating elements of the descriptions of the cortex used in [1] and [88] into a general hydrodynamic theory of active compressible nematic fluids [85], and converted to a suitable surface description using the thin film limit [175]. The two mechanisms listed above are incorporated via two different active stresses in this description of the cortex, as shown in

Equation 2.45 for the cortical flow velocity v (reproduced here):

$$
\begin{aligned}
&-\lambda_H \left[\text{div grad}\, \vec{v} + \mathcal{K}\vec{v} + \frac{1}{3}\text{grad div}\, \vec{v} \right] + \vec{v} \\
&\qquad\qquad = \lambda_A \text{grad} \left(\frac{M}{M + M_*} \right) + \lambda_N \text{grad} \left[\left(\frac{M}{M + M_*} \right) \left(\frac{1}{2\sqrt{2}} \|\mathbf{Q}\| \mathbf{g} + \frac{1}{2}\mathbf{Q} \right) \right]
\end{aligned}
$$

where M is the myosin concentration [1], Q characterises the local alignment of actin filaments [88] and the parameters λ_H, λ_A and λ_N characterise the passive and active stresses in the cortex relative to frictional drag with respect to the eggshell and cytoplasm – with λ_H characterising the passive viscous stress, λ_A characterising the active isotropic stress and λ_N characterising the active anisotropic stress generated by the local alignment of actin filaments (see section 2.3 for details). In the cytoplasmic flow-dependent mechanism, only the active isotropic stress characterised by λ_A is considered [1, 77]; while in the pseudocleavage furrow-dependent mechanism, the active anisotropic stress is also considered [88]. In effect, the strength of the pseudocleavage furrow-dependent mechanism is characterised by λ_N. Note that the active isotropic stress is generated solely by the action of myosin motors in the cortex, while the active anisotropic stress is generated as a result of local alignment of actin filaments and their interaction with the myosin motors. This active anisotropic stress is responsible for the contractile nature of the pseudocleavage furrow [88]. Such a distinction effectively implies two different descriptions of the cortex in the two mechanisms of AP axis alignment considered here: the cytoplasmic flow-dependent mechanism effectively considers an active isotropic cortex with only myosin motors as relevant for force generation, while the pseudocleavage furrow-dependent mechanism considers the full active nematic description with both myosin motors and actin filaments relevant for force generation in the cortex. These three parameters, along with d that characterises the cortical drag on the male pronucleus (see Equation 2.49) comprise the full set of model parameters that need to be determined for numerical simulations of the theoretical model. These parameters are determined by calibrating the model with experimentally observed cortical flows, as described in subsection 2.3.3 and subsection 4.3.2.

The experimental methods and materials are detailed in chapter 3. In particular, the image analysis used to track the male pronucleus as it migrates towards the posterior end (that is, the closest tip of the embryo) is described. This migration of the male pronucleus, termed posteriorisation, is used as the readout of the AP axis alignment – given the role of the male pronucleus as an organizer of AP axis establishment via the centrosomes associated with it. Specifically, the "Posteriorisation velocity" of the male pronucleus – the component of its velocity that is parallel to the cortex is obtained as a function of the "Angular position" of the male pronucleus – the angle between the long axis and the line connecting the center of the male pronucleus to the center of the embryo.

The experimental results and their comparisons to numerical simulations are detailed in chapter 4. In section 4.1, it is observed in unperturbed embryos that the posteriorisation velocity is faster at higher angular positions, indicating that the rate of re-orientation of the AP axis increases the further away the male pronucleus is from the posterior pole. In section 4.2, embryos with reduced cortical flows generated using *mlc-4* RNAi show highly diminished posteriorisation velocity of the male pronucleus at all angular positions compared to unperturbed embryos, and a lack of posteriorisation of the male pronucleus – demonstrating that cortical flows are essential for AP axis alignment.

In section 4.3, the role of the pseudocleavage furrow in AP axis alignment is investigated. Embryos deficient in a pseudocleavage furrow, but with cortical flows comparable to unperturbed embryos, are generated using a double RNAi of *nop-1; mel-11*. These pseudocleavage furrow-deficient embryos exhibit slower posteriorisation velocity compared to unperturbed embryos (which do have a pseudocleavage furrow) for all angular positions of the male pronucleus observed. However, unlike the *mlc-4* RNAi embryos, these pseudocleavage furrow-deficient embryos do exhibit posteriorisation of the male pronucleus, and thus AP axis alignment – albeit at a slower rate compared to unperturbed embryos. These experimental observations indicate a role for the pseudocleavage furrow in the dynamics of AP axis alignment. To further investigate the role of the pseudocleavage furrow – and specifically to understand the relative contributions of the pseudocleavage furrow-dependent mechanism and cytoplasmic flow-dependent mechanism – these experimental results are compared to numerical simulations of the theoretical model introduced in chapter 2. Numerical simulations of the full theoretical model, including both the cytoplasmic flow-dependent and pseudocleavage furrow-dependent mechanisms and calibrated using experimentally observed cortical flows in the unperturbed embryos (yielding $\lambda_H = 10\,\mu\mathrm{m}$, $\lambda_A = 11.5\,\mu\mathrm{m}^2\,\mathrm{s}^{-1}$, $\lambda_N = 152.5\,\mu\mathrm{m}^2\,\mathrm{s}^{-1}$), recapitulate the observed posteriorisation velocity in unperturbed embryos for a fitted value of $d = 0.61$, for angular positions in 0–21 deg. Numerical simulations of the theoretical model lacking in the pseudocleavage furrow-dependent mechanism (setting $\lambda_N = 0\,\mu\mathrm{m}^2\,\mathrm{s}^{-1}$ and calibrated using experimentally observed cortical flows in the *nop-1; mel-11* RNAi embryos (yielding $\lambda_H = 11\,\mu\mathrm{m}$, $\lambda_A = 11.5\,\mu\mathrm{m}^2\,\mathrm{s}^{-1}$) with $d = 0.61$ can capture the observed posteriorisation velocity in pseudocleavage furrow-deficient embryos for angular positions in 0–21 deg. Altogether, these observations – both in experiments and in numerical simulations – demonstrate that the pseudocleavage furrow-dependent mechanism is the predominant mechanism of AP axis alignment in unperturbed embryos, with a minor role played by the cytoplasmic flow-dependent mechanism that is evident in the pseudocleavage furrow-deficient embryos.

How does this square with the previous observations that the pseudocleavage furrow is largely dispensable for proper AP axis formation [130, 165]? First, due to the geometrical constraints on the embryo during fertilisation, the sperm entry site is typically on the future posterior tip of embryo [6]. Thus, in the typical case, AP axis is already aligned with the long axis of the embryo. Second, while the pseudocleavage furrow plays a predominant role in AP axis alignment, the slower AP axis alignment driven by cytoplasmic flows can still correct for small deviations of the AP axis from the long axis. Third, incomplete AP axis alignment at the establishment phase – which has been the focus of this thesis – can be corrected later by slow movement of PAR domains in a mechanism independent of flows in the actomyosin cortex [164, 167]. Thus, multiple redundant mechanisms ensure proper positioning of the AP axis even if the pseudocleavage furrow fails to form.

Cytoplasmic flows have been observed as a general mechanism for repositioning of various structures in the cytoplasm in many biological systems, such as chloroplasts in *Chara corallina* [210], cytoplasmic components and nuclei in *Drosophila* [8, 211], and spindle in the human and mouse oocytes [212, 213]. In systems such as *C. elegans* embryo, *Drosophila*, human and mouse oocytes, cortical flows drive these cytoplasmic flows [137, 211–213]. The work presented here demonstrates another mechanism by which cortical flows can influence the positioning of internal structures of the cell, via the repositioning of a contractile ring – the pseudocleavage furrow. Such a contractile ring arises in the *C. elegans* cortex as a result of the nematic ordering in the cortex conferred on it by the actin filaments [88]. Given the importance of the actomyosin cortex in development in multiple different organisms [3], it would be interesting to study the effect of such properties of the cortex on the positioning of structures in the cytoplasm in different organisms.

In section 4.4, the role of embryo geometry in AP axis alignment in *C. elegans* embryos is investigated. Reducing the aspect ratio of the ellipsoid used in the numerical simulations of the full theoretical model predicted that AP axis alignment should be slower in rounder embryos (embryos with a smaller aspect ratio compared to unperturbed embryos). To test this prediction, rounder embryos were generated using RNAi of *ima-3*. It is observed that the theoretical model simulated using an ellipsoid with the average aspect ratio of these rounder embryos can recapitulate the experimentally observed posteriorisation velocity in these rounder embryos for the same set of model parameters used for the unperturbed embryos. That is, experimental observations confirm the predictions from the numerical simulations: slower AP axis alignment observed in rounder embryos is quantitatively consistent with the predictions made by the theoretical model. Interestingly, the change in volume between the rounder embryos and unperturbed embryos is found to be not important for the difference in AP axis alignment between the two sets of embryos. As previous results indicated a predominant role for the pseudocleavage furrow in AP axis alignment, an effective model of a contractile ring that slips on the surface of a fixed ellipsoid is proposed to mimic the repositioning of the pseudocleavage furrow during AP axis alignment. Such an effective model – comprising only of two features of the full theoretical model: ellipsoidal geometry and contractile ring – is found to capture the relation between embryo geometry and AP axis alignment. Altogether, these observations – both in experiments and in numerical simulations – demonstrate that AP axis alignment is sensitive to the geometry of the *C. elegans* embryo, in a manner that is captured by the pseudocleavage furrow-dependent mechanism. This further confirms the predominant role of the pseudocleavage furrow in AP axis alignment in *C. elegans* embryos.

Altogether, the work presented in this thesis shows that AP axis alignment in the *C. elegans* embryo is driven by active mechanical flows in the actomyosin cortex that generate two distinct mechanisms for AP axis alignment: pseudocleavage furrow-dependent mechanism and cytoplasmic flow-dependent mechanism. The pseudocleavage furrow-dependent mechanism is the predominant mechanism of AP axis alignment, and arises as a consequence of the active anisotropic stresses in the actomyosin cortex due to alignment of actin filaments in the cortex. The cytoplasmic flow-dependent mechanism is a subsidiary mechanism, and arises as a consequence of active isotropic stresses in the cortex due to action of myosin motors alone. Furthermore, embryo geometry is shown to have an influence on AP axis alignment in *C. elegans* embryos. Such a relation betwen the two is also shown to be consistent with this predominant role of the pseudocleavage furrow in AP axis alignment in *C. elegans* embryos.

Many of the processes involved in the establishment of AP axis are not unique to the *C. elegans* embryos. Body axes establishment is often mediated by self-organised pattern formation processes [2, 214], with important role for mechanical forces [3, 215–218] – such as the mechanochemical feedback between PAR proteins and myosin motors in the actomyosin cortex that establish the AP axis in *C. elegans* embryo [1]. Additionally, geometric features in the embryo have been observed to direct the orientation of body axis during development – as reviewed in chapter 1. The work on AP axis alignment in *C. elegans* embryos presented in this thesis indicates that the interplay between mechanical forces in the embryo and such geometric features may robustly orient the body axes relative to the geometry of the embryo. It would be interesting to investigate if such an interplay between mechanics and geometry is a general feature of body axes establishment in development of multi-cellular organisms.

Appendix

Legend of attached movies:

Movie 1:

AP axis alignment observed in *C. elegans* embryos labelled with PAR-2::GFP (cyan) denoting pPARs domain and PAR-6::mCherry (magneta) denoting aPARs domain. Anterior to the left, posterior to the right. Note the movement of the male pronucleus towards the posterior end with the posterior pPARs domain on the cortex. Scale bar: 10 µm.

Movie 2:

Posteriorisation of the male pronucleus – dark circle in the cytoplasm towards the posterior end – observed in unperturbed *C. elegans* embryos labelled with NMY-2::GFP (gray). Anterior to the left, posterior to the right. Note the movement of the male pronucleus towards the posterior end with the myosin depletion domain on the cortex. Note also the constriction in the middle of the embryo – the pseudocleavage furrow. Scale bar: 10 µm.

Movie 3:

No posteriorisation of the male pronucleus – dark circle in the cytoplasm towards the posterior end – observed in *mlc-4* RNAi *C. elegans* embryos labelled with NMY-2::GFP (gray). Anterior to the left, posterior to the right. Male pronucleus does not move towards the posterior end. Scale bar: 10 µm.

Movie 4:

No AP axis alignment observed in *mlc-4* RNAi *C. elegans* embryos labelled with PAR-2::GFP (cyan) denoting pPARs domain and PAR-6::mCherry (magneta) denoting aPARs domain. Anterior to the left, posterior to the right. pPARs domain does not move towards the posterior end. Scale bar: 10 µm.

Movie 5:

Slower posteriorisation of the male pronucleus – dark circle in the cytoplasm towards the posterior end – observed in *nop-1; mel-11* RNAi *C. elegans* embryos labelled with NMY-2::GFP (gray). Anterior to the left, posterior to the right. Male pronucleus does move towards the posterior end, but slower compared to that observed for the unperturbed embryos. Scale bar: 10 µm.

Movie 6:

Slower posteriorisation of the male pronucleus – dark circle in the cytoplasm towards the posterior end – observed in round *ima-3* RNAi *C. elegans* embryos labelled with NMY-2::GFP (gray). Anterior to the left, posterior to the right. Male pronucleus does move towards the posterior end, but slower compared to that observed for the unperturbed embryos. Scale bar: 10 µm.

Movie 7:

Double myosin depletion domain and double pseudocleavage furrow observed in *air-1* RNAi *C. elegans* embryos labelled with NMY-2::GFP (gray). Anterior to the left, posterior to the right. Embryo polarises along the long axis, without needing the posteriorisation of the male pronucleus. Scale bar: 10 µm.

Movie 8:

No movement of the myosin depletion domain observed in *air-1; mel-11* RNAi in *nop-1* mutant *C. elegans* embryos labelled with NMY-2::GFP (gray). Anterior to the left, posterior to the right. The myosin depletion domain – indicating the posterior domain – forms away from the posterior end (towards the top right of the embryo), and does not recenter towards the posterior. Scale bar: 10 µm.

Movie 9:

Posteriorisation of the male pronucleus – dark circle in the cytoplasm towards the posterior end – observed in unperturbed *C. elegans* embryos labelled with TUB::GFP (cyan) and NMY-2::mKate (magneta). Anterior to the left, posterior to the right. Note the centrosomes – labelled with TUB::GFP – associated with the male pronucleus. Scale bar: 10 µm.

Movie 10:

Posteriorisation of the male pronucleus – dark circle in the cytoplasm towards the posterior end – observed in *goa-1; gpa-16 C. elegans* embryos labelled with TUB::GFP (cyan) and NMY-2::mKate (magneta). Anterior to the left, posterior to the right. Note the centrosomes – labelled with TUB::GFP – associated with the male pronucleus. Separation between centrosomes is smaller than that observed in unperturbed embryos. Scale bar: 10 µm.

Legend of attached datasets:

For each experimental condition described in this thesis in chapter 4, following datasets for each movie is recorded:

Male pronucleus tracking (nuclTrack.csv):

Dataset that records the male pronucleus trajectory observed in the movie. This csv file has the following columns: time (s), x-coordinate of pronucleus center (µm), y-coordinate of pronucleus center (µm), angular position (deg), x-coordinate of closest point on cortex (µm), y-coordinate of closest point on cortex (µm), x-component of velocity of the male pronucleus (µm/s), y-component of velocity of the male pronucleus (µm/s), posteriorisation velocity (µm/s). See chapter 3 for details.

Boundary fit to ellipse (axes.csv):

Dataset that records the elliptical fits to the embryo boundary in the movie. This csv file has the following columns: time (s), length of semi-major axis of instantenous fitted ellipse (µm), length of semi-minor axis of instantenous fitted ellipse (µm). See chapter 3 for details.

Arclength along the cortex (arclength.csv):

Dataset that records the arclength coordinates (used for cortical flows) along the embryo boundary for the movie. This csv file has a single row, recording the distance of the points on the cortex from the posterior pole along the cortex.

Cortical flows (flows.csv):

Dataset that records the cortical flows at the arclength coordinates along the embryo boundary for the movie. This csv file has variable number of columns equal to numbr of columns in the arclength.csv file + 1. First column is time (s). All the rest of the columns record cortical flow velocity (µm/s) at the corresponding arclength coordinates.

Bibliography

[1] Peter Gross et al. "Guiding self-organized pattern formation in cell polarity establishment". In: *Nature Physics* 15.3 (2019), pp. 293–300.

[2] Bob Goldstein and Gary Freeman. "Axis specification in animal development". In: *BioEssays* 19.2 (1997), pp. 105–116.

[3] Peter Gross, K Vijay Kumar, and Stephan W Grill. "How active mechanics and regulatory biochemistry combine to form patterns in development". In: *Annual review of biophysics* 46 (2017), pp. 337–356.

[4] Hans Meinhardt. "Models for patterning primary embryonic body axes: the role of space and time". In: *Seminars in cell & developmental biology*. Vol. 42. Elsevier. 2015, pp. 103–117.

[5] Hans Meinhardt. "Models of biological pattern formation: from elementary steps to the organization of embryonic axes". In: *Current topics in developmental biology* 81 (2008), pp. 1–63.

[6] Bob Goldstein and Steven N Hird. "Specification of the anteroposterior axis in *Caenorhabditis elegans*". In: *Development* 122.5 (1996), pp. 1467–1474.

[7] Mahamar Dicko et al. "Geometry can provide long-range mechanical guidance for embryogenesis". In: *PLoS computational biology* 13.3 (2017), e1005443.

[8] Margot E Quinlan. "Cytoplasmic streaming in the Drosophila oocyte". In: *Annual review of cell and developmental biology* 32 (2016), pp. 173–195.

[9] Joshua M Shulman, Richard Benton, and Daniel St Johnston. "The Drosophila homolog of *C. elegans* PAR-1 organizes the oocyte cytoskeleton and directs oskar mRNA localization to the posterior pole". In: *Cell* 101.4 (2000), pp. 377–388.

[10] Acaimo González-Reyes and Daniel St Johnston. "Role of oocyte position in establishment of anterior-posterior polarity in Drosophila". In: *Science* 266.5185 (1994), pp. 639–642.

[11] KE Von Baer. "Entwicklungsgeschichte des Hunchens im Eie". In: *Bonnträger, Königsb* 315 (1828).

[12] Shimshon Kochav and Hefzibah Eyal-Giladi. "Bilateral symmetry in chick embryo determination by gravity". In: *Science* 171.3975 (1971), pp. 1027–1029.

[13] Patrick PL Tam. "Embryonic axes: the long and short of it in the mouse". In: *Current Biology* 14.6 (2004), R239–R241.

[14] Stefano Vianello and Matthias P Lutolf. "Understanding the mechanobiology of early mammalian development through bioengineered models". In: *Developmental cell* 48.6 (2019), pp. 751–763.

[15] Ryuji Hiramatsu et al. “External mechanical cues trigger the establishment of the anterior-posterior axis in early mouse embryos”. In: *Developmental cell* 27.2 (2013), pp. 131–144.

[16] Isao Matsuo and Ryuji Hiramatsu. “Mechanical perspectives on the anterior-posterior axis polarization of mouse implanted embryos”. In: *Mechanisms of development* 144 (2017), pp. 62–70.

[17] Susan Strome. “Generation of cell diversity during early embryogenesis in the nematode *Caenorhabditis elegans*”. In: *International review of cytology* 114 (1989), pp. 81–123.

[18] Nigel Chaffey. *Alberts, B., Johnson, A., Lewis, J., Raff, M., Roberts, K. and Walter, P. Molecular biology of the cell. 4th edn.* 2003.

[19] D Bray. “Cell movements: from molecules to motility, 2nd edn New York”. In: *NY: Garland Publishing.[Google Scholar]* (2001).

[20] Daniel A Fletcher and R Dyche Mullins. “Cell mechanics and the cytoskeleton”. In: *Nature* 463.7280 (2010), pp. 485–492.

[21] Francisco Rivero et al. “The role of the cortical cytoskeleton: F-actin crosslinking proteins protect against osmotic stress, ensure cell size, cell shape and motility, and contribute to phagocytosis and development”. In: *Journal of Cell Science* 109.11 (1996), pp. 2679–2691.

[22] Harald Herrmann et al. “Intermediate filaments: from cell architecture to nanomechanics”. In: *Nature reviews Molecular cell biology* 8.7 (2007), pp. 562–573.

[23] Pierre Gönczy et al. “Spindle Positioning during the Asymmetric First Cell Division of *Caenorhabditis elegans* Embroyos”. In: *The Cell Cycle and Development: Novartis Foundation Symposium 237*. Vol. 237. Wiley Online Library. 2001, pp. 164–181.

[24] Harold P Erickson. “Evolution of the cytoskeleton”. In: *Bioessays* 29.7 (2007), pp. 668–677.

[25] Guillaume Salbreux, Guillaume Charras, and Ewa Paluch. “Actin cortex mechanics and cellular morphogenesis”. In: *Trends in cell biology* 22.10 (2012), pp. 536–545.

[26] Thomas D Pollard and John A Cooper. “Actin and actin-binding proteins. A critical evaluation of mechanisms and functions”. In: *Annual review of biochemistry* 55.1 (1986), pp. 987–1035.

[27] Thomas D Pollard, Laurent Blanchoin, and R Dyche Mullins. “Molecular mechanisms controlling actin filament dynamics in nonmuscle cells”. In: *Annual review of biophysics and biomolecular structure* 29.1 (2000), pp. 545–576.

[28] Geoffrey M Cooper, Robert E Hausman, and Robert E Hausman. *The cell: a molecular approach.* Vol. 4. ASM press Washington, DC, 2007.

[29] A Ott et al. “Measurement of the persistence length of polymerized actin using fluorescence microscopy”. In: *Physical Review E* 48.3 (1993), R1642.

[30] Frederick Gittes et al. “Flexural rigidity of microtubules and actin filaments measured from thermal fluctuations in shape.” In: *The Journal of cell biology* 120.4 (1993), pp. 923–934.

[31] Ikuko Fujiwara, Dimitrios Vavylonis, and Thomas D Pollard. “Polymerization kinetics of ADP-and ADP-Pi-actin determined by fluorescence microscopy”. In: *Proceedings of the National Academy of Sciences* 104.21 (2007), pp. 8827–8832.

[32] Dimitrios Vavylonis, Qingbo Yang, and Ben O’Shaughnessy. “Actin polymerization kinetics, cap structure, and fluctuations”. In: *Proceedings of the National Academy of Sciences* 102.24 (2005), pp. 8543–8548.

[33] Albrecht Wegner. “Treadmilling of actin at physiological salt concentrations: An analysis of the critical concentrations of actin filaments”. In: *Journal of Molecular Biology* 161.4 (1982), pp. 607–615.

[34] Thomas D Pollard and Gary G Borisy. “Cellular motility driven by assembly and disassembly of actin filaments”. In: *Cell* 112.4 (2003), pp. 453–465.

[35] Joseph W Sanger. “Changing patterns of actin localization during cell division.” In: *Proceedings of the National Academy of Sciences* 72.5 (1975), pp. 1913–1916.

[36] Margaret Clarke and James A Spudich. “Nonmuscle contractile proteins: the role of actin and myosin in cell motility and shape determination”. In: *Annual review of biochemistry* 46.1 (1977), pp. 797–822.

[37] E Nogales, SG Wolf, and KH Downing. “Structure of the ab-tubulin dimer by electron crystallography (vol. 391, pg. 199, 1998)”. In: *Nature* 393 (1998), p. 191.

[38] Viktória Hunyadi et al. “Why is the microtubule lattice helical?” In: *Biology of the Cell* 99.2 (2007), pp. 117–128.

[39] Martin Chalfie and J Nichol Thomson. “Organization of neuronal microtubules in the nematode *Caenorhabditis elegans*.” In: *The Journal of cell biology* 82.1 (1979), pp. 278–289.

[40] MC Ledbetter and KR Porter. “A” microtubule” in plant cell fine structure”. In: *The Journal of cell biology* 19.1 (1963), pp. 239–250.

[41] Joe Howard and Anthony A Hyman. “Dynamics and mechanics of the microtubule plus end”. In: *Nature* 422.6933 (2003), pp. 753–758.

[42] A Mikhailov and GG Gundersen. “Relationship between microtubule dynamics and lamellipodium formation revealed by direct imaging of microtubules in cells treated with nocodazole or taxol”. In: *Cell motility and the cytoskeleton* 41.4 (1998), pp. 325–340.

[43] Chad G Pearson and Kerry Bloom. “Dynamic microtubules lead the way for spindle positioning”. In: *Nature reviews Molecular cell biology* 5.6 (2004), pp. 481–492.

[44] Stephan W Grill et al. “The distribution of active force generators controls mitotic spindle position”. In: *Science* 301.5632 (2003), pp. 518–521.

[45] Stephan W Grill, Karsten Kruse, and Frank Jülicher. “Theory of mitotic spindle oscillations”. In: *Physical review letters* 94.10 (2005), p. 108104.

[46] Ana Pimenta-Marques and Monica Bettencourt-Dias. “Pericentriolar material”. In: *Current Biology* 30.12 (2020), R687–R689.

[47] Douglas R Kellogg, Michelle Moritz, and Bruce M Alberts. “The centrosome and cellular organization”. In: *Annual review of biochemistry* 63.1 (1994), pp. 639–674.

[48] Mónica Bettencourt-Dias. “Q&A: Who needs a centrosome?” In: *BMC biology* 11.1 (2013), pp. 1–7.

[49] Anatoly B Kolomeisky and Michael E Fisher. “Molecular motors: a theorist’s perspective”. In: *Annu. Rev. Phys. Chem.* 58 (2007), pp. 675–695.

[50] Jonathon Howard and RL Clark. “Mechanics of motor proteins and the cytoskeleton”. In: *Appl. Mech. Rev.* 55.2 (2002), B39–B39.

[51] Ronald D Vale. “The molecular motor toolbox for intracellular transport”. In: *Cell* 112.4 (2003), pp. 467–480.

[52] Anders E Carlsson. “Contractile stress generation by actomyosin gels”. In: *Physical Review E* 74.5 (2006), p. 051912.

[53] Wonmuk Hwang and Matthew J Lang. “Mechanical design of translocating motor proteins”. In: *Cell biochemistry and biophysics* 54 (2009), pp. 11–22.

[54] Kenneth C Holmes. *Myosin structure In: Coluccio LM, ed. Myosins: a superfamily of molecular motors. Proteins and cell regulation, Vol. 7.* 2008.

[55] Miguel Vicente-Manzanares et al. “Non-muscle myosin II takes centre stage in cell adhesion and migration”. In: *Nature reviews Molecular cell biology* 10.11 (2009), pp. 778–790.

[56] Julien Robert-Paganin et al. “Force generation by myosin motors: a structural perspective”. In: *Chemical reviews* 120.1 (2019), pp. 5–35.

[57] Enrique M De La Cruz and E Michael Ostap. “Relating biochemistry and function in the myosin superfamily”. In: *Current opinion in cell biology* 16.1 (2004), pp. 61–67.

[58] H Lee Sweeney and Anne Houdusse. “Structural and functional insights into the myosin motor mechanism”. In: *Annual review of biophysics* 39 (2010), pp. 539–557.

[59] Matthew J Tyska and David M Warshaw. “The myosin power stroke”. In: *Cell motility and the cytoskeleton* 51.1 (2002), pp. 1–15.

[60] Mihály Kovács et al. “Functional divergence of human cytoplasmic myosin II: kinetic characterization of the non-muscle IIA isoform”. In: *Journal of Biological Chemistry* 278.40 (2003), pp. 38132–38140.

[61] Fei Wang et al. “Kinetic mechanism of non-muscle myosin IIB: functional adaptations for tension generation and maintenance”. In: *Journal of Biological Chemistry* 278.30 (2003), pp. 27439–27448.

[62] Richard Niederman and Thomas D Pollard. “Human platelet myosin. II. In vitro assembly and structure of myosin filaments.” In: *The Journal of cell biology* 67.1 (1975), pp. 72–92.

[63] Rohit K Mahajan and Joel D Pardee. “Assembly mechanism of Dictyostelium myosin II: Regulation by K+, Mg2+, and actin filaments”. In: *Biochemistry* 35.48 (1996), pp. 15504–15514.

[64] Xiaoxin Susan Xu et al. “During multicellular migration, myosin ii serves a structural role independent of its motor function”. In: *Developmental biology* 232.1 (2001), pp. 255–264.

[65] Daisuke Mizuno et al. “Nonequilibrium mechanics of active cytoskeletal networks”. In: *Science* 315.5810 (2007), pp. 370–373.

[66] Gary Laevsky and David A Knecht. “Cross-linking of actin filaments by myosin II is a major contributor to cortical integrity and cell motility in restrictive environments”. In: *Journal of cell science* 116.18 (2003), pp. 3761–3770.

[67] Sebastian Fürthauer. “Active Chiral Processes in Soft Biological Matter”. PhD Thesis. Technische Universität Dresden, 2012.

[68] K Vijay Kumar. “The actomyosin cortex of cells: A thin film of active matter”. In: *Journal of the Indian Institute of Science* 101.1 (2021), pp. 97–112.

[69] Andrew G Clark, Kai Dierkes, and Ewa K Paluch. “Monitoring actin cortex thickness in live cells”. In: *Biophysical journal* 105.3 (2013), pp. 570–580.

[70] D Bray and JG White. “Cortical flow in animal cells”. In: *Science* 239.4842 (1988), pp. 883–888.

[71] John H Hartwig and Michelle DeSisto. “The cytoskeleton of the resting human blood platelet: structure of the membrane skeleton and its attachment to actin filaments.” In: *The Journal of cell biology* 112.3 (1991), pp. 407–425.

[72] J Eo Heuser and MeW Kirschner. “Filament organization revealed in platinum replicas of freeze-dried cytoskeletons.” In: *The Journal of cell biology* 86.1 (1980), pp. 212–234.

[73] Nobuhiro Morone et al. “Three-dimensional reconstruction of the membrane skeleton at the plasma membrane interface by electron tomography”. In: *The Journal of cell biology* 174.6 (2006), pp. 851–862.

[74] Ohad Medalia et al. “Macromolecular architecture in eukaryotic cells visualized by cryoelectron tomography”. In: *Science* 298.5596 (2002), pp. 1209–1213.

[75] Devrim Pesen and Jan H Hoh. “Micromechanical architecture of the endothelial cell cortex”. In: *Biophysical journal* 88.1 (2005), pp. 670–679.

[76] Arnab Saha et al. “Determining physical properties of the cell cortex”. In: *Biophysical journal* 110.6 (2016), pp. 1421–1429.

[77] Mirjam Mayer et al. “Anisotropies in cortical tension reveal the physical basis of polarizing cortical flows”. In: *Nature* 467.7315 (2010), pp. 617–621.

[78] Marco Fritzsche et al. “Actin kinetics shapes cortical network structure and mechanics”. In: *Science advances* 2.4 (2016), e1501337.

[79] Martin P Stewart et al. “Hydrostatic pressure and the actomyosin cortex drive mitotic cell rounding”. In: *Nature* 469.7329 (2011), pp. 226–230.

[80] Patricia Kunda et al. “Moesin controls cortical rigidity, cell rounding, and spindle morphogenesis during mitosis”. In: *Current biology* 18.2 (2008), pp. 91–101.

[81] Matteo Rauzi and Pierre-François Lenne. “Cortical forces in cell shape changes and tissue morphogenesis”. In: *Current topics in developmental biology* 95 (2011), pp. 93–144.

[82] Adam C Martin. “Pulsation and stabilization: contractile forces that underlie morphogenesis”. In: *Developmental biology* 341.1 (2010), pp. 114–125.

[83] Jian Zhou, Hye Young Kim, and Lance A Davidson. "Actomyosin stiffens the vertebrate embryo during crucial stages of elongation and neural tube closure". In: (2009).

[84] Justin S Bois, Frank Jülicher, and Stephan W Grill. "Pattern formation in active fluids". In: *Physical review letters* 106.2 (2011), p. 028103.

[85] Frank Jülicher, Stephan W Grill, and Guillaume Salbreux. "Hydrodynamic theory of active matter". In: *Reports on Progress in Physics* 81.7 (2018), p. 076601.

[86] Sybren Ruurds De Groot and Peter Mazur. *Non-equilibrium thermodynamics*. Dover Publications Inc., Mineola, N. Y., 1984.

[87] Jacques Prost, Frank Jülicher, and Jean Francois Joanny. "Active gel physics". In: *Nature Physics* 11 (2015), pp. 111–117.

[88] Anne-Cecile Reymann et al. "Cortical flow aligns actin filaments to form a furrow". In: *Elife* 5 (2016), e17807.

[89] K. Kruse et al. "Asters, Vortices, and Rotating Spirals in Active Gels of Polar Filaments". In: *Phys. Rev. Lett.* 92 (7 Feb. 2004), p. 078101. DOI: `10.1103/PhysRevLett.92.078101`. URL: `https://link.aps.org/doi/10.1103/PhysRevLett.92.078101`.

[90] Guillaume Salbreux et al. "Theory of nematic and polar active fluid surfaces". In: *Phys. Rev. Research* 4 (2022), p. 033158.

[91] Karsten Kruse et al. "Generic theory of active polar gels: a paradigm for cytoskeletal dynamics". In: *The European Physical Journal E* 16 (2005), pp. 5–16.

[92] John Toner and Yuhai Tu. "Long-range order in a two-dimensional dynamical XY model: how birds fly together". In: *Physical review letters* 75.23 (1995), p. 4326.

[93] John Toner and Yuhai Tu. "Flocks, herds, and schools: A quantitative theory of flocking". In: *Physical review E* 58.4 (1998), p. 4828.

[94] Yuhai Tu, John Toner, and Markus Ulm. "Sound waves and the absence of Galilean invariance in flocks". In: *Physical review letters* 80.21 (1998), p. 4819.

[95] R Aditi Simha and Sriram Ramaswamy. "Hydrodynamic fluctuations and instabilities in ordered suspensions of self-propelled particles". In: *Physical review letters* 89.5 (2002), p. 058101.

[96] Yashodhan Hatwalne et al. "Rheology of active-particle suspensions". In: *Physical review letters* 92.11 (2004), p. 118101.

[97] J Elgeti, ME Cates, and D Marenduzzo. "Defect hydrodynamics in 2D polar active fluids". In: *Soft Matter* 7.7 (2011), pp. 3177–3185.

[98] D Marenduzzo, E Orlandini, and JM Yeomans. "Hydrodynamics and rheology of active liquid crystals: a numerical investigation". In: *Physical review letters* 98.11 (2007), p. 118102.

[99] Suzanne M Fielding, Davide Marenduzzo, and Michael E Cates. "Nonlinear dynamics and rheology of active fluids: Simulations in two dimensions". In: *Physical Review E* 83.4 (2011), p. 041910.

[100] Luca Giomi et al. "Excitable patterns in active nematics". In: *Physical review letters* 106.21 (2011), p. 218101.

[101] Stefan Günther and Karsten Kruse. “Spontaneous waves in muscle fibres”. In: *new Journal of physics* 9.11 (2007), p. 417.

[102] Shiladitya Banerjee and M Cristina Marchetti. “Instabilities and oscillations in isotropic active gels”. In: *Soft Matter* 7.2 (2011), pp. 463–473.

[103] Jonas Ranft et al. “Fluidization of tissues by cell division and apoptosis”. In: *Proceedings of the National Academy of Sciences* 107.49 (2010), pp. 20863–20868.

[104] Pierre-Gilles De Gennes and Jacques Prost. *The physics of liquid crystals*. 83. Oxford university press, 1993.

[105] Lars Onsager. “Reciprocal relations in irreversible processes. I.” In: *Physical review* 37.4 (1931), p. 405.

[106] Lars Onsager. “Reciprocal relations in irreversible processes. II.” In: *Physical review* 38.12 (1931), p. 2265.

[107] P Mazur and SR De Groot. “On onsager’s relations in a magnetic field”. In: *Physica* 19.1-12 (1953), pp. 961–970.

[108] H Bo Go Casimir. “On Onsager’s principle of microscopic reversibility”. In: *Reviews of Modern Physics* 17.2-3 (1945), p. 343.

[109] Pierre Curie. “On symmetry in physical phenomena, symmetry of an electric field and of a magnetic field”. In: *Journal de Physique* 3 (1894), p. 401.

[110] Ronald G Larson. *The structure and rheology of complex fluids*. Vol. 150. Oxford university press New York, 1999.

[111] Brenner S Wood WB. “The nematode *Caenorhabditis elegans*”. In: *Cold Spring Harbor Laboratory* 1.988 (1988), pp. 1091–1105.

[112] Sydney Brenner. “The genetics of *Caenorhabditis elegans*”. In: *Genetics* 77.1 (1974), pp. 71–94.

[113] Sydney Brenner. “Nature’s gift to science”. In: *CHEMBIOCHEM-WEINHEIM-* 4 (2003), pp. 683–687.

[114] Eric S Haag. “The evolution of nematode sex determination: *C. elegans* as a reference point for comparative biology.” In: *WormBook* (2005), p. 1.

[115] Ann K Corsi, Bruce Wightman, and Martin Chalfie. “A transparent window into biology: a primer on *Caenorhabditis elegans*”. In: *Genetics* 200.2 (2015), pp. 387–407.

[116] Seung-Jae Lee and Cynthia Kenyon. “Regulation of the longevity response to temperature by thermosensory neurons in *Caenorhabditis elegans*”. In: *Current biology* 19.9 (2009), pp. 715–722.

[117] John E Sulston et al. “The embryonic cell lineage of the nematode *Caenorhabditis elegans*”. In: *Developmental biology* 100.1 (1983), pp. 64–119.

[118] Judith Kimble and David Hirsh. “The postembryonic cell lineages of the hermaphrodite and male gonads in *Caenorhabditis elegans*”. In: *Developmental biology* 70.2 (1979), pp. 396–417.

[119] J Sulston, M Dew, and S Brenner. “Dopaminergic neurons in the nematode *Caenorhabditis elegans*”. In: *Journal of Comparative Neurology* 163.2 (1975), pp. 215–226.

[120] Patrick J Hu. “Dauer”. In: *WormBook: The Online Review of C. elegans Biology* (2007).

[121] *C. elegans* Sequencing Consortium*. “Genome sequence of the nematode *C. elegans*: a platform for investigating biology”. In: *Science* 282.5396 (1998), pp. 2012–2018.

[122] Ravi S Kamath and Julie Ahringer. “Genome-wide RNAi screening in *Caenorhabditis elegans*”. In: *Methods* 30.4 (2003), pp. 313–321.

[123] Martin Chalfie et al. “Green fluorescent protein as a marker for gene expression”. In: *Science* 263.5148 (1994), pp. 802–805.

[124] Thomas Boulin, John F Etchberger, and Oliver Hobert. “Reporter gene fusions”. In: *WormBook: The Online Review of C. elegans Biology* (2006).

[125] Mirjam Mayer. “Mechanics of the *C. elegans* cell cortex”. PhD Thesis. Technische Universität Dresden, 2010.

[126] Stephan Q Schneider and Bruce Bowerman. “Cell polarity and the cytoskeleton in the *Caenorhabditis elegans* zygote”. In: *Annual review of genetics* 37.1 (2003), pp. 221–249.

[127] Lesilee Rose and Pierre Gönczy. “Polarity establishment, asymmetric division and segregation of fate determinants in early *C. elegans* embryos”. In: *WormBook: The Online Review of C. elegans Biology* (2014).

[128] Maria L. Begasse and Anthony A. Hyman. “The First Cell Cycle of the *Caenorhabditis elegans* Embryo: Spatial and Temporal Control of an Asymmetric Cell Division”. In: *Cell Cycle in Development*. Ed. by Jacek Z. Kubiak. Berlin, Heidelberg: Springer Berlin Heidelberg, 2011, pp. 109–133. ISBN: 978-3-642-19065-0. DOI: `10.1007/978-3-642-19065-0_6`. URL: `https://doi.org/10.1007/978-3-642-19065-0_6`.

[129] Adrian A Cuenca et al. “Polarization of the *C. elegans* zygote proceeds via distinct establishment and maintenance phases”. In: (2003).

[130] Carrie R Cowan and Anthony A Hyman. “Asymmetric cell division in *C. elegans*: cortical polarity and spindle positioning”. In: *Annu. Rev. Cell Dev. Biol.* 20 (2004), pp. 427–453.

[131] Stephanie Schonegg and Anthony A Hyman. “CDC-42 and RHO-1 coordinate actomyosin contractility and PAR protein localization during polarity establishment in *C. elegans* embryos”. In: *Development* (2006).

[132] Kevin Fe O’Connell, Kara N Maxwell, and John O White. “The spd-2 gene is required for polarization of the anteroposterior axis and formation of the sperm asters in the *Caenorhabditis elegans* zygote”. In: *Developmental biology* 222.1 (2000), pp. 55–70.

[133] Matthew R Wallenfang and Geraldine Seydoux. “Polarization of the anterior–posterior axis of *C. elegans* is a microtubule-directed process”. In: *Nature* 408.6808 (2000), pp. 89–92.

[134] Carrie R Cowan and Anthony A Hyman. “Centrosomes direct cell polarity independently of microtubule assembly in *C. elegans* embryos”. In: *Nature* 431.7004 (2004), pp. 92–96.

[135] Wendy Johnston and James Dennis. “The eggshell in the *C. elegans* oocyte-to-embryo transition”. In: *Genesis (New York, N.Y. : 2000)* 50 (Apr. 2012), pp. 333–49. DOI: `10.1002/dvg.20823`.

[136] V Nigon, P Guerrier, and H Monin. “L’architecture polaire de l’oeuf et les mouvements des constituants cellulaires au cours des premières étapes du développement chez quelques nématodes”. In: *Bull. Biol. Fr. Belg* 93 (1960), pp. 131–202.

[137] Ritsuya Niwayama, Kyosuke Shinohara, and Akatsuki Kimura. “Hydrodynamic property of the cytoplasm is sufficient to mediate cytoplasmic streaming in the Caenorhabiditis elegans embryo”. In: *Proceedings of the National Academy of Sciences* 108.29 (2011), pp. 11900–11905.

[138] Pierre Gönczy. “Mechanisms of asymmetric cell division: flies and worms pave the way”. In: *Nature reviews Molecular cell biology* 9.5 (2008), pp. 355–366.

[139] Carsten Hoege and Anthony A Hyman. “Principles of PAR polarity in *Caenorhabditis elegans* embryos”. In: *Nature reviews Molecular cell biology* 14.5 (2013), pp. 315–322.

[140] Judith Kimble and Sarah L Crittenden. “Germline proliferation and its control”. In: *WormBook: The Online Review of C. elegans Biology* (2005).

[141] Fumio Motegi and Geraldine Seydoux. “The PAR network: redundancy and robustness in a symmetry-breaking system”. In: *Philosophical Transactions of the Royal Society B: Biological Sciences* 368.1629 (2013), p. 20130010.

[142] Charles F Lang and Edwin Munro. “The PAR proteins: from molecular circuits to dynamic self-stabilizing cell polarity”. In: *Development* 144.19 (2017), pp. 3405–3416.

[143] Bob Goldstein and Ian G Macara. “The PAR proteins: fundamental players in animal cell polarization”. In: *Developmental cell* 13.5 (2007), pp. 609–622.

[144] Juergen A Knoblich. “Asymmetric cell division during animal development”. In: *Nature reviews Molecular cell biology* 2.1 (2001), pp. 11–20.

[145] Su Guo and Kenneth J Kemphues. “par-1, a gene required for establishing polarity in *C. elegans* embryos, encodes a putative Ser/Thr kinase that is asymmetrically distributed”. In: *Cell* 81.4 (1995), pp. 611–620.

[146] Kenneth J Kemphues et al. “Identification of genes required for cytoplasmic localization in early *C. elegans* embryos”. In: *Cell* 52.3 (1988), pp. 311–320.

[147] Nathan W Goehring et al. “PAR proteins diffuse freely across the anterior–posterior boundary in polarized *C. elegans* embryos”. In: *Journal of Cell Biology* 193.3 (2011), pp. 583–594.

[148] Charlotte M Schubert et al. “MEX-5 and MEX-6 function to establish soma/germline asymmetry in early *C. elegans* embryos”. In: *Molecular cell* 5.4 (2000), pp. 671–682.

[149] Zdeněk Petrášek et al. “Characterization of protein dynamics in asymmetric cell division by scanning fluorescence correlation spectroscopy”. In: *Biophysical journal* 95.11 (2008), pp. 5476–5486.

[150] Nathan W Goehring et al. “Polarization of PAR proteins by advective triggering of a pattern-forming system”. In: *Science* 334.6059 (2011), pp. 1137–1141.

[151] Sundar R. Naganathan. “Regulation of mesoscale physical properties of the *C. elegans* actomyosin cortex”. PhD Thesis. Technische Universität Dresden, 2012.

[152] Sasha De Henau et al. “Mitochondria-derived H2O2 promotes symmetry breaking of the *C. elegans* zygote”. In: *Developmental cell* 53.3 (2020), pp. 263–271.

[153] Peng Zhao et al. “Aurora-A breaks symmetry in contractile actomyosin networks independently of its role in centrosome maturation”. In: *Developmental cell* 48.5 (2019), pp. 631–645.

[154] Jacob D Reich et al. “Regulated activation of the PAR polarity network ensures a timely and specific response to spatial cues”. In: *Current Biology* 29.12 (2019), pp. 1911–1923.

[155] Sukriti Kapoor and Sachin Kotak. “Centrosome Aurora A regulates RhoGEF ECT-2 localisation and ensures a single PAR-2 polarity axis in *C. elegans* embryos”. In: *Development* 146.22 (2019), dev174565.

[156] Kerstin Klinkert et al. “Aurora A depletion reveals centrosome-independent polarization mechanism in *Caenorhabditis elegans*”. In: *Elife* 8 (2019), e44552.

[157] Dominika Bienkowska and Carrie R Cowan. “Centrosomes can initiate a polarity axis from any position within one-cell *C. elegans* embryos”. In: *Current biology* 22.7 (2012), pp. 583–589.

[158] Fumio Motegi et al. “Microtubules induce self-organization of polarized PAR domains in *Caenorhabditis elegans* zygotes”. In: *Nature cell biology* 13.11 (2011), pp. 1361–1367.

[159] Fumio Motegi and Asako Sugimoto. “Sequential functioning of the ECT-2 RhoGEF, RHO-1 and CDC-42 establishes cell polarity in *Caenorhabditis elegans* embryos”. In: *Nature cell biology* 8.9 (2006), pp. 978–985.

[160] Edwin Munro, Jeremy Nance, and James R Priess. “Cortical flows powered by asymmetrical contraction transport PAR proteins to establish and maintain anterior-posterior polarity in the early *C. elegans* embryo”. In: *Developmental cell* 7.3 (2004), pp. 413–424.

[161] Alicia G Gubieda et al. “Going with the flow: insights from *Caenorhabditis elegans* zygote polarization”. In: *Philosophical Transactions of the Royal Society B* 375.1809 (2020), p. 20190555.

[162] Donald L Riddle et al. *C. elegans Ii.* Cold spring harbor laboratory press, 1997.

[163] Kenji Kimura and Akatsuki Kimura. “Cytoplasmic streaming drifts the polarity cue and enables posteriorization of the *Caenorhabditis elegans* zygote at the side opposite of sperm entry”. In: *Molecular Biology of the Cell* 31.16 (2020). PMID: 32459552, pp. 1765–1773. DOI: `10.1091/mbc.E20-01-0058`.

[164] Matthäus Mittasch et al. “Non-invasive perturbations of intracellular flow reveal physical principles of cell organization”. In: *Nature cell biology* 20.3 (2018), pp. 344–351.

[165] Lesilee S Rose et al. “Pseudocleavage is dispensable for polarity and development in *C. elegans* embryos”. In: *Developmental biology* 168.2 (1995), pp. 479–489.

[166] Betül Senay Aras et al. “The importance of mechanical constraints for proper polarization and psuedo-cleavage furrow generation in the early *Caenorhabditis elegans* embryo”. In: *PLoS computational biology* 14.7 (2018), e1006294.

[167] Raphaela Geßele et al. “Geometric cues stabilise long-axis polarisation of PAR protein patterns in C. elegans”. In: *Nature communications* 11.1 (2020), p. 539.

[168] Seth Zonies et al. “Symmetry breaking and polarization of the *C. elegans* zygote by the polarity protein PAR-2”. In: *Development* 137.10 (2010), pp. 1669–1677.

[169] Yu Chung Tse et al. “RhoA activation during polarization and cytokinesis of the early *Caenorhabditis elegans* embryo is differentially dependent on NOP-1 and CYK-4”. In: *Molecular biology of the cell* 23.20 (2012), pp. 4020–4031.

[170] Archit Bhatnagar et al. “Axis convergence in C. elegans embryos”. In: *bioRxiv* (2023). DOI: `10.1101/2023.03.27.534329`. eprint: `https://www.biorxiv.org/content/early/2023/05/16/2023.03.27.534329.full.pdf`. URL: `https://www.biorxiv.org/content/early/2023/05/16/2023.03.27.534329`.

[171] Sungrim Seirin Lee and Tatsuo Shibata. “Self-organization and advective transport in the cell polarity formation for asymmetric cell division”. In: *Journal of theoretical biology* 382 (2015), pp. 1–14.

[172] Jacob Halatek and Erwin Frey. “Rethinking pattern formation in reaction–diffusion systems”. In: *Nature Physics* 14.5 (2018), pp. 507–514.

[173] François B Robin et al. “Single-molecule analysis of cell surface dynamics in Caenorhabditis elegans embryos”. In: *Nature methods* 11.6 (2014), pp. 677–682.

[174] Anne Sailer et al. “Dynamic opposition of clustered proteins stabilizes cortical polarity in the C. elegans zygote”. In: *Developmental cell* 35.1 (2015), pp. 131–142.

[175] Ingo Nitschke et al. “Nematic liquid crystals on curved surfaces: a thin film limit”. In: *Proceedings of the Royal Society A: Mathematical, Physical and Engineering Sciences* 474.2214 (2018), p. 20170686.

[176] Michael Nestler et al. “Properties of surface Landau–de Gennes Q-tensor models”. In: *Soft matter* 16.16 (2020), pp. 4032–4042.

[177] Marino Arroyo and Antonio DeSimone. “Relaxation dynamics of fluid membranes”. In: *Physical review E* 79.3 (2009), p. 031915.

[178] Ingo Nitschke, Sebastian Reuther, and Axel Voigt. “Liquid crystals on deformable surfaces”. In: *Proceedings of the Royal Society A* 476.2241 (2020), p. 20200313.

[179] Hajime Tanaka and Takeaki Araki. “Simulation method of colloidal suspensions with hydrodynamic interactions: Fluid particle dynamics”. In: *Physical review letters* 85.6 (2000), p. 1338.

[180] Michael Nestler, Ingo Nitschke, and Axel Voigt. “A finite element approach for vector- and tensor-valued surface PDEs”. In: *Journal of Computational Physics* 389 (2019), pp. 48–61. DOI: `10.1016/j.jcp.2019.03.006`.

[181] X. Li et al. “Solving PDE’s in complex geometries: A diffuse domain approach”. In: *Commun. Math. Sci.* 7 (2009), pp. 81–107.

[182] Mirna Kramer. “Linking cytoplasmic flows to the centering mechanism of the anterior-posterior body axis in *C. elegans*”. Master Thesis. Technische Universität Dresden, 2015.

[183] Wei Sun Park et al. “Comprehensive identification of PIP3-regulated PH domains from C. elegans to H. sapiens by model prediction and live imaging”. In: *Molecular cell* 30.3 (2008), pp. 381–392.

[184] Nathan C Shaner et al. “Improved monomeric red, orange and yellow fluorescent proteins derived from Discosoma sp. red fluorescent protein”. In: *Nature biotechnology* 22.12 (2004), pp. 1567–1572.

[185] Lisa Timmons, Donald L Court, and Andrew Fire. “Ingestion of bacterially expressed dsRNAs can produce specific and potent genetic interference in Caenorhabditis elegans”. In: *Gene* 263.1-2 (2001), pp. 103–112.

[186] Arthur D Edelstein et al. “Advanced methods of microscope control using μManager software”. In: *Journal of biological methods* 1.2 (2014).

[187] Johannes Schindelin et al. “Fiji: an open-source platform for biological-image analysis”. In: *Nature methods* 9.7 (2012), pp. 676–682.

[188] Melissa Linkert et al. “Metadata matters: access to image data in the real world”. In: *Journal of Cell Biology* 189.5 (2010), pp. 777–782.

[189] Python Core Team. *Python: A dynamic, open source programming language.* Python version 3.8. Python Software Foundation. 2019. URL: `https://www.python.org/`.

[190] MATLAB. *version 9.0.0.341360 (R2016a).* Natick, Massachusetts: The MathWorks Inc., 2016.

[191] Michiyoshi Kuwahara et al. “Processing of RI-angiocardiographic images”. In: *Digital processing of biomedical images* (1976), pp. 187–202.

[192] ImageJ. *ImageJ User Guide.* URL: `https://imagej.nih.gov/ij/docs/guide/146-28.html#sub:Threshold...[T]` (visited on 02/11/2023).

[193] G. Bradski. “The OpenCV Library”. In: *Dr. Dobb’s Journal of Software Tools* (2000).

[194] Christoph Gohlke. *Read and write TIFF files.* https://github.com/cgohlke/tifffile. 2019. DOI: `https://doi.org/10.5281/zenodo.6795860`.

[195] Pauli Virtanen et al. “SciPy 1.0: Fundamental Algorithms for Scientific Computing in Python”. In: *Nature Methods* (2020). DOI: `https://doi.org/10.1038/s41592-019-0686-2`.

[196] Charles R Harris et al. “Array programming with NumPy”. In: *Nature* 585.7825 (2020), pp. 357–362. ISSN: 1476-4687. DOI: `10.1038/s41586-020-2649-2`. URL: `https://doi.org/10.1038/s41586-020-2649-2`.

[197] Antoni Buades, Bartomeu Coll, and Jean-Michel Morel. “Non-local means denoising”. In: *Image Processing On Line* 1 (2011), pp. 208–212.

[198] William Thielicke and Eize Stamhuis. “PIVlab–towards user-friendly, affordable and accurate digital particle image velocimetry in MATLAB”. In: *Journal of open research software* 2.1 (2014).

[199] Markus Raffel, Christian E Willert, Jürgen Kompenhans, et al. *Particle image velocimetry: a practical guide.* Vol. 2. Springer, 1998.

[200] Christopher A Shelton et al. “The nonmuscle myosin regulatory light chain gene mlc-4 is required for cytokinesis, anterior-posterior polarity, and body morphology during Caenorhabditis elegans embryogenesis”. In: *The Journal of cell biology* 146.2 (1999), pp. 439–451.

[201] Alisa J Piekny and Paul E Mains. “Rho-binding kinase (LET-502) and myosin phosphatase (MEL-11) regulate cytokinesis in the early Caenorhabditis elegans embryo”. In: *Journal of cell science* 115.11 (2002), pp. 2271–2282.

[202] Fereshteh R Najafabadi, Mark Leaver, and Stephan W Grill. "Orchestrating Non-muscle myosin II filament assembly at the onset of cytokinesis". In: *Molecular Biology of the Cell* (2022), mbc–E21.

[203] Kenneth G Geles and Stephen A Adam. "Germline and developmental roles of the nuclear transport factor importin (α) 3 in C. elegans". In: *Development* 128.10 (2001), pp. 1817–1830.

[204] B Sönnichsen et al. "Full-genome RNAi profiling of early embryogenesis in Caenorhabditis elegans". In: *Nature* 434.7032 (2005), pp. 462–469.

[205] Alessandro De Simone, François Nédélec, and Pierre Gönczy. "Dynein transmits polarized actomyosin cortical flows to promote centrosome separation". In: *Cell reports* 14.9 (2016), pp. 2250–2262.

[206] Eva Hannak et al. "Aurora-A kinase is required for centrosome maturation in Caenorhabditis elegans". In: *The Journal of cell biology* 155.7 (2001), pp. 1109–1116.

[207] Monica Gotta and Julie Ahringer. "Distinct roles for Gα and G$\beta\gamma$ in regulating spindle position and orientation in Caenorhabditis elegans embryos". In: *Nature cell biology* 3.3 (2001), pp. 297–300.

[208] Tu Nguyen-Ngoc, Katayoun Afshar, and Pierre Gönczy. "Coupling of cortical dynein and Gα proteins mediates spindle positioning in Caenorhabditis elegans". In: *Nature cell biology* 9.11 (2007), pp. 1294–1302.

[209] Kelly Colombo et al. "Translation of polarity cues into asymmetric spindle positioning in Caenorhabditis elegans embryos". In: *Science* 300.5627 (2003), pp. 1957–1961.

[210] Raymond E Goldstein and Jan-Willem van de Meent. "A physical perspective on cytoplasmic streaming". In: *Interface focus* 5.4 (2015), p. 20150030.

[211] Victoria E Deneke et al. "Self-organized nuclear positioning synchronizes the cell cycle in Drosophila embryos". In: *Cell* 177.4 (2019), pp. 925–941.

[212] Kexi Yi et al. "Dynamic maintenance of asymmetric meiotic spindle position through Arp2/3-complex-driven cytoplasmic streaming in mouse oocytes". In: *Nature cell biology* 13.10 (2011), pp. 1252–1258.

[213] HaiYang Wang et al. "Symmetry breaking in hydrodynamic forces drives meiotic spindle rotation in mammalian oocytes". In: *Science advances* 6.14 (2020), eaaz5004.

[214] Marc Kirschner John Gerhart. *Cells, Embryos, And Evolution.* Blackwell Science, 1997. ISBN: 0-86542-574-4.

[215] Naor Sagy et al. "Prediction and control of symmetry breaking in embryoid bodies by environment and signal integration". In: *Development* 146.20 (Oct. 2019). dev181917. ISSN: 0950-1991. DOI: `10.1242/dev.181917`. URL: `https://doi.org/10.1242/dev.181917`.

[216] Fred Etoc et al. "A balance between secreted inhibitors and edge sensing controls gastruloid self-organization". In: *Developmental cell* 39.3 (2016), pp. 302–315.

[217] Zhechun Zhang et al. "Mouse embryo geometry drives formation of robust signaling gradients through receptor localization". In: *Nature communications* 10.1 (2019), pp. 1–14.

[218] Stefan Münster et al. “Integrin-mediated attachment of the blastoderm to the vitelline envelope impacts gastrulation of insects”. In: *BioRxiv* (2018), p. 421701.

List of publications

Archit Bhatnagar, Michael Nestler, Peter Groß, Mirna Kramer, Mark Leaver, Axel Voigt, Stephan W. Grill
Axis convergence in *C. elegans* embryos
Manuscript submitted

Rana Amini, Archit Bhatnagar, Raimund Schlüßler, Stephanie Möllmert, Jochen Guck, Caren Norden
Amoeboid-like migration ensures correct horizontal cell layer formation in the developing vertebrate retina
eLife 11:e76408

Acknowledgements

As is usually the case, this thesis would not have been possible without a lot of people. I would like to thank as many as possible here, but my apologies in advance if I miss anyone. First and foremost, I would like to thank Stephan for giving me the opportunity to work in the awesome Grill lab. I'll be forever grateful for both his scientific guidance and feedback throughout the project and his guidance and encouragement for my personal development. I would like to thank him especially for supporting me through the tough times during the start of my PhD. I would also like to thank my TAC committee, Frank Jülicher and Elisabeth Fischer-Friedrich, for their criticisms and advice on the project, which helped in its development. I also thank the LMF (especially Britta) for amazing microscope support, Carolyn from the international office for support in dealing with housing and visa, and Ivan Baines for his help during the earlier parts of my PhD.

A big thanks goes to Peter Groß, who started this project before I joined with Mirna Kramar and Michael Nestler, and introduced me to the wonderful world of experimental biophysics with *C. elegans* worms. Peter patiently taught me how to work with *C. elegans* worms, how to use (and not break) the microscope and subsequent analysis of the images taken during microscopy. I am very thankful for Peter's guidance in both scientific and non-scientific matters. I also thank Mark Leaver for his guidance through the later parts of the PhD project, for his help on genetic manipulations in *C. elegans*, and for patiently listening to my ramblings. Thanks also to my collaborators from TU Dresden, Michael Nestler and Axel Voigt, for a fruitful collaboration and the numerous numerical simulations that support and advance the work described in this thesis. I would also like to thank all those who corrected and provided feedback on my thesis, in spite of their busy schedule.

The Grill lab is an amazing place to work in, thanks in no small part to the amazing people that make up the lab. Thanks to everyone in the lab for making this awesome place – Peter, Lokesh, Arjun, Teije, Argo, Mark, Saurabh, Júlia, Victoria, Jóse, Sandeep, Christoph, Pranay, Tina Wiegand, Julia Pfanzelter, Rana, Yahor, Andrea, Kyle, Debayan, Jamie, Adrian, Patrick, Arittri, Jan, Isabel, Lutz, Gisela – I apologize if I missed anyone. I thank Lokesh for his "life advices", and for the board game nights. Thanks to Arjun for all the discussions, and for letting me ramble on various topics during our walks back from work to home. I also thank the Dutch faux-Jesus of the lab, Teije, who was always ready to help with his genetics knowledge and more. Thanks to Victoria and Argo for helpful discussions on PhD life and beyond. Thanks to Andrea, Debayan and Jamie for help with the microscope after the GPU surgery, and also to Jamie for his advice on writing. I would also like to thank Yahor and Arjun for the evergreen discussions on crazy experimental and theory ideas. Thanks also to the technicians – Karin, Tina Neumann and Friedricke – who helped me settle in the lab at the start, and were always ready to help me out with any experimental setup, however crazy it sounded. The Grill lab was (and is) my second home away from home, and I would thank everyone in the lab for making it so.

I would also like to thank the Brian, Birgit and Cassandra from the PhD office, who helped me navigate the intricacies of the bureaucracy of the PhD program and that of the TU Dresden. Thanks also the IMPRS 2018 selection batch, who became some of my closest friends in Dresden – Adrian, Isabel, Aryaman, Manan, Abhijeet and others. I will never forget the crazy and wonderful time I had during the PhD party preparation with them. I would also like to thank Kaushik, Anatol, Huang, Matthäus and Joy for their help and advice at the start of my PhD that led me to the Grill lab – and thanks especially to Kaushik without whom I would have struggled in my early days in Dresden. I would also like to thank the MPI-CBG board game group of Regis, Albine, Tyler, Ilker and others that introduced me to board games. Thanks also to Pandemic board games group of Ilker, Lokesh and Tyler, who kept me sane during the pandemic in 2020 and after. I would also like to acknowledge "Elbe ke albele": Aryaman, Manan, Abhijeet and Alishan, who have been amazing friends during my stay here in Dresden.

Finally, I would like to thank my parents and sister, without whose support and encouragement I would never be here in the first place – and to whom this thesis is dedicated. I do not have the words to express my thanks to them, and am deeply indebted to their support.

Erklärung entsprechend § 5.5 der Promotionsordnung

Hiermit versichere ich, dass ich die vorliegende Arbeit mit dem Titel "Elucidating the mechanism of AP axis alignment in the *C. elegans* embryo" ohne unzulässige Hilfe Dritter und ohne Benutzung anderer als der angegebenen Hilfsmittel angefertigt habe; die aus fremden Quellen direkt oder indirekt übernommenen Gedanken sind als solche kenntlich gemacht. Die Arbeit wurde bisher weder im Inland noch im Ausland in gleicher oder ähnlicher Form einer anderen Prüfungsbehörde vorgelegt.

Die Dissertation wurde im Zeitraum vom 23.09.2018 bis 28.03.2023 verfasst und von Prof. Dr. Stephan W. Grill am Max-Planck-Institut für molekulare Zellbiologie und Genetik, Dresden betreut.

Meine Person betreffend erkläre ich hiermit, dass keine früheren erfolglosen Promotionsverfahren stattgefunden haben. Ich erkenne die Promotionsordnung des Bereiches für Mathemathik und Naturwissenschaften, Technische Universität Dresden vom 23.02.2011 an.

Dresden, den 28.03.2023

Declaration according to § 5.5 of the doctoral regulations

I hereby certify that I have prepared this thesis entitled "Elucidating the mechanism of AP axis alignment in the *C. elegans* embryo" without the unauthorized assistance of third parties and without the use of any aids other than those indicated; the ideas taken directly or indirectly from outside sources are identified as such. The thesis has not been submitted to any other examination authority in the same or a similar form, neither in Germany nor abroad.

The dissertation was written in the period from 23.09.2018 to 28.03.2023 and supervised by Prof. Dr. Stephan W. Grill at the Max Planck Institute for Molecular Cell Biology and Genetics, Dresden.

I hereby declare that no previous unsuccessful doctoral procedures have taken place. I declare that I recognize the doctoral regulations of the Bereich für Mathemathik und Naturwissenschaften of the Technische Universität Dresden dated 23.02.2011.

Dresden, 28.03.2023